



HAL
open science

Tracing lithium mobility in polymer-ceramic solid-electrolyte: insights from lithium isotopic labelling, combined ToF-SIMS/ssNMR characterisation, and numerical simulations

Thomas Meyer

► To cite this version:

Thomas Meyer. Tracing lithium mobility in polymer-ceramic solid-electrolyte: insights from lithium isotopic labelling, combined ToF-SIMS/ssNMR characterisation, and numerical simulations. Chemical engineering. Université Grenoble Alpes [2020-..], 2023. English. NNT: 2023GRALI111. tel-04824584

HAL Id: tel-04824584

<https://theses.hal.science/tel-04824584v1>

Submitted on 7 Dec 2024

HAL is a multi-disciplinary open access archive for the deposit and dissemination of scientific research documents, whether they are published or not. The documents may come from teaching and research institutions in France or abroad, or from public or private research centers.

L'archive ouverte pluridisciplinaire **HAL**, est destinée au dépôt et à la diffusion de documents scientifiques de niveau recherche, publiés ou non, émanant des établissements d'enseignement et de recherche français ou étrangers, des laboratoires publics ou privés.

THÈSE

Pour obtenir le grade de

DOCTEUR DE L'UNIVERSITÉ GRENOBLE ALPES

École doctorale : I-MEP2 - Ingénierie - Matériaux, Mécanique, Environnement, Energétique, Procédés, Production

Spécialité : 2MGE - Matériaux, Mécanique, Génie civil, Electrochimie

Unité de recherche : CEA Grenoble / LITEN

Analyse de la mobilité du lithium dans un électrolyte solide polymère-céramique : apports du traçage isotopique du lithium, de la caractérisation combinée ToF-SIMS/ssNMR et de la simulation numérique

Tracing lithium mobility in polymer-ceramic solid-electrolyte: insights from lithium isotopic labelling, combined ToF-SIMS/ssNMR characterisation, and numerical simulations

Présentée par :

Thomas MEYER

Direction de thèse :

Eric DE VITO

DIRECTEUR DE RECHERCHE, CEA centre de Grenoble, Université Grenoble Alpes

Directeur de thèse

Thibaut GUTEL

INGENIEUR-CHERCHEUR, HDR, CEA centre de Grenoble, Université Grenoble Alpes

Co-encadrant de thèse

Michel BARDET

INGENIEUR HDR, CEA Centre de Grenoble, Université Grenoble Alpes

Co-encadrant de thèse

Hervé MANZANAREZ

INGENIEUR CHERCHEUR, CEA centre de Grenoble

Co-encadrant de thèse

Rapporteurs :

Laure MONCONDUIT

DIRECTRICE DE RECHERCHE, CNRS délégation Occitanie Est

Philippe MOREAU

PROFESSEUR DES UNIVERSITES, Université de Nantes

Thèse soutenue publiquement le **5 décembre 2023**, devant le jury composé de :

Eric DE VITO

DIRECTEUR DE RECHERCHE, CEA centre de Grenoble

Directeur de thèse

Laure MONCONDUIT

DIRECTRICE DE RECHERCHE, CNRS délégation Occitanie Est

Rapporteuse

Philippe MOREAU

PROFESSEUR DES UNIVERSITES, Université de Nantes

Rapporteur

Yann BULTEL

PROFESSEUR DES UNIVERSITES, Grenoble INP

Président

Elodie SALAGER

CHARGÉE DE RECHERCHE, CNRS délégation Limousin Poitou-Charentes

Examinatrice

Anja HENSS

ASSOCIATE PROFESSOR, Justus-Liebig Universität Giessen

Examinatrice

Invités :

Margaud LECUYER

INGENIEURE DOCTEURE, Blue Solutions

Jean ALMORIC

INGENIEUR DOCTEUR, Orsay Physics



Remerciements

Ces travaux de thèse ont été réalisés au commissariat à l'énergie atomique et aux énergies alternatives (CEA) à Grenoble au sein de différents laboratoires dont le LCAE, LM, RM et LMP. Je tiens à remercier mon directeur de thèse, Eric De Vito, et mes encadrants, Thibaut Gutel, Michel Bardet et Hervé Manzanarez pour leur précieux soutien tout au long de ma thèse. Merci pour tout ce que vous m'avez transmis. Je ressors enrichi humainement et scientifiquement de ces trois années passées à vos côtés. Merci pour votre investissement et vos encouragements quotidiens qui ont été essentiels pour mener ce travail à son terme. Cette thèse s'inscrit aussi dans un projet interne CEA plus vaste, le programme FOCUS batterie. Merci à Didier Jamet d'avoir orchestré des rencontres entre doctorants en promouvant les échanges entre expérimentateurs et modélisateurs.

Merci à l'ensemble du jury pour sa venue à Grenoble et pour avoir conduit à des discussions scientifiques enrichissantes et approfondies. Le temps des échanges a été un réel plaisir. Je suis profondément reconnaissant envers Laure Monconduit et Philippe Moreau, les rapporteurs scientifiques de ma thèse. Leur intérêt manifesté à l'égard de mes travaux ainsi que leurs retours détaillés et leurs questions précises m'ont permis d'exposer la complexité de mon sujet de thèse. Je tiens également à remercier Anja Henss et Elodie Salager, examinatrices, ainsi que Yann Bultel, président du jury, pour avoir accepté de participer à l'évaluation de ma thèse et pour avoir apporté leur expertise respective. Je suis également reconnaissant envers Margaud Lécuyer et Jean Almoríc, membres invités, dont les contributions ont permis d'enrichir les discussions et ont contribué à situer l'importance de mes recherches dans le contexte industriel, que ce soit dans le domaine de la fabrication de batteries ou dans le développement d'instruments de pointe.

Un grand merci tout particulier à Manon Berthault dont les travaux de recherches ont été cruciaux pour la réalisation des miens. Ses travaux m'ont fait gagner un précieux temps et démarrer sur des bases solides. Merci pour le riche manuscrit sur lequel j'ai pu m'appuyer et pour ses réponses à mes diverses questions !

Merci infiniment à Pierre-Alain Bayle et Katharina Märker pour leur disponibilité et leur aide en RMN à l'état solide. Toujours là pour me dépanner sur l'équipement ou les interprétations des données !

Merci à Claire Villevieille et à Jean Baptiste Sirven d'avoir accepté de faire partie de mon comité de suivi de thèse au travers duquel ils ont à chaque fois soulevé des aspects de mon sujet pertinents à étudier. Vos retours ont toujours été un moteur pour avancer.

Merci à Doriane Gallot—Duval et Jean Baptiste Sirven pour notre collaboration très enrichissante. L'implication de Doriane a été d'une grande valeur pour la réussite de nos projets communs. C'était un plaisir d'échanger ensemble tout au long de ma thèse.

Je souhaite également remercier Jean Almoríc et Thibault Genieys d'Orsay Physics pour avoir initié une étude commune prometteuse. Leurs techniques de caractérisation avancées ont permis de mener à bien mon projet de thèse et en parallèle de mettre en lumière les performances de leurs équipements.

Je tiens aussi à remercier Paul Aguirre pour avoir mis au point un logiciel de traitement de données ToF-SIMS sur Python accélérant grandement le traitement des données et le rendant plus fiable. Merci pour sa présence et son soutien tout au long de ma thèse.

Merci à Eléonore Mourad et Julien Lavie qui n'ont pas hésité à me prendre sous leurs ailes pendant leur présence au CEA et avec qui j'ai beaucoup appris.

Merci à Claire Deilhes pour m'avoir aidé à réaliser des analyses FTIR et pour avoir pris des nouvelles des avancées de ma thèse.

Merci à Marie-Eve Yvenat, Lionel Blanc et Benoit Chavillon d'avoir pris le temps de mettre en place des premiers dépôts de Li-métal par dépôt PVD sur mes matériaux.

Il m'est indispensable de remercier sincèrement le noyau de doctorants à la PFNC avec qui les journées de travail passent tellement vite ! et notamment avec le noyau dur du bureau C159 ! Mention spéciale pour Tarek Spelta, Roman Charvier et Roberto Fantin ! Je n'oublie pas non plus les stagiaires, alternants (pour certains devenus doctorant entre-temps), doctorants, post-doctorants et ingénieurs/chercheurs que j'ai eu la chance de rencontrer pendant ma thèse.

La phase de rédaction de la thèse n'est pas des plus facile. Merci notamment à Tarek Spelta, Julie Michel, Claire Guyot et Julia Levy. Entre les astuces sur Word ou Origin, les pique-niques dans les parcs pendant la canicule, le soutien moral et les courses contre la montre pour sortir à temps des locaux, cette période a été plus agréable à traverser grâce à vous !

Merci également à Justin Bouvet et Mélanie Pichardo pour leur accueil dans leur bureau toujours plein de bonne humeur ! Et un grand merci à Mélanie Pichardo pour son soutien constant depuis la première heure sur Grenoble ! La découverte de cette ville et de ces alentours a été épique ensemble !

Je tiens à remercier toutes les personnes qui m'ont accompagné et soutenu pendant mes trois ans de thèse au sein de CEA, notamment mes collègues et experts du LCAE, L2PC, LM, RM et LMP. Ce fut un grand plaisir de travailler ou d'échanger avec chacun d'entre vous. Espérons que nos chemins se croiseront à nouveau dans le futur.

Je ne peux pas clore mes remerciements sans évoquer tous ceux et celles qui m'ont permis d'en arriver là à leur manière. Me lancer dans un tel projet de recherche a été possible en grande partie grâce à mes enseignantes de collège, Virginie Bove, et de lycée, Nathalie Staat, qui m'ont donné le goût pour les sciences et notamment la Physique-Chimie. Puis, c'est au sein de l'ENSMAS (ex-ENSCBP) que j'ai eu l'opportunité de me spécialiser en chimie des matériaux pour le stockage et la conversion d'électricité au travers d'enseignements de qualité et de stages d'ingénieur dans le domaine des batteries qui ont été très formateurs. C'est pourquoi je tiens sincèrement à remercier notamment Liliane Guerlou-Demourgues, Laurence Croguennec, Andrew Naylor et Yvan Reynier.

Enfin, je remercie ma famille et mes amis pour leur soutien et leurs encouragements.

Table of Contents

Abbreviations list.....	8
Abstract.....	9
Résumé.....	10
General introduction	12
Chapter I. State-of-the-art: Lithium tracing for the characterisation of solid-state lithium metal batteries	18
I.1. Solid-state lithium metal batteries	19
1.1. Solid-state electrolyte properties	20
a. Poly(ethylene oxide) (PEO)-based electrolyte.....	20
b. Oxide-based ceramic electrolytes.....	22
1.2. Interest of composite solid-state electrolytes	25
I.2. Lithium isotopic labelling as a tool to trace lithium	27
2.1. Definitions laying foundations of the following works.....	27
a. Lithium isotopic abundance.....	27
b. Lithium isotopic labelling and tracing	28
c. Lithium mobility	28
2.3. Various characterisation techniques allowing lithium isotopic analyses	29
a. Secondary-ion mass spectrometry (SIMS) and time-of-flight SIMS (ToF-SIMS)	29
b. Nuclear magnetic resonance (NMR)	32
c. Inductively coupled plasma mass spectrometry (ICP-MS) technique.....	35
d. Laser-induced breakdown self-reversal isotopic spectrometry (LIBRIS)	36
f. Neutron diffraction.....	37
g. Summary.....	38
2.2. Battery applications of lithium isotopic tracing	39
Conclusion	51
Chapter II. Methodologies development to accurately determine lithium isotopic abundance	52
II.1. Solid-state electrolytes preparation and electrochemical tests on specify devices	53
1.1. Polymer electrolytes preparation with a lithium salt enriched in ⁶ Li	53
a. The selected materials: poly(ethylene oxide) (PEO) and lithium salt (LiTFSI).....	53
b. Polymer electrolytes preparation	54
1.2. Commercial ceramics and dispersion preparation.....	55

a. LLZTO ceramic pellet.....	55
b. LLZTO ceramic particles	57
c. Dispersion preparation of a polymer electrolyte containing ceramic particles	57
1.3. Electrochemical experiments performed on various devices	57
a. Electrochemical impedance spectrometry (EIS).....	58
b. Chronoamperometry (CA) technique	58
c. Chronopotentiometry (CP) technique.....	59
II.2. Determination of relevant parameters of ToF-SIMS and ssNMR techniques for lithium isotopes characterisation	60
2.1. Relative lithium isotopic abundance determination by ToF-SIMS	60
2.2. Absolute lithium isotopic abundance determination by high-resolution ssNMR.....	64
II.3. Determination of lithium isotopic abundance with the developed methodologies	69
3.1. Polymer electrolytes characterised by ToF-SIMS.....	69
3.2. Polymer electrolytes characterised by high-resolution ssNMR.....	71
3.3. Comparison of the results.....	73
Conclusion	75
Chapter III. Lithium dynamics investigated in a polymer electrolyte by advanced characterisation techniques based on the lithium isotopic labelling.....	76
III.1. Description of the experimental setup to study lithium dynamics	77
1.1. <i>In-plane</i> configuration	77
1.2. Experimental protocols and sample preparation.....	77
III.2. Determination of lithium dynamics through <i>in-plane</i> devices.....	79
2.1. Characterisation of lithium dynamics in <i>in-plane</i> devices by ToF-SIMS	79
2.2. Characterisation of lithium dynamics in <i>in-plane</i> devices by modelling	83
2.3. Deeper interpretation of ToF-SIMS results thanks to numerical simulations	86
III.3. Lithium dynamics determination in the <i>in-plane</i> device after 120 <i>h</i> at 60° C	90
3.1. Surface analyses of the <i>in-plane</i> device by ToF-SIMS	91
3.2. Global analyses of the <i>in-plane</i> device by high-resolution ssNMR.....	92
3.3. Deeper interpretation of ToF-SIMS results thanks to numerical simulations	94
Conclusion	99
Chapter IV. Lithium dynamics through an <i>in-plane</i> and a <i>sandwich</i> device.....	100
IV.1. Lithium diffusion through the <i>in-plane</i> device under voltage.....	101
1.1. Description of the <i>in-plane</i> device assembly	101
1.2. Electrochemical results.....	103

a. Electrochemical impedance spectroscopy (EIS) characterisation	103
b. Chronoamperometry (CA) sequence	105
1.3. Advanced characterisations based on lithium isotopic tracing	108
a. ToF-SIMS characterisations.....	108
b. High-resolution ssNMR characterisations.....	114
1.4. A modelling approach to better understand lithium dynamics	119
a. Description of the geometries and involved dynamics	119
b. Use of the generalised mixing model (GMM)	121
c. Use of an isotopic mixing model (IMM)	128
IV.2. Lithium dynamics through the <i>sandwich</i> device under electrical current	138
2.1. Description of the <i>sandwich</i> device	138
2.2. Electrochemical results.....	140
a. Electrochemical impedance spectroscopy (EIS) characterisation	140
b. A chronopotentiometry (CP) sequence	141
2.3. Advanced characterisations based on lithium isotopic tracing.....	142
a. ToF-SIMS characterisations.....	142
b. High-resolution ssNMR characterisations.....	147
2.4. Modelling approach to better understand lithium dynamics	152
a. Description of the <i>sandwich</i> geometry	152
b. Use of an isotopic mixing model (IMM).....	153
Conclusion	161
Chapter V. Lithium dynamics through a composite solid-state electrolyte: A ceramic dispersion in a polymer matrix	162
V.1. Lithium dynamics through a composite solid-state electrolyte	163
5.1. Description of the <i>dispersion</i> device	163
5.2. Electrochemical results.....	164
a. Electrochemical impedance spectroscopy (EIS) characterisation	164
b. A chronopotentiometry (CP) sequence	165
5.3. Advanced characterisations.....	167
a. High-resolution ssNMR characterisations	167
b. ToF-SIMS characterisations.....	176
c. Orthogonal ToF-SIMS characterisation coupled with focused ion beam scanning electron microscopy (FIB-SEM) characterisations.....	177
5.4. Perspectives.....	188

Conclusion	189
General conclusion and perspectives	190
References.....	193
Appendices – Chapter I.....	204
Appendices – Chapter II.....	207
Appendices – Chapter III.....	208
Appendices – Chapter IV	215
Appendices – Chapter V	223
Appendices – Résumé étendu en français.....	224

Abbreviations list

ALD: Atomic Layer Deposition	LMIG: Liquid Metal Ion Gun
ASSB: All-Solid-State Battery	LMP: Lithium Metal Polymer
CA: ChronoAmperometry	MAS: Magic Angle Spinning
CP: ChronoPotentiometry	MC-ICP-MS: Multi-Collector Inductively Coupled Plasma Mass Spectrometry
2DLA: 2 Dimensional Large Area	NMR: Nuclear Magnetic Resonance
EIS: Electrochemical Impedance Spectroscopy	OCV: Open Circuit Voltage
FIB-SEM: Focused Ion Beam Scanning Electron Microscopy	o-ToF-SIMS: orthogonal ToF-SIMS
FID: Free Induced Decay	PECVD: Plasma-Enhanced Chemical Vapor Deposition
FWHM: Full Width at Half Maximum	PEO: Poly(Ethylene Oxide)
GD-SF-MS: Glow Discharge Sector Field Mass Spectrometry	SEI: Solid Electrolyte Interface
GMM: Generalised Mixing Model	SEM: Scanning Electron Microscope
ICP-MS: Inductively Coupled Plasma Mass Spectrometry	SIMS: Secondary Ion Mass Spectrometry
IMM: Isotopic Mixing Model	SPE: Solid Polymer Electrolyte
LA-ICP-MS: Laser Ablation Inductively Coupled Plasma Mass Spectrometry	SSE: Solid-State Electrolyte
LIBRIS: Laser-Induced Breakdown self-Reversal Isotopic Spectrometry	ssNMR: solid-state Nuclear Magnetic Resonance
LIBS: Laser-Induced Breakdown Spectrometry	ToF-SIMS: Time-of-Flight Secondary Ion Mass Spectrometry
LITFSI: Lithium bis(trifluoromethanesulfonyl) imide	UHV: Ultra-High Vacuum
LLZO: Lithium Lanthanum Zirconium Oxide	
LLZTO: Tantalum doped Lithium Lanthanum Zirconium Oxide	

Abstract

Today, most of the commercially available Li-ion batteries use liquid electrolyte (a lithium salt dissolved in an organic solvent). Substituting liquid electrolyte by a solid-state one is considered as a highly promising way to increase electrochemical performances and safety of the next lithium battery generation. Indeed, composite solid-state electrolytes are designed to combine the positive features of polymer and ionic conductive ceramic electrolytes. Improving their critical properties such as ionic conductivity and processability is a crucial step required to be competitive with liquid electrolytes.

My work focuses on understanding Li⁺ ions diffusion mechanisms occurring within solid-state electrolytes composed of poly(ethylene oxide) containing lithium bis(trifluoromethanesulfonyl)imide as lithium salt, and the garnet-type ceramic (Li_{6.4}La₃Zr_{1.4}Ta_{0.6}O₁₂). To study lithium mobility, time-of-flight secondary ion mass spectrometry (ToF-SIMS) and high-resolution solid-state nuclear magnetic resonance (ssNMR) are two complementary advanced techniques allowing studies based on lithium isotopic tracing. A chemical analysis by ToF-SIMS allows to determine at the surface ⁶Li isotopic abundance from intensities of ⁶Li⁺ and ⁷Li⁺ fragments at submicronic scale. On the other hand, probing the chemical environments of ⁶Li and ⁷Li nuclei by ssNMR allows to estimate ⁶Li abundance in bulk by combining ⁶Li and ⁷Li absolute integrals. Furthermore, lithium quantification is possible by using ssNMR. In this work, ToF-SIMS and ssNMR are combined together to develop robust methodologies based on the study of polymer electrolytes prepared with various ⁶Li abundances. Both data acquisition conditions and data processing are optimised, allowing ⁶Li abundance estimation of a solid lithiated material with a high precision of 1% and 2%, respectively.

These methodologies are implemented to characterise Li⁺ ions diffusion (including self-diffusion) after applying a chronoamperometry or a chronopotentiometry (CP) sequence at 60° C on electrochemical systems. They are based on two geometries growing in complexity, namely *in-plane* and *sandwich*. A positive electrode in lithium enriched at 95.4% in ⁶Li and a negative electrode in lithium at natural isotopic abundance (7.6% of ⁶Li) are used. The ⁶Li-foil induces ⁶Li⁺ ions diffusion through the device already containing lithium at natural isotopic abundance. Lithium dynamics effects can be investigated by detecting both isotopes. ssNMR characterisations prove that, after applying a CP sequence, ⁶Li⁺ ions diffuse through all the layers of a *sandwich* device because ⁶Li abundance estimation is higher than ⁶Li natural abundance. Finally, Li⁺ ions diffusion is thoroughly studied through a third device composed of a polymer electrolyte matrix containing a dispersion of ceramic particles. Such composite electrolyte could be implemented in commercial solid-state batteries. According to ssNMR characterisations, ceramic particles have a greater ⁶Li content than the polymer electrolyte matrix after applying a CP sequence. Furthermore, models of lithium isotopic exchanges are described. They take into account continuity equations solving non-equilibrium transport under voltage, and electrochemical transfers at interfaces. Implementing experimental results into numerical simulations enable to extract critical parameters such as Li⁺ ions self-diffusion coefficient in solid-state electrolytes or lithium transfer properties at interfaces. With the help of relevant physical models, strategies can be developed to improve solid-state electrolyte design.

All these results obtained by using lithium isotopic tracing illustrate the strengths of the methodologies presented in this work. They provide new keys to a better understanding of Li⁺ ions diffusion pathways in these complex devices. Methodologies may also be adapted to investigate lithium dynamics in solid materials for other applications.

Résumé

Aujourd'hui, la plupart des batteries Li-ion commercialisées utilisent un électrolyte liquide (un sel de lithium dissous dans un solvant organique). Sa substitution par un électrolyte solide pourrait améliorer les performances électrochimiques et la sécurité de la future génération de batteries au lithium. Les électrolytes solides composites sont conçus pour combiner les avantages des électrolytes polymère et céramique. Améliorer leur conductivité ionique et leur mise en forme est crucial pour qu'ils soient compétitifs par rapport aux électrolytes liquides.

Mon travail porte sur la compréhension des mécanismes de diffusion du lithium dans des électrolytes solides composés de poly(oxyéthylène) contenant du lithium bis(trifluorométhanesulfonyl) imide, et de céramique grenat ($\text{Li}_{6,4}\text{La}_3\text{Zr}_{1,4}\text{Ta}_{0,6}\text{O}_{12}$). Pour étudier la mobilité du lithium, les informations fournies par la spectrométrie de masse à ions secondaires à temps de vol (ToF-SIMS) et par la résonance magnétique nucléaire à l'état solide haute-résolution (ssNMR) sont associées. Ces deux techniques d'analyse complémentaires permettent des analyses fondées sur le traçage isotopique du lithium. Une analyse chimique par ToF-SIMS permet de déterminer en surface l'abondance en ${}^6\text{Li}$ à partir des intensités des fragments ${}^6\text{Li}^+$ et ${}^7\text{Li}^+$ à une échelle submicrométrique. Sonder l'environnement chimique du ${}^6\text{Li}$ et ${}^7\text{Li}$ par ssNMR dans le volume du matériau permet d'estimer l'abondance en ${}^6\text{Li}$ en combinant leurs intégrales absolues. De plus, la quantification des isotopes du lithium est possible en ssNMR. Ces travaux décrivent des méthodologies ToF-SIMS et ssNMR robustes permettant l'analyse d'électrolytes polymères présentant différentes abondances en ${}^6\text{Li}$. L'acquisition des données et leur traitement sont optimisés afin d'obtenir une incertitude de 1% et de 2% sur l'abondance en ${}^6\text{Li}$, respectivement.

Ces méthodologies sont mises en œuvre pour étudier la diffusion du lithium (incluant l'autodiffusion) après application d'une chronoampérométrie ou d'une chronopotentiométrie (CP) à 60° C sur des systèmes électrochimiques spécifiques. Ces derniers présentent deux géométries de complexité croissante, appelées « *in-plane* » et « *sandwich* ». Une électrode positive de lithium enrichi à 95.4% en ${}^6\text{Li}$ et une électrode négative de lithium à l'abondance naturelle (7.6% de ${}^6\text{Li}$) sont utilisées. Le feuillard de ${}^6\text{Li}$ induit la diffusion des ions ${}^6\text{Li}^+$ au travers d'un système contenant déjà du lithium à l'abondance naturelle. Son comportement peut être étudié en détectant alors ses deux isotopes. Il est prouvé par ssNMR que les ions ${}^6\text{Li}^+$ diffusent au travers de toutes les couches du système « *sandwich* » après l'application d'une CP car les estimations de l'abondance en ${}^6\text{Li}$ sont supérieures à l'abondance naturelle. Pour finir, la diffusion du lithium au travers d'un électrolyte polymère contenant une dispersion de particules de céramique est méticuleusement étudiée. Un tel électrolyte composite pourrait être mis en œuvre dans des batteries « tout-solide » commerciales. D'après les caractérisations par ssNMR, les particules de céramique contiennent plus de ${}^6\text{Li}$ que le polymère après application d'une CP. Des modèles décrivant les échanges isotopiques du lithium ont été développés. Ils prennent en compte des équations de continuité résolvant le transport hors équilibre sous champ, ainsi que les transferts électrochimiques aux interfaces. La comparaison des résultats expérimentaux aux simulations numériques conduit à déterminer des paramètres importants tels que le coefficient d'autodiffusion du lithium ou les propriétés de transfert aux interfaces. Avec des modèles physiques adaptés, des stratégies peuvent être développées pour améliorer la conception des électrolytes solides.

Les résultats obtenus offrent ainsi de nouvelles clés de compréhension des chemins de diffusion du lithium dans ces matériaux. Ces méthodologies peuvent en outre être adaptées à d'autres applications ou à d'autres matériaux contenant du lithium.

General introduction

- **Energy transition towards full electrification**

The main goal of the Paris Agreement adopted in 2015 lies in global warming limit below 2° C. [1] This objective can be reached by reducing drastically the emitted greenhouse gas. Several countries have established their own energy transition plans to achieve this target. Germany has committed to reducing its greenhouse gas emissions by almost 90% by 2050, and United Kingdom to eliminate entirely them. [1] The Paris Agreement has also stated that developed countries have to provide financial support to developing countries to face climate challenges.

The development of electric vehicles (EV) is presented as one way among the potential routes to reduce greenhouse gas emissions. Such objective is included in many energy transition plans established by developed countries. Wu and Zhang studied the real impact of EVs on air pollutants and greenhouse gases, depending on the country where they are used. [2] Their results demonstrated that using EVs has a huge effect on CO₂ emission reduction, compared to the use of conventional gasoline internal combustion engine vehicles (ICEV). Nonetheless, the associated air pollution due to other gases, such as SO₂ or NO_x, differs regarding countries. [2]

The development of EVs transfers pollution from the use phase of ICEV to the production phase which highly depend on the origin of electricity. [2] Nuclear power and hydropower are the main sources of electrical energy in France (76.1%) and in Brazil (75.2%), respectively. [2] This is why replacement of a gasoline ICEV by a plug-in hybrid electric vehicles (PHEV) leads to a CO₂ emission reduction of 2365 and 2356 $kg \cdot year^{-1}$, respectively. [2] Even higher reduction is estimated at 2834 and 2823 $kg \cdot year^{-1}$, with the use of EVs. [2] On the contrary in China, the primary source of electrical energy is derived from coal. Thus the use of EVs is not efficient to reduce CO₂ emission in this country. To conclude, the real impact of EVs development depends on the energy mix of each country.

Various batteries technologies are currently investigated. Ma *et al.* presented several research strategies, such as lithium-oxygen or lithium-sulfur, sodium-ion, potassium-ion or solid-state lithium batteries (Figure 0-1). [3]

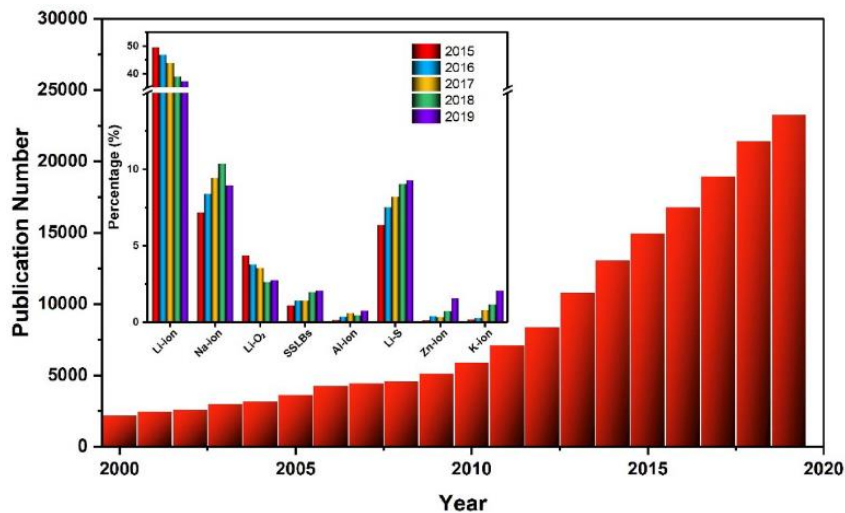


Figure 0-1. Publications related to battery concerns from 2000 to 2019. The insert highlights the publication percentage investigating Li-ion, Na-ion, Li-O₂, solid-state lithium-ion battery technologies (SSLB), Al-ion, Li-S, Zn-ion and K-ion battery. [3]

Ma *et al.* have listed battery technologies identified in articles published between 2000 and 2019 (Figure 0-1). The number of publications increases exponentially. The main studied technology is currently the Li-ion battery.

- **Li-ion battery**

The Nobel Prize in chemistry 2019 was awarded to three scientists for their contributions paving the way to lithium-ion batteries development and commercialisation. Stanley Whittingham built the first operating lithium battery in the 1970s. It was composed of a titanium disulfide (TiS₂) positive electrode and a lithium metal negative electrode. One advantage of TiS₂ during lithium intercalation lies in the fact that it presents a limited lattice expansion. [4] However, this technology was unsafe due to the use of lithium perchlorate dissolved in dioxolane as liquid electrolyte and metallic anode leading to dendrite growth. Thus, short-circuits and explosions could occur. Goodenough *et al.* replaced the titanium disulfide positive electrode material by lithiated cobalt oxide (LiCoO₂), which has also a good ability to intercalate lithium ions in this lamellar structure. [5] This switch of material allows to increase the battery voltage from 2 V to 4 V. Furthermore, LiCoO₂ has a theoretical energy density of 1.11 kWh · kg_{AM}⁻¹ (considering only the amount of active material (AM)). [5] Finally, Yoshino suggested to replace the lithium metal negative electrode by a petroleum coke avoiding the use of lithium in metallic state. The first Li-ion batteries were commercialised by Sony in 1991.

A Li-ion battery converts electrical energy into chemical energy. This process is reversible, meaning that the battery can be charged again after that the stored chemical energy has been delivered during the discharge of the battery. The Li-ion battery principle is schematised on Figure 0-2.

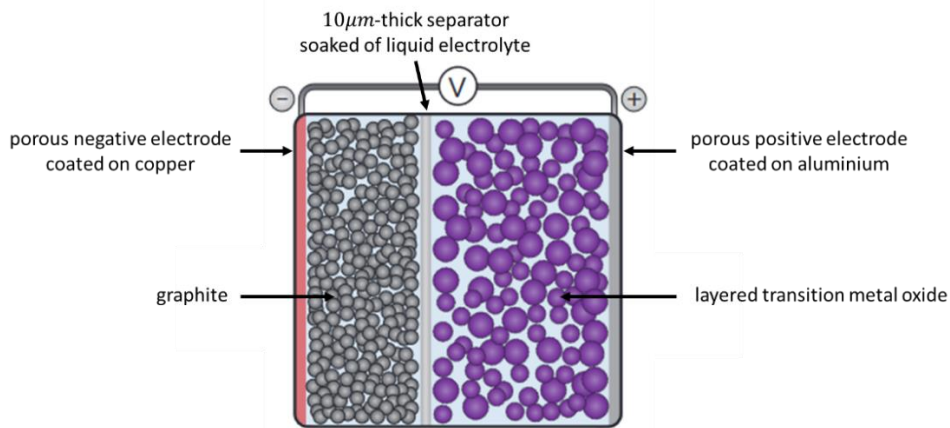


Figure 0-2. Schematic of a Li-ion battery. [6]

Li-ion batteries are composed of three components, a positive electrode, a negative electrode and a separator in-between soaked in liquid electrolyte (Figure 0-2). Liquid electrolyte can easily infiltrate the porous electrodes. [7] Insertion of lithium ions in the electrode materials can occur at triple points linking active material, electronic conductor and liquid electrolyte standing for lithium ionic conductor. [7] Organic liquid fills the voids and enhances the contact at the interface. [8] Furthermore, they are low cost electrolytes and their preparation is simple. [6] Table 0-1 sums up the advantages and drawbacks of Li-ion battery technology.

Table 0-1. Advantages and drawbacks of a conventional Li-ion battery containing a liquid electrolyte. [6] [9] [10] [11] [12]

Li-ion battery	
Advantages	Drawbacks
<ul style="list-style-type: none"> - High voltage: 3.6 V - High energy density: [160; 260] Wh · kg⁻¹ - High power density: [0.5; 1] kW · kg⁻¹ - Lifetime > 3000 cycles - Large operating temperature: [-20;60] °C - Low self-discharge: [2; 8]% per month - Fast charge possible 	<ul style="list-style-type: none"> - Limited stability at high temperature (Degradation over 65°C) - Use of flammable organic liquid electrolytes - Use critical raw materials (Co, Ni, Li) - Sensitive to overcharge

To enhance Li-ion battery performances, all components in particular electrode materials have been improved in the 20 last years and engineering developments have been implemented. Now, they have almost reached their theoretical limits in terms of electrochemical performances. [6] [13] A switch of technology may be a solution to reach even higher energy densities. A way to achieve better electrochemical performances is to develop a disruptive technology such as lithium metal battery. [14] Previously, lithium metal was discarded due to safety issues while using it with liquid electrolyte. Currently, lithium metal as negative electrode can be used in combination with a solid-state electrolyte (SSE). It is seen as the « Holy Grail » to significantly improve battery energy density. [3] [13]

To conclude, conventional lithium-ion batteries still have drawbacks, that can be overcome without a breakthrough technology. Within this scope, solid-state batteries and more specifically the SSEs they contain can represent a promising solution. It will be the prime motivation of this thesis.

- **Insights of solid-state electrolytes (SSE)**

The energy density can be significantly increased by using lithium metal as the negative electrode. [6] It can provide a theoretical capacity of $3,860 \text{ mAh} \cdot \text{g}^{-1}$ and a low potential ($-3.04 \text{ V vs. } H^+/H$). [3] A way to improve lithium metal safely consists in replacing the liquid electrolyte by a SSE, providing higher energy density than conventional Li-ion batteries with carbonates-based liquid electrolytes. The latter are inefficient against dendrite growth, whereas SSEs may impede such detrimental effects. Additionally, SSEs are non-flammable and non-volatile, compared with their counterparts. [11] However, the development of SSEs is not easy for commercial applications, such as electric vehicles. Higher ionic conductivities at typical operating temperatures, higher cycle life, and the possibility of fast charging are required. More specifically some challenges still have to be solved such as intimate contact between lithium metal/SSE or electrode materials/SSE interface. [3] In such context, SSEs need to be investigated in order to select the most promising ones and to enhance their electrochemical performances. Different SSEs can be mixed in order to combine various advantages of each SSE. Among the numerous questions that remain to be answered, the dynamics of lithium in SSEs stands as a key point. This PhD work strives to answer it.

- **Investigation of lithium dynamics through SSEs based on lithium isotopic tracing**

In this PhD work, we investigate lithium mobility in polymer-ceramic SSE known as composite or hybrid electrolytes. Lithium isotopic labelling, combined with time-of-flight secondary ion mass spectrometry (ToF-SIMS) and high-resolution solid-state nuclear magnetic resonance spectroscopy (ssNMR) characterisations, and with numerical simulations are the cornerstones of this research work. Various studies offered the opportunity to developed ToF-SIMS and high-resolution ssNMR methodologies in order to characterise lithium isotopic abundance of battery materials. Indeed, our group has already demonstrated the power of this approach while studying graphite and silicon anodes with liquid electrolytes in particular some investigations related to the solid electrolyte interface (SEI) formation. [15] [16]

This thesis is divided in five chapters. The first chapter relates the interest of solid-state batteries. A specific attention is paid on SSE materials. Studies investigating mainly battery materials based on lithium isotopic labelling are discussed. The advanced characterisation techniques implemented to trace lithium isotopes are presented and compared.

The second chapter introduces the studied materials and the used techniques. Some ToF-SIMS and high-resolution ssNMR methodologies are established to accurately determine

lithium isotopic abundance. Relevant parameters to characterise lithium isotopes are detailed. Furthermore, the developed methodologies are optimised and validated on polymer electrolytes having known lithium isotopic abundances.

The third chapter deals with lithium dynamics investigation in a polymer electrolyte at 60° C. Here, a specific configuration namely *in-plane* is set up in order to facilitate the determination of lithium self-diffusion coefficient in the polymer electrolyte, by combining ToF-SIMS experimental results with numerical simulations.

The fourth chapter focuses on two configurations growing in complexity. The *in-plane* configuration is still considered, but a constant voltage is applied in addition to temperature. An alternative *sandwich* configuration is also designed in order to introduce a ceramic pellet in between two polymer electrolyte layers. Lithium dynamics are studied after applying a constant current density. In both cases, a positive electrode in lithium enriched at 95.4% in ${}^6\text{Li}$ and a negative electrode in lithium at natural isotopic abundance (7.6% of ${}^6\text{Li}$) are used to perform lithium isotopic labelling.

Finally, a polymer electrolyte matrix containing ceramic particles is investigated. The configuration of such composite SSE was named *dispersion*. Lithium dynamics after applying a constant current density are characterised by high-resolution ssNMR and orthogonal ToF-SIMS.

Chapter I. State-of-the-art: Lithium tracing for the characterisation of solid-state lithium metal batteries

Nowadays, the majority of commercially available Li-ion batteries contains liquid electrolytes. The latter are continually evolving to become more efficient and reliable in terms of electrochemical performances and safety. A disruptive battery technology based on solid-state electrolyte (SSE) could overcome Li-ion battery limits. However, SSEs still need to be investigated to reach the targeted properties. Among all the SSEs, composites made of a dispersion of a conductive ceramic particles blend into a polymer matrix containing a lithium salt, may be the most promising. They are expected to merge the different material strengths in terms of electrochemical performances, stability and processability. To make these systems viable for a commercial use, enhancing their ionic conductivity is vital. A better understanding of the mechanisms governing lithium ions transport within these materials and through the existing interfaces is thus mandatory. Lithium behaviour in the bulk and at the interfaces remains unclear and requires further understanding. [17] Firstly, objectives leading to the development of solid-state batteries are detailed, and the studied SSE materials are presented. Then, essential concepts are defined in order to set the framework of this PhD work. Principle of advanced characterisation techniques allowing to trace lithium isotopes are presented and comparisons are drawn based on information they provide. Finally, studies involving lithium isotopic tracing in various scientific domains including battery materials are discussed.

I.1. Solid-state lithium metal batteries

All-solid-state batteries (ASSBs) are only composed of solid components even for the electrolyte. Their working principle is the same as liquid electrolyte-based Li-ion batteries as presented in the general introduction. During the charge step, lithium ions are forced to move from the positive electrode to the lithium negative electrode. [8] Thus, lithium ions move through the SSE, before plating on the lithium anode. The ASSB principle is schematised on Figure I-1.

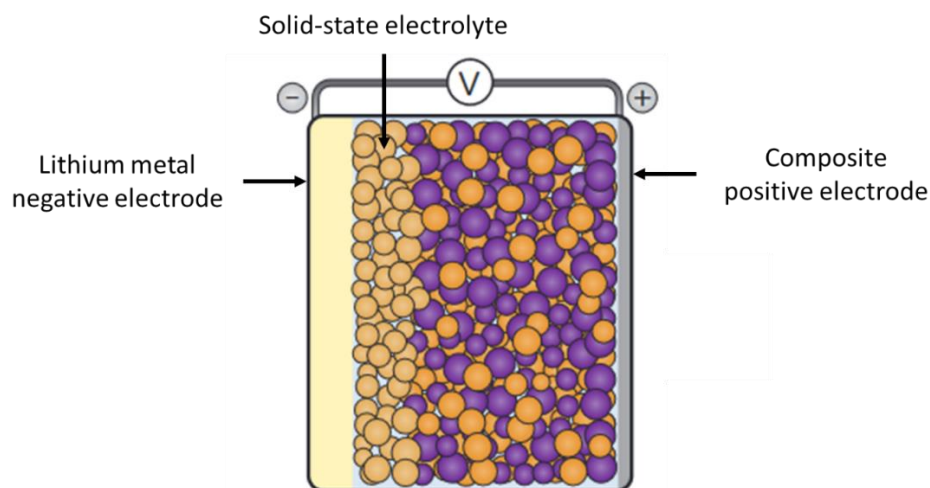


Figure I-1. Schematic of an ASSB. [6]

As previously mentioned, lithium metal anode has been initially implemented in batteries before the development of the Li-ion concept. The main interest to use lithium as the negative electrode lies in its specific properties (high specific capacity, lightness, low potential). Indeed, it has a standard potential of -3.05 V/ESH and a specific capacity of $3,862 \text{ Ah} \cdot \text{kg}^{-1}$. [18] [19] The use of lithium metal has to be mastered. Indeed, challenges to commercialise Li-metal batteries are the following:

- To avoid lithium dendrite growth, and thus any short-circuit or explosion by using SSE
- To find SSEs chemically compatible with Li-metal
- To improve interfaces stability and lithium transfer at the interfaces in order to enhance ionic conductivity of the SSE
- To obtain electrochemical performances competitive with liquid electrolytes
- Availability of the resources

Technologies based on Li metal was discarded due to safety issues [20], except Lithium Metal Polymer (LMP[®]) technology commercialised by Blue Solutions. LMP batteries are composed of a lithium foil as the anode, and lithium iron phosphate (LiFePO_4) as the cathode. A solid-state poly(ethylene oxide) (PEO)-based electrolyte containing a lithium salt is used in-between both electrodes. Recently, thanks to SSEs, the use of Li-metal as a negative electrode is considered again and could lead to a significantly increase of the energy density from $250 \text{ Wh} \cdot \text{kg}^{-1}$ to $400 \text{ Wh} \cdot \text{kg}^{-1}$. [6] Indeed, SSEs are non-flammable and non-volatile

compared with liquid electrolytes. [11] Thus, devices are expected to be safer. [21] However, one of the weaknesses of solid-state batteries lies in the lower ionic conductivities (10^{-6} to $10^{-4} S \cdot cm^{-1}$ at $30^{\circ} C$) compared to liquid ones (10^{-2} to $10^{-3} S \cdot cm^{-1}$). [6] [21] SSEs properties are described in the following section.

1.1. Solid-state electrolyte properties

A SSE acts at the same time as an electrolyte and as a separator between both electrodes. Consequently, it has to be a good ionic conductor with a negligible electronic conductivity. An ideal SSE has to fulfil the following criteria which can be interdependent [22] [23]:

- an ionic conductivity competitive with those of liquid electrolytes, ($> 10^{-3} S \cdot cm^{-1}$ at RT) on a large range of temperature,
- a negligible electronic conductivity,
- to be (electro-)chemically stable against both lithium metal and positive electrode material,
- a good mechanical stability,
- to provide intimate contacts with the Li anode and with the positive electrode leading to low resistances at the interfaces,
- to avoid dendrite growth.

SSEs are divided into two types: organic polymer or ionic conductive ceramic, which can also be combined to form a third class known as “composite” or “hybrid” SSEs. [6] Properties of polymer and ceramic based SSEs are presented in sections a) and b), respectively.

a. Poly(ethylene oxide) (PEO)-based electrolyte

Solid-state polymer electrolytes (SPE) are usually based on a lithium salt dissolved in a polymer matrix. The emerging class of ionic polymer called “single-ion” is not considered in this part. SPE have many advantages [6] [23] [24]:

- they are electrochemically stable against lithium metal, limiting the evolution of interfacial resistance,
- they are safe (non-flammable, non-toxic, do not generate gas),
- they can be implemented as a thin film using dry process (solvent free),
- they are able to compensate of volume changes.

A specific attention has to be paid on polymer crystallinity to reach a sufficient ionic conductivity. Polymers can be crystalline, semi-crystalline or amorphous (Figure I-2).

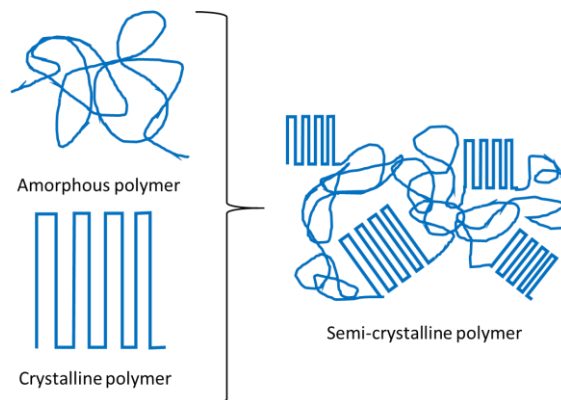


Figure I-2. Schematic of amorphous, crystalline and semi-crystalline polymers.

The combination of the host polymer and the lithium salt has to be carefully chosen. For instance, the host polymer must present a high dielectric constant, and the salt lattice energy should be low. It will facilitate salt dissociation and enhance the ionic conductivity. [25] Notice that the ionic conductivity of SPEs is promoted by low crystallinity, low glass transition temperature (T_g , -64°C for PEO), free volume and temperature. [24] As free volumes increase with temperature segmental motion is facilitated.

PEO is the most famous polymer which has a good electrochemical stability against lithium and an excellent compatibility with lithium salts. [26] [27] It is widely investigated, even with modelling approaches. [28] Figure I-3 presents its repeating unit.

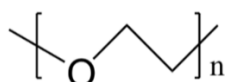


Figure I-3. Repeating unit of poly(ethylene oxide) (PEO).

There are an ether bond and a lot of accessible coordinate sites in the PEO backbone. Li^+ ions transport can occur intrachain and interchain. [29] On Figure I-4, Li^+ ions are moving from a solvation site to another. They are surrounded by five oxygens of a PEO chain.

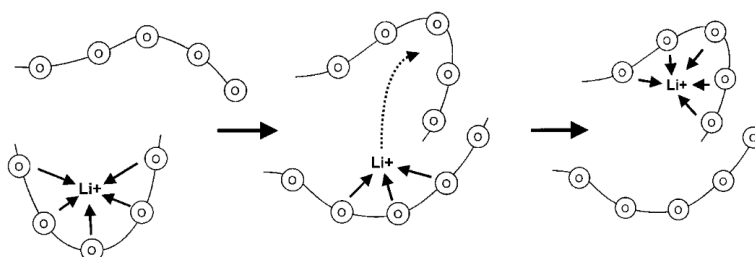


Figure I-4. Schematic of the segmental motion into the PEO matrix. The circles represent the ether bonds of PEO. [25]

Li^+ ions transport in PEO is possible thanks to the polymer segments motions in the amorphous domains of the polymer. [25] [30] This movement will ease lithium progression from site to site. Thus, lithium ionic conductivity is improved. [31] On the contrary, crystalline

domains are insulating which affects the ionic conductivity. [30] Reducing the crystallinity ratio of a semi-crystalline polymer can enhance its ionic conductivity. Stolwijk *et al.* demonstrated that increasing lithium bis(trifluoromethanesulfonyl) imide (LiTFSI) salt concentration in PEO leads to reduce its crystallinity. Thus, the salt concentration modulates ionic conductivity of the polymer electrolyte. [32] On the other hand, highly crystalline polymers would increase mechanical strength and allow to mitigate dendrite growth.

PEO electrolyte works well at temperature above 60°C but its ionic conductivity is low at 25°C. According to Zhang *et al.*, pure PEO ionic conductivity was estimated at $7.5 \times 10^{-6} S \cdot cm^{-1}$ and at $9 \times 10^{-4} S \cdot cm^{-1}$ at 25°C and 80°C, respectively. Heating above the PEO melting temperature (65°C) explains such ionic conductivity difference. [24] [33] This can be an issue since their operating temperature has to match the targeted application. [24] However, above 60°C the PEO layer is unable to suppress the growth of lithium dendrites. [25] This is related to its low melting point (65°C). [24] A compromise has to be found between the highest ionic conductivity and an acceptable mechanical strength. [25]

b. Oxide-based ceramic electrolytes

Inorganic SSEs are conductive in crystalline or glassy state and also play the role of a separator between both electrodes. Thus, they should be good lithium ionic conductors with a negligible electronic conductivity. Oxide and sulfide-based SSEs are the two main inorganic classes and compared in Table I-1.

Table I-1. Comparison between oxide and sulfide based SSEs. [8] [14]

	Oxide	Sulfide
Ionic conductivity at room temperature	Low: $10^{-4} - 10^{-2} S \cdot cm^{-1}$	Fast: $10^{-2} S \cdot cm^{-1}$
Electrochemical stability	Large stability window	Narrow stability window
Mechanical stability	Brittle, cracks may occur	Ductile, less sensitive to crack
Safety	Non-flammable	H ₂ S release
Sintering	High temperature	Room temperature

Oxide-based electrolytes are compatible with lithium metal. They have a large stability window and they are non-flammable. However, compared to sulfide-base electrolytes, they have a lower ionic conductivity, a higher sintering temperature and are brittle. Thus, despite their short stability window and the release of hydrogen sulfide (H₂S), this type of inorganic electrolyte is also widely studied. One of the drawbacks of the oxide-based SSEs is that they require a high sintering temperature (above 1,000°C) to densify the material. [34] However, Gao *et al.* recently obtained an ionic conductivity of $8.02 \times 10^{-5} S \cdot cm^{-1}$ at 30°C by characterising a LiBH₄-modified Tantalum doped Lithium Lanthanum Zirconium Oxide (LLZTO) pellet pressed under 300 MPa. [35] It becomes competitive compared to sulfide-based SSEs preparation.

Here, a focus on the oxide properties is presented. Indeed, only few SSE allow the use of Li-metal as negative electrode due to electrochemical stability (Figure I-5).

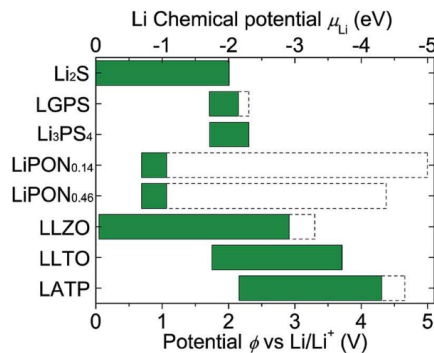


Figure I-5. Electrochemical stability window of various inorganic SSEs. [36]

$\text{Li}_7\text{La}_3\text{Zr}_2\text{O}_{12}$ (LLZO) presents the largest electrochemical stability window between 0.05 and 2.91 V vs. Li^+/Li . [36] Below 0.05 V vs. Li^+/Li , the reduction of the LLZO occurs forming components, such as Zr_3O and Li_2O . Above 2.91 V vs. Li^+/Li , the oxidation of the LLZO occurs forming components, such as Li_2O_2 and $\text{La}_2\text{Zr}_2\text{O}_7$. [36] It has an ionic conductivity around $10^{-4} - 10^{-3} \text{ S} \cdot \text{cm}^{-1}$ at room temperature. [37] Its structure is presented on Figure I-6. The main drawback is poor solid/solid contact at the interface. [38] Indeed, the high interface resistance at the LLZO/Li interface can be explained by non-ideal physical contact. [39] Thus, it induces a high global resistance of the system leading to affect the ionic conductivity.

Thangadurai *et al.* was the first to develop a garnet-type solid electrolyte, $\text{Li}_5\text{La}_3\text{M}_2\text{O}_{12}$ ($\text{M} = \text{Nb}, \text{Ta}$), with an ionic conductivity of $1 \times 10^{-6} \text{ S} \cdot \text{cm}^{-1}$ at room temperature. [40]

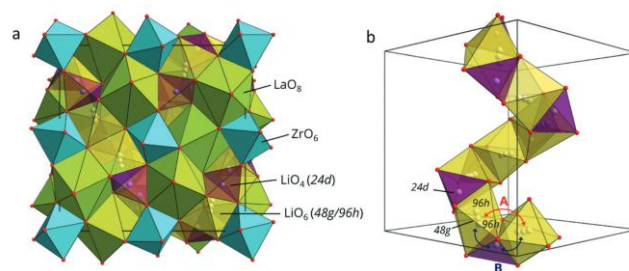


Figure I-6. Chemical structure of $\text{Li}_7\text{La}_3\text{Zr}_2\text{O}_{12}$ (LLZO). « (a) Crystal structure of cubic $\text{Li}_7\text{La}_3\text{Zr}_2\text{O}_{12}$ and (b) Wyckoff positions of the Li^+ ions. The centres of tetrahedral and octahedral sites are noted as 24d and 48g sites, respectively, and the 96h sites are slightly displaced off the 48g sites. LiO_6 and LiO_4 connection and the two possible Li migration pathways (A and B), adapted from [41] Path B is the most likely mechanism of Li migration in LLZO. ». [37]

A way to improve the Li/SSE contact is to add a coating around the SSEs. Wang *et al.* have coated LLZO with a ZnO layer by using atomic layer deposition (ALD). [42] The added layer of 50 nm thick clearly improved the contact at the $\text{Li}_{6.85}\text{La}_{2.9}\text{Ca}_{0.1}\text{Zr}_{1.75}\text{Nb}_{0.25}\text{O}_{12}/\text{Li}$ interface. Indeed, adding a thin coating allows to decrease the initial interfacial resistance of

2,000 $\Omega \cdot \text{cm}^2$ to 20 $\Omega \cdot \text{cm}^2$. Furthermore, this coating is stable during the plating/stripping mechanisms. Luo *et al.* have deposited a lithiated silicon coating of 10 nm by plasma-enhanced chemical vapor deposition (PECVD). [39] It improves the wettability of lithium metal by decreasing the Li/LLZO interfacial resistance from 925 to 127 $\Omega \cdot \text{cm}^2$. Design of future SSEs might be inspired from these results. Dubey *et al.* enhanced the initially poor wettability between the lithium metal and the LLZO by adding antimony (Sb) at the interface. [43] It led to decrease the interfacial resistance down to 4.1 $\Omega \cdot \text{cm}^2$. Such a decrease is explained by the formation of a Li-Sb alloy characterised by XPS, which enhances electronic percolation at the LLZO/Li interface.

To sum up, ASSBs containing inorganic SSE are presented as a new solution to obtain safe and long cycle life batteries with higher energy density than conventional Li-ion batteries. [8] However, between two solids poor Li^+ ions transport at the interface induces high interfacial resistance. It is one key point which hinders their application. [8] To face this issue, developing composite SSEs made of polymer and ceramic stands as a solution for enhancing their performances. It will be discussed in the following section.

1.2. Interest of composite solid-state electrolytes

A ceramic dispersion within a polymer matrix holds significant promise for commercialisation of ASSBs thanks to its potential to enhance battery safety and to increase energy density. [6] [44] In order to be commercialised ASSBs need to present high-power density as well as high energy density. Indeed, high power density is required to perform fast charging. [6] Table I-2 sums up the interests of combining properties of polymer and ceramic SSEs.

Table I-2. Interests of combining properties of polymer and ceramic SSEs. [6] [8] [11] [29] [45] [46]

Polymer electrolyte (PEO+LiTFSI)	Ceramic electrolyte (LLZTO)
Benefits	
<ul style="list-style-type: none"> - Non-flammable and non-volatile → safe in term of materials - Negligible electronic conductivity 	
<ul style="list-style-type: none"> - Low interfacial resistance contact at the interface with electrode materials - Flexible, easy to implement - Temperature preparation between 25 and 60° C 	<ul style="list-style-type: none"> - High interfacial resistance contact at the interface with electrode materials - Difficult to implement - High temperature sintering - Brittle
<ul style="list-style-type: none"> - Low ionic conductivity ($< 10^{-4} S \cdot cm^{-1}$) - Possible formation of lithium dendrites - Poor thermal and chemical stability 	<ul style="list-style-type: none"> - High ionic conductivity ($10^{-3} - 10^{-2} S \cdot cm^{-1}$) - Allows the use of Li-metal - Good thermal, chemical, and mechanical stability
Drawbacks	
<ul style="list-style-type: none"> - Ionic conductivity still low compared with liquid electrolyte 	

A focus has been done on composite SSEs which will be studied in this thesis. At 25°C, the garnet-type nanoparticles of $Li_{6.4}La_3Zr_{1.4}Ta_{0.6}O_{12}$ (LLZTO) ceramic has an ionic conductivity of $10^{-3} S \cdot cm^{-1}$. [22] Adding polymer such as PEO leads to a decrease of the ionic conductivity down to $10^{-4} S \cdot cm^{-1}$. [45] Such effect can be explained by the strong Li-O links that decreases lithium ions mobility. [47] Furthermore, tortuosity is enhanced, affecting lithium ions transport. [47] However, polymer offers good contact at the interface, it is flexible and easy to implement. [46] PEO is compatible with most of the lithium salts, such as LiTFSI or $LiClO_4$. [26] [48] PEO chains movement ensures lithium ions transport through the polymer membrane. However, they are inefficient to avoid lithium dendrite growth. Adding ceramic could allow the use of lithium metal as the negative electrode. [45] [49] This would increase the charge density. Ceramic has to have good thermal, chemical and mechanical stability. [45] [50] However, contact issue between two solids can be solved by using a polymer layer. Indeed, such material flexible and easy to implement offers good contact between materials.

LLZTO were dispersed into a PEO matrix. Ionic conductivity of $2.1 \times 10^{-4} S \cdot cm^{-1}$ at 30 °C and $5.6 \times 10^{-4} S \cdot cm^{-1}$ at 60 °C were reached. [21] According to Zhang *et al.* the addition of LLZTO particles enhances electrochemical stability and avoid lithium dendrite formation. [21] Furthermore, such device presents a large electrochemical window of 4.7 V and a maximum Li^+ transference number of 0.46 for a PEO membrane containing 12.7 vol% of LLZTO particles. This value is double the Li^+ transference number of pure PEO (0.22). [21]

Zheng and Hu studied lithium diffusion in a composite SSE composed of LLZO and PEO by high-resolution ssNMR. [46] They demonstrated that Li^+ ions pathways may depend on the electrolyte composition. Strong resistances at the different interfaces affect the ionic of the whole system. To improve them and more specifically the ones between the ceramic and the polymer, Li^+ ions behaviour at the interface has to be better understood.

To conclude, some key points have to be solved in order to open the way to the solid-state batteries development at the industrial scale. Firstly, lithium dynamics have to be enhanced specifically at the various interfaces. Furthermore, the mechanical pressure applied on the device during cycling has to be investigated because it affects electrical performances and stability over time. Finally, in order to substantially boost energy density, it is imperative to explore innovative methods to make the use of lithium metal possible as the negative electrode in lithium-ion batteries. We need however to gain a better understanding of lithium transport dynamics. The use of materials enriched in 6Li isotopes can be relevant to label the lithium of a specific component of the device and thus to facilitate their tracing. The functioning and interests of such experiments are explained in section I.2.

I.2. Lithium isotopic labelling as a tool to trace lithium

2.1. Definitions laying foundations of the following works

a. Lithium isotopic abundance

Two isotopes are related to the same nucleus. They have the same number of protons (Z) but a different number of neutrons (N) leading to a difference of mass. There are two stable isotopes in the lithium case, ${}^6_3\text{Li}$ and ${}^7_3\text{Li}$. Their mass (Z+N) differs by the mass of one neutron. Notice that isotopes of a nucleus present similar chemical properties because they have the same number of protons.

The abundance of an element refers to its proportion on Earth (natural state) or in a material. Here, the isotopic abundance is considered as the relative amount of an isotope compared to the total amount all the isotopes of the same atom. Thus, lithium isotopic abundances ($\% {}^i\text{Li}$) are given by the following Equation I-1 and Equation I-2:

$$\% {}^6\text{Li} = \frac{n {}^6\text{Li}}{n {}^7\text{Li} + n {}^6\text{Li}} \quad \text{I-1}$$

$$\% {}^7\text{Li} = \frac{n {}^7\text{Li}}{n {}^7\text{Li} + n {}^6\text{Li}} \quad \text{I-2}$$

with $n {}^i\text{Li}$ (mol), the number of moles of the ${}^i\text{Li}$ isotope.

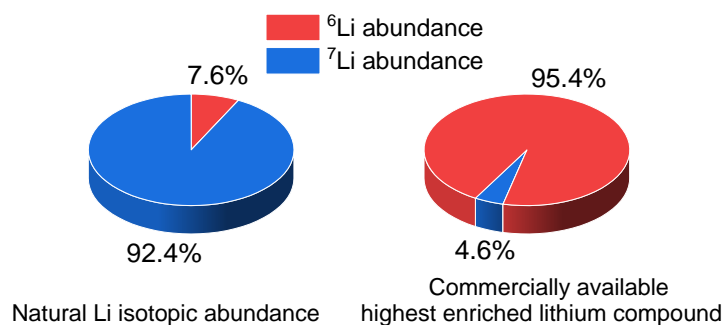


Figure I-7. Natural lithium isotopic abundance in conventional compounds versus in the commercially available highest enriched lithium compounds.

On one hand, when our work referred to a compound at lithium natural isotopic abundance, $\% {}^6\text{Li}$ and $\% {}^7\text{Li}$ are equal to 7.6% of ${}^6\text{Li}$ and 92.4% of ${}^7\text{Li}$, respectively (Figure I-7). [47] [52] On other hand, commercially available compounds with 95.4% of ${}^6\text{Li}$ and 4.6% of ${}^7\text{Li}$ have been used to prepare enriched lithium isotopic materials at various levels.

Lithium isotopic ratio is also used in literature. [52] It compares the relative isotope proportions in a given material (Equation I-3).

$$\text{Li}_{ratio} = \frac{{}^6\text{Li}}{{}^7\text{Li}} \quad \text{I-3}$$

The lithium isotope composition, $\delta^7\text{Li}_{\text{L-SVEC}}$, is expressed by Equation I-4,

$$s \delta^7\text{Li}_{\text{L-SVEC}} = \left(\frac{\frac{{}^7\text{Li}}{{}^6\text{Li}}_{\text{sample}}}{\frac{{}^7\text{Li}}{{}^6\text{Li}}_{\text{standard}}} - 1 \right) \times 10^3 \quad \text{I-4}$$

with $\frac{{}^7\text{Li}}{{}^6\text{Li}} = 12.019$, the ratio relative to standard lithium (L-SVEC). [53] Penniston-Dorland *et al.* have listed several works, which reveal that lithium isotope composition ($\delta^7\text{Li}$) can vary from -15 ‰ to 45 ‰ on Earth. [54]

The following section will explain how such variables can be determined and used to investigate origin of materials and lithium dynamics. Lithium isotopic tracing can be applied to various applications, with a specific focus on battery. It is discussed in the following section.

b. Lithium isotopic labelling and tracing

Lithium isotopic labelling consists in enriching in ${}^6\text{Li}$ a specific component of a system containing lithium at natural isotopic abundance. Materials with a higher ${}^6\text{Li}$ abundance than the ${}^6\text{Li}$ natural abundance are quite expensive, and as previously mentioned, ${}^6\text{Li}$ and ${}^7\text{Li}$ have the same chemical properties. The only interest of lithium isotopic labelling is to be able to distinguish lithium coming from a specific component compared to lithium present in the system. Thus, lithium isotopic tracing can be carried out to track lithium paths and/or interactions with its environment.

Lithium isotopic tracing is based on the estimation of lithium isotopic abundance or lithium isotopic ratio. Indeed, these two variables will be modified while performing experiment with materials labelled in ${}^6\text{Li}$. Lithium isotopic tracing consists in estimating these modifications thanks to advanced characterisation techniques. Various lithium behaviours can be investigated. Some of them are mentioned in the following sections.

c. Lithium mobility

Lithium self-diffusion is a process describing a disordered lithium motion in a material, without applying any external stress. In battery field, such notion is important because it directly affects the ionic conductivity of the material.

On the contrary, lithium migration is a process describing an oriented lithium motion, by applying an external stress. In battery field, this process occurs for instance while applying a constant current during charge or discharge cycles.

“Lithium dynamics” or “lithium diffusion” terminologies are used in this work to name both processes (lithium self-diffusion and lithium migration) which can take place simultaneously. Lithium dynamics can be investigated based on advanced characterisation techniques that can detect simultaneously or separately ${}^7\text{Li}$ and ${}^6\text{Li}$ isotopes. The main ones are presented in the section 2.3.

2.3. Various characterisation techniques allowing lithium isotopic analyses

a. Secondary-ion mass spectrometry (SIMS) and time-of-flight SIMS (ToF-SIMS)

- *Secondary-ion mass spectrometry (SIMS)*

Secondary-ion mass spectrometry (SIMS) enables surface characterisation of the sample. The principle of the SIMS technique is described in a simplified form on Figure I-8.

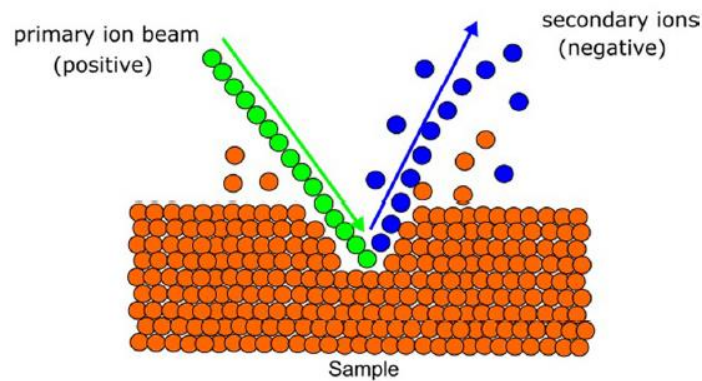


Figure I-8. Schematic of the SIMS principle. [55]

The surface of the sample is sputtered by a focused and continuous beam represented in green on Figure I-8. Several primary ion sources exist, such as Cs^+ or O^- . [55] Secondary ions are ejected (blue) by the incident ion beam. The polarity of the collected secondary ions is determined by polarising the sample. Firstly, the secondary ions are extracted by an electrostatic sector creating electric fields. Then, a magnetic deflection spectrometer modifies the electric fields to extract specific secondary ions. Finally, secondary ions are detected by varying the magnetic field to deflect the selected ones. Thus, the detection is sequential, meaning that secondary ions are detected one after the other. The magnetic spectrometer separates the secondary ions by their mass-to-charge ratio $\left(\frac{m}{z}\right)$. The various selected secondary ions are not detected at the same depth in the sample. [56] Isotopes can be detected with a high sensitivity. [55] [57]

The parameter determining lateral resolution is the minimum primary ion beam spot size. Either mass resolution or lateral resolution can be promoted regarding the used settings. On one hand, it is possible to reach a mass resolution higher than 6,000 with a lateral resolution of $5 \mu\text{m}$. [58] On the other hand, the lateral resolution can be increased up to 300 nm to the detriment of the mass resolution which will be around 1. [58]

The drawbacks of the technique are related to high variation in element sensitivity and matrix effects. [57] Isotope relative quantification requires to previously characterise reference samples with the same matrix.

- *Time-of-flight secondary-ion mass spectrometry (ToF-SIMS)*

Historically, J. J. Thomson opened the way to the time-of-flight secondary ion mass spectrometry (ToF-SIMS) technique. [59] He determined in 1887 the $\frac{e}{m}$ ratio, with e the charge of an electron and m its mass. Then, he demonstrated in 1910 that gas, atoms and ions are ejected from a solid surface with cathode copper rays while sputtering. He worked on metals and other solids, such as graphite or volcanic dust. [59] Nowadays, this characterisation technique is widely used in microelectronics. [60] Other fields such as cosmochemistry, [61] battery materials [62] and more recently biology [63] benefit from ToF-SIMS characterisation technique.

ToF-SIMS spectrometry allows the study of surface chemistry through the detection of molecular fragments extracted from the surface of the sample by using a primary ion beam. This is a localised analysis at the submicronic scale. ToF-SIMS has excellent mass resolution, sensitivity and high lateral resolution, providing chemical information at the surface of the sample. [64] [65] [66] [67] Light elements can be detected, such as hydrogen or lithium. Furthermore, isotopes can be distinguished because it is a mass spectrometry method. The principle of the ToF-SIMS technique is described on Figure I-9.

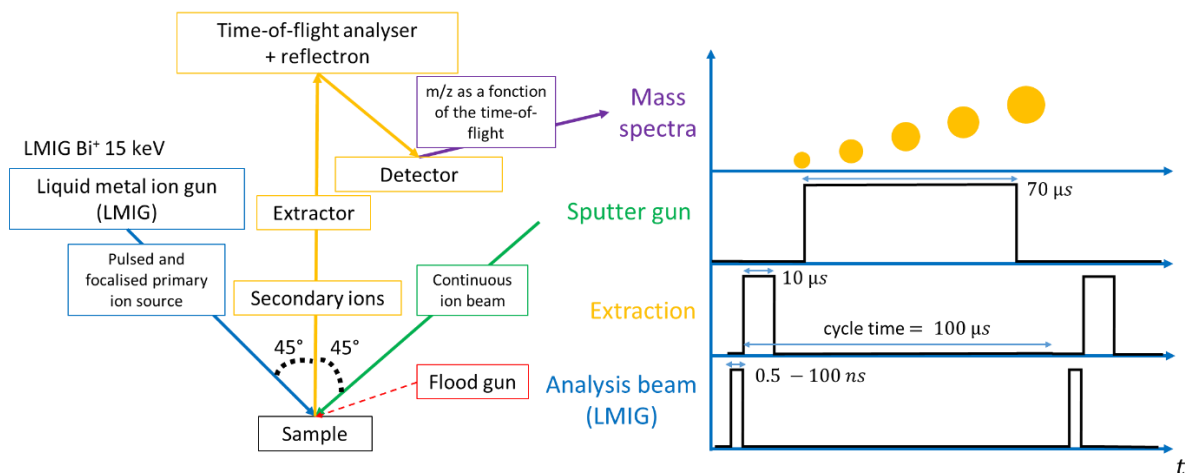


Figure I-9. Principle of the ToF-SIMS technique.

As in SIMS, the sample is placed into an ultra-high vacuum (UHV) analysis chamber with a pressure below 10^{-9} mbar. The characterisation of air-sensitive samples can occur without prior exposure to ambient air before insertion into the UHV chamber by a sealed box. [62] The analysis beam is based on a liquid metal ion gun (LMIG) forming a 45° angle relatively to the normal of the sample. [68] On Figure I-9, a pulsed ($0.5 - 100$ ns) and focused ion beam allows ejecting the molecular fragments from the surface of the sample by sputtering accelerated primary ions on it. [62] [64] The fact that the analyser beam is pulsed and focused allows time-of-flight determination. [62] A very low primary ion dose (due to the pulsing mode) is applied on the surface of the sample, around 2×10^{12} ions \cdot cm $^{-2}$. [69] Thus, it is considered that experiments are performed in a static mode and that they are

non-destructive. Only the extreme surface is characterised by using a pulsed beam, rather than a continuous one as in SIMS. The molecular fragments ejected from the extreme surface of the sample are extracted by a polarised electric field localised between the surface of the sample and the analyser. Positive or negative analyses can be performed according to the polarisation direction. This analyser can separate them with a reflection system, as a function of their mass-to-charge ratio $\left(\frac{m}{z}\right)$. The lightest ions reach the detector at first. [62] [70] Time-of-flight of the secondary ions (t_{TOF}) is directly related to their weight and can thus be estimated. More details are provided in Appendix A-I-1. *Time-of-flight and ionisation yield notions*. A mass spectrum calibration is achieved with known ions. Two-dimensional images can be obtained from the mass spectra. Furthermore, three-dimensional analyses can also be performed by sputtering the surface of the sample in order to access to buried interfaces. [64]

ToF-SIMS is a powerful technique, in particular because of parallel mass detection. [64] [70] [71] A single analysis provides access to all ejected positive or negative molecular fragments contained within the mass range, which is determined by the cycle time parameter described above. Moreover, experimental data can be processed after the analyses. It is a huge advantage of this technique. Acquisition parameters have to be appropriate to get wanted information. A compromise must be established between a satisfactory mass resolution and a sufficient lateral resolution. It depends on the chosen primary beam. To distinguish isotopes, analyses have to be performed with a high mass resolution. Lithium isotopic ratio $\left(\frac{{}^6\text{Li}}{{}^7\text{Li}}\right)$ can thus be estimated.

ToF-SIMS analyses can offer high mass resolution, high sensitivity (*ppm*) or high lateral resolution ($> 100 \text{ nm}$), depending on the acquisition parameters. [64] [72] However, in most of the analyses, a compromise has to be found between a high mass resolution, and a high lateral resolution. ToF-SIMS provides a far better spatial resolution compared to X-ray photoelectron spectroscopy (XPS) ($<300 \text{ nm}$ vs. $10 \mu\text{m}$). [73]

Since ${}^7\text{Li}^+$ molecular fragment reaches the detector more than 600 ns after ${}^6\text{Li}^+$ molecular fragment, ToF-SIMS analyses can easily separate lithium isotopes. Both isotopes contained in a given matrix have an equivalent ionisation yield and detection efficiency. [74] Thus, lithium isotopic ratio or lithium isotopic abundance can be determined from the measured intensities of ${}^6\text{Li}^+$ and ${}^7\text{Li}^+$ molecular fragments. [64] Experimental data have to be carefully processed after the acquisition to accurately estimate lithium isotopic abundance.

Two-dimensional (2D) images can be obtained from the mass spectra. Furthermore, it is also possible to carry out three-dimensional (3D) analyses by sputtering the sample with another (not pulsed) ion beam, such as Cs^+ , O_2^+ or argon clusters (Ar_n^+). Having access to buried interfaces by ToF-SIMS can be difficult and requires sputtering the sample. It is important to consider the evolution kinetic at the interfaces. In particular, the analyses should not modify the material. The sputter gun has to be tuned to limit any material alteration of the chemical composition during the sputtering steps. [64] On Figure I-9, the interlaced mode is represented. The sample is sputtered during the time-of-flight of the secondary ions while they are in the analyser. Another sputter mode called “non-interlaced” can be used. It allows sample relaxation because the sputtering occurs only after the set cycle time.

As a first approach, ToF-SIMS is not a quantitative technique. However, Henss *et al.* investigated calcium distribution and quantification in bone cross sections by ToF-SIMS and XPS. [73] They demonstrated that a linear response exists between the calcium amount in a calibration reference sample and the Ca^+ signal intensity. Thus, it is possible to quantify calcium by using mineralised hydroxyapatite collagen with various calcium content as calibration reference samples. ToF-SIMS 2D analyses with a lateral resolution of $1\ \mu\text{m}$ were obtained by using a low current bunched mode. XPS and ToF-SIMS results were thus confronted. Both techniques led to coherent results and validated the ToF-SIMS methodology using reference samples to perform quantification. Notice that calibration samples with a similar matrix were chosen to avoid any matrix effect. To conclude, calibration sample quality affects the quantification accuracy.

b. Nuclear magnetic resonance (NMR)

- *Liquid-state nuclear magnetic resonance (NMR)*

Nuclear magnetic resonance (NMR) analyses provide global information on lithium ions environment and quantitative experiments can lead to the determination of ^7Li and ^6Li concentrations, but it can probe isotopes only one by one due to their respective resonance frequencies. The principle of the NMR technique is described on Figure I-10.

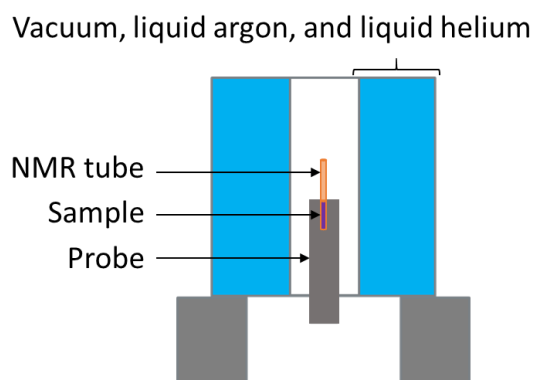


Figure I-10. Schematic of an NMR spectrometer.

To carry out NMR experiments, the sample is placed in a homogeneous and strong magnetic field created nowadays by a superconducting magnet. The NMR probe consists of a coil that is used to excite the sample with appropriate radio frequencies and to record the NMR response signal of the spin system. These different events are defined by pulse sequences.

Historically, the nuclear spin was discovered theoretically by Pauli in 1924. [75] Liquid-state NMR was then developed to characterise the chemical environments of the probing atom. It allows a global, non-destructive and non-contact analysis of a liquid sample and provides fast results with low sample consumption. [76] It is commonly used to follow

chemical reactions at different steps in organic chemistry. NMR can only probe nuclei having a magnetic moment which behaves as a magnet. The magnetic moment μ is expressed by the following Equation I-5,

$$\mu = \gamma \cdot I \quad \text{I-5}$$

with γ ($\text{rad} \cdot \text{s}^{-1} \cdot \text{T}^{-1}$) the nuclear gyromagnetic ratio and I the nuclear spin. The nuclear spin is an intrinsic property. For nuclei, spin quantum number can only take half-integer or integer discrete values in quantum mechanics.

The sample is placed in a stationary strong magnetic field B_0 created by a superconducting magnet. The spins of the sample align along B_0 direction. An alternating magnetic field B_1 oscillating at the frequency ω_0 is applied within a perpendicular plan to B_0 .

When the excitation frequency matches the Larmor frequency of the spins ($|\nu_0| = \frac{|\gamma|B_0}{2\pi}$), their time domain response (FID for Free Induction Decay) is acquired. It is due to the recovery of magnetisations to their equilibrium state. Notice that ν_0 is modulo the chemical shielding and other potential interactions. Therefore, the recorded FID contains all information on nucleus chemical environment. [76] Pulsed NMR useful for the chemist, delivers frequency information (chemical shifts), which need to be Fourier transform to FID. Notice that FID behaviours also depend on the dynamics of the spin systems (mainly T2 and T1 known as transverse and longitudinal relaxation times, respectively). From the spin response, their local chemical environment can be determined. More details are provided in Appendix A-I-2. *Description of NMR pulse sequence and signal acquisition.*

- *High-resolution solid-state nuclear magnetic resonance (ssNMR)*

Contrary to ToF-SIMS analyses, high-resolution solid-state nuclear magnetic resonance spectroscopy (ssNMR) provides a global analysis of the sample at the atomic scale. Nuclei chemical environment can be determined. The obvious advantage of high-resolution ssNMR is to analyse solid samples. No dissolution is required. Therefore, the atomic structure can be investigated by analysing the isotropic signals and potentially their spinning sidebands. [77] [78] ^6Li and ^7Li high-resolution ssNMR can be performed without dissolving the samples, that was not the case for liquid NMR. The principle of the NMR technique is described on Figure I-11.

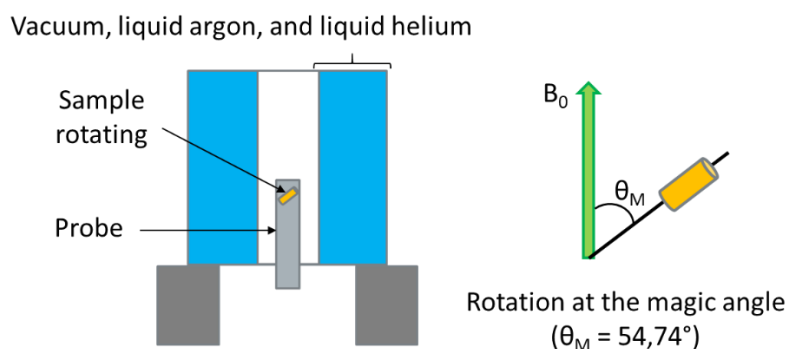


Figure I-11. Principle of the high-resolution ssNMR technique.

The high-resolution ssNMR principle is the same as the NMR principle. However, one of the main challenges is to obtain high resolute spectra while analysing solid materials. During ssNMR analyses, both isotropic and anisotropic NMR interactions affect the NMR spectra. Anisotropic interactions lead to broad NMR signals. Furthermore, broad peaks can hide several isotropic chemical shifts. The main challenge lies in enhancing the NMR spectra resolution. The main discovery allowing to obtain high-resolution ssNMR spectra is based on the magic angle spinning developed at the end of the 1950's. Lowe published ssNMR characterisations of CaF_2 and Teflon by probing ^{19}F while rotating the sample in 1959. [79] The "magic angle spinning" concept was not yet established but a rotation of the sample was applied while acquiring data. However, the presence of sidebands due to the angular speed was already understood by comparing non-spinning and spinning spectra. Lowe demonstrated that the sample must be rotated along an axis oriented at 54.7° from the magnetic field. [79] This angle will be called later, the "magic angle spinning". Lowe refers also to Andrews *et al.* who published ssNMR studied on NaCl in 1958. [80] They were probing Na^{23} while rotating the sample.

^6Li and ^7Li quantitative characterisations are possible, while using appropriate acquisition conditions and an optimised way to execute data processing. [16] It allows to estimate lithium isotope abundances and lithium concentration. ^6Li and ^7Li are quadrupolar nuclei by definition because their nuclear spin is higher than $\frac{1}{2}$ (Appendix -Table A-I-1). Thus, their quadrupolar moment is coupled to B_0 and it will induce peak broadening. To perform quantitative high-resolution ssNMR analyses on a quadrupolar nucleus may present a greater challenge than on a nucleus with a nuclear spin of $\frac{1}{2}$. The non-spherically symmetric charge distribution of quadrupolar nuclei can be an explanation. [78] To probe quadrupolar nuclei with a high quadrupolar coupling, short pulses around 30° are generally recommended. [78] However, it leads to decrease the detected signal compared with a 90° pulse. Isotropic signal and spinning sidebands are detected on spectra, while probing an atom having quadrupolar spins. [77] [78] Thus, high-resolute spectra are obtained by applying a pulse sequence which has to be well designed.

c. Inductively coupled plasma mass spectrometry (ICP-MS) technique

Inductively coupled plasma mass spectrometry (ICP-MS) is a highly sensitive technique allowing to quantify elements. The principle of the ICP-MS technique is described on Figure I-12.

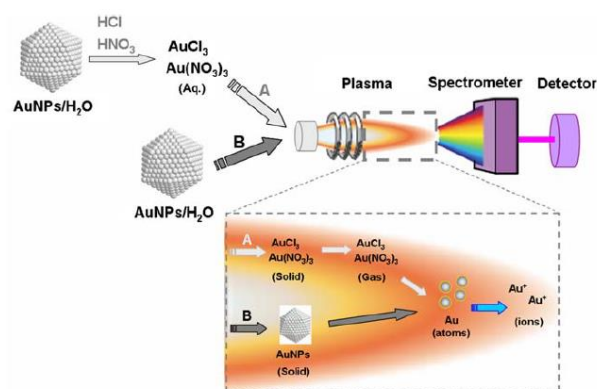


Figure I-12. ICP-MS principle in the case of gold nanoparticles. [81]

A high-temperature plasma is created to break down the chemical compounds present in the samples to induce ions formation. Following this step, the produced ions in the plasma are detected by a mass spectrometer allowing to quantify them. ICP-MS can detect almost all the elements of the periodic table except hydrogen, nobles gases, and atoms which are difficult to liquefy such as C, O, N, F and Cl. [82] Furthermore, ICP-MS also allows to distinguish isotopes. [82] It has a high sensitivity of $0.15 \mu\text{g} \cdot \text{l}^{-1}$ or few $\text{ng} \cdot \text{l}^{-1}$ thanks to high ionisation yields and quadripolar filters. Multicollectors allow parallel detection of several ions within the same mass range such as isotopes. [83] Therefore, quantification of isotopic ratio is possible, though matrix effects can affect their accuracy. [81] Paucot and Potin-Gautier explained that it is possible to consider that the intensity of various detected isotopes is proportional to the isotopic abundance. [82] However, various interferences can affect the results, such as spectral, polyatomic and isobaric interferences.

Strengths of the technique are based on an easy calibration, no sample inhomogeneity issue and a high sensitivity. [57] However, the required dissolution step before injecting the resulting liquid in the mass spectrometer may be a drawback. [57] Sample preparation can difficultly be compared to other techniques. [82] Acid digestion at specific temperatures or vapour phase decomposition pre-treatments are performed to liquefy solids. Laser ablation inductively coupled plasma mass spectrometry (LA-ICP-MS) can also be used to characterise the surface of solid samples. Lithium isotopic abundance can be estimated by LA-ICP-MS with an uncertainty of 2 ‰. [84]

d. Laser-induced breakdown self-reversal isotopic spectrometry (LIBRIS)

Laser-induced breakdown self-reversal isotopic spectrometry (LIBRIS) is based on the same principle as laser-induced breakdown spectrometry (LIBS) technique. The principle of the LIBS technique is described on Figure I-13.

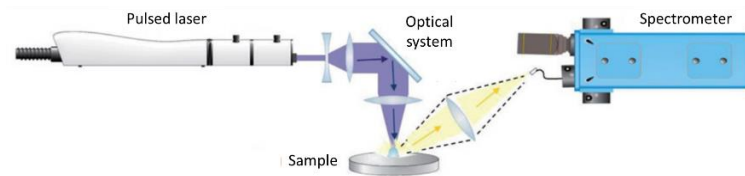


Figure I-13. Schematic of the LIBS principle. [85]

LIBS is an elemental analysis involving optical emission spectrometry and allows to characterise solid, liquid or gaseous samples. [85] The surface of the sample is vaporised by a pulsed laser which is focused on the surface of the sample (Figure I-13). A plasma is generated. The optical emission spectrum of the plasma is analysed. Excited ions in the plasma undergo de-excitation, emitting characteristic light within a large wavelength range depending on the sample elemental composition. [85] Thus, the presence of several elements can be detected at the same time.

In LIBS, a fraction of the emission of the most intense atomic lines can be absorbed by the plasma itself. This so-called “self-absorption” phenomenon can be so pronounced that the lines become reversed, as shown on Figure I-25.A. The principle of the LIBRIS technique lies in the linear dependence of the wavelength of the resulting absorption dip on the isotopic abundance. [86] The measurement range is rather small. It is equal to the isotopic shift between ${}^6\text{Li}$ and ${}^7\text{Li}$ isotopes, i.e. 15.8 pm for the 670.776 nm line. The LIBRIS technique can still allow lithium isotopic analysis after determining a calibration curve with reference samples. A lateral resolution of $250 \text{ }\mu\text{m}$ can be reached in standard ablation conditions, down to $7 \text{ }\mu\text{m}$ with specific settings. [87] Moreover, sample preparation is easy and experiments can be performed under air or under an argon flux to enhance ${}^6\text{Li}$ abundance determination. [87]

f. Neutron diffraction

The principle of neutron diffraction technique is described on Figure I-14.

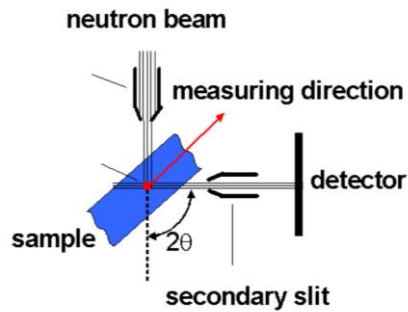


Figure I-14. Principle of neutron diffraction technique. [88]

A neutron beam is created, for instance, from a reactor producing continuously neutrons thanks to nuclear fission of heavy atomic nuclei, such as ^{235}U . Neutrons interact with atoms of the sample. They are scattered by atomic nuclei. Thus, neutron diffraction enables the determination of the atom nuclei positions in a crystalline material for instance. [89] It is possible to analyse the bulk of the samples. Light atoms can be probed and it is a non-destructive experiment. [88] Several studies carry out hydrogen replacement by deuterium in order to increase the scattering power to obtain higher quality spectra. [89] Furthermore, it can theoretically distinguish lithium isotopes. However, the large absorption and incoherent length density scattering of ^6Li make its detection difficult. [90] Neutron diffraction is more sensitive to ^7Li (compared to ^6Li detection).

g. Summary

Table I-3 provides a summary of advantages and drawbacks of the presented advanced techniques allowing to characterise both lithium isotopes.

Table I-3. Comparison of advanced techniques allowing to characterise both lithium isotopes.

Technique	Benefits	Drawbacks
SIMS / ToF-SIMS	<ul style="list-style-type: none"> - chemical information - extreme surface analysis - high sensitivity (<i>ppb / ppm</i>) - high lateral resolution (<i>300 nm / < 100 nm</i>) - high mass resolution (<i>6,000 / 12,000</i>) - parallel mass detection (for ToF-SIMS) - 3D analyses (by using ion or FIB gun) - analyses in an UHV chamber 	<ul style="list-style-type: none"> - matrix effect on the ionisation yield - complex quantification (matrix effects) - no global analysis information - sequential mass detection (for SIMS)
ssNMR	<ul style="list-style-type: none"> - chemical environment information - concentration determination in bulk analysis - spin dynamics information 	<ul style="list-style-type: none"> - more sensitive to ⁷Li compared to ⁶Li - cannot probe both lithium isotopes during the same analysis - the normalisation factor has to be estimated for each given matrix - broad contributions - long analysis time - loose of lateral resolution
ICP-MS	<ul style="list-style-type: none"> - elemental information - concentration determination in bulk analysis - high sensitivity - global analysis - no sample inhomogeneity issue - easy calibration to determine lithium isotopic ratio 	<ul style="list-style-type: none"> - requires sample dissolution - loose of lateral resolution - no localised analysis
LIBRIS	<ul style="list-style-type: none"> - surface chemical information - parallel element detection - fast acquisition (<few minutes) - no specific sample preparation is required before analysis 	<ul style="list-style-type: none"> - analyses under ambient air or un argon flow - low lateral resolution (<i>7 μm - 250 μm</i>) compared to SIMS and ToF-SIMS - matrix effect on the calibration curve determination - no global analysis information
Neutron diffraction	<ul style="list-style-type: none"> - chemical information - atomic position information - more sensitive to ⁷Li 	<ul style="list-style-type: none"> - sample may be deuterated to detect lithium - more sensitive to ⁷Li compared to ⁶Li - difficult access to neutron facilities

All these techniques can detect both lithium isotopes simultaneously, except liquid NMR and ssNMR. One characterisation technique may hold greater relevance than the others. Depending on the anticipated outcomes, the characteristics of the sample and the properties being investigated, or even the targeted application. In this thesis work, SSEs have to be characterised. Neutron diffraction is more sensitive to ^7Li . Thus, it is supposed to work with materials enriched in ^6Li and to track ^7Li . Furthermore, sample may be deuterated to enhance lithium detect. Thus, this technique seems difficult to setup. Liquid NMR and ICP-MS are also widely used to characterise lithium into various samples. However, they require a conditioning step that induce a loss of lateral resolution and may be detrimental to the overall study. [91] Characterisation techniques that offer the possibility to keep materials under controlled atmosphere during an analysis are also mandatory for battery applications. Indeed, ambient air can alter the surface chemistry of the sample. Thus, ICP-MS, LA-ICP-MS and LIBRIS technique will not be selected. Nonetheless, LIBRIS technique has a great potential and is still under development. Instrumental studies in order to improve lateral resolution are currently being carried out. Furthermore, specific setups might be developed to perform LIBRIS analyses under inert atmosphere. In the end, ToF-SIMS and high-resolution ssNMR do allow characterisation of solid samples, while keeping them under inert atmosphere. Furthermore, they can provide complementary information. More detailed explanations are provided on these two advanced characterisation techniques, which have been selected to investigate lithium dynamics through SSEs.

2.2. Battery applications of lithium isotopic tracing

Significant conclusions can be drawn from the estimation of lithium isotopic abundance of lithiated materials but also from its evolution according various parameters (time, temperature, age, etc...). Lithium isotopic tracing consists in using an enriched material in ^6Li to track ^6Li dynamics in the whole device. [91] This tool is necessary when the system already contains lithium since it enables to differentiate the injected lithium from the one present. Thus, a very precise estimation of lithium isotopic abundance is mandatory to follow Li^+ ions dynamics in its environment.

Several sectors such as medicine, biochemistry, geology, and energy resort to lithium isotopic tracing. Thanks to an enriched lithium chloride solution in ^6Li ($^6\text{LiCl}$) and neutron irradiation, Glaros *et al.* determined lithium amount in various animal body parts, by analysing the expired air with specific gas separation equipment. [92] Balter and Vigier compared lithium isotopic abundance changes between sheep organs. Thus, lithium therapeutic dose concentration could be adapted. [93] Their work was based on multi-collector inductively coupled plasma mass spectrometry (MC-ICP-MS) characterisations. Based on these works, lithium treatments could be adjusted. MC-ICP-MS technique is commonly used to track ^6Li . Millot and Négrel demonstrated that comparing lithium isotopic variations help to better understand geological events. [94] Human industrial activities effects on the environment were estimated by analysing lithium isotopic abundance in waterways.

The following part is dedicated to the development of lithium isotopic tracing for battery applications.

Recently, Desaulty *et al.* provided a method based on lithium isotopic tracing to identify the lithium source by determining lithium isotopic ratio. [52] This methodology is based on the fact that lithium isotopic ratio depends on the geological site where lithium was extracted. [52] Desaulty *et al.* study deals with battery materials as traceability of lithium origin, which one of the criteria having the highest impact on the environment (Figure I-15).

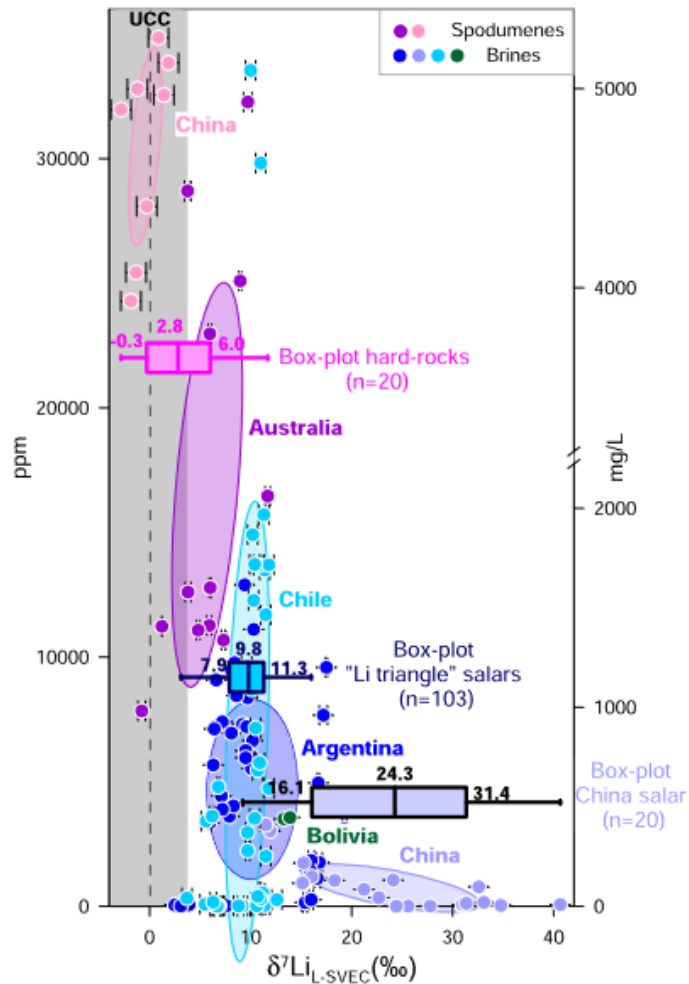


Figure I-15. Lithium isotopic composition $\delta^7\text{Li}_{L-SVEC}$ ($L-SVEC$: the ratio relative to standard lithium) versus lithium content (ppm, $\text{mg} \cdot \text{l}^{-1}$) for several lithium sources. [52]

Figure I-15 illustrates $\delta^7\text{Li}_{L-SVEC}$ variations as a function of its origin (cf. 2.1). Furthermore, Figure I-15 highlights some countries where lithium can be extracted such as Australia, China, Argentina, and Bolivia. Others countries are also producing lithium, such as Chile, Brazil, Zimbabwe, and Portugal.

Battery materials characterisations is increasingly using lithium tracing to investigate lithium behaviour in complex devices and it is particularly relevant to study ASSBs. The development of these electrolyte materials is driven by expected significant improvements related to enhance safety and to increase energy densities. These new perspectives bring new

challenges especially due to interfaces issues which need to be better understood. Industries aim to introduce batteries with higher energy densities and to make of non-flammable solid electrolytes. To obtain an efficient solid electrolyte, various criteria need to be considered such as ionic conductivity, lithium-ion transport number and electrochemical, thermal and mechanical stabilities. The implementation of lithium metal as a negative electrode is one of the main objectives. As previously mentioned, this could lead to increase energy densities. However, several significant technological challenges need to be overcome, including the formation of dendrites leading to short circuits, or generation of high interface resistances impeding lithium transfers. [1] By introducing some specific components enriched in ^6Li , lithium tracing could advantageously be used to study ASSBs limitations. It could help to gain a more precise understanding of lithium transport dynamics in the whole device by revealing fundamental information such as lithium pathways demonstrating ways to optimise cell design.

A corpus of articles published between 2011 and 2023 are discussed in the following part. They deal with ^6Li tracing in battery materials. A specific attention is paid on the characterisation techniques used in order to track lithium isotopes. To carry out such experiments, tracers enriched in ^6Li are needed. Publications are gathered according the used technique.

- *SIMS and ToF-SIMS characterisations*

One of the first studies involving lithium isotopic tracing by ToF-SIMS, was published in 2011 by Lu and Harris to better understand lithium behaviour in battery materials. [95] Their aim was to characterise lithium dynamics using ToF-SIMS in the case of a SEI electrochemically grown on copper foil in $^7\text{LiClO}_4$ based liquid electrolyte. The SEI layer was studied by lithium isotopic tracing after soaking samples in $^6\text{LiBF}_4$ solution during various contact times. $^6\text{LiBF}_4$ was used as a tracer to distinguish lithium ions located in the electrolyte from those coming from the SEI. The $\frac{^6\text{Li}}{^7\text{Li}}$ ratio was determined from the $^6\text{Li}^+$ and $^7\text{Li}^+$ intensities as a function of the SEI depth. The assumptions are that Li^+ ions can diffuse along grain boundaries composing the SEI or through pores, while applying a galvanostatic discharge of the half coin cell. Authors considered that electroneutrality conservation requires that BF_4^- should be transported simultaneously with Li^+ ions. Three-dimensional ToF-SIMS characterisations allowed to estimate $^6\text{Li}^+$ ions migration in depth. After contact time of 30 s or 3 min, the estimated ratio is 0.85 on the surface of the SEI and decreases until it stabilises above 0.4 at 20 nm. After 15 min of contact time, the enrichment profile is different (purple dots on Figure I-16.a). Indeed, the ratio is above 1.2 on the surface and exceeds 1.6 at 5 nm to finally decrease until 0.65 at 20 nm. These results provide information about SEI porosity. The first part of the layer (about 5 nm thick) seems more porous than the rest of the SEI. These results were later confirmed by Shi *et al.* in 2012 (Figure I-16.a). [96]

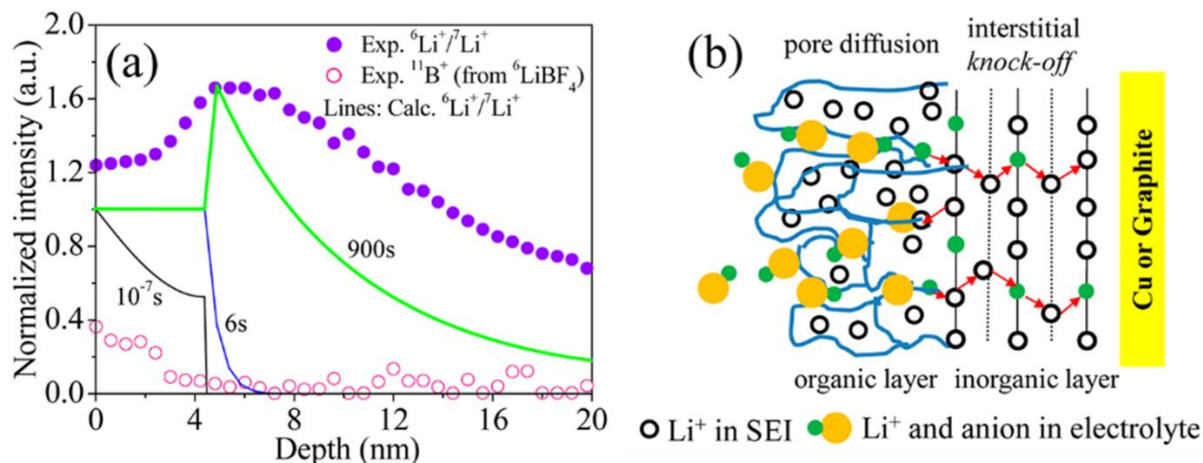


Figure I-16. a) ToF-SIMS characterisation of the ${}^7\text{LiClO}_4$ SEI after 15 min of immersion in ${}^6\text{LiBF}_4$ electrolyte. b) Schematic of the proposed formation mechanism of the SEI: “The open circles represent the Li^+ already in the SEI. In the porous organic layer, the blue solid lines denote channels through which Li^+ in the electrolyte (green filled circles) transports with anions (yellow filled circles) via pore diffusion. The red arrows denote that only Li^+ can diffuse in the dense inorganic layer via the knock-off mechanism”. [96]

Shi *et al.* also concluded that the SEI film is composed of two layers by using a diffusion model. On Figure I-16.a, the green solid curve corresponds to their simulated result. They estimated the thickness of the organic layer at 5 nm by obtaining the same unexpected isotope ratio $\frac{{}^6\text{Li}^+}{{}^7\text{Li}^+}$ profile as the one obtained experimentally by Lu and Harris. (Figure I-16.a). On Figure I-16.b, a schematic of lithium dynamics leading to the SEI formation are presented.

Liu *et al.* also studied the SEI formation and composition. [97] Their setup and ToF-SIMS results are presented on Figure I-17.

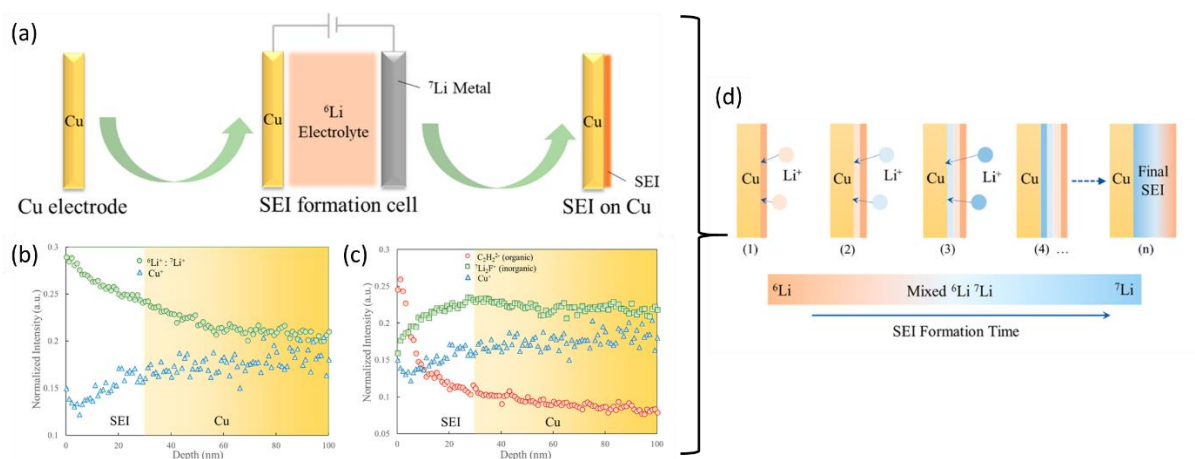


Figure I-17. a) Sample preparation and ToF-SIMS depth profiles of the SEI on Cu electrode surface: b) ${}^6\text{Li}:{}^7\text{Li}$ ratio and Cu^+ ; c) C_2H_2^- (organic), Li_2F^- (inorganic), and Cu^+ . d) Proposed SEI formation mechanism. [97]

Liu *et al.* also concluded that the SEI is formed of several layers. [97] High $\frac{{}^6\text{Li}}{{}^7\text{Li}}$ ratio was observed close to the electrolyte/SEI interface compared with the $\frac{{}^6\text{Li}}{{}^7\text{Li}}$ ratio estimated near the SEI/Cu interface (Figure I-17). Therefore, they assumed that SEI formation starts from the electrolyte side and grows close to the copper. Even if both ToF-SIMS and XPS results confirm the SEI two-layer structure (organic and inorganic), only ${}^6\text{Li}$ tracing enables to understand which layer is formed first. The strength of lithium isotopic tracing allowed them to deeper understand the formation of this passivation layer by using a 1 M solution of ${}^6\text{LiBF}_4$.

Some other publications reported the use of ToF-SIMS or SIMS advanced techniques to trace ${}^6\text{Li}$. Hüger *et al.* published two publications on lithium permeation processes within battery materials. [98] [99] They determined two permeation mechanisms of lithium within amorphous silicon by characterising modifications of the lithium isotope fraction measured by SIMS. They also studied the same type of permeation processes within coated multilayers of lithium niobate (LiNbO_3). The protection of electrodes by coating thin films aims at improving performances Li-ion battery electrodes by increasing lifespan for instance. ${}^6\text{LiNbO}_3$ was used to track lithium permeability through ultrathin layer made of either Cr, Si or C. The goal was to find the most appropriate one. Characterisations were performed by SIMS at room temperature and by neutron diffraction while heating at 100° C. By SIMS, lithium isotopic abundance was determined as a function of the sputtering time. The conclusion is that, at room temperature, lithium permeation is faster through carbon ultrathin layers compared to silicone and chromium, even if lithium permeability through chromium can be improved by heating at 100° C.

Lithium diffusion coefficient in amorphous lithium phosphate Li_3PO_4 and in spinel oxide $\text{Li}_x\text{Mn}_2\text{O}_4$ thin films was estimated by combining lithium labelling with secondary ion mass spectrometry (SIMS). [74] [100] Kuwata *et al.* obtained lithium self-diffusion coefficient in Li_3PO_4 which is an option as SSEs by estimating ${}^6\text{Li}$ abundance with an uncertainty of 5%. [74]

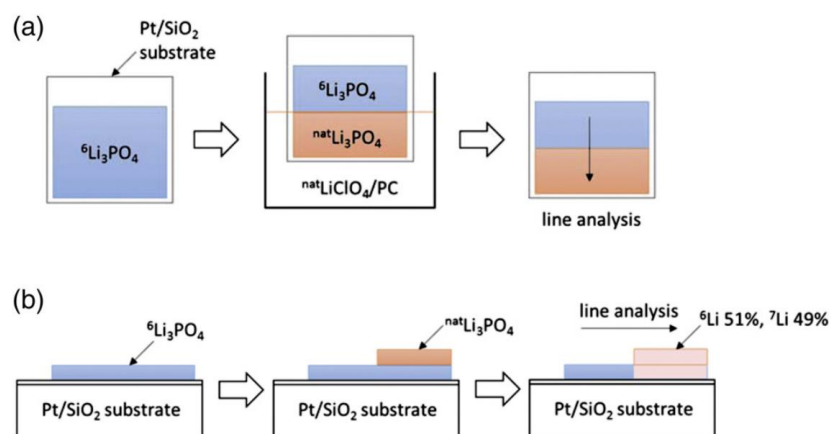


Figure I-18. Setups allowing to study lithium dynamics through lithium phosphate Li_3PO_4 by using lithium isotopic labelling: a) ion-exchange method, and b) mask method. [74]

At 60° C, the lithium diffusion coefficient in amorphous lithium phosphate Li_3PO_4 was estimated at $1.20 \times 10^{-11} \text{ cm}^2 \cdot \text{s}^{-1}$ with the ion-exchange method and at $1.14 \times 10^{-11} \text{ cm}^2 \cdot \text{s}^{-1}$ with the mask method. [74] These methods are presented on Figure I-18. They are both coherent. The highest diffusion coefficient lithium in $\text{Li}_x\text{Mn}_2\text{O}_4$ ($7.7 \times 10^{-13} \text{ cm}^2 \cdot \text{s}^{-1}$) was obtained when lithium relative concentration x is equal to 0.72. [100] It was determined by applying the ion-exchange method. Such information can allow to optimise material composition.

Berthault *et al.* also worked on Li^+ ions dynamics through the SEI formed on graphite-based electrodes (Figure I-19). [15]

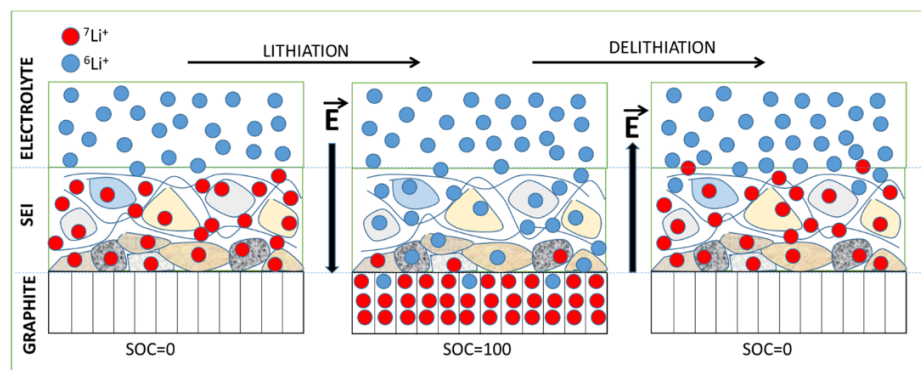


Figure I-19. Lithium isotopic ion exchanges occurring during lithiation or delithiation process of a graphite electrode. [15]

To track lithium isotopes, a half-cell using graphite electrode in coin format is charged in standard conditions in order to create a SEI with lithium natural isotopic abundance. Then, they took out and washed the graphite electrode before reassembling it in a new cell against a ^6Li -foil and a liquid electrolyte enriched in ^6Li at 95%. They finally characterised the SEI lithium isotopic abundance after a lithiation and after a delithiation step by performing ToF-SIMS. Results are presented on Figure I-19. They demonstrated that Li^+ ions contained into the SEI still play a role in lithium diffusion processes. It could not be observed without using lithium isotopic tracing. Furthermore, they estimated the thickness of the inorganic layer at 2.3 nm.

- *Solid-state nuclear magnetic resonance (ssNMR)*

Berthault *et al.* used lithium tracing to characterise lithium behaviour between a liquid electrolyte enriched in ^6Li and a silicon-based electrode. [16] They performed ^6Li and ^7Li high-resolution ssNMR (Figure I-20). While probing solid, the rotation at the magic angle spinning allows to obtain high resolute spectra.

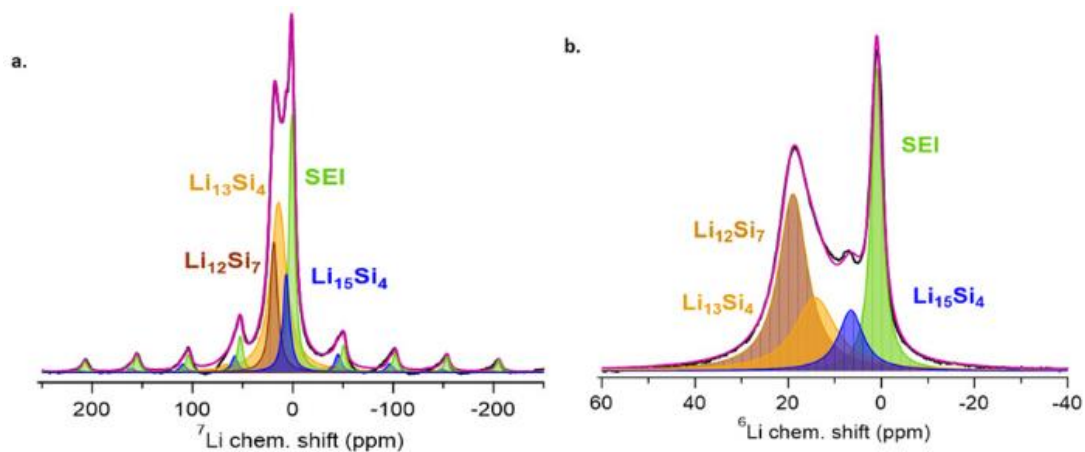


Figure I-20. ${}^7\text{Li}$ (a) and ${}^6\text{Li}$ (b) NMR spectra of lithiated silicon-based electrode in the case of lithium natural isotopic abundance soaked into a ${}^6\text{Li}$ -electrolyte (charge limited to $1,000 \text{ mAh} \cdot \text{g}^{-1}$). [16]

They developed a specific methodology to estimate lithium isotopic abundances by high-resolution ssNMR (Figure I-20). ${}^6\text{Li}$ and ${}^7\text{Li}$ analyses cannot be performed using the same acquisition settings. Thus, Berthault *et al.* developed a methodology to combine ${}^6\text{Li}$ and ${}^7\text{Li}$ spectra. The determination of a normalisation factor by characterising a reference sample at lithium natural isotopic abundance allows an accurate estimation of lithium isotopic abundances of the other samples. After 52 *h* of contact time, the soaked electrode (initially at lithium natural isotopic abundance) was containing 74% of ${}^7\text{Li}$. They demonstrated that there are fast liquid/solid isotopic exchanges after 1 *h* of contact time between the electrode and the electrolyte. Furthermore, they detected a slower dynamic: ${}^6\text{Li}^+$ ions diffuse through the silicon bulk. Thus, silicon was enriched in ${}^6\text{Li}$ over the cycling steps. Lithium isotopic exchanges were highlighted by ${}^6\text{Li}$ and ${}^7\text{Li}$ high-resolution ssNMR characterisations. All these results were complemented with ToF-SIMS and liquid-state NMR. A better understanding of lithium dynamics in such materials could lead to enhance electrode design.

Chang *et al.* worked on the lithium dendrites growth issue, which is one of the reason why Li-foil is not widely used in commercial batteries. [101]

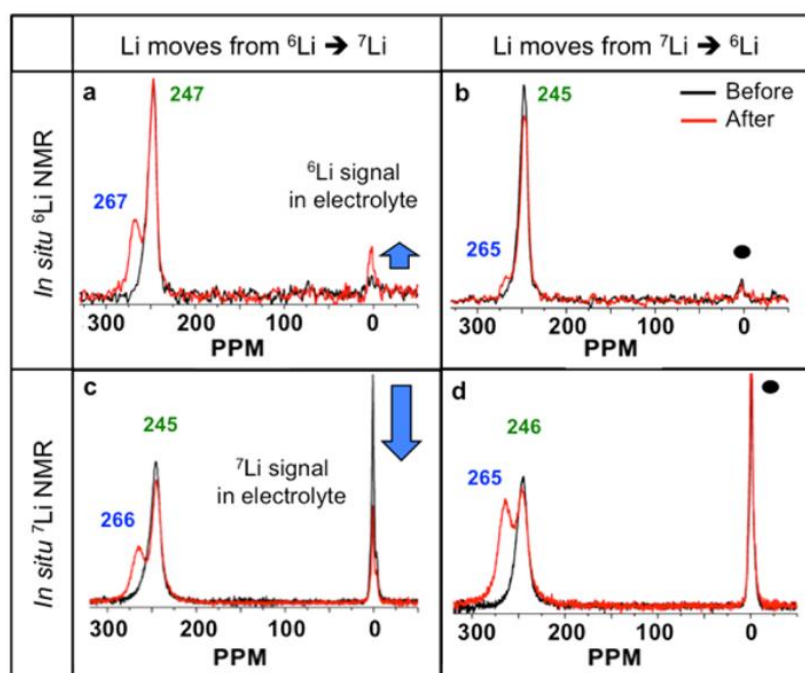


Figure I-21. “Change of ${}^6\text{Li}$ and ${}^7\text{Li}$ NMR spectra before and after growth of microstructures: comparison of in situ (a, b) ${}^6\text{Li}$ and (c, d) ${}^7\text{Li}$ NMR spectra of the cell composed of a ${}^6\text{Li}$ metal and ${}^7\text{Li}$ metal foil separated by a glass microfiber separator soaked of electrolyte, after current flow at 1.1 mA/cm^2 for 240 min. In panels a and c, Li^+ ions move from the ${}^6\text{Li}$ to ${}^7\text{Li}$ strip, and in panels b and d, Li ions move from the ${}^7\text{Li}$ to ${}^6\text{Li}$ strip. The black spectra correspond to the pristine state (before passing current), and the red spectra correspond to the final state (after current flow). The arrows refer to the change in intensity of electrolyte, and the dots indicate no noticeable change in intensity.” [101]

The goal of their work is to understand lithium microstructure growth in a Li/Li symmetric battery containing a carbonate liquid-based electrolyte (1M LiPF_6 : EC/DMC). It corresponds to lithium dendrites formation. By applying a current, ${}^6\text{Li}^+$ ions migration was forced from a ${}^6\text{Li}$ -foil enriched at 95% in ${}^6\text{Li}$ to a ${}^7\text{Li}$ -foil at lithium natural isotopic abundance. The use of two lithium foils at different lithium isotopic abundance allows to determine the origin of shift and peak intensity variations. The peak detected around 245 ppm is attributed to lithium microstructure. Modifications can be due either to microstructure formation or to changes in the bulk Li-foil. The enrichment in ${}^6\text{Li}$ helps to assign the origin of the probed lithium. On Figure I-21, lithium isotopic migration is highlighted. The effect of the applied pressure on lithium stripping process have been investigated by NMR. Notice that in this study, NMR experiments were performed *in situ*. Thus, no rotation at the magic angle spinning was possible, leading to broad peaks.

Lithium dynamics were characterised by Zheng and Hu in a composite SSE (Figure I-22).

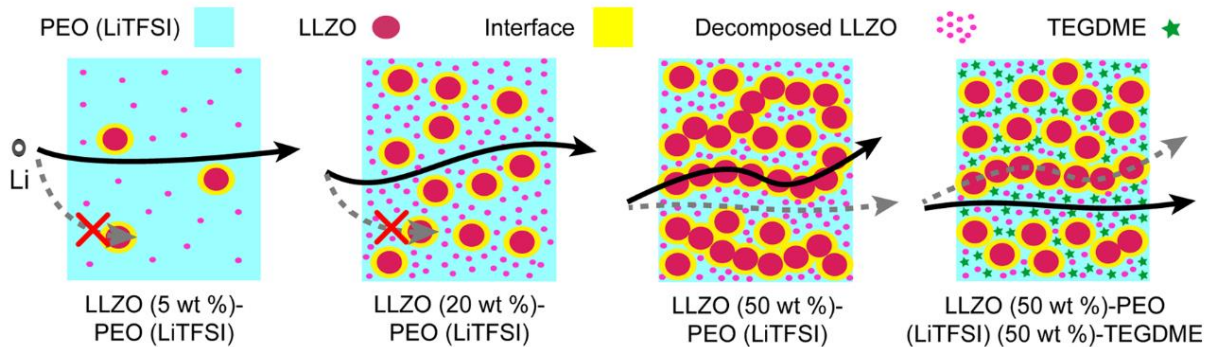


Figure I-22. Schematic of Li^+ ions pathways within a polymer electrolyte matrix (PEO+LiTFSI) containing various wt% of LLZO ceramic particles. [46]

They worked on a composite SSE made of a polymer electrolyte (PEO+LiTFSI) containing ionic conductive ceramic particle ($\text{Li}_7\text{La}_3\text{Zr}_2\text{O}_{12}$, LLZO). [46] They performed ^6Li high-resolution ssNMR experiments in order to demonstrate that resistances at the interfaces affect the ionic conductivity of the whole device. Lithium tracing allowed them to observe that the ceramic nanoparticles concentration into polymer membrane impacts Li^+ ions pathways. Indeed, for polymer electrolyte containing less than 50 wt% of LLZO, lithium ions diffuse through the polymer matrix because ceramic particles do not percolate. On the other hand, while polymer membrane containing 50 wt% of LLZO, ceramic particle percolation occurs and modifies lithium diffusion pathways, which mainly take place through the ceramic particles. As high-resolution ssNMR can distinguish lithium chemical environment, ^6Li abundance in both materials could be compared between a reference sample at natural abundance and tested ones.

- *Inductively Coupled Plasma Mass Spectrometer (ICPMS)*

Recently, Morita *et al.* demonstrated that it is possible to use lithium separation method by ionic conductor in order to enrich a lithium hydroxide solution in ${}^6\text{Li}$ in just one step by applying a specific voltage profile (Figure I-23). [102]

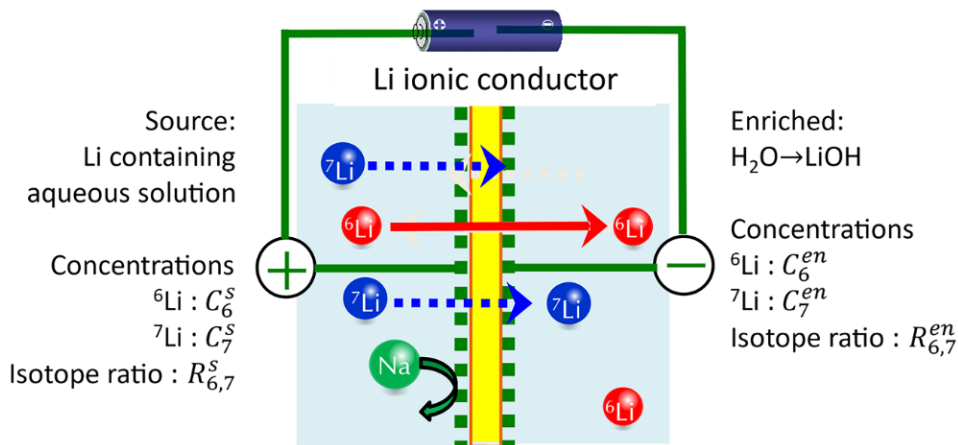


Figure I-23. Schematic of ${}^6\text{Li}$ enrichment by using a lithium separation method by ionic conductor. [102]

On Figure I-23, a thin layer of $\text{Li}_{0.29}\text{La}_{0.57}\text{TiO}_3$ (schematised by a yellow bar) was used as ionic conductor in-between both electrodes. A voltage was applied to speed up the enrichment process. Lithium isotope separation was possible because their mass differs, which induces different extraction speed. They mentioned that lithium isotope diffusion coefficient ratio ($D_{{}^6\text{Li}}/D_{{}^7\text{Li}}$) is approximately equal to 1.08. ${}^6\text{Li}$ and ${}^7\text{Li}$ concentrations were measured by ICP-MS. Morita *et al.* mentioned that a high separation factor D of 1.06 was determined using the following Equation I-6,

$$D = \frac{\text{Isotopic ratio into the } {}^6\text{Li enriched solution}}{\text{Isotopic ratio into the source solution}} \quad \text{I-6}$$

Schwarzburger *et al.* studied a solution of butyl lithium (BuLi) enriched in ${}^6\text{Li}$ put in contact with pre-lithiated TiS_2 single crystals. [103] Their objective was to identify irreversible steps during the lithiation process, such as the octane formation at the TiS_2 surface. LA-ICP-MS was used to track ${}^6\text{Li}$ and ${}^7\text{Li}$ in lithiated titanium disulfide (LiTiS_2) single crystals. Lithium self-diffusion coefficients were extracted by fitting isotopic exchange results with numerical fittings based on the Fick's second law. Lithium diffusion coefficient was estimated at $4.68 \pm 0.55 \times 10^{-14} \text{ m}^2 \cdot \text{s}$ in ${}^6\text{LiTiS}_2$ at 22°C . Furthermore, by performing ${}^6\text{Li}$ tracing, some crucial steps of lithium intercalation in TiS_2 single crystals from a BuLi solution were explained.

Anode, cathode and electrolyte of $\text{LiNi}_{0.6}\text{Mn}_{0.2}\text{Co}_{0.2}\text{O}_2$ (NMC622)/graphite based battery were studied by Diehl *et al.* while using of liquid electrolyte (${}^6\text{LiPF}_6$) enriched at $93.25\% \pm 2.21\%$ in ${}^6\text{Li}$ (Figure I-24). [91]

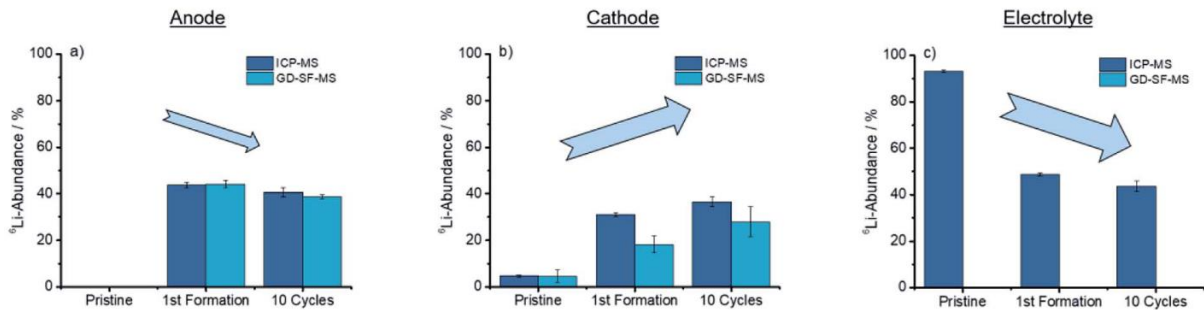


Figure I-24. ${}^6\text{Li}$ abundance a) in the graphite anode, b) in the NMC622 cathode, and c) in the liquid electrolyte determined by ICP-MS and GD-SF-MS after cycling a $\text{LiNi}_{0.6}\text{Mn}_{0.2}\text{Co}_{0.2}\text{O}_2$ /graphite based battery. [91]

On Figure I-24, despite variations between ICP-MS and glow discharge sector field mass spectrometry (GD-SF-MS) results, these techniques provide similar trends on the estimated lithium isotopic abundance over charge/discharge cycles. ${}^6\text{Li}$ abundance decreases in the anode and in the electrolyte, whereas it increases in the cathode. They demonstrated that lithium isotopic abundance is affected by the applied C-rate. They also observed a fast isotope mixing kinetics during the first charge/discharge cycle. In the end, they suggested to perform SIMS analyses in order to obtain lithium isotopic distribution on the studied electrodes.

- *Laser-induced breakdown self-reversal isotopic spectrometry (LIBRIS)*

A new methodology, called LIBRIS was recently developed by Touchet *et al.* (Figure I-25). [86] Lithium isotopic abundance of samples can be determined by such characterisation technique.

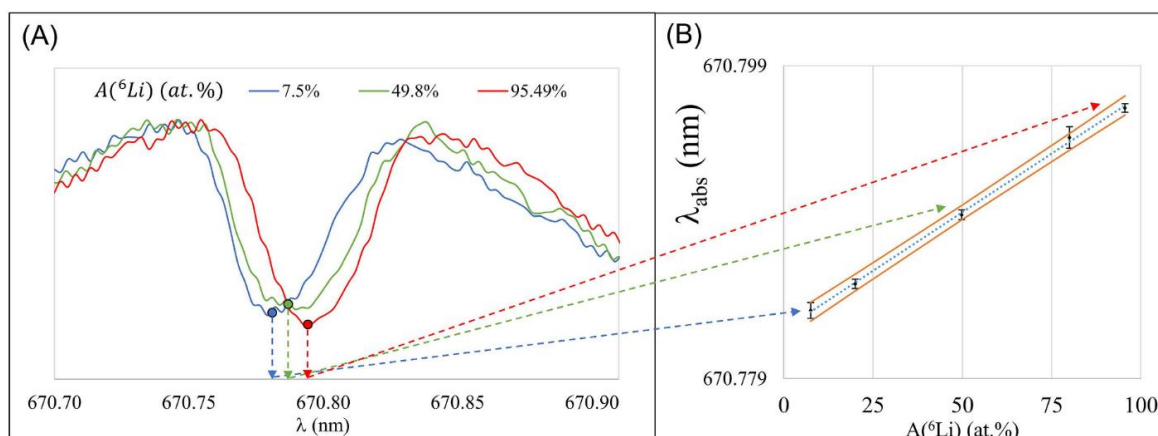


Figure I-25. A) LIBRIS spectra obtained on three lithium carbonates with various ${}^6\text{Li}$ abundance of 7.5%, 49.8% and 95.5% B) Calibration curve obtained from LIBRIS analyses. [86]

Touchet *et al.* prepared three samples with a ${}^6\text{Li}$ abundance of 7.5%, 49.8% and 95.5% by mixing two different powders of lithium carbonate: one at lithium natural isotopic abundance and the other enriched at 95.5% in ${}^6\text{Li}$. LIBRIS characterisation of these samples enable to obtain a calibration curve allowing to estimate ${}^6\text{Li}$ abundance of an unknown sample within the same matrix. The lateral resolution of the analysis was $250\ \mu\text{m}$. Ultraviolet laser ablation in ambient air leads to a 21% uncertainty on the ${}^6\text{Li}$ abundance of samples containing 50% of ${}^6\text{Li}$. Touchet *et al.* also demonstrated that working under argon flux reduces the uncertainty down to 13%.

More recently, Gallot--Duval *et al.* used the same methodology to track lithium isotopes into Li_2CO_3 and a polymer electrolyte, PEO+LiTFSI which can be used for solid-state batteries. [87] They obtained two calibration curves of the ${}^6\text{Li}$ isotopic abundance, one for PEO+LiTFSI and one for Li_2CO_3 (Figure I-26).

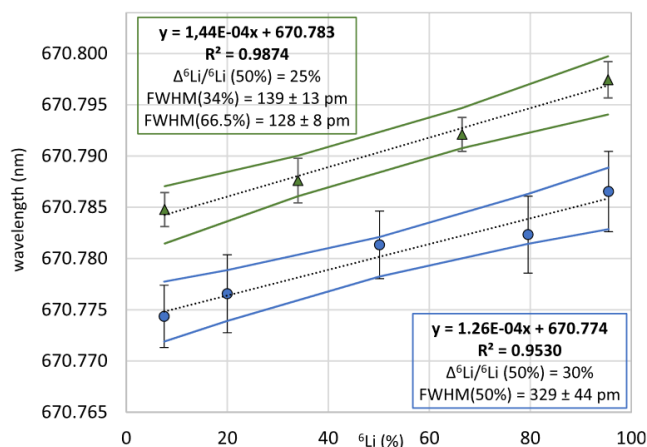


Figure I-26. Calibration curves obtained from LIBRIS analyses performed on PEO+LiTFSI (triangles) and on Li_2CO_3 (dots). $\frac{\Delta \text{}^6\text{Li}}{\text{}^6\text{Li}}$ (50%) represents the uncertainty of ${}^6\text{Li}$ abundance of samples containing 50% of ${}^6\text{Li}$, and the absorption dip full width at half-maximum (FWHM).

Figure I-26 highlights that LIBRIS can provide a fast determination (between few seconds to few minutes) of lithium isotopic abundances with an uncertainty of 30% and 25% on the ${}^6\text{Li}$ abundance determination of lithium carbonate and polymer electrolyte, respectively. Furthermore, the lateral resolution is estimated at $7 \mu\text{m}$.

Conclusion

ASSBs are an attractive alternative to traditional lithium-ion batteries thanks to their potential for higher energy density and enhanced safety. One of the main objectives is to design an ASSB containing lithium metal at the anode. Thus, the energy density is expected to be significantly increased. Composite SSEs are even more promising for the development of ASSBs because they combine benefits of inorganic SSEs and polymer SSEs. However, they are known to have low ionic conductivity, compared to traditional liquid electrolytes, due to high interfacial resistances. Therefore, it is essential to deeper understand parameters that control lithium dynamics within these composite materials. A way to investigate lithium transport mechanisms into these solid materials already containing lithium lies in performing lithium isotopic tracing experiments. They are based on the use of materials enriched in ${}^6\text{Li}$. Some advanced characterisation techniques allowing to detect simultaneously or separately ${}^7\text{Li}$ and ${}^6\text{Li}$ isotopes have been briefly detailed. The choice of the technique will depend on the nature of the material, and also on the required information. A summary of various benefits and drawbacks related to each technique is provided. Then, their applications were demonstrated throughout relevant articles involving the use of lithium isotopic labelling. Notice that lithium isotopic tracing is used to study battery materials only from 2011. All these research works aim at a better understanding of lithium dynamics in battery materials. For instance, the estimation of lithium self-diffusion coefficient, the choice of best permeable ultrathin layers, formation mechanisms of the SEI and its thickness could be successfully studied. Furthermore, electrodes or composite SSEs compositions could be optimised in order to improve electrochemical performances of the devices. Finally, lithium microstructures such as lithium dendrites formation was studied to better understand this unwanted process.

Chapter II. Methodologies development to accurately determine lithium isotopic abundance

As presented in chapter I, there is a significant interest to increase electrochemical performances of lithium batteries. Lithium isotopic tracing can be seen as a powerful tool to enhance the understanding of lithium dynamics in existing systems or in new battery components especially electrode materials and electrolytes (liquid or solid). More precisely, lithium labelling can help to investigate lithium behaviour at the various interfaces present in the electrochemical system.

Firstly, the polymer, the lithium salt and the ionic conductive ceramic studied in this work are presented. Electrochemical tests are also described. Then, the most relevant parameters of ToF-SIMS and ssNMR techniques for lithium isotopes characterisation are determined. These methodologies provide accurate lithium isotopic abundance estimations of lithiated materials. Finally, to demonstrate their robustness, the developed methodologies are applied on polymer electrolytes with various ^6Li abundances.

This chapter is heavily inspired from our publication: "Lithium Self-diffusion in a Polymer Electrolyte for Solid-State Batteries: ToF-SIMS/high-resolution ssNMR Correlative Characterization and Modeling Based on Lithium Isotopic Labeling" published in ACS Applied Material & Interfaces in 2023. [104]

II.1. Solid-state electrolytes preparation and electrochemical tests on specify devices

In an all-solid-state battery (ASSB), the electrolyte acts as lithium ions conductor and as a separator between the two electrodes. An ideal solid-state electrolyte should provide a high ionic conductivity ($> 10^{-4} S \cdot cm^{-1}$ at RT), a negligible electronic conductivity to avoid self-discharge ($< 10^{-12} S \cdot cm^{-1}$ at RT), a large electrochemical stability window (0 to 5 V vs. Li^+/Li), a good chemical and mechanical stability regarding the electrodes material and a large operating temperature range suited to the intended application (-40 to +70°C). [22]

1.1. Polymer electrolytes preparation with a lithium salt enriched in 6Li

a. The selected materials: poly(ethylene oxide) (PEO) and lithium salt (LiTFSI)

Polymer membranes were made of poly(ethylene oxide) (PEO) (Sigma-Aldrich, Mw: 300,000, purity $> 99\%$) and lithium bis(trifluoromethanesulfonyl)imide (LiTFSI) (Sigma-Aldrich, purity $> 99.95\%$). Figure II-1 and Figure II-2 illustrate their semi-developed formula.

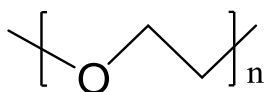


Figure II-1. Semi-developed formula of the poly(ethylene oxide) (PEO), with n the number of repeated units of the polymer.

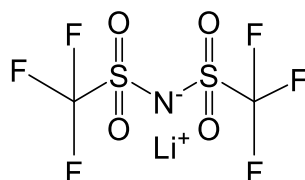


Figure II-2. Semi-developed formula of lithium bis(trifluoromethanesulfonyl)imide (LiTFSI) salt.

LiTFSI ($LiN(SO_2CF_3)_2$) was chosen because it is compatible and soluble in PEO polymer matrix. [105] The LiTFSI salt is available at lithium natural isotopic abundance (92.4% 7Li and 7.6% 6Li noted 7LiTFSI), but also enriched at 95.4% in 6Li (4.6% 7Li and 95.4% 6Li noted 6LiTFSI) (Sigma-Aldrich, purity $> 98\%$). This last grade was used to modify the lithium natural isotopic abundance in polymer electrolytes. The synthesis of 6LiTFSI enriched in 6Li was investigated by using a $^6LiOH \cdot H_2O$ precursor enriched in 6Li . Mixing $^6LiOH \cdot H_2O$ and HTFSI in water lead to the preparation of 6LiTFSI after drying due to an acid-base reaction. However, a commercial salt was used for this work to guarantee the quality and accuracy enriched 6LiTFSI . Working with 6LiTFSI offers the opportunity to follow dynamics of lithium ions contained in a polymer electrolyte.

Polymer powder was dried during a five-day under dynamic vacuum at 60 °C. The lithium salts were also dried during five days, but at 150 °C. Various ratio of ${}^7\text{LiTFSI}$ and ${}^6\text{LiTFSI}$ were mixed to obtain polymer electrolyte with several ${}^6\text{Li}$ abundances. Karl Fisher analyses confirmed that lithium salt was containing only 2 ppm of water and can be considered as battery grade.

b. Polymer electrolytes preparation

Polymer electrolytes preparation was performed in a dry room. PEO and LiTFSI were dissolved in a blend of two anhydrous solvents: 1,3-dioxolane (Diox) (Sigma-Aldrich, anhydrous, purity > 99.8%) and 1,2-dimethoxyethane (DME) (Sigma-Aldrich, anhydrous, purity > 99.5%). The $\frac{OE}{Li}$ ratio was set at 16:1, which is equivalent to a lithium salt concentration of 1.2 M. The solution was casted on copper foil after a 48 h stirring at 50° C. Then, the film is dried during 24 h under dynamic vacuum at 60 °C allowing to evaporate the solvents. The polymer electrolyte thickness was measured at 100 μm .

Four polymer electrolytes with various lithium isotopic abundances were prepared. Table II-1 sums up the expected lithium isotopic abundances of each polymer electrolyte based on mass calculations.

Table II-1. Polymer electrolytes made of PEO and LiTFSI at 1.2 M, with various expected lithium isotopic abundances.

Polymer electrolyte	% ${}^7\text{Li}$ (%)	% ${}^6\text{Li}$ (%)	Used salts
A (reference sample)	92.4 \pm 0.1	7.6 \pm 0.1	${}^7\text{LiTFSI}$
B	66.1 \pm 0.1	33.9 \pm 0.1	${}^7\text{LiTFSI}$ and ${}^6\text{LiTFSI}$
C	33.6 \pm 0.1	66.4 \pm 0.1	${}^7\text{LiTFSI}$ and ${}^6\text{LiTFSI}$
D	4.6 \pm 0.1	95.4 \pm 0.1	${}^6\text{LiTFSI}$

Electrolyte A was prepared using only the commercial lithium salt, ${}^7\text{LiTFSI}$. Later, this polymer electrolyte will be used as a reference sample to determine the lithium isotopic abundance in others by advanced characterisation techniques based on lithium isotopic tracing. Electrolyte D was also prepared with commercial lithium salt ${}^6\text{LiTFSI}$ enriched at 95.4% in ${}^6\text{Li}$. Lithium isotopic abundances in electrolytes A and D were set according to the datasheets provided by supplier. Thus, the uncertainty is set at 0.1%. Electrolytes B and C were obtained by mixing the two commercial salts in various proportions. Thus, lithium isotopic abundances in electrolytes B and C were estimated from the weighed masses. To determine the error, an uncertainty (Δm_{Li}) of 10^{-4} g was associated to the weighing salts inside an argon-filled glovebox. According to Equation II-8, lithium isotopic abundances uncertainty of electrolytes B and C was also estimated at 0.1%. It is clear that the uncertainty in mass measurement can be considered as negligible regarding the uncertainty associated with the lithium isotopic abundance.

The mixing step might also increase uncertainty if lithium salts are not evenly distributed within the solution. A mixing time of 48 h at 50° C ensures a homogeneous

distribution of the lithium salts into the polymer membrane. Electrolyte A at lithium natural isotopic abundance was used as the reference electrolyte in all the following results. Figure II-3 is an example of a polymer electrolyte casted on a copper foil.

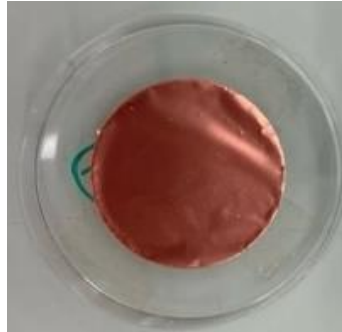


Figure II-3. Polymer electrolyte disk punched after casting on copper foil and dried at 60° C under dynamic vacuum.

On Figure II-3 the polymer electrolyte is not easily visible because it is translucent.

1.2. Commercial ceramics and dispersion preparation

a. LLZTO ceramic pellet

The selected ceramic is a garnet-type ceramic, the $\text{Li}_{6.4}\text{La}_3\text{Zr}_{1.4}\text{Ta}_{0.6}\text{O}_{12}$ (LLZTO). Redhammer *et al.* determined by performing neutron diffraction that LLZTO crystallises in $Ia\bar{3}d$ space group. [106] Figure II-4 schematises the chemical structure of the LLZTO ceramic.

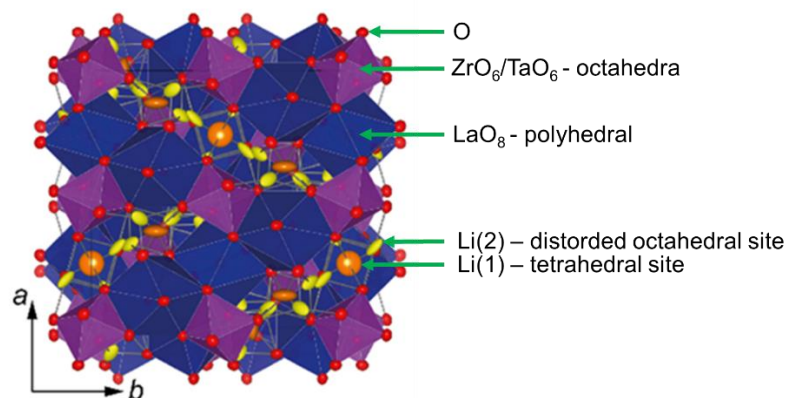


Figure II-4. Chemical structure of the $\text{Li}_{6.5}\text{La}_3\text{Zr}_{1.5}\text{Ta}_{0.5}\text{O}_{12}$ ceramic. Images modified from [106].

On Figure II-4, atoms organisation is clearly described by Redhammer *et al.* [106] Oxygen atoms are forming polyhedral around other atoms. LaO_8 polyhedral are represented in blue. Zr^{4+} and Ta^{5+} added by doping are occupying regular octahedral sites represented in purple. The way they are connected with each other by their edge designs lithium pathways through the ceramic. Lithium ions are either occupying 24d tetrahedral sites (Li(1) in orange) or 96h distorted octahedral sites (Li(2) in yellow).

The used LLZO ceramic pellet doped with tantalum (Ta) is commercially available (Ampcera®). The pellet is 0.7 mm thick, and has a diameter of 14 mm. The supplier has estimated its ionic conductivity between $4 \times 10^{-4} \text{ S} \cdot \text{cm}^{-1}$ and $10^{-3} \text{ S} \cdot \text{cm}^{-1}$ at room temperature. Lithium concentration is estimated at 33.81 M.

It was established in previous works that substituting zirconium (Zr) by Ta enhances chemical properties. This substitution is favoured because they are both inert against lithium metal. [107] The presence of Ta stabilises the cubic garnet structure, which is more ionic conductive than the tetragonal phase composing LLZO. Indeed, $\text{Li}_{6.7}\text{La}_3\text{Zr}_{1.7}\text{Ta}_{0.3}\text{O}_{12}$ presents an ionic conductivity of $9.6 \times 10^{-4} \text{ S} \cdot \text{cm}^{-1}$ [108] whereas $\text{Li}_7\text{La}_3\text{Zr}_2\text{O}_{12}$ has an ionic conductivity of only $1.63 \times 10^{-6} \text{ S} \cdot \text{cm}^{-1}$ at room temperature. [109] Regarding literature, the $\text{Li}_{6.75}\text{La}_3\text{Zr}_{1.75}\text{Ta}_{0.25}\text{O}_{12}$ ionic conductivity is $2.9 \times 10^{-4} \text{ S} \cdot \text{cm}^{-1}$ at 25° C for instance. [110] Moreover, Yang *et al.* have demonstrated that added 1 wt% of Li_3PO_4 increases the ionic conductivity up to $7.2 \times 10^{-4} \text{ S} \cdot \text{cm}^{-1}$ at 25° C. [110]

It is known that LLZTO is sensitive to air and moisture. [111] Thus, CO_2 , Li_2CO_3 and LiOH can be formed at the surface after air exposure, increasing the contact resistance of the ceramic pellet. LLZTO was stored and handled inside an argon-filled glovebox before being used. Ceramic pellets were packaged into non-hazardous mineral oil. The provided protocol was followed to remove it. The first micrometres were polished with an 800-grit sand paper. Then, pellets were washed with anhydrous acetone.

The X-ray diffraction pattern presented on Figure II-5 was obtained by characterising the LLZTO pellet with the Brüker D8Advance equipment.

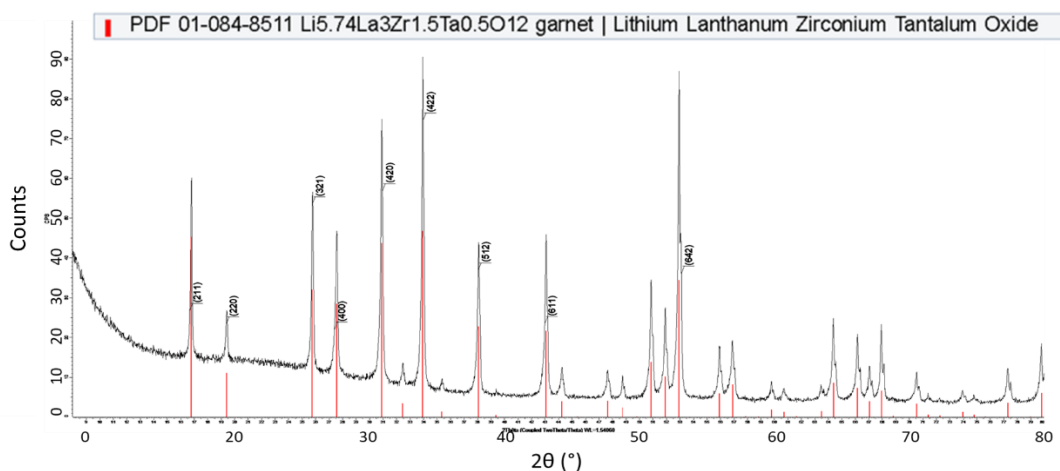


Figure II-5. X-ray diffraction pattern of the LLZTO pellet.

On Figure II-5, LLZTO ceramic pattern was identified from the database. [112] All peaks are assigned. Thus, no crystallised impurity was detected.

b. LLZTO ceramic particles

Ceramic nanoparticles are composed of $\text{Li}_{6.4}\text{La}_3\text{Zr}_{1.4}\text{Ta}_{0.6}\text{O}_{12}$ (Ta-doped LLZO, LLZTO) (Ampcera®, purity > 99.9%). Their composition and their structure are identical compared to that of the ceramic pellet. Their diameter is between 400 and 600 nm. Their theoretical density is $5.5 \text{ g} \cdot \text{cm}^{-3}$ and their ionic conductivity is estimated between $5 \times 10^{-4} \text{ S} \cdot \text{cm}^{-1}$ and $10^{-3} \text{ S} \cdot \text{cm}^{-1}$ at room temperature by the supplier.

The ionic conductivity of the polymer electrolyte is significantly lower compared to that of the ceramic pellet. [45] Thus, adding ceramic particles into the electrolyte might lead to increase the global ionic conductivity.

c. Dispersion preparation of a polymer electrolyte containing ceramic particles

To prepare a composite electrolyte, 0.78 g of LLZTO particles were mixed with 0.7 g of polymer electrolyte in a blend of solvents. The composite electrolyte is containing 52.7 wt%, corresponding to 20 vol% (Appendix A-II-1. *Composite electrolyte preparation*). The mixture was placed into a Teflon vial with a 20 mm-diameter ball of yttria-stabilised zirconia. The vial was sealed in pouch packaging under vacuum at 100 mbar because it had to be stirred outside the dry room. A three-dimensional dynamic mixer (TURBULA®) was used to stir during 5 h. The mixture was then casted on Teflon plate in the dry room. The coating was dried 48 h at 60° C, under dynamic vacuum to extract solvents.

After the drying process, the composite electrolyte thickness was measured at 181 μm in average. Disks of 16 μm in diameter were punched. They were placed between a ^6Li -foil and a ^7Li -foil. The ^6Li -foil was prepared from chunks laminated at 290 μm and the commercial ^7Li -foil was 100 μm thick. Coin cell assembly was carried out in the dry room and coin cells were sealed in an argon-filled glovebox.

1.3. Electrochemical experiments performed on various devices

An EIS spectrum was recorded before and after applying an electrochemical stress. Chronoamperometry (CA) technique as well as chronopotentiometry (CP) technique were investigated. These techniques are presented in the following sections.

a. Electrochemical impedance spectrometry (EIS)

Electrochemical impedance spectroscopy (EIS) offers the opportunity to estimate chemical properties based on electrical analyses in frequency. The characterisation technique is performed to determine the ionic conductivity (σ) of a material by measuring the electrical resistance (R) of the material. R corresponds to the ability of a material to resist the electric current. [113] σ expression is given by the following Equation II-1,

$$\sigma = \frac{e}{R \cdot S} \quad \text{II-1}$$

with e the thickness (cm), R the resistance (Ω), and S the contact surface (cm^2). To determine the resistance from the Nyquist plot, an equivalent electrical circuit is used. [114]

During the acquisition, a sinusoidal perturbation of few millivolts is applied on a device. The resulting current is measured. Results are presented in a Nyquist plot: $Re(Z)$ as a function of $-Im(Z)$. R corresponds to the real part of the impedance $Re(Z)$. Thus, the ionic conductivity can be calculated from Equation II-1.

A VMP-300 equipment was used for EIS measurement on a device maintained under 1 bar pressure. The EIS spectra were potentiostatically measured at a specific voltage with an oscillation of 70 mV amplitude over frequencies standing from 7 MHz to 100 mHz. The recorded EIS were fitted using ZFit software implemented in EC-Lab V11.43. The equivalent circuit $R_1 + \frac{Q_2}{R_2}$ was used to determine resistances R_1 and R_2 . R_1 is related to the resistance of the connectors, which is negligible compared with R_2 , which corresponds to the resistance of the device. All electrochemical tests were performed at 60° C. The temperature was monitored close to the sample by a probe placed into the oven and directly connected to the Biologic equipment.

b. Chronoamperometry (CA) technique

The chronoamperometry (CA) technique consists in applying a constant voltage, while recording the current as a function of time. This technique can be used to investigate diffusion coefficient in battery materials, such as electrode materials. [115]

A CA sequence with a constant voltage set at 0.25 V was applied on an *in-plane* device during lithium diffusion experiments. The device is presented in chapter III. This setup device will be described in chapter III and chapter IV. Polarisation effects were avoided because the CA technique sets the voltage and tracks the current. However, the 7 mm distance between both electrodes requires the application of a rather low voltage to observe lithium diffusion.

c. Chronopotentiometry (CP) technique

The chronopotentiometry (CP) technique consists in applying a constant current between both electrodes, while recording the voltage as a function of time.

A CP with a constant current density set at $50 \mu A \cdot cm^{-2}$ was applied on the *sandwich* and the *dispersion* devices during lithium diffusion experiments. The devices are presented in chapter IV and V, respectively. These devices will be described in chapter IV and chapter V, respectively. The specific capacity Q ($A \cdot h$) is proportional to the duration of the electrochemical step, according to Equation II-2.

$$Q = I \cdot t \quad \text{II-2}$$

with $I(A)$ the current and $t(h)$ the time of the chronoamperometry sequence. The amount of exchanged lithium, n_{Li} (mol), is expressed by the following Equation II-3,

$$n_{Li} = \frac{3600 \times Q}{F} \quad \text{II-3}$$

with F , the Faraday constant ($F = 96,485 C \cdot mol^{-1}$). Then, a percentage of exchanged lithium compared to the amount of lithium contained in the polymer electrolyte, $\%n_{Li}$ (%), can be calculated by using the following Equation II-4,

$$\%n_{Li} = \frac{n_{Li}}{n_{Li}(polymer)} \cdot 100 \quad \text{II-4}$$

with $n_{Li}(polymer)$, the amount of lithium contained into the polymer electrolyte.

The presented materials will be characterised by performing mainly ToF-SIMS and high-resolution ssNMR. These two advanced techniques were already presented in chapter I. Here, specific aspects will be discussed in order to explain how to set up experiment providing accurate determination of Li isotopic abundances.

II.2. Determination of relevant parameters of ToF-SIMS and ssNMR techniques for lithium isotopes characterisation

2.1. Relative lithium isotopic abundance determination by ToF-SIMS

Based on the acquisition settings, ToF-SIMS characterisation can offer local chemical information with high mass resolution ($\frac{m}{\Delta m} = 10,000$) [72], high sensitivity (*ppm*) [58] and relatively good lateral resolution ($< 100/200 \text{ nm}$). [71] The time-of-flight of both lithium isotopes differs by more than 600 ns , depending on the used equipment. Thus, ToF-SIMS technique can distinguish lithium isotopes.

Surface of the polymer electrolytes was characterised by ToF-SIMS by using an ION-TOF ToF-SIMS 5 spectrometer. Polymer electrolytes were stuck on a sample holder with the help of a double-side copper tape. A sealed vessel allowed to transfer samples from a dry room to the ToF-SIMS ultra-high vacuum (UHV) analysis chamber without any exposure to atmosphere. The pressure in the analysis chamber was below $6 \times 10^{-9} \text{ mbar}$. A monoatomic bismuth gun (Bi^+) at 15 keV with an incidence of 45° was used. ToF-SIMS allows to characterise the chemical composition of the extreme surface of materials. Indeed, only few nanometres were analysed. Saturation effects appear in standard conditions. To avoid them, the primary ion chopper width was set at 6 ns empirically, which corresponds to a current intensity of 0.18 pA . The chopper width effect will be discussed later. Surfaces of $300 \times 300 \mu\text{m}^2$ were characterised. They were segmented into $65,536 \text{ pixels}$ ($256 \times 256 \text{ pixels}^2$). The positive acquisition mode was selected to exhibit greater sensitivity to the Li^+ signal. During analysis, positive and negative molecular fragments are ejected from the surface of the sample. A negative polarisation applied to the analyser column allows only the collection of the positive molecular fragments. The cycle time was set at $100 \mu\text{s}$. It has a direct impact on the highest mass that can be detected (mass range being proportional to the cycle time). Images are resulting from a superimposition of 46 scans acquired with $1 \text{ shot} \cdot \text{pixel}^{-1}$. Surfaces were analysed by using a “random” acquisition mode, which allows to apply fewer local strains on polymer electrolytes and avoid unwanted charge effects. An electron flood gun was also turned on to improve charging effects compensation of those insulating samples. The electron flood gun has an energy of 21 V and a delay of $1 \mu\text{s}$. ION-TOF in-house software Measurement Explorer® was used to process experimental data.

According to literature, $^7\text{Li}^+$ and $^6\text{Li}^+$ molecular fragments present identical ionisation yield and detection efficiency for a given matrix. [74] Thus, lithium isotopic abundances ($\%^k\text{Li}$) can be estimated from the measured intensities. [15],[100],[116],[117]

$\%^k\text{Li}$ expressions are given by the following Equations II-5 and II-6,

$$\%^7\text{Li} = \frac{I(^7\text{Li}^+)}{I(^7\text{Li}^+) + I(^6\text{Li}^+)} \cdot 100 \quad \text{II-5}$$

$$\%^6\text{Li} = \frac{I(^6\text{Li}^+)}{I(^7\text{Li}^+) + I(^6\text{Li}^+)} \cdot 100 \quad \text{II-6}$$

where $I(^k\text{Li}^+)$ is the intensity of the molecular fragment $^k\text{Li}^+$ with $k = 6 \text{ or } 7$.

ToF-SIMS is not a quantitative technique because ionisation yield highly depends on matrix effects. [118] However, as already mentioned in chapter I, a way to perform quantification of an element in an unknown sample was developed by Henss *et al.* [73] This is why in our work, lithium isotopic abundance of the LiTFSI is studied into the polymer matrix, in which LiTFSI is incorporated to form the polymer electrolyte.

To determine lithium isotopic abundance in polymer electrolytes by ToF-SIMS, the appropriate acquisition parameters had to be tuned. The way to process the resulting data were also meticulously investigated. A polymer electrolyte at lithium natural isotopic abundance (electrolyte A) was used as a reference sample. Thus, matrix effect differences are negligible between samples. [73] To be validated, the developed methodology should lead to an estimation of 92.4% of ^7Li for the reference sample.

A single analysis can provide both isotope intensities thanks to parallel mass detection. However, standard acquisition parameters may lead to saturated signals. The determination of lithium isotopic abundance is thus discussed below (Figure II-6).

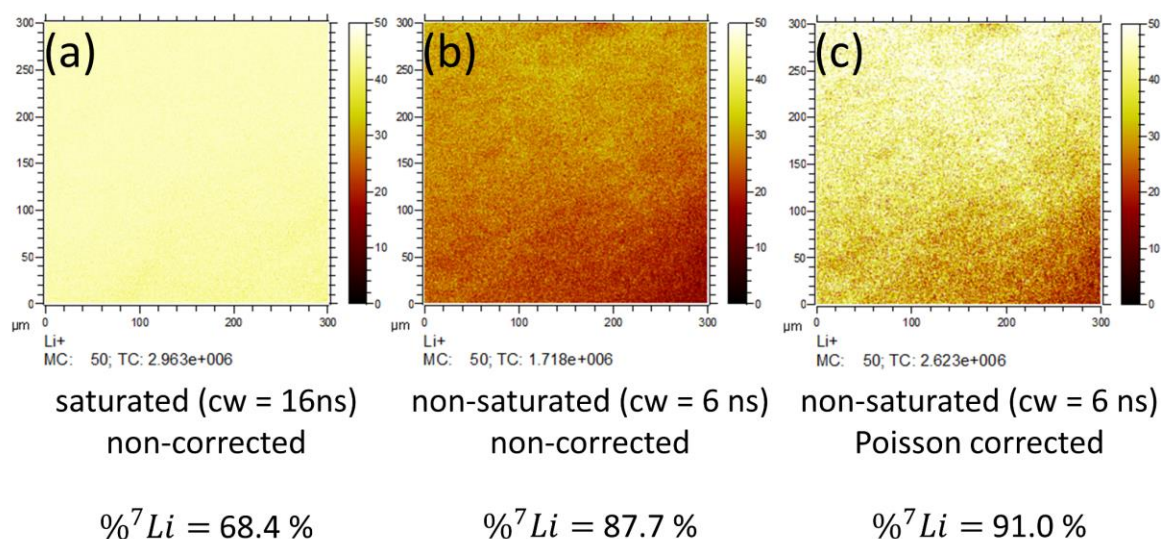


Figure II-6. $^7\text{Li}^+$ ToF-SIMS analyses of a polymer electrolyte at lithium natural isotopic abundance. Chopper width (cw) effect (a \rightarrow b) and Poisson correction effect (b \rightarrow c). $\% ^7\text{Li}$ calculated in the three cases. The selected primary gun was set to Bi^+ 15 keV with a beam current of 1.1 pA (a) or 0.18 pA (b-c).

It is mandatory to obtain non-saturated signals in order to allow further relative quantification. Otherwise, lithium isotopic abundance would be wrongly estimated. On Figure II-6.a, ^7Li abundance in electrolyte A was estimated at 68.4% instead of the expected 92.4% using standard parameters. Inaccurate estimation of $^7\text{Li}^+$ intensity was obviously due to a saturation effect. Electrolyte A contains 1.2 M of lithium corresponding to a concentration of 1.1 M of ^7Li . The saturation effects can be explained by the high ^7Li concentration. Moreover, the positive mode exhibits a strong sensitivity to molecular fragments generated as positive ions such as Li^+ . Switching to negative mode may be a solution to avoid any saturation effect of Li^+ signal as Li^- presents a lower stability. Nevertheless, it might not be efficient to detect $^6\text{Li}^-$ because ^6Li abundance of 7.6% is low. Carrying out experiments in

positive mode is more relevant to detect lithium. Thus, another way to avoid saturation effect had to be prospected.

Although all signal intensities will be decreased, the easiest way to face saturation issues is to simply reduce the current of the Bi⁺ primary ion beam. It can be achieved by shortening its pulse length. Set at 16 ns in standard conditions, the pulse length was empirically decreased down to 6 ns, inducing an ion beam current decay from 1.1 to 0.18 pA. Thus, the sample was less subject to the Bi⁺ ion beam exposition, though the molecular fragments yield was lower. However, the goal was reached because non-saturated signals were obtained. On Figure II-6.b, an estimation of 87.7% of ⁷Li was obtained with non-saturated signals. The value is closer compared to the previous estimation. However, there is still a 4.7% gap with the expected ⁷Li abundance.

After determining the best conditions to perform data acquisition, raw data treatment is also examined. Data processing is investigated on non-saturated signals in the following discussion.

ToF-SIMS detection is based on a “single ion count” mode. [119] It means that only one secondary ion can be detected per microchannel and per shot. Thus, counted ions are underestimated when an excessive number of identical secondary ions are reaching the detector simultaneously. Indeed, microchannels are saturated. Molecular fragments ejected from the surface of the sample are thus miscounted.

A certain amount of time is necessary between each detection event by the same channel. This delay is called the dead time of the detector. [120] It is intrinsic to the equipment. It is set to 15 ns for the TOF-SIMS 5 instrument used in this study. The amount of molecular fragments reaching the detector within the dead time can be estimated by applying a Poisson correction. [119] The number of missed events can then be calculated. Therefore, corresponding intensities can be corrected. The expression of the Poisson corrected intensity, $I_{corrected}$, is given by Equation II-7.

$$I_{corrected} = -N \cdot \ln\left(1 - \frac{I_{measured}}{N}\right) \quad \text{II-7}$$

with $I_{measured}$ the measured intensity by the detector and N the number of shots applied on each pixel.

The linearity response is enhanced at least up to 3.5 $count \cdot shot^{-1}$. [119] The correction is significant only if the primary ion pulse width is lower than dead time. Furthermore, the number of shots per pixel has to be high enough to be relevant for statistical estimation, as it is a method based on statistics. Both conditions were achieved in this work.

The polymer electrolyte at lithium natural isotopic abundance (electrolyte A) was also used to evaluate the effect of the Poisson correction (Figure II-7).

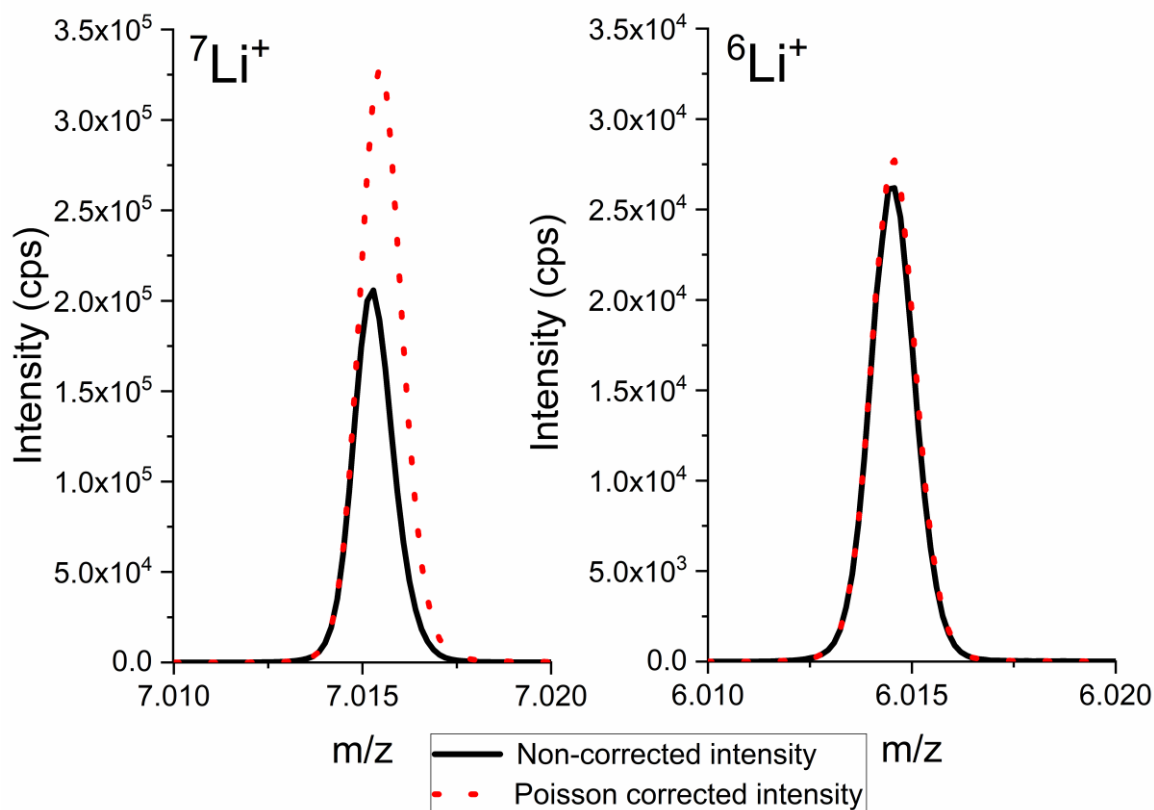


Figure II-7. ${}^7\text{Li}^+$ (left) and ${}^6\text{Li}^+$ (right) ToF-SIMS mass spectra of the polymer electrolyte A at lithium natural isotopic abundance. Comparison between non-corrected intensity (solid black line) with the Poisson corrected intensity (dotted red line). The selected primary gun was Bi^+ at 15 keV with a beam current of 0.18 pA.

On Figure II-7, solid black lines represent the non-corrected intensities. Notice that the scale on the vertical axis is different on both spectra. ${}^7\text{Li}^+$ intensity is higher than 200,000 counts, whereas ${}^6\text{Li}^+$ intensity is almost ten times less. The dotted red lines represent intensities obtained after applying a Poisson correction. The effect of the Poisson correction is noticeable on the ${}^7\text{Li}$ spectrum (Figure II-7). Even without reaching saturation, the number of ${}^7\text{Li}^+$ counts is still very high. As previously explained, applying the dead time correction allows to evaluate the total of undetected events (dotted red line). Therefore, a more accurate estimation of ${}^7\text{Li}$ abundance can be obtained by taking into account the missed ${}^7\text{Li}^+$ molecular fragments. On Figure II-6.c, 91% of ${}^7\text{Li}$ was estimated when applying a Poisson correction to non-saturated signals. The Poisson correction allows an accurate compensation of the ${}^7\text{Li}^+$ molecular fragments not detected by the detector. The electrolyte was at lithium natural isotopic abundance. Thus, the correction has just few impacts on ${}^6\text{Li}^+$ intensity. Indeed, the detector was easily able to count most of the molecular fragments. Only 6% of ${}^6\text{Li}^+$ ions reached the detector within the dead time and were missed, to be compared to the 35% missed ${}^7\text{Li}^+$ ions (Figure II-7).

To investigate the consistency of these ToF-SIMS characterisations, an uncertainty was calculated. A standard deviation of 3.2% on the measured intensities was estimated on reference electrolyte (electrolyte A) on the basis of ten ToF-SIMS analyses. According to

Equation II-8, lithium isotopic abundances are determined by ToF-SIMS with an uncertainty of 1%. This low uncertainty may be also explained by the high sensitivity of the ToF-SIMS technique to lithium detection, which is equal to 0.34 ppm. [58]

Equation II-8 allows to estimate ToF-SIMS uncertainties on the determination of the lithium isotopic abundance. Formula dedicated to errors propagation was used to calculate uncertainties of expected lithium isotopic abundance estimated in the analysed polymer electrolytes. This equation is based on partial derivative of functions. The uncertainty of each variable is considered. Only the first-order Taylor series was taken into account (Equation II-8). [121] [122] The uncertainty expression of f , Δf , is given by

$$\Delta f(u_1, \dots, u_n) = \sqrt{\sum_{i=1}^n \left(\frac{\partial f}{\partial u_i}\right)^2 \cdot |\Delta u_i|^2} \quad \text{II-8}$$

with u_i variables of the function f and Δu_i the uncertainty of u_i .

ToF-SIMS characterisations only affect the extreme surface of the samples. Thus, high-resolution ssNMR can still be performed on the same samples in order to provide global information afterwards. We also focused our interest in improving quantification methodology related to high-resolution ssNMR analyses of ${}^6\text{Li}$ and ${}^7\text{Li}$ nuclei.

2.2. Absolute lithium isotopic abundance determination by high-resolution ssNMR

Contrary to ToF-SIMS analyses, high-resolution ssNMR provides a global analysis of the sample at the atomic scale. Nuclei chemical environment can be determined. For instance, lithium contained in ceramics or in a polymer matrix can be distinguished from the chemical shift of the isotropic peaks. [48] High-resolution ssNMR might allow to determine factors that impact on the ionic conductivity such as lithium diffusion pathways. Lithium behaviour at the interfaces is not clearly understood. [46] Comparing the amount of ${}^6\text{Li}$ and ${}^7\text{Li}$ in a reference sample and in a sample, which has undergone electrochemical stress can provide clues to understand lithium diffusion pathways. [48]

High-resolution ssNMR can be seen as an effective advanced technique to probe the atomic structure of a material. Therefore, it will be used to better understand lithium transport mechanisms at the atomic scale. The ssNMR signal is proportional to the lithium natural isotopic abundance. Thus, ${}^6\text{Li}$ abundance can be estimated. Specific methodologies were developed to accurately determine ${}^6\text{Li}$ abundance. Optimal acquisition settings have to be determined to carry out ${}^7\text{Li}$ and ${}^6\text{Li}$ experiments in quantitative conditions. Then, a proper manner to combine ${}^7\text{Li}$ and ${}^6\text{Li}$ data will be discussed in detail.

High-resolution ssNMR allows quantification of lithium amounts by probing either ${}^6\text{Li}$ or ${}^7\text{Li}$. However, it is not true when working on samples enriched in ${}^6\text{Li}$ with unknown ${}^6\text{Li}$

abundance. Both ${}^6\text{Li}$ and ${}^7\text{Li}$ nuclei have to be probed in such case. This section will explain how to carry out lithium isotopic abundance characterisations, and how to properly combine ${}^6\text{Li}$ and ${}^7\text{Li}$ results.

At first sight, probing ${}^7\text{Li}$ may offer an easier detection thanks to its high abundance of 92.4% compared to ${}^6\text{Li}$. Furthermore, it has a high relative receptivity (0.29 compared to ${}^1\text{H}$). However, ${}^6\text{Li}$ absolute quadrupolar moment ($-0.0808 \times 10^{-30} \text{ m}^2$) is lower in absolute value than ${}^7\text{Li}$ absolute quadrupolar moment ($-4.01 \times 10^{-30} \text{ m}^2$), leading to narrower spectral bands than those obtained for ${}^7\text{Li}$. [123] ${}^6\text{Li}$ high-resolution ssNMR characterisations remain challenging due to ${}^6\text{Li}$ low natural isotopic abundance of 7.6% and long relaxation times compared to ${}^7\text{Li}$.

An NMR spectrometer Brüker Avance NEO 500 MHz was used to perform high-resolution solid-state NMR of ${}^6\text{Li}$ and ${}^7\text{Li}$ at room temperature. An 11.7467 T magnetic field was used to acquire all spectra. This magnetic field is equivalent to a 500.130 MHz magic angle spinning (MAS) NMR frequency for ${}^1\text{H}$. ${}^6\text{Li}$ and ${}^7\text{Li}$ high-resolution ssNMR analyses were carried out to determine lithium isotopic abundance in polymer electrolyte. ${}^6\text{Li}$ and ${}^7\text{Li}$ operating Larmor frequencies are 73.61 and 194.38 MHz, respectively. The calibration of the nuclei chemical shifts was performed by using a lithium phosphate powder (Li_3PO_4) as a reference. Samples were placed in sealed inserts designed to be compatible with 4 mm MAS rotors. Inserts are made of polychlorotrifluoroethylene (CFCl-CF_2)_n, Kel-F). They avoid air contamination during sample transfer from a dry room or from an argon-filled glovebox to the spectrometer. Samples are also protected during the acquisitions. Inserts were introduced into 4 mm MAS rotors made of zirconia (ZrO_2). Notice that using inserts allows to keep clean rotors. The speed of the rotors rotation was set at 10,000 Hz at the magic angle (54.44°). [77] The power was established at 190 W, the receiver gain at 101 and the number of accumulated transients at 64 for both nuclei. 19,230 and 2,890 points were acquired in time domain for ${}^7\text{Li}$ or ${}^6\text{Li}$ free induction decay (FID), respectively. It is due to their spectral width, which corresponds at 192,307 and 28,901 Hz. 32,768 digital points were considered to carry out the Fourier transformation.

Here, ${}^6\text{Li}$ and ${}^7\text{Li}$ quadrupolar behaviour in polymer electrolytes was evaluated by obtaining nutation curves for a 90° pulse. The pulse length needs to be meticulously selected to carry out lithium isotopic abundance characterisations. Indeed, its value impacts the global signal intensity. [78] Probed nuclei have to be excited with a specific pulse length in order to obtain a linear response for each nucleus, whatever their quadrupolar coupling constant. Nutation curves for a 90° were acquired to determine the right pulse length for ${}^6\text{Li}$ (Figure II-8) and ${}^7\text{Li}$ (Figure II-9).

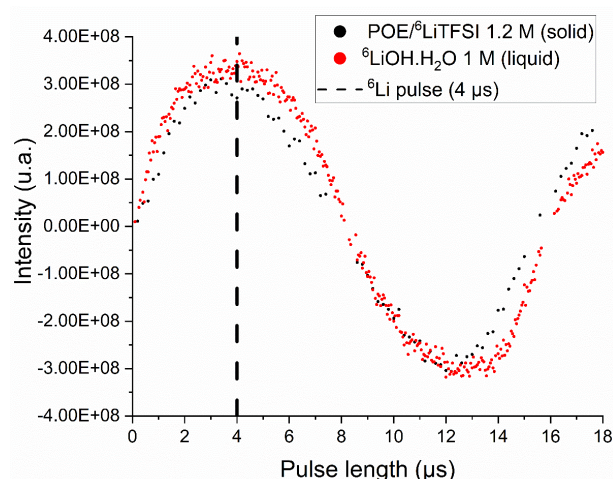


Figure II-8. Nutation curves obtained from the ${}^6\text{Li}$ MAS NMR spectra of a polymer electrolyte (electrolyte D) and ${}^6\text{LiOH}\cdot\text{H}_2\text{O}$ both enriched in ${}^6\text{Li}$. The signal intensity is plotted as a function of pulse length. By comparing both curves, ${}^6\text{Li}$ pulse was set at $4\ \mu\text{s}$, as the maximum signal intensity was reached in these conditions.

On Figure II-8, a $1\ \text{M}$ liquid solution of ${}^6\text{LiOH}$ was used as a reference (dotted red line). The liquid present negligible quadrupolar interactions. It seems to be also the case for the polymer electrolyte enriched at 95.4% in ${}^6\text{Li}$ (electrolyte D). It can be explained by the ${}^6\text{Li}$ nuclear spin of 1, relatively close to $\frac{1}{2}$. Sample enriched in ${}^6\text{Li}$ was used to increase signal/noise ratio. An estimation of the maximum pulse length still providing a linear response was obtained by comparing the nutation curves. It was estimated at $4\ \mu\text{s}$.

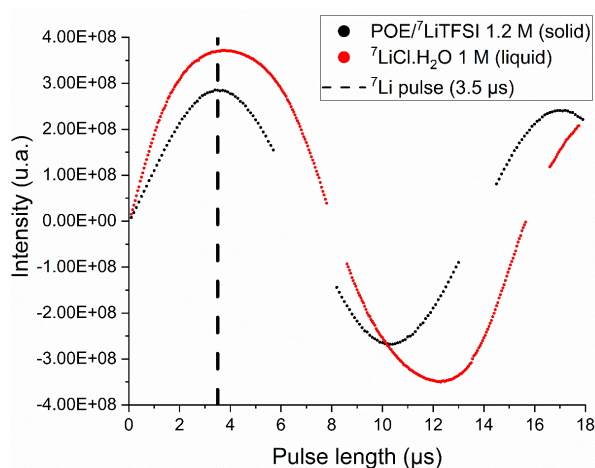


Figure II-9. Nutation curves obtained from the ${}^7\text{Li}$ MAS NMR spectra of an electrolyte at lithium natural isotopic abundance (electrolyte A) and ${}^7\text{LiCl}\cdot\text{H}_2\text{O}$. The signal intensity is plotted as a function of pulse length. By comparing both curves, ${}^7\text{Li}$ pulse was set at $3.5\ \mu\text{s}$, as the maximum signal intensity was reached in both cases, in these conditions.

On Figure II-9, a $1\ \text{M}$ liquid solution of ${}^6\text{LiOH}$ was used as a reference (dotted red line). The liquid present negligible quadrupolar interactions. However, the polymer electrolyte at lithium natural isotopic abundance (electrolyte A) is slightly quadrupolar. It can be explained by the ${}^6\text{Li}$ nuclear spin of $\frac{3}{2}$. The maximum pulse length providing a linear response was estimated at $3.5\ \mu\text{s}$.

To sum up, regarding the nutation curves of ${}^6\text{Li}$ (Figure II-8) and ${}^7\text{Li}$ (Figure II-9) the proper pulse length can be set. The following ${}^6\text{Li}$ and ${}^7\text{Li}$ high-resolution ssNMR analyses will be performed by applying a 90° single-pulse excitation sequence, with a pulse length of either at 4 and $3.5\ \mu\text{s}$, respectively. It is also required to wait a sufficient amount of time called “recycling delay” between each applied pulse in order to let the system recover its whole magnetisation. This recycling delay (D_1) has to be at least higher than $5 \cdot T_1$, with T_1 the spin lattice relaxation time of the probed nucleus. T_1 value variation is related to the material structure of the probed nucleus and to the temperature of the sample during acquisition. [124] An estimation of T_1 has to be achieved for each nucleus. Inversion-recovery sequences allowed estimating the corresponding T_1 . [125] Figure II-10 is an example of the inversion-recovery results, while probing ${}^6\text{Li}$ in a polymer electrolyte.

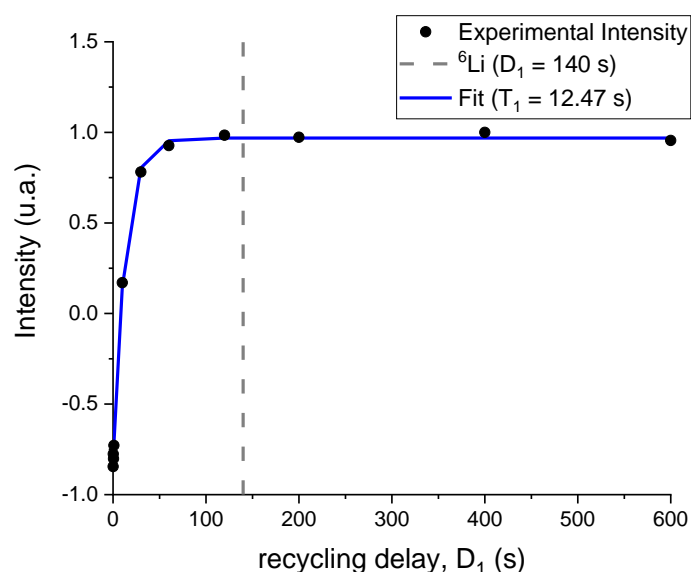


Figure II-10. Example of an inversion-recovery sequence: ${}^6\text{Li}$ ssNMR analyses of PEO/LiTFSI at lithium natural isotopic abundance.

On Figure II-10, several experiments were carried out with a recycling delay (D_1) set at 0.1, 0.3, 0.6, 1, 10, 30, 60, 120, 200, 400 and 600 s. The aim was to determine the minimum D_1 value allowing to work in quantitative conditions. The saturated plateau means that the completely relaxed equilibrium state was reached. Thus, D_1 was set at 140 s to be sure to get all the signal intensity. Using the same procedure, the recycling delay was set to 70 s while probing the ${}^7\text{Li}$ nucleus. A substantial portion of the signal was obtained in a reasonable amount of time.

To conclude, the pulse lengths were set at 4 and $3.5\ \mu\text{s}$ for ${}^6\text{Li}$ and ${}^7\text{Li}$ nuclei, respectively. The responses are linear and the maximum intensity can be recorded in these conditions. To ensure consistent results, it is necessary to set various acquisition parameters identically for each experiment probing both lithium isotopes such as the rotation speed, the excitation pulse and its corresponding recycling delay. Additional settings can be modified, including the number of scans or the receiver gain. However, they have to be used to normalise the resulting signal to combine ${}^6\text{Li}$ and ${}^7\text{Li}$ results.

To determine lithium isotopic abundance of a probed sample, a reference sample with a known lithium isotopic abundance has to be characterised using the same acquisition conditions. The reference sample matrix has to be identical compared with the unknown one, otherwise non-consistent lithium isotopic abundance would be estimated after data processing. To combine ${}^6\text{Li}$ and ${}^7\text{Li}$ spectra, a normalisation factor (S) was calculated from electrolyte A. Indeed, ${}^6\text{Li}$ and ${}^7\text{Li}$ results cannot be directly compared because probe adjustments are carried out to probe each isotope. Tuning and matching were modified due to different ${}^6\text{Li}$ and ${}^7\text{Li}$ Larmor frequencies. S expression is given in the following Equation II-9,

$$S = \frac{I_{ref}({}^7\text{Li})}{I_{ref}({}^6\text{Li})} \cdot \frac{\%{}^6\text{Li}}{\%{}^7\text{Li}} \quad \text{II-9}$$

with $I_{ref}({}^k\text{Li})$ the ${}^k\text{Li}$ absolute integral of electrolyte A used as a reference sample, and $\%{}^k\text{Li}$ the expected abundance in ${}^k\text{Li}$, with $k = 6$ or 7 . The integrals have to be normalised by the number of scans and/or by the receiver gain if these acquisition parameters are modified between ${}^6\text{Li}$ and ${}^7\text{Li}$ experiments. It is not necessary to normalise $I({}^k\text{Li})$ by the lithium mass as the same sample is probed in both analyses. Based on Equation II-9, S was estimated at 15 by characterising electrolyte A. The expression of ${}^7\text{Li}$ abundance, $\%{}^7\text{Li}$, is provided by the following Equation II-10,

$$\%{}^7\text{Li} = \frac{100}{1 + S \cdot \frac{I_{sample}({}^6\text{Li})}{I_{sample}({}^7\text{Li})}} \quad \text{II-10}$$

with $I_{sample}({}^k\text{Li})$ the normalised ${}^k\text{Li}$ absolute integral of the probed sample, with $k = 6$ or 7 . Equation II-10 was obtained through the resolution of the two-equation system II-11 and II-12,

$$\frac{\%{}^6\text{Li}}{\%{}^7\text{Li}} = S \cdot \frac{I_{sample}({}^6\text{Li})}{I_{sample}({}^7\text{Li})} \quad \text{II-11}$$

$$\%{}^7\text{Li} + \%{}^6\text{Li} = 100\% \quad \text{II-12}$$

Details on how to obtain integral values are mentioned in this paragraph. Data treatment such as phasing and automatic baseline correction was done with the software TopSpin 3.6.2[®] provided by Brüker. Notice that an exponential line broadening factor of 20 Hz was also applied on raw data. ${}^6\text{Li}$ and ${}^7\text{Li}$ absolute integrals of high-resolution ssNMR spectra (I) were obtained by integrating spectra on 10 ppm and on 300 ppm centered on the origin (0 ppm), respectively. Integration must take into account spinning sidebands to obtain consistent results. Thus, the integrated window is broader on ${}^7\text{Li}$ spectra compared to the ${}^6\text{Li}$ ones. The software developed by Massiot *et al.* named Dmfit[®] was used to extract data and

plot spectra. [126] Spectrum deconvolution can be achieved when several contributions overlap. It will be the case for sample containing a lithium salt and a lithiated ceramic.

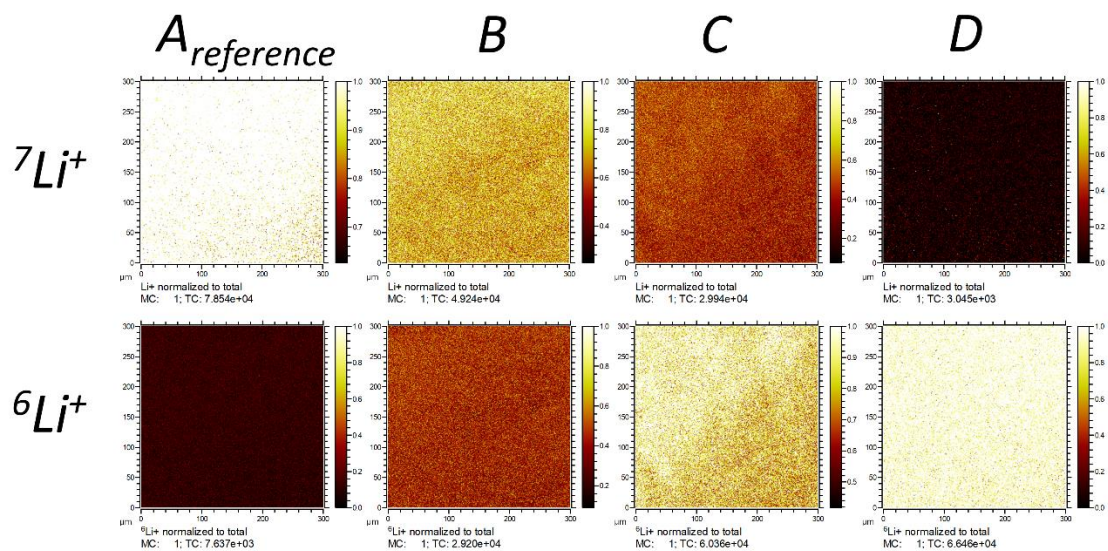
Three analyses of a polymer electrolyte at lithium natural isotopic abundance were performed by ssNMR to estimate a standard deviation. Uncertainties were determined by considering a 0.5% standard deviation on the absolute integral intensity values. Therefore, lithium isotopic abundance can be determined by high-resolution ssNMR with a maximum uncertainty of 2% (Equation II-8).

The ToF-SIMS and high-resolution ssNMR methodologies are applied on polymer electrolytes presented in section 1.1 to be validated and optimised.

II.3. Determination of lithium isotopic abundance with the developed methodologies

3.1. Polymer electrolytes characterised by ToF-SIMS

As said before, ToF-SIMS is a powerful technique allowing the discrimination of lithium isotopes. The methodology described in section 2.2.a is applied to characterise four polymer electrolytes presented in Table II-1. The obtained ToF-SIMS images are presented on Figure II-11.



<i>Expected</i>	<i>92.4 % ${}^7\text{Li}$</i>	<i>66.1 % ${}^7\text{Li}$</i>	<i>33.6 % ${}^7\text{Li}$</i>	<i>4.6 % ${}^7\text{Li}$</i>
<i>Li abundances</i>	<i>7.6 % ${}^6\text{Li}$</i>	<i>33.9 % ${}^6\text{Li}$</i>	<i>66.4 % ${}^6\text{Li}$</i>	<i>95.4 % ${}^6\text{Li}$</i>

Figure II-11. Four polymer electrolytes (A, B, C, and D) with various ${}^6\text{Li}$ abundances were analysed by ToF-SIMS. Their expected lithium isotopic abundances are mentioned. Normalised ${}^7\text{Li}^+$ and ${}^6\text{Li}^+$ intensities by the total ion counts can be compared. The selected primary gun was Bi^+ 15 keV with a current of 0.18 pA.

The total intensity was checked to be sure that signals were homogeneous on the selected area. A Poisson correction was applied to non-saturated signals. Intensities were normalised by the total intensity for an easier visual comparison. The evolution trend of ${}^7\text{Li}^+$ and ${}^6\text{Li}^+$ intensities was coherent with the expected ratio. Lithium isotopic abundance was estimated from ToF-SIMS images over their processing improvements (Figure II-11).

While modifying the way to process raw data, evolution of polymer electrolyte ${}^7\text{Li}$ abundances estimated by ToF-SIMS was investigated (Figure II-12).

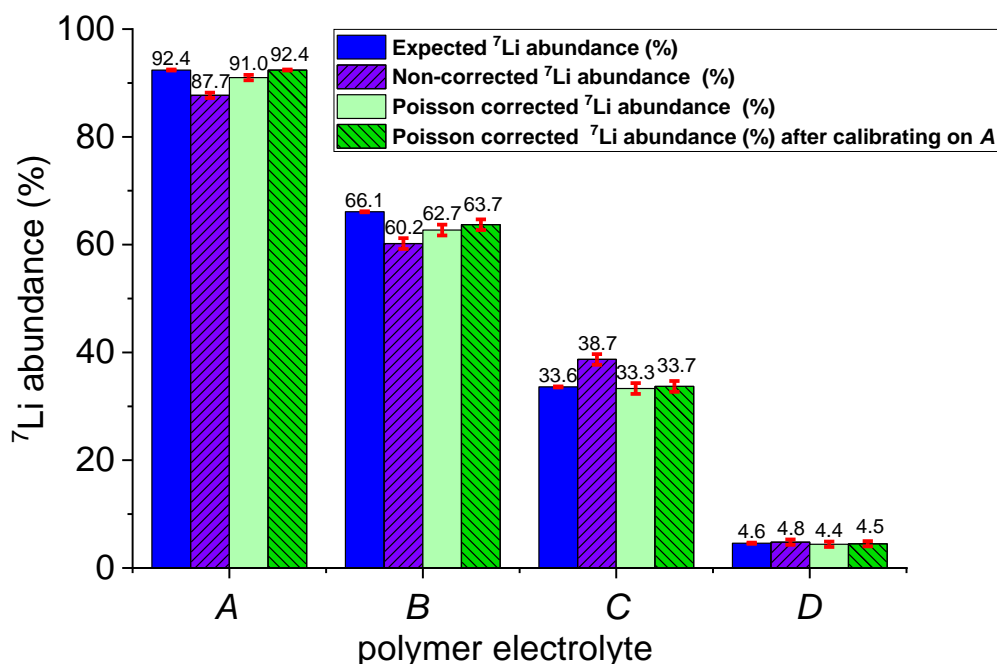


Figure II-12. Comparison of expected ${}^7\text{Li}$ abundances (blue bars) for electrolytes A, B, C and D described in Table II-1, with the ones determined by ToF-SIMS: lithium isotopic abundances obtained from raw data (purple bars); effect of the Poisson correction (light-green bars); and effect of the deviation correction (green bars).

On Figure II-12, the quantification of lithium isotopic abundances of three processing steps are presented for each polymer electrolyte. They were calculated using Equation II-5 and Equation II-6. Only ${}^7\text{Li}$ abundance is presented on Figure II-12 as ${}^6\text{Li}$ and ${}^7\text{Li}$ abundances are obviously dependant one with each other. The expected ${}^7\text{Li}$ abundances estimated by weighing the lithium salts correspond to the blue bars (Table II-1). Raw data of electrolytes A, B and C processed without applying any correction led to far ${}^7\text{Li}$ abundances compared to the expected ones (hatched purple bars on Figure II-12). Processing data by applying a Poisson correction allowed to obtain more consistent ${}^7\text{Li}$ abundances. They are presented by light-green bars. For electrolyte A, 91.0% of ${}^7\text{Li}$ was estimated instead of the 87.7% of ${}^7\text{Li}$ without using a Poisson correction. Similarly, for electrolytes B and C, corrected data with a Poisson correction led to an estimation of 62.7% instead of 60.2%, and to 33.3% instead of 38.7% of ${}^7\text{Li}$, respectively. Therefore, it is essential to apply the Poisson correction to more accurately estimate lithium isotopic abundances from ToF-SIMS analyses. [119] Finally, the estimated ${}^7\text{Li}$ abundances were adjusted by assuming that electrolyte A is at lithium natural

isotopic abundance. The hatched green bars represent the calibration effect. The final ${}^7\text{Li}$ abundance estimations of electrolytes *B* and *C* are 63.7 and 33.7%, respectively.

Electrolyte *D* was prepared with pure ${}^6\text{LiTFSI}$. It contains only 4.6% of ${}^7\text{Li}$. The advantage is that no saturation effect should occur with such low amount of ${}^7\text{Li}$. Furthermore, high sensitivity of ToF-SIMS technique (*ppm*) allows its detection. [72] Without applying any correction, the ${}^7\text{Li}$ abundance is slightly overestimated at 4.8%. On the contrary, a Poisson correction leads to a slight underestimation of ${}^7\text{Li}$ abundance at 4.4%. Notice that the Poisson correction has a lower impact of the estimated ${}^7\text{Li}$ abundance in electrolyte *D* compared with the other electrolytes because the detector was able to count most of the ${}^7\text{Li}^+$ ejected molecular fragments. Finally, the ${}^7\text{Li}$ abundance slightly increases to 4.5% by using electrolyte *A* as a reference sample.

To conclude, ToF-SIMS characterisations led to accurate lithium isotopic abundance estimations. It was achieved by using the correct acquisition conditions allowing to avoid any saturation effect, and by correcting molecular fragments intensities by using a Poisson correction. The appropriate acquisition parameters and data processing are crucial to precisely estimate lithium isotopic abundance in a polymer electrolyte.

3.2. Polymer electrolytes characterised by high-resolution ssNMR

High-resolution ssNMR characterisations were performed on the same four polymer electrolytes characterised by ToF-SIMS. ${}^6\text{Li}$ (left) and ${}^7\text{Li}$ (right) were probed (Figure II-13) to estimate lithium isotopic abundances with the help of the previously determined normalisation factor (Equation 7).

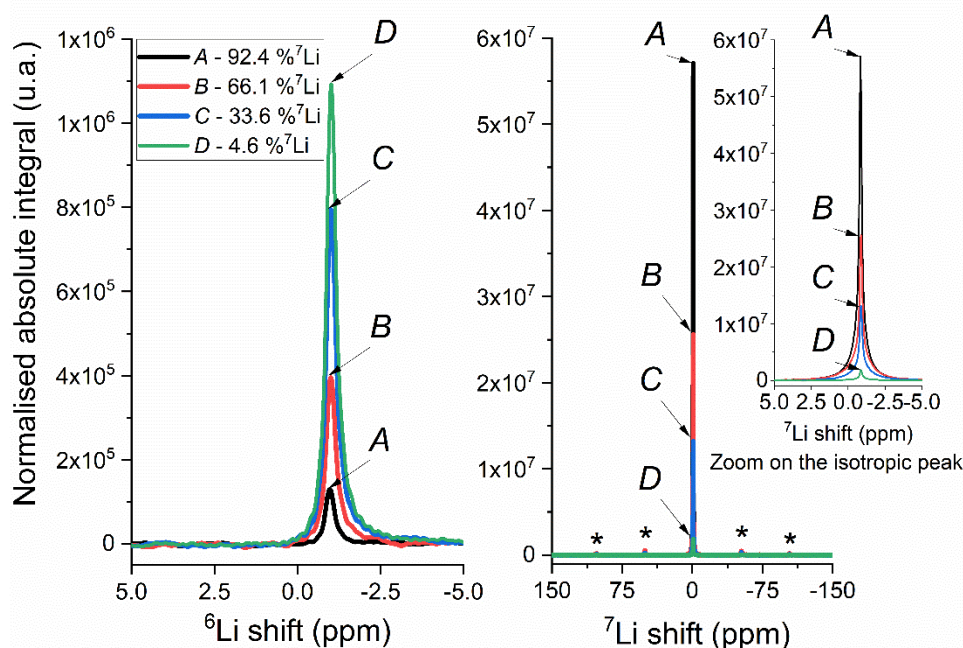


Figure II-13. ${}^6\text{Li}$ (left) and ${}^7\text{Li}$ (right) high-resolution ssNMR spectra of four polymer electrolytes with various ${}^6\text{Li}$ abundances. Spinning sidebands are indicated by asterisks.

On Figure II-13, the overlapping of the four high-resolution ssNMR spectra points out that polymer electrolytes contain different ${}^6\text{Li}$ abundances. The integrals of ${}^6\text{Li}$ and ${}^7\text{Li}$ high-resolution ssNMR spectra presented on Figure II-13 were obtained with the TopSpin 3.6.2[®] software. On ${}^7\text{Li}$ spectra, spinning sidebands intensities present a relatively low intensity compared with the isotropic peak. However, they have to be considered, while measuring the absolute integrals. Anisotropic quadrupolar interactions induce spinning sidebands on ${}^7\text{Li}$ spectra. The magic angle spinning averages most of them. The rotation speed may be increased to better average quadrupolar interactions. On ${}^6\text{Li}$ spectra, no spinning sideband is observed (Figure II-13). ${}^6\text{Li}$ has a lower absolute quadrupolar moment ($-0.0808 \times 10^{-30} \text{ m}^2$) than ${}^7\text{Li}$ ($-4.01 \times 10^{-30} \text{ m}^2$), which can explain the absence of spinning sideband on ${}^6\text{Li}$ spectra. Furthermore, the spectral resolution on ${}^6\text{Li}$ spectra is improved, though the relative receptivity compared to ${}^1\text{H}$ is lower in ${}^6\text{Li}$ than in ${}^7\text{Li}$ (8.50×10^{-3} vs. 0.29).

Determination of ${}^7\text{Li}$ abundances in polymer electrolytes B, C, and D were achieved by using electrolyte A as a reference sample at lithium natural isotopic abundance (Figure II-14).

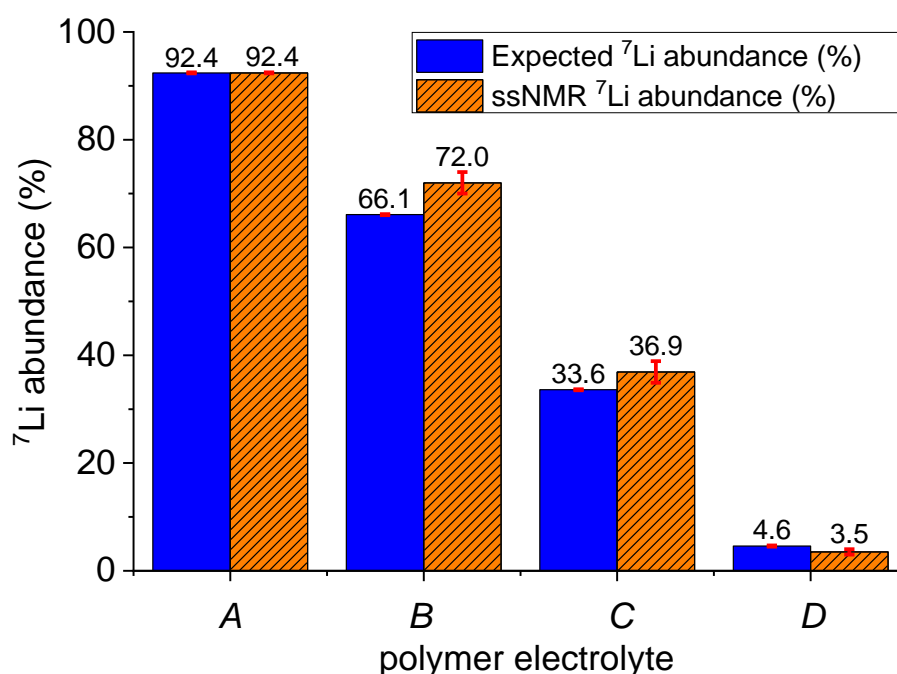


Figure II-14. Comparison of expected ${}^7\text{Li}$ abundances (blue bar) with the ones estimated by high-resolution ssNMR (hatched orange bar). Uncertainties are represented by red bars.

According to the developed methodology, ${}^7\text{Li}$ abundance in polymer electrolytes B, C and D are estimated at 72.0, 36.9 and 3.5%, respectively. Data are reported on Figure II-14 (hatched orange bars). ${}^7\text{Li}$ abundances determined by ssNMR have the same order of magnitude compared with the expected ${}^7\text{Li}$ abundances by weighing (blue bar). High-resolution ssNMR characterisations seem to overestimate ${}^7\text{Li}$ abundances.

Moreover, one of the strengths of high-resolution ssNMR experiments lies in lithium amount quantification on the basis of the absolute integral values. Indeed, this is made possible because such integrals are proportional to the probed atom concentration. [127] Table II-2 sums up ${}^7\text{Li}$ amount in each electrolyte.

Table II-2. Comparison of the ${}^7\text{Li}$ amounts calculated by weighting the electrolytes with the ones estimated by high-resolution ssNMR.

Polymer electrolyte	Amount of ${}^7\text{Li}$ calculated ($n_{{}^7\text{Li}}$)	
	by weight (mol)	by high-resolution ssNMR (mol)
A (reference sample)	1.4×10^{-5}	/
B	6.2×10^{-6}	5.9×10^{-6}
C	3.8×10^{-6}	3.4×10^{-6}
D	5.5×10^{-7}	3.1×10^{-7}

To carry out lithium quantification and thus to estimate the ${}^7\text{Li}$ amount within samples, the polymer electrolyte A was used as reference. Its insert contains 14.79 mg of polymer electrolyte. Regarding the polymer electrolyte preparation and the fact that this reference sample is at lithium natural isotopic abundance, $1.4 \times 10^{-5} \text{ mol}$ of ${}^7\text{Li}$ were probed. Other samples were characterised within the exactly same acquisition conditions. According to Table II-2, the ${}^7\text{Li}$ amounts estimated by high-resolution ssNMR are consistent with the amounts calculated by weighing the polymer electrolytes. Coherence of both ${}^7\text{Li}$ amounts validates that high-resolution ssNMR experiments were performed in quantitative conditions.

3.3. Comparison of the results

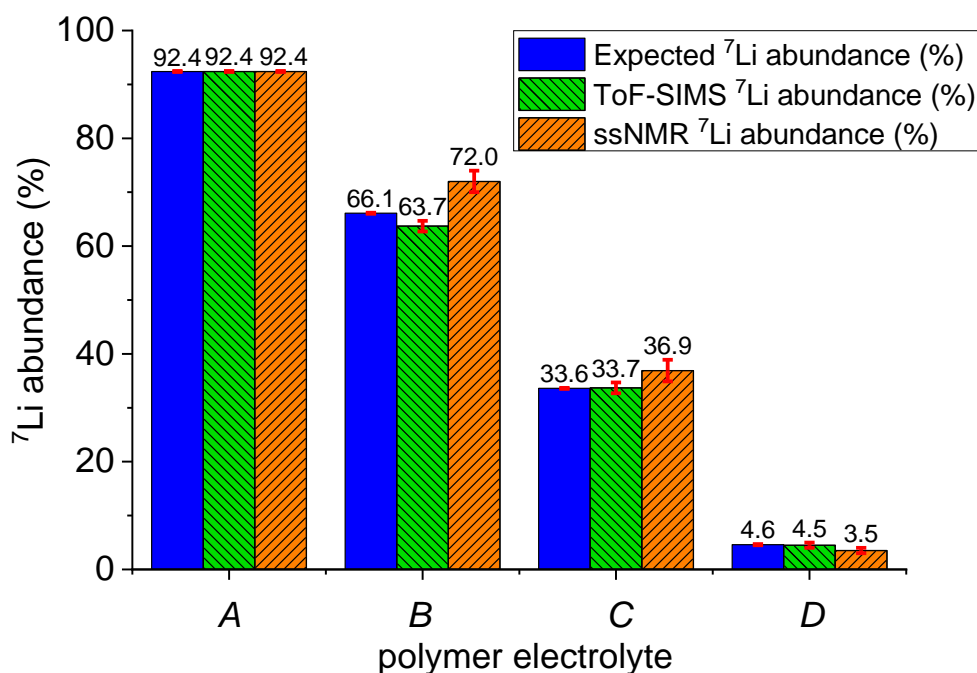


Figure II-15. Comparison of expected ${}^7\text{Li}$ abundances (blue bar) with the ones estimated by ToF-SIMS (green bar) or by high-resolution ssNMR (orange bar). Uncertainties are represented by red bars.

The specific methodologies developed in chapter II allow precise determination of lithium isotopic abundance in polymer electrolytes by using ToF-SIMS (green bars) as well as high-resolution ssNMR (orange bars). The estimation of ^7Li abundance by both techniques can easily be compared on Figure II-15. ToF-SIMS estimations seem closer to the expected ^7Li abundance compared with high-resolution ssNMR ones. The accuracy of ToF-SIMS results may be explained by the parallel mass detection of both lithium isotopes. Thus, ToF-SIMS data processing is relatively simple compared with the ssNMR one. Nevertheless, whatever the characterisation technique, results are close to the expected ones. The same trend can be observed between the four samples. Furthermore, complementary information can be deduced from both techniques. ToF-SIMS analyses offer local chemical information of the surface, while high-resolution ssNMR analyses offer global information on lithium chemical environment within the electrolytes. One of the biggest strengths of ToF-SIMS technique is that all molecular fragments can be detected at the same time thanks to parallel mass detection of a full mass range, whereas additional ssNMR experiments would be required to probe other nuclei, such as carbon from the polymer membrane or fluor from the lithium salt.

One characterisation technique may be more relevant than the other, based on the required information. They have their own advantages and limitations. ToF-SIMS experiments lead to fast surface characterisations, allowing simultaneous detection of lithium isotopes. Therefore, lithium isotopic abundance can be determined straight away after a quick acquisition contrary to high-resolution ssNMR experiments. However, no absolute lithium quantification is possible by ToF-SIMS. On the other hand, non-simultaneous ^6Li and ^7Li high-resolution ssNMR characterisations can last a minimum of 2 h 30 and 1 h 30, respectively. Nevertheless, one of the main advantages of high-resolution ssNMR is to carry out lithium isotopic abundance characterisations into the bulk of the material. Additionally, this technique can distinguish lithium which is contained in the polymer electrolyte from the one contained into the ceramic. Indeed, the chemical environment of the probed nucleus is determined.

Conclusion

PEO containing LiTFSI has already been widely studied as solid-state electrolyte. Here, precise ToF-SIMS and high-resolution ssNMR methodologies were developed on polymer electrolytes with various ${}^6\text{Li}$ abundances to be validated and to be optimised. It was demonstrated that ToF-SIMS and high-resolution ssNMR characterisations can offer accurate estimations of lithium isotopic abundance with an uncertainty of 1% and 2%, respectively. To achieve this high precision, methodologies are considering acquisition conditions as well as data processing steps. Both advanced techniques are complementary. On one hand, ToF-SIMS provides a local characterisation of the surface offering chemical information. Molecular fragments are detected at a micrometric scale. The estimation of lithium isotopic abundance is based on the measured ${}^6\text{Li}^+$ and ${}^7\text{Li}^+$ molecular fragments intensities. On the other hand, ${}^6\text{Li}$ and ${}^7\text{Li}$ high-resolution ssNMR characterisations provide global information on lithium chemical environments. Furthermore, lithium isotopic abundance can also be estimated by probing ${}^6\text{Li}$ and ${}^7\text{Li}$ high-resolution ssNMR spectra. Additionally, lithium isotopes quantification is possible, whereas it was not the case with ToF-SIMS characterisations. Notice that these methodologies can be applied on other lithiated materials.

The developed methodologies will be useful to precisely characterise lithium self-diffusion in chapter III and lithium diffusion phenomenon under an electrical stress in chapters IV and V.

Chapter III. Lithium dynamics investigated in a polymer electrolyte by advanced characterisation techniques based on the lithium isotopic labelling

This chapter aims at investigating lithium dynamics in a polymer electrolyte, which could be implemented in solid-state batteries. First experiments involving lithium isotopic labelling are set up. Methodologies developed in chapter II are used to describe lithium exchanges between a lithium foil enriched at 95.4% in ${}^6\text{Li}$ (${}^6\text{Li}$ -foil), and a polymer membrane containing a lithium salt at lithium natural isotopic abundance. The use of a ${}^6\text{Li}$ -foil allows to track lithium in a material already containing lithium at natural abundance. ToF-SIMS and high-resolution ssNMR correlative lithium isotopic characterisations will provide complementary information on lithium exchange dynamics in an *in-plane* device. Furthermore, a modelling approach also based on lithium isotopic labelling will offer a deeper understanding of lithium behaviour in each material and at their interface by providing exchange dynamics at the interface and lithium self-diffusion into both materials.

This chapter is heavily inspired from our publication: “Lithium Self-Diffusion in a Polymer Electrolyte for Solid-State Batteries: ToF-SIMS/ssNMR Correlative Characterization and Modeling Based on Lithium Isotopic Labeling” published in ACS Applied Material & Interfaces in 2023. [104]

III.1. Description of the experimental setup to study lithium dynamics

1.1. *In-plane* configuration

The geometry of the *in-plane* device is presented on Figure III-1. It is composed of a lithium foil and a polymer electrolyte. Such configuration is used to characterise lithium self-diffusion at 60°C in each material and lithium exchanges at the interface between both materials.

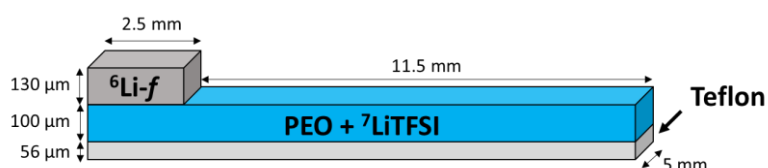


Figure III-1. Schematic of the *in-plane* configuration composed of polymer membrane (PEO) containing a lithium salt (LiTFSI) at lithium natural isotopic abundance with a lithium foil enriched in ${}^6\text{Li}$ (${}^6\text{Li}$ -foil) stuck on one extremity. Dimensions of the device lying on a Teflon sheet are indicated.

The polymer electrolyte is made of PEO containing 1.2 M of LiTFSI. Rectangles of $14 \times 5 \text{ mm}^2$ were cut in a casted polymer electrolyte film. They were deposited on a thin Teflon sheet (Figure III-1). A lithium foil enriched at 95.4% in ${}^6\text{Li}$ was stuck on one extremity of a polymer membrane containing LiTFSI at lithium natural isotopic abundance (7.6% in ${}^6\text{Li}$). Thus, there was a lithium isotopic concentration difference between both materials. It induces spontaneous ${}^6\text{Li}^+$ ions diffusion from the ${}^6\text{Li}$ -foil into the polymer electrolyte. This exchange process can be tracked thanks to lithium isotopic abundance variations. Otherwise, it could not be possible. It occurs without external driving force in order to reach thermodynamic equilibrium. More specifically, no electrochemical force is applied. Thus, lithium self-diffusion was induced only beneath the influence of Brownian motion at a specific temperature. [128]

1.2. Experimental protocols and sample preparation

A device was assembled in an *in-plane* configuration (Figure III-1). Even if experiments were carried out in a dry room, precautions were taken because PEO and LiTFSI are highly hydroscopic. The device was sealed under vacuum at 100 mbar into an air-tight pouch to limit the water intake of the membrane. Then, the assembly was left in an oven at 60 °C during several contact times. The use of the expression “contact time” will always implies a “contact time between a ${}^6\text{Li}$ -foil and a polymer electrolyte” in this manuscript. Furthermore, when it is mentioned that the polymer electrolyte is at lithium natural isotopic abundance, it is a language shortcut meaning that the lithium salt used to make the polymer electrolyte is at lithium natural isotopic abundance. Lithium exchanges will be estimated over time. Characterisations were performed after 24 h, 72 h and 255 h of contact time at 60°C. Sample

preparation is necessary before ToF-SIMS analyses. It was performed at room temperature to prevent as much as possible evolution of lithium relative abundance in polymer electrolyte. The preparation steps are described on Figure III-2.

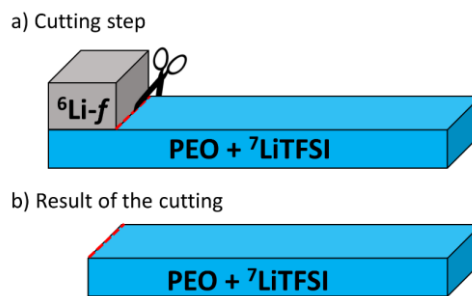


Figure III-2. Description of sample preparation at room temperature. a) The ${}^6\text{Li}$ -foil is removed by cutting prior to ToF-SIMS analyses. b) Obtained sample after the cutting step.

First trials were performed at room temperature. (Appendix A-III-1. *Lithium self-diffusion at room temperature (25° C)*). The conclusion is that no lithium exchange occurs at room temperature. Thus, considered contact times correspond only to the duration during which the device stays in the oven at 60° C. Times just after assembly and before disassembling have not to be taken into account. Furthermore, the ${}^6\text{Li}$ -foil was not removed. Its lithium isotopic abundance could be determined. However, the 130 μm thick ${}^6\text{Li}$ -foil presence creates a hidden area due to shading effects. To facilitate the accessibility of the edge of the polymer electrolyte on the side of the ${}^6\text{Li}$ -foil, the electrolytes were cut to take out the ${}^6\text{Li}$ -foil (Figure III-2). On the same time, the polymer electrolyte under the ${}^6\text{Li}$ -foil was also removed.

A device in the *in-plane* configuration was set up and kept at 60° C during 120 *h*. Then, combined ToF-SIMS and high-resolution ssNMR were performed to confirm the relevance of the developed methodologies. ToF-SIMS analyses were carried out first. Indeed, even if high-resolution ssNMR is a non-destructive technique, the sample preparation requires to dismantle the electrolyte to introduce it into an insert for acquisition. The polymer electrolyte could not be used for further characterisation after high-resolution ssNMR analyses. A three-dimensional schematic of the device emphasises that ToF-SIMS analyses lead to extreme surface characterisation, less than 1 *nm*, whereas high-resolution ssNMR technique provides bulk analyses (Figure III-3).

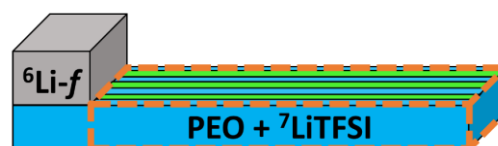


Figure III-3. Description of the polymer electrolyte domains analysed by ToF-SIMS (green surfaces) and by high-resolution ssNMR (volume contained in the orange dotted box).

Only the green surfaces on top of the polymer electrolyte were analysed by ToF-SIMS (Figure III-3). Then, the polymer electrolyte volume contained in the orange dotted box was introduced into an insert and probed by high-resolution ssNMR (Figure III-3). Finally, the ToF-SIMS and high-resolution ssNMR experimental data were compared with numerical simulations results.

III.2. Determination of lithium dynamics through *in-plane* devices

2.1. Characterisation of lithium dynamics in *in-plane* devices by ToF-SIMS

ToF-SIMS characterisations were performed on the device described on Figure III-4. The same acquisition parameters mentioned in chapter II were used: an analysed Bi^+ beam at 15 keV with a chopper width of 6 ns. Therefore, lithium isotopic abundance can be accurately estimated.

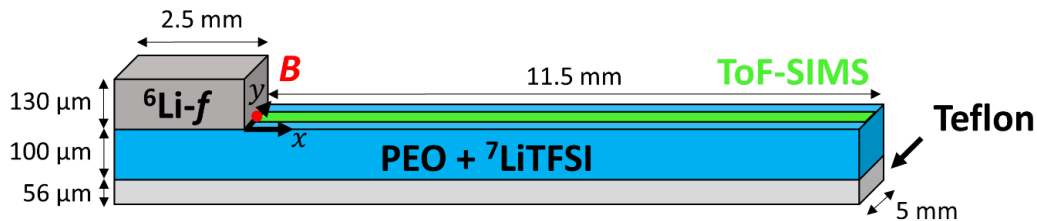


Figure III-4. ToF-SIMS characterisation of the accessible polymer electrolyte surface (green area) contained in the (xy) plan. The red point B corresponds to the edge of the polymer electrolyte on the side of the ^6Li -foil. Dimensions of the device lying on a Teflon sheet are indicated.

The green surface of the polymer electrolyte on plane (xy) was characterised by ToF-SIMS. (Figure III-4). A surface of $0.4 \times 11.4 \text{ mm}^2$ was scanned from the red point B to the edge of the polymer electrolyte on the side of the ^6Li -foil. The scan direction is along the x -axis. The dimensions are configured by making use of a “Two-Dimensional Large Area” (2DLA) scan mode on the ION-TOF ToF-SIMS 5. The 2DLA mode performs an automatic mapping of 114 analyses of $0.2 \times 0.2 \text{ mm}^2$. Edge effects can be avoided while scanning surfaces smaller than 0.4 mm^2 . To improve the signal-to-noise ratio, each image results from a superimposition of 10 scans acquired with $1 \text{ shot} \cdot \text{pixel}^{-1}$. Images are divided into 14,400 pixels ($120 \times 120 \text{ pixels}^2$), and obtained with a “random acquisition” mode. This specific random mode consists of analysing pixels in disorder to avoid any charging effect around the analysed surface. Chemical molecular fragments were mapped after 24 h of contact time at 60° C (Figure III-5). In this chapter, the Poisson correction was applied on all the presented ToF-SIMS results.

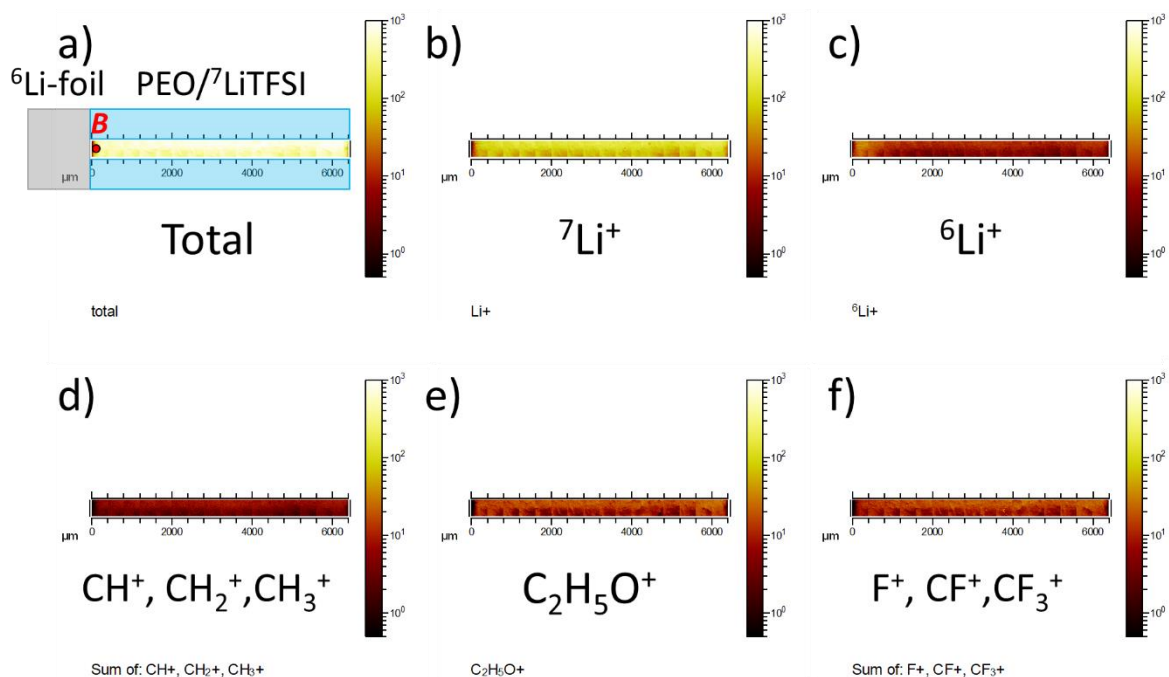


Figure III-5. ToF-SIMS 2DLA scan on the surface of a polymer electrolyte from B ($x_B = 0 \mu\text{m}$), after 24 h of contact time at 60°C : a) Intensity of all detected molecular fragments, b) Intensity of $^7\text{Li}^+$, and c) Intensity of $^6\text{Li}^+$ d) Sum of the CH^+ , CH_2^+ and CH_3^+ intensities e) Intensity of $\text{C}_2\text{H}_5\text{O}^+$, and f) Sum of the F^+ , CF^+ and CF_3^+ intensities.

Figure III-5 presents the obtained images with the 2DLA scan mode of a polymer electrolyte from B ($x_B = 0 \mu\text{m}$) after 24 h at 60°C . The automatic 2DLA mapping enhances the continuity between each analysed area. Indeed, manual movement led to discontinuities between analysed areas and made difficult data treatment. However, the z-alignment procedure (consisting in optimising the distance between the sample and the analyser lens to get the maximum intensity) must be applied before the global acquisition: it cannot be modified afterwards between each mapping. Thus, the roughness of the polymer electrolyte can affect the obtained results. Peak splitting can be observed on the mass spectrum, and it is mandatory to take it into account.

On Figure III-5.c, a higher $^6\text{Li}^+$ enrichment of the polymer electrolyte close to the edge of the ^6Li -foil can be observed on the first $800 \mu\text{m}$, compared to the rest of the polymer electrolyte. However, ToF-SIMS characterisations are not quantitative. Thus, lithium isotopic abundances have to be calculated from both $^7\text{Li}^+$ and $^6\text{Li}^+$ measured intensities (Figure III-5.b and Figure III-5.c). Molecular fragments characteristic from the polymer electrolyte, such as CH^+ , CH_2^+ , CH_3^+ (Figure III-5.d) and $\text{C}_2\text{H}_5\text{O}^+$ (Figure III-5.e) or characteristic from the lithium salt, such as F^+ , CF^+ and CF_3^+ (Figure III-5.f) were detected. It confirms that the detected lithium comes from the polymer electrolyte. Parallel mass detection is a strong asset of this characterisation technique.

ToF-SIMS 2DLA analyses on the surface of a polymer electrolyte from B, after 24, 72 and 255 h of contact time at 60°C are presented on Figure III-6.

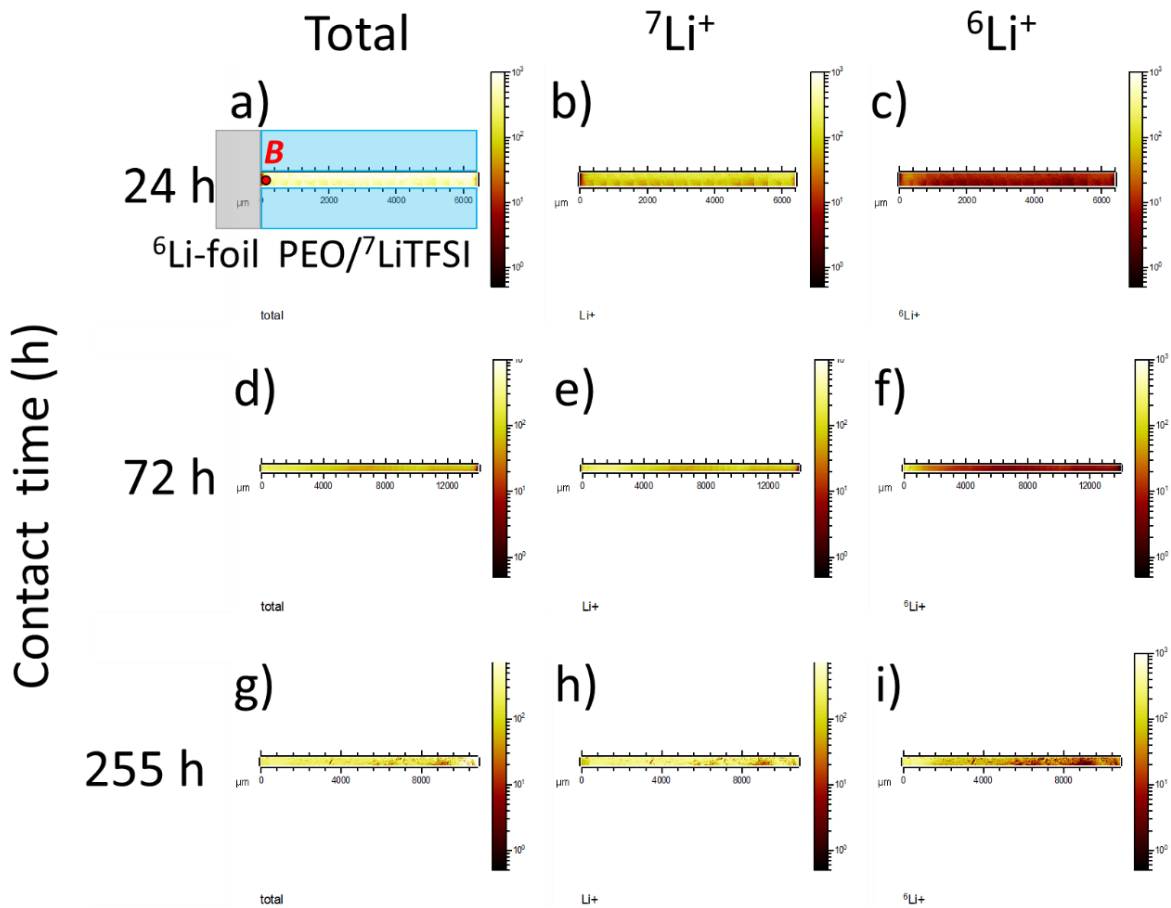


Figure III-6. ToF-SIMS 2DLA scan on the surface of three polymer electrolytes from B ($x_B = 0 \mu\text{m}$), after 24, 72 and 255 h of contact time at 60°C , respectively: a, d and g) Intensity of all the detected molecular fragments, b, e and h) Intensity of ${}^7\text{Li}^+$, and c, f and i) Intensity of ${}^6\text{Li}^+$.

A logarithmic scale is used to facilitate images comparison obtained by ToF-SIMS after 24, 72 and 255 h of contact time (Figure III-6). A different device was needed for each studied contact time because lithium diffusion was almost stopped by cooling the sample. On Figure III-6.a, Figure III-6.d and Figure III-6.g intensities are homogeneous. The ${}^7\text{Li}^+$ molecular fragments were detected all along the polymer electrolyte in each case (Figure III-6.b, Figure III-6.e and Figure III-6.h). On Figure III-6.c, a low ${}^6\text{Li}^+$ enrichment can be observed close to the edge of the ${}^6\text{Li}$ -foil (B) after 24 h of contact time. An enrichment in ${}^6\text{Li}$ is more visible on Figure III-6.f. The first 1,200 μm from B seem enriched in ${}^6\text{Li}$ after 72 h of contact time. On Figure III-6.i, a high ${}^6\text{Li}^+$ enrichment can be clearly observed on the first 1,600 μm from B , after 255 h of contact time. Furthermore, ${}^6\text{Li}^+$ ions still diffuse beyond 4,800 μm .

It is mandatory to compare ${}^7\text{Li}^+$ and ${}^6\text{Li}^+$ intensities to get an accurate estimation of lithium isotopic abundances. The equations mentioned in chapter II were used to calculate ${}^6\text{Li}$ and ${}^7\text{Li}$ abundances from B to the end of the polymer electrolyte, or at least until reaching the lithium natural isotopic plateaux. The following curves presented on Figure III-7 could be obtained by averaging the 240 *pixels* sharing the same x -coordinate.

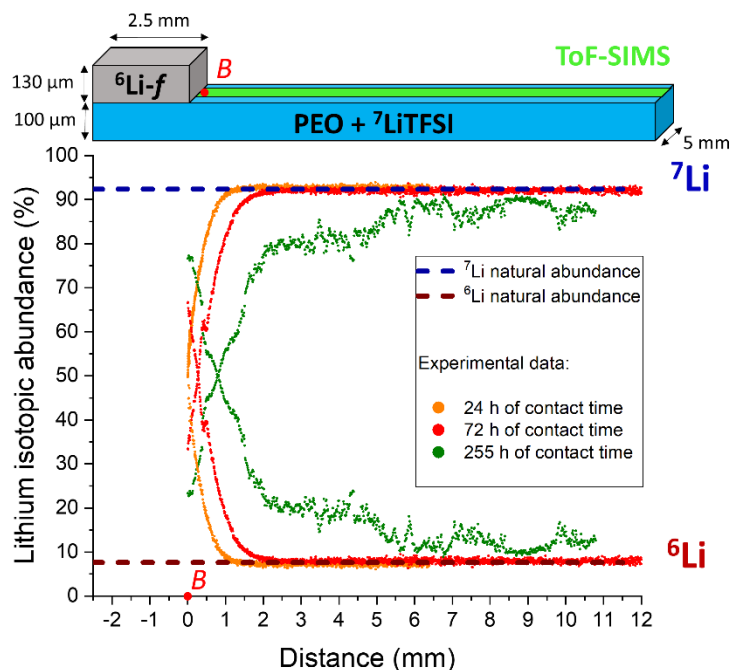


Figure III-7. Lithium isotopic abundance profiles along a polymer electrolyte determined by ToF-SIMS after three various contact times of 24 h (orange), 72 h (red), and 255 h (green) with ${}^6\text{Li}$ -foil at 60 °C. Each analysis was performed on different samples. The point B stands for the edge of the polymer electrolyte on the ${}^6\text{Li}$ -foil side. The dotted lines correspond to lithium natural isotopic abundance plateaus.

Figure III-7 represents the evolution of lithium isotopic abundances as a function of the distance from the ${}^6\text{Li}$ -foil to the end of the polymer electrolyte. Three experiments were carried out for various contact times of 24 h (orange), 72 h (red), and 255 h (green). The 2DLA scan start at the edge of the ${}^6\text{Li}$ -foil, which is materialised by the point B on Figure III-7. This position was set arbitrary at 0 mm. The part of the electrolyte under ${}^6\text{Li}$ -foil was not considered. Analyses were carried out along the accessible surface of the polymer electrolyte. Close to the previous location of ${}^6\text{Li}$ -foil, an enrichment in ${}^6\text{Li}$ was detected. After a contact time of 24 h, 50.3% of ${}^6\text{Li}$ were detected at the edge (B) of the polymer electrolyte on the side of the ${}^6\text{Li}$ -foil. After 72 h and 255 h, 66.5 and 76.6% of ${}^6\text{Li}$ were detected at B, respectively. The lithium isotopic abundance is gradually converging to lithium natural isotopic abundance as the analysed area moves away from the ${}^6\text{Li}$ -foil. ${}^6\text{Li}$ and ${}^7\text{Li}$ natural isotopic plateaus are represented by the horizontal dotted lines, in brown for ${}^6\text{Li}$ and in blue for ${}^7\text{Li}$. They facilitate the determination of Li^+ ions diffusion distance along the polymer electrolyte. For relatively short contact times, typically 24 h and 72 h, ${}^6\text{Li}^+$ ions have diffused through 1.11 and 2.39 mm from B, respectively. These estimations are more accurate than considering only ${}^6\text{Li}$ intensity images because ToF-SIMS is not a quantitative technique. Furthermore, at lithium natural isotopic abundance there is already 7.6% of ${}^6\text{Li}$. Thus, the presence of ${}^6\text{Li}^+$ ions in the polymer electrolyte does not necessary imply an enrichment in ${}^6\text{Li}$ coming from the ${}^6\text{Li}$ -foil. An estimation of lithium isotopic abundance must be performed. Experimental results obtained after 255 h of contact time present less consistency compared to the others. In particular, it is more difficult to determine the exact length of the lithium diffusion front. Indeed, alterations of lithium self-diffusion paths, but also a competition between bulk and surface phenomena can occur since after more than 10 days in the oven. Some irregularities

were exacerbated on the electrolyte surface. ToF-SIMS is an extreme surface sensitive technique in the static mode. [73] Thus, differences between the surface and the bulk of a sample can be observed due to inhomogeneities. [73] Quality of the results highly depends on the surface state. [73] Indeed, the roughness of the surface alters the quality of the measurements. Even if uncertainties might be increased, the main trends are maintained in this experiment. ${}^6\text{Li}^+$ ions have diffused through at least 3 mm from B along the polymer electrolyte after 255 h of contact time. The results highlight that the longer the contact time, the further ${}^6\text{Li}^+$ ions diffuse through the electrolyte. In order to better interpret the ToF-SIMS results, a model based on the *in-plane* configuration was developed as described on Figure III-1. Modelling can help to validate experimental results and to estimate lithium diffusion coefficients. Furthermore, it can also provide valuable information on lithium behaviour at the ${}^6\text{Li}$ -foil/polymer interface. Indeed, even if it was not characterised experimentally, it was assumed that an enrichment of the polymer electrolyte in ${}^6\text{Li}$ implies an enrichment of the ${}^6\text{Li}$ -foil in ${}^7\text{Li}$. The developed model should be able to verify this hypothesis, to quantify lithium exchanges at the ${}^6\text{Li}$ -foil/polymer interface and to determine numerical parameters playing a major role in lithium exchanges and lithium self-diffusion.

2.2. Characterisation of lithium dynamics in *in-plane* devices by modelling

The developed model aims at describing lithium exchanges between a ${}^6\text{Li}$ -foil and a polymer electrolyte at lithium natural isotopic abundance. Lithium self-diffusion in polymer electrolyte and in the ${}^6\text{Li}$ -foil are also modelled in the same time. The *in-plane* configuration geometry described on Figure III-1 was modelled with COMSOL Multiphysics 6.0[®]. The experimental geometric parameters are used in the COMSOL model. Parameters of interest are presented on Figure III-8.

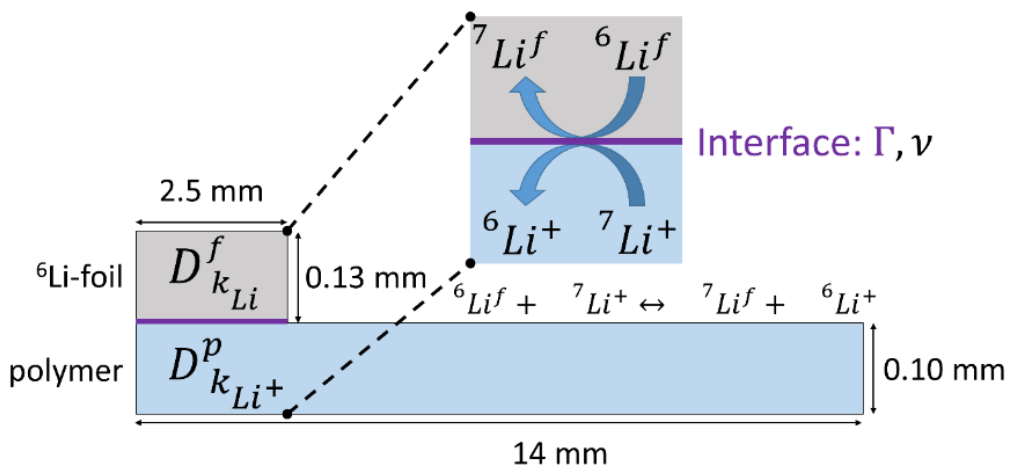


Figure III-8. Geometry implemented in COMSOL to simulate by modelling lithium exchanges at the ${}^6\text{Li}$ -foil/polymer electrolyte interface, and lithium self-diffusion through the polymer electrolyte and the ${}^6\text{Li}$ -foil.

Multiple parameters were required to carry out numerical simulations. They are listed in Table III-1. Their abbreviation, meaning, numerical value and unit are specified.

Table III-1. Parameters implemented in the model to characterise lithium dynamics in the in-plane device at 60° C. Their meaning, numerical value and unit are specified.

Parameter	Meaning	Numerical value	Unit
c_0	Li concentration in ${}^6\text{Li}$ -foil	76,805	$\text{mol} \cdot \text{m}^{-3}$
c	Li salt concentration in polymer electrolyte	1,250	$\text{mol} \cdot \text{m}^{-3}$
$\%{}^6\text{Li}^f$	Initial ${}^6\text{Li}$ isotopic abundance in ${}^6\text{Li}$ -foil	95.4	%
$\%{}^6\text{Li}^p$	Initial ${}^6\text{Li}$ isotopic abundance in polymer	7.6	%
$D_{6\text{Li}}^f = D_{7\text{Li}}^f$	${}^{6/7}\text{Li}$ self-diffusion coefficient in ${}^6\text{Li}$ -foil	10^{-14}	$\text{m}^2 \cdot \text{s}^{-1}$
$D_{6\text{Li}^+}^p = D_{7\text{Li}^+}^p$	${}^{6/7}\text{Li}^+$ self-diffusion coefficient in polymer electrolyte	1.6×10^{-12}	$\text{m}^2 \cdot \text{s}^{-1}$
ν	Spontaneous transfer frequency	2.0×10^{-9}	s^{-1}

Table III-1 sums up parameters playing a role in lithium dynamic. The lithium concentration in ${}^6\text{Li}$ -foil (c_0) is calculated with the following Equation III-1,

$$c_0 = \frac{1}{V_{\text{Li}}^m} \quad \text{III-1}$$

with V_{Li}^m ($\text{m}^3 \cdot \text{mol}^{-1}$) the molar volume of a lithium atom. c_0 was set regarding a V_{Li}^m of $13.02 \times 10^{-6} \text{m}^3 \cdot \text{mol}^{-1}$, leading to a concentration of $76,805 \text{mol} \cdot \text{m}^{-3}$. The same calculations were presented by Gunnarsdóttir *et al.* [129] The volume of a lithium atom ($V_{\text{Li}}^{\text{atm}}$) could be estimated from V_{Li}^m with the Equation III-2,

$$V_{\text{Li}}^{\text{atm}} = \frac{V_{\text{Li}}^m}{N_A} \quad \text{III-2}$$

with N_A (mol^{-1}), the Avogadro constant ($= 6.0221 \times 10^{23} \text{mol}^{-1}$). Thus, $V_{\text{Li}}^{\text{atm}}$ was estimated at $2.162 \times 10^{-29} \text{m}^3$. This value is important when the lithium volume fraction will be modelled in chapter IV.

The lithium salt concentration in the polymer electrolyte (c) was set considering the preparation protocol. The information given by the suppliers allowed setting up the initial ${}^6\text{Li}$ isotopic abundance for both materials. A set of three parameters is formed with the ${}^6\text{Li}$ diffusion coefficient in the ${}^6\text{Li}$ -foil ($D_{6\text{Li}}^f$), the ${}^6\text{Li}^+$ diffusion coefficient in the polymer electrolyte ($D_{6\text{Li}^+}^p$) and the spontaneous transfer frequency between both domains (ν). It describes lithium molecular dynamics in both domains and at the interface (Γ) between the ${}^6\text{Li}$ -foil and the polymer electrolyte. Parameters were optimised to fit the experimental data. Numerical values of diffusion parameters, such as lithium self-diffusion coefficient and spontaneous transfer frequency at the interface (Γ) will be estimated by comparing experimental results with the simulated ones. A strength of this model lies in the modelling of lithium self-diffusion in the depth of the ${}^6\text{Li}$ -foil. Furthermore, careful attention was devoted to describe spontaneous lithium isotopic exchanges at the Γ interface (Figure III-8). The model relies on the Fick's second law, given by the following Equation III-3,

$$\frac{\partial c_j^i}{\partial t} = -\nabla \cdot \mathbf{J}_j^i + E_j^i \Big|_{\Gamma} \quad \text{III-3}$$

with c_j^i ($\text{mol} \cdot \text{m}^{-3}$), the lithium concentration and \mathbf{J}_j^i ($\text{mol} \cdot \text{m}^{-2} \cdot \text{s}^{-1}$), the flux of lithium isotope j (^7Li or ^6Li) in domain i (the polymer domain (p) or the ^6Li -foil domain (f)). E_j^i is an added source term ($\text{mol} \cdot \text{m}^{-3} \cdot \text{s}^{-1}$) applied at the interface (Γ) between the ^6Li -foil and the polymer electrolyte to describe lithium exchanges. \mathbf{J}_j^i and $E_j^i \Big|_{\Gamma}$ are expressed by the following Equations III-4 and III-5,

$$\mathbf{J}_j^i = -D_j^i \nabla c_j^i \quad \text{III-4}$$

with D_j^i ($\text{m}^2 \cdot \text{s}^{-1}$) the self-diffusion coefficient of lithium isotope j in domain i .

$$E_j \Big|_{\Gamma} = e_j^{\rightarrow} \Big|_{\Gamma} - e_j^{\leftarrow} \Big|_{\Gamma} \quad \text{III-5}$$

with e_j^{\rightarrow} and e_j^{\leftarrow} ($\text{mol} \cdot \text{m}^{-3} \cdot \text{s}^{-1}$) standing for the back and forward spontaneous flux of lithium isotopes at the interface Γ between both materials. The Equation III-6 corresponds to the exchange source term of $^6\text{Li}^+$ from ^6Li -foil to the polymer electrolyte ($E_{^6\text{Li}}^p \Big|_{\Gamma}$).

$$E_{^6\text{Li}}^p \Big|_{\Gamma} = e_{^6\text{Li}}^{\rightarrow} \Big|_{\Gamma} - e_{^6\text{Li}}^{\leftarrow} \Big|_{\Gamma} = \frac{\nu}{c_0} \cdot (c_{^6\text{Li}}^f \cdot c_{^7\text{Li}^+}^p - c_{^6\text{Li}^+}^p \cdot c_{^7\text{Li}}^f) \quad \text{III-6}$$

The exchange source term expression (Equation III-6) is established based on the spontaneous transfer frequency between both materials, ν (s^{-1}), the initial lithium concentration in the ^6Li -foil, c_0 ($\text{mol} \cdot \text{m}^{-3}$), and c_j^i ($\text{mol} \cdot \text{m}^{-3}$). It allows to estimate the amount of $^6\text{Li}^+$ ions added into the polymer electrolyte from the ^6Li -foil. It also takes into account that statistically few $^6\text{Li}^+$ ions of the polymer electrolyte can leave the polymer electrolyte to go into the ^6Li -foil. The Equation III-7 corresponds to the exchange source term of $^6\text{Li}^+$ ions from the polymer electrolyte to the ^6Li -foil ($E_{^6\text{Li}}^f \Big|_{\Gamma}$).

$$E_{^6\text{Li}}^f \Big|_{\Gamma} = e_{^6\text{Li}}^{\rightarrow} \Big|_{\Gamma} - e_{^6\text{Li}}^{\leftarrow} \Big|_{\Gamma} = \frac{\nu}{c_0} \cdot (c_{^7\text{Li}}^f \cdot c_{^6\text{Li}^+}^p - c_{^7\text{Li}^+}^p \cdot c_{^6\text{Li}}^f) \quad \text{III-7}$$

Notice that $E_{^6\text{Li}}^f \Big|_{\Gamma}$ is equal to $-E_{^6\text{Li}}^p \Big|_{\Gamma}$. Furthermore, equalities III-8 and III-9 are assumed according to electroneutrality.

$$E_{^6\text{Li}}^p \Big|_{\Gamma} = E_{^7\text{Li}}^f \Big|_{\Gamma} \quad \text{III-8}$$

$$E_{^6\text{Li}}^f \Big|_{\Gamma} = E_{^7\text{Li}}^p \Big|_{\Gamma} \quad \text{III-9}$$

Equalities III-8 and III-9 are translating the fact that if a lithium from the lithium foil diffuses to the polymer electrolyte, a lithium ion from the polymer electrolyte diffuses to the lithium foil at the same time. This hypothesis is based on the conservation of the electroneutrality, which can be expressed by the following Equation III-10,

$$\nu_{f \rightarrow p} = -\nu_{p \rightarrow f} \quad \text{III-10}$$

with ν (s^{-1}), the spontaneous transfer frequency between both domains, the ${}^6\text{Li}$ -foil (f) and the polymer electrolyte (p).

Regarding recent publication from Morita *et al.*, ${}^6\text{Li}$ diffusion is 8% faster than ${}^7\text{Li}$ diffusion. [102] It is assumed that such low difference cannot be perceptible by ToF-SIMS characterisation. A prior study conducted by Ilott and Jerschow has shown that the slight mass difference between both lithium isotopes is neglected in the context of diffusion kinetics. [130] Therefore, it was postulated that the self-diffusion coefficients of both lithium isotopes would be equal within each domain. The assumption can be translated by the following equalities presented on Equation III-11,

$$D_{6\text{Li}}^f = D_{7\text{Li}}^f \text{ and } D_{6\text{Li}^+}^p = D_{7\text{Li}^+}^p \quad \text{III-11}$$

with $D_{j\text{Li}}^f$ ($m^2 \cdot s^{-1}$), the $j\text{Li}$ self-diffusion coefficient in the ${}^6\text{Li}$ -foil and $D_{j\text{Li}^+}^p$ ($m^2 \cdot s^{-1}$), the $j\text{Li}^+$ self-diffusion coefficient in polymer electrolyte.

The model developed model was confronted to experimental data. The goal was to validate and to optimise it. Thus, numerical simulations were carried out in the same experimental conditions in order to extract lithium diffusion coefficients from the simulated curves, matching the experimental ones.

2.3. Deeper interpretation of ToF-SIMS results thanks to numerical simulations

A two-dimensional diffusion model was developed to understand lithium dynamics in the *in-plane* device at 60° C described on Figure III-8. A transport equation (Equation III-12) is applied to model lithium diffusion in both domains, the ${}^6\text{Li}$ -foil (f) and the polymer electrolyte (p). The divergence of the ${}^6\text{Li}$ flux (J_j^i) describes lithium diffusion in both materials. In addition, an exchange source term (E_j^i) expresses lithium isotopic exchanges at the interface (Γ). Here, $D_{6\text{Li}}^f$, $D_{6\text{Li}^+}^p$ and ν are the three relevant parameters. Their values were adjusted through the comparison of numerical simulations and experimental results. To accomplish this comparison, specific values were taken into account, such as ${}^6\text{Li}$ abundance at the edge of the polymer electrolyte on the side of the ${}^6\text{Li}$ -foil (B). The intersection position between the ${}^6\text{Li}$ and ${}^7\text{Li}$ curves (x_1), and the position when the lithium natural isotopic abundance plateaux are reached (x_2). These parameters are represented on Figure III-9.

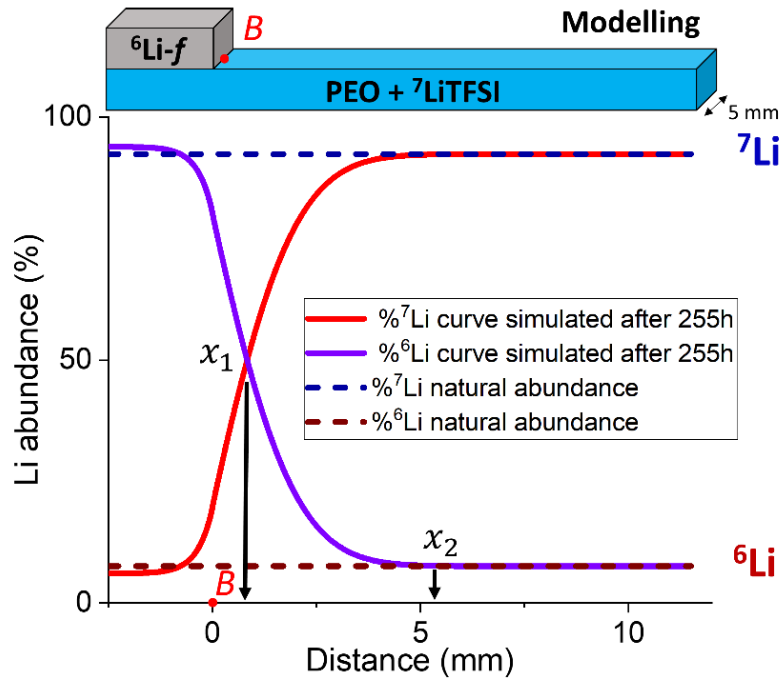


Figure III-9. Lithium isotopic abundances profiles modelled at 60 °C in the in-plane device after 255 h of contact time. Specific results were checked to estimate the consistency of the numerical simulation. The enrichment in ${}^6\text{Li}^+$ was compared with experiments at x_B , x_1 , and x_2 .

Figure III-9 illustrates the position of B , x_1 and x_2 to avoid any misinterpretation. Several numerical simulations were run with various sets of parameters (Appendix A-III-2. *Parametric studies to set appropriate numerical value of $D_{6\text{Li}^+}^p$, $D_{6\text{Li}^+}^f$ and ν*). From the comparison between experimental results and numerical simulations, the model presenting the highest consistency was obtained by setting $D_{6\text{Li}^+}^f$, $D_{6\text{Li}^+}^p$, and ν at $10^{-14} \text{ m}^2 \cdot \text{s}^{-1}$, $1.6 \times 10^{-12} \text{ m}^2 \cdot \text{s}^{-1}$, and $2 \times 10^{-9} \text{ s}^{-1}$, respectively. The results shown on Figure III-10 were obtained with this specific set of parameters.

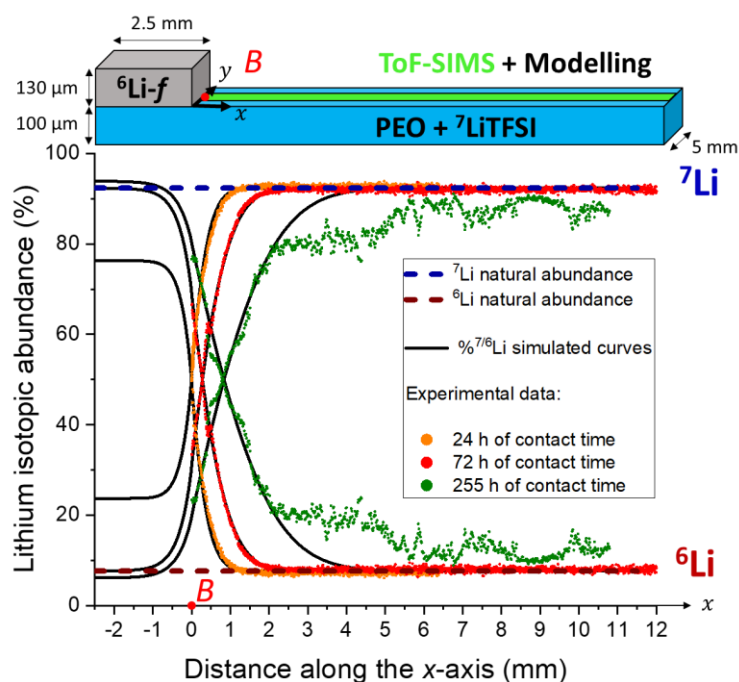


Figure III-10. Comparison of lithium isotopic abundance profiles at 60 °C in a polymer electrolyte determined by ToF-SIMS (coloured dotted lines) and simulated (solid black lines) at three various contact times of 24 h, 72 h, and 255 h. Each analysis was performed on different samples.

Lithium exchanges between both materials were simulated at 60 °C after 24 h, 72 h and 255 h of contact time. On Figure III-10 solid black curves correspond to simulated ones. Coloured dotted curves were obtained by ToF-SIMS. They were already discussed on Figure III-7. The first lithium isotopic abundance values obtained at the edge (B) of the polymer electrolyte on the side of the ${}^6\text{Li}$ -foil were crucial to set up the parameters. They were reported in Table III-2.

Table III-2. Comparison between experimental and modelled results of ${}^6\text{Li}$ abundances at the edge (B) of the polymer electrolyte on the side of the ${}^6\text{Li}$ -foil.

Contact time (h)	24 h	72 h	255 h
Experimental % ${}^6\text{Li}$ in B (%)	50.3 ± 1	66.5 ± 1	76.6 ± 1
Modelling % ${}^6\text{Li}$ in B (%)	48.9	68.9	80.2

After a contact time of 24 h, 50.3% of ${}^6\text{Li}$ were detected experimentally at the edge of the polymer electrolyte on the side of the ${}^6\text{Li}$ -foil (B), and 48.9% of ${}^6\text{Li}$ were calculated by modelling (Table III-2). After 72 h and 255 h of contact time, 68.9 and 80.2% of ${}^6\text{Li}$ were calculated by modelling in B, respectively. Results generated by the numerical simulations are relatively coherent compared with the experimental ones. As previously seen, 66.5 and 76.6% of ${}^6\text{Li}$ were detected in B, after 72 h and 255 h of contact time, respectively. A specific attention had been also paid to the intersection position (x_1) of the ${}^6\text{Li}$ and ${}^7\text{Li}$ curves. It obviously occurs when both isotopic abundances are equal to 50%, but it does not occur at the same distance from the ${}^6\text{Li}$ -foil. They were reported in Table III-3.

Table III-3. Comparison between experimental and simulated results of the intersection position (x_1) between the ${}^6\text{Li}$ and ${}^7\text{Li}$ curves, occurring for % ${}^6\text{Li}$ = % ${}^7\text{Li}$ = 50%

Contact time (h)	24 h	72 h	255 h
Experimental x_1 -intersection (μm)	5 ± 1	273 ± 1	813 ± 1
Modelling x_1 -intersection (μm)	-5	270	840

After a contact time of 24 h, curves intersection occurred at 5 μm far from the ${}^6\text{Li}$ -foil, experimentally (Table III-3). After 72 h and 255 h of contact time, it occurred at 273 μm and 813 μm far from the ${}^6\text{Li}$ -foil, respectively. Modelling results differ from 3 to 27 μm (Table III-3). The experimental and the simulated results are leading to the same position of the intersection. Thus, they are in accordance. The diffusion distance along the polymer electrolyte was also considered to optimise the model. The experimental and simulated ones were reported in Table III-4.

Table III-4. Comparison between experimental and simulated results of the position (x_2), when the lithium natural isotopic abundance plateaux were reached.

Contact time (h)	24 h	72 h	255 h
Experimental x_2 position (mm)	1.11 ± 1	2.39 ± 1	/
Modelling x_2 position (mm)	1.49	2.79	5.54

After 24 h and 72 h of contact time, the lithium isotopic plateaux were reached at 1.11 and 2.39 mm far from the ${}^6\text{Li}$ -foil, respectively (Table III-4). These distances were calculated by modelling at 1.49 and 2.79 mm far from the ${}^6\text{Li}$ -foil, respectively. After a contact time of 255 h, it was supposed that ${}^6\text{Li}^+$ ions have diffused through at least 3 mm from B. However, the experimental setup led to uncertainty of tens of micrometres on the in B position. It is due to the ${}^6\text{Li}$ -foil cutting, and has an impact on the estimated diffusion distance. The numerical simulations led to the conclusion that the lithium isotopic plateaux were reached at 5.54 mm far from the ${}^6\text{Li}$ -foil. It was not necessary to set different values for $|v_{f \rightarrow p}|$ and $|v_{p \rightarrow f}|$. Thus, electroneutrality is guaranteed (Equation III-10).

The determined $D_{6\text{Li}}^f$, $D_{6\text{Li}^+}^p$, and ν values were compared with values reported in previous works. Messer and Noak estimated a lithium self-diffusion coefficient in pure lithium of $5 \times 10^{-14} \text{ m}^2 \cdot \text{s}^{-1}$ at 60 °C, by performing nuclear magnetic relaxation. [131] In 2010, Dologlou has mentioned Messer and Noak. [132] Experimentally, lithium self-diffusion coefficient in pure lithium of $7.65 \times 10^{-15} \text{ m}^2 \cdot \text{s}^{-1}$ at 25 °C and $2.16 \times 10^{-13} \text{ m}^2 \cdot \text{s}^{-1}$ at 77 °C. [131] Dologlou obtained relatively coherent results by modelling. Lithium self-diffusion coefficient in pure lithium were estimated at $6.12 \times 10^{-15} \text{ m}^2 \cdot \text{s}^{-1}$ at 25 °C and $1.87 \times 10^{-13} \text{ m}^2 \cdot \text{s}^{-1}$ at 77 °C. [132] Here, the estimation of $D_{6\text{Li}}^f$ is in-between, which is coherent regarding the operating temperature of 60 °C. This value has the same order of magnitude and is close to the estimation provided by numerical simulations ($10^{-14} \text{ m}^2 \cdot \text{s}^{-1}$).

The $D_{6\text{Li}^+}^p$ has already been investigated in literature. Chauvin *et al.* provided an estimation of lithium diffusion coefficient of $5.6 \pm 0.2 \times 10^{-12} \text{ m}^2 \cdot \text{s}^{-1}$ at 73 °C in PEO having the same studied molecular weight ($M_w = 300,000 \text{ g} \cdot \text{mol}^{-1}$), but with a lower lithium concentration ($\frac{OE}{Li} = 60$ instead of 16). [133] They obtained this result by performing

pulsed-field gradient (PFG) NMR spectroscopy. Timachova *et al.* carried out the same PFG-NMR experiments but at higher temperature and various salt concentrations. [134] They provided an estimation of $1.5 \times 10^{-11} \text{ m}^2 \cdot \text{s}^{-1}$ at 90 °C with the same studied lithium concentration ($\frac{OE}{Li} = 16$), but with a lower molecular weight ($M_w = 4,000 \text{ g} \cdot \text{mol}^{-1}$). These values are close to the one obtained by numerical simulations ($1.6 \times 10^{-12} \text{ m}^2 \cdot \text{s}^{-1}$). Variation arises from a combination of factors such as temperature, PEO molecular weight, and lithium concentration.

Finally, no literature could be found regarding the spontaneous transfer frequency ν . Thus, the combination of ToF-SIMS results with numerical simulations offered the possibility to obtain a first estimation of the spontaneous transfer frequency to describe lithium behaviour at the interface between a ${}^6\text{Li}$ -foil and a polymer electrolyte (Γ). All the results led to better describe lithium behaviour in such device.

The surface of the ${}^6\text{Li}$ -foil in contact with the polymer electrolyte could have been characterised by ToF-SIMS to detect a possible ${}^7\text{Li}$ enrichment. However, as the polymer electrolyte is stuck to the ${}^6\text{Li}$ -foil, it is not possible to access the interface Γ . A sputtering process could be considered, but even a Cs^+ ion beam at a high energy of 4 kV would not be enough to remove more than 50 μm of polymer. Furthermore, the polymer electrolyte could be degraded under such high energy Cs^+ ion beam.

III.3. Lithium dynamics determination in the *in-plane* device after 120 h at 60° C

The *in-plane* device was characterised with the developed methodologies dedicated to study lithium dynamics through the whole *in-plane* device. Lithium exchanges were analysed at 60 °C after 120 h of contact time between a lithium foil enriched in ${}^6\text{Li}$ and a polymer membrane containing a lithium salt at lithium natural isotopic abundance. ToF-SIMS and high-resolution ssNMR characterisations were performed. The previously described COMSOL model was also used to deeper understand the lithium isotopic exchanges at the interface between both materials. A schematic of the device reminds the initial enrichment in ${}^6\text{Li}$ of each domain (Figure III-11).

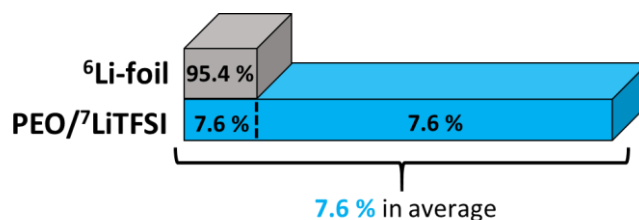


Figure III-11. Schematic of the *in-plane* configuration highlighting initial enrichment in ${}^6\text{Li}$ of each material.

Initially, the ${}^6\text{Li}$ -foil was enriched at 95.4% in ${}^6\text{Li}$ and all the polymer electrolyte was at lithium natural isotopic abundance (Figure III-11).

3.1. Surface analyses of the *in-plane* device by ToF-SIMS

ToF-SIMS 2DLA scan was performed on the surface of the device from the ${}^6\text{Li}$ -foil to the polymer electrolyte, after 120 h of contact time at 60° C (Figure III-12). The same acquisition parameters described in part III.2 were used.

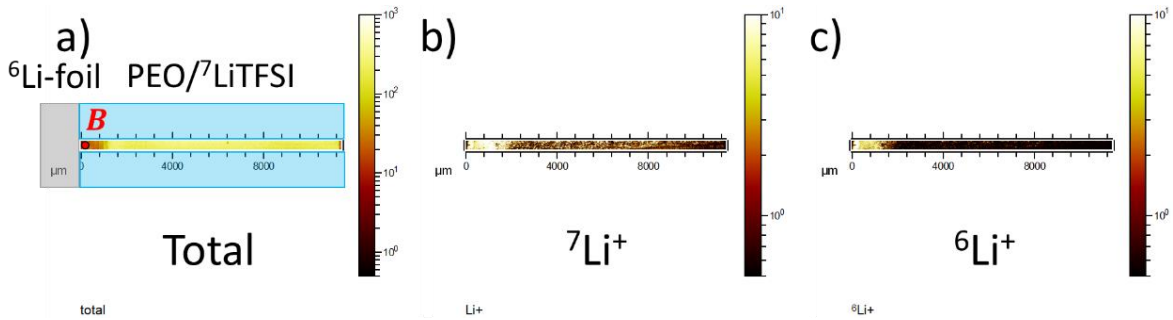


Figure III-12. ToF-SIMS 2DLA scan on the surface of a polymer electrolyte from B ($x_B = 0 \mu\text{m}$), after 120 h of contact time at 60° C: a) Intensity of all the detected molecular fragments, b) Intensity of ${}^7\text{Li}^+$, and c) Intensity of ${}^6\text{Li}^+$.

The ${}^7\text{Li}^+$ and ${}^6\text{Li}^+$ recorded intensities (Figure III-12) were processed to estimate lithium isotopic abundance as a function of the distance from the ${}^6\text{Li}$ -foil (x_B set at 0 mm) to the opposite edge of the polymer electrolyte. Results are presented on Figure III-13.

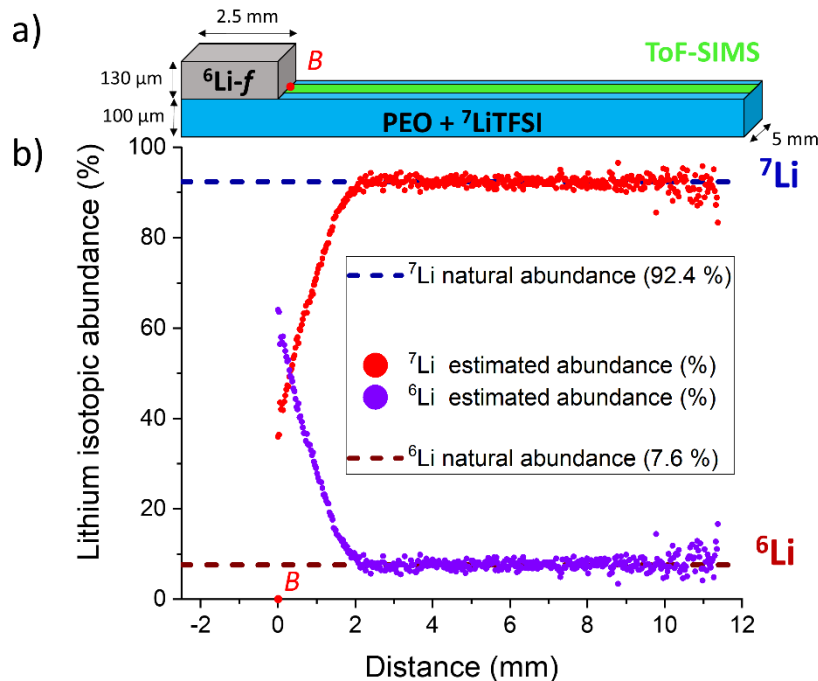


Figure III-13. a) Setup of the *in-plane* device allowing to estimate lithium self-diffusion in each material and lithium exchanges at the interface. The red point B indicates the edge of the polymer electrolyte on the side of the ${}^6\text{Li}$ -foil. The green area corresponds to the analysed area. b) ToF-SIMS characterisation of lithium isotopic abundance profiles through the polymer electrolyte after 120 h at 60° C.

Exclusively the polymer electrolyte surface that is reachable was scanned linearly (Figure III-13.a). The presence of the ${}^6\text{Li}$ -foil prevents to analyse the whole polymer electrolyte surface. Thus, ToF-SIMS characterisations do not provide indication about lithium behaviour under the ${}^6\text{Li}$ -foil. On Figure III-13.b, lithium isotopic abundance was only estimated on the surface of the polymer electrolyte as a function of the distance from B . To improve statistics, each point on the curves was obtained by averaging the lithium isotopic abundance of the pixels having the same x -coordinate. At $60\text{ }^\circ\text{C}$, ${}^6\text{Li}^+$ enrichment was detected along almost 2 mm in the polymer electrolyte. It occurred during the heating due to a ${}^6\text{Li}^+$ ions gradient between both materials in contact. Further than 2 mm , lithium isotopic abundances reached lithium natural isotopic abundances. Thus, the polymer electrolyte far from the ${}^6\text{Li}$ -foil was still not affected by lithium isotopic exchanges which occurred at the interface. ToF-SIMS analyses provide only extreme surface information on the chemical composition. Nonetheless, the ${}^6\text{Li}$ abundance estimations on the surface of the polymer electrolyte may be extended to its volume. This assumption is done because the thickness of the polymer electrolyte was negligible compared to its length ($100\text{ }\mu\text{m} \ll 13.9\text{ mm}$). In other words, estimated lithium isotopic abundances on top of the polymer electrolyte should be the same in depth. The average ${}^6\text{Li}$ abundance on the electrolyte surface was approximated to 11.8% of ${}^6\text{Li}$. This estimation was obtained by averaging each ${}^6\text{Li}$ abundance value along the polymer electrolyte.

No detection of the ${}^6\text{Li}$ -foil signal occurred. Indeed, the polymer electrolyte domain having the ${}^6\text{Li}$ -foil on top was previously removed to avoid any shading effect due to the $130\text{ }\mu\text{m}$ -thick ${}^6\text{Li}$ -foil. The detected intensity of the molecular fragments is affected by the roughness of the polymer electrolyte. However, the estimated Li abundances are not impacted by the roughness because it is defined as the relative ratio of ${}^7\text{Li}^+$ and ${}^6\text{Li}^+$ intensities. Notice that ${}^7\text{Li}^+$ and ${}^6\text{Li}^+$ fragments are expected to present the same ionisation yield at each point, regardless of the polymer electrolyte topology.

3.2. Global analyses of the *in-plane* device by high-resolution ssNMR

Complementary characterisations were performed by high-resolution ssNMR. A 4-mm insert was filled with the same polymer electrolyte previously analysed by ToF-SIMS. The part covered by the ${}^6\text{Li}$ -foil was not analysed to maintain coherence with ToF-SIMS characterisations. In contrast to ToF-SIMS analyses lateral resolution is lost, but the bulk of the electrolyte is probed. A mass of 6.4 mg of polymer electrolyte was collected. Regarding polymer electrolyte preparation, it means that the insert was containing $6.4 \times 10^{-6}\text{ mol}$ of lithium. Figure III-14.a emphasizes that high-resolution ssNMR characterisations probe the whole polymer electrolyte contained in the orange dotted box. ${}^6\text{Li}$ and ${}^7\text{Li}$ nuclei were probed using the acquisition parameters as specified in chapter II (Figure III-14.b).

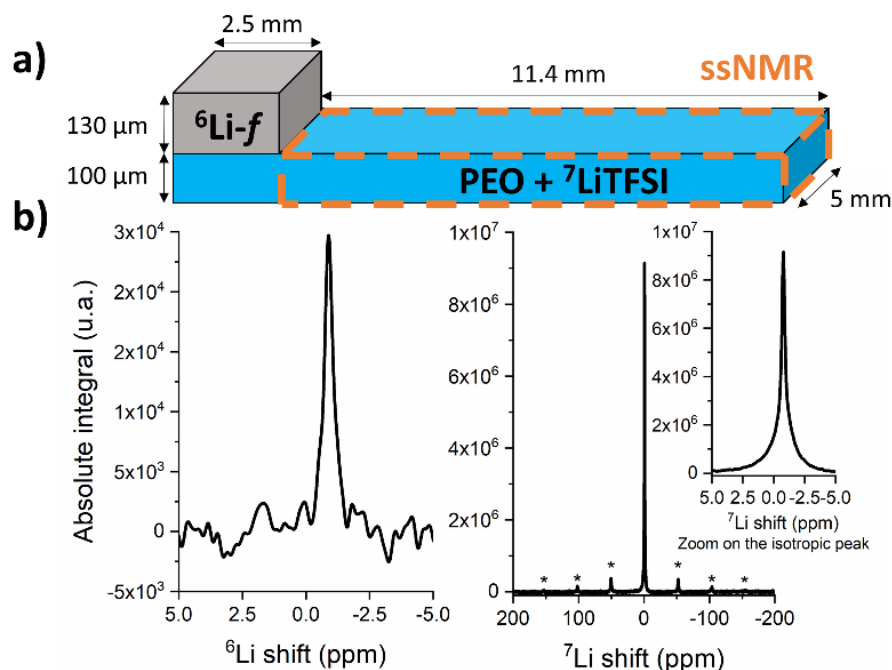


Figure III-14. a) Schematic of the setup allowing to estimate lithium isotopic abundances in the device after 120 h at 60 °C. b) ^6Li (left) and ^7Li (right) high-resolution ssNMR spectra of the polymer electrolyte. Asterisks indicate spinning sidebands.

^6Li and ^7Li results were combined using the polymer electrolyte A as a reference and its corresponding normalisation factor. ^6Li abundance was estimated at 13.1% by high-resolution ssNMR (Figure III-14). This value is close to the ToF-SIMS estimation of 11.8% of ^6Li . Concordance between the surface estimation by ToF-SIMS and the bulk estimation by high-resolution ssNMR of lithium isotopic abundances confirms that the surface is representative of the bulk in such geometry. Jeanne-Brou *et al.* have also observed that in a geometry where the thickness is negligible compared to the length. [135] Furthermore, high-resolution ssNMR analyses allowed determining that the polymer electrolyte contains $5.5 \times 10^{-6} \text{ mol}$ of lithium. This lithium amount was close to the $6.4 \times 10^{-6} \text{ mol}$ of lithium estimated by weighing the polymer electrolyte. More precisely, the electrolyte contained $7.3 \times 10^{-7} \text{ mol}$ of ^6Li after 120 h of contact time at 60 °C. ^6Li amount was higher than the $4.2 \times 10^{-7} \text{ mol}$ of ^6Li present in a polymer electrolyte of equal weight at lithium natural isotopic abundance. Thus, the enrichment in ^6Li was precisely quantified by high-resolution ssNMR.

On Figure III-14.b, only one isotropic contribution was detected on both spectra, which corresponds to the chemical environment of the lithium contained into the polymer electrolyte. On the left, the ^6Li spectrum is plotted. The chemical shift of the isotropic peak is -0.9 ppm . On the right, the ^7Li spectrum is plotted. The chemical shift of the isotropic peak is -0.8 ppm . Additional peaks appear on the spectrum. The distance from the isotropic peak to the peaks indicated by asterisks are separated by around 51.3 ppm corresponding to the rotation frequency of $10,000 \text{ Hz}$ (Appendix A-III-3. Conversion of ppm in Hz). Thus, asterisks indicate spinning sidebands.

Lithium exchanges occur at the ${}^6\text{Li}$ -foil/polymer electrolyte interface. However, this buried interface was not accessible by ToF-SIMS. It was thus impossible to characterise polymer electrolyte enrichment in ${}^6\text{Li}$ and isotopic interdiffusion at the interface region. Manual removal was tested, but led to a rough polymer surface difficult to characterise by ToF-SIMS. It also led to a partial loss of information, as the polymer electrolyte sticks on the ${}^6\text{Li}$ -foil. The polymer electrolyte below the ${}^6\text{Li}$ -foil could be more easily analysed by high-resolution ssNMR, but results would have been difficult to compare with ToF-SIMS characterisations. It appeared that a modelling approach could provide the opportunity to study the lithium isotopes behaviour at the ${}^6\text{Li}$ -foil/ polymer electrolyte interface.

3.3. Deeper interpretation of ToF-SIMS results thanks to numerical simulations

The lithium exchanges model described in part III.2.2. was used to run a simulation of lithium exchanges after 120 h at 60° C. The simulated results were compared with the experimental ones obtained by ToF-SIMS on Figure III-15.

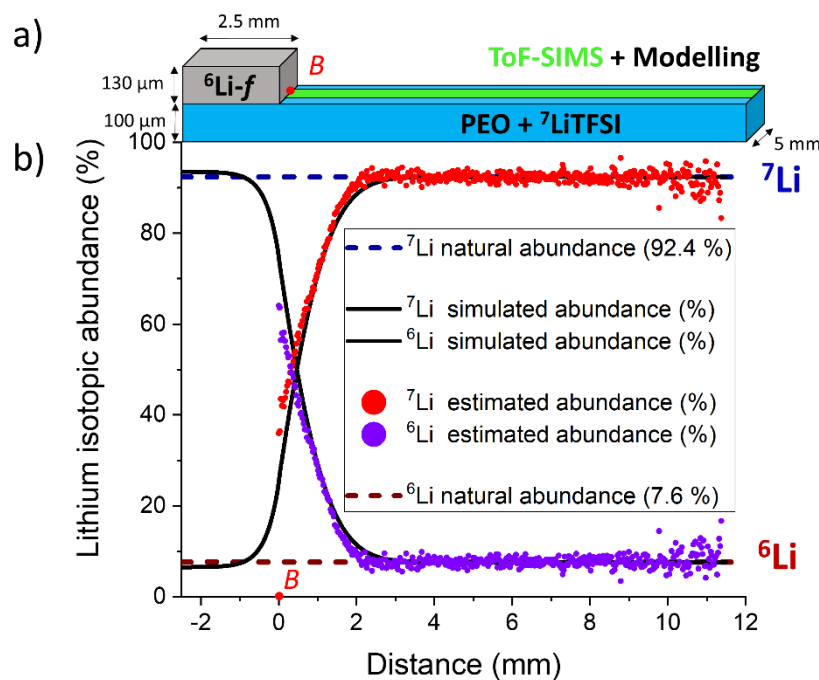


Figure III-15. Comparison between experimental (coloured dotted lines) and simulated (black solid lines) results. Lithium isotopic abundances of the polymer electrolyte were plotted as a function of the distance from the ${}^6\text{Li}$ -foil (B).

On Figure III-15, the experimental and simulated results are compared. After a contact time of 24 h, 64.0% of ${}^6\text{Li}$ were detected experimentally at the edge of the polymer electrolyte on the side of the ${}^6\text{Li}$ -foil (B) and 74.6% of ${}^6\text{Li}$ were calculated by modelling. The experimental value seems low compared to the simulated one. It might be due to a loss of

information at the edge of the electrolyte while cutting the electrolyte to remove the ${}^6\text{Li}$ -foil. Then, curves intersection occurred at $320\ \mu\text{m}$ far from the ${}^6\text{Li}$ -foil, experimentally. Regarding the numerical simulation, it should occur at $458\ \mu\text{m}$ far from the ${}^6\text{Li}$ -foil. Finally, the lithium isotopic plateaux were reached at $2.32\ \text{mm}$ far from the ${}^6\text{Li}$ -foil. This distance was estimated by modelling at $3.69\ \text{mm}$ far from the ${}^6\text{Li}$ -foil. Their superimposition highlights that the set of parameters previously determined is quite coherent. The studied case was carried out months after the first characterisations of lithium exchanges. Furthermore, the same polymer electrolyte composition was used but the polymer electrolyte was not issued from the same casting. This may explain the larger gaps between experimental and simulated values.

Numerical simulations not only provided access to the surface of material, but also to the bulk. Figure III-16 was obtained by modelling lithium exchanges in the *in-plane* device during $120\ \text{h}$ at $60^\circ\ \text{C}$. ${}^6\text{Li}$ abundance variations were calculated in each point of the *in-plane* device.

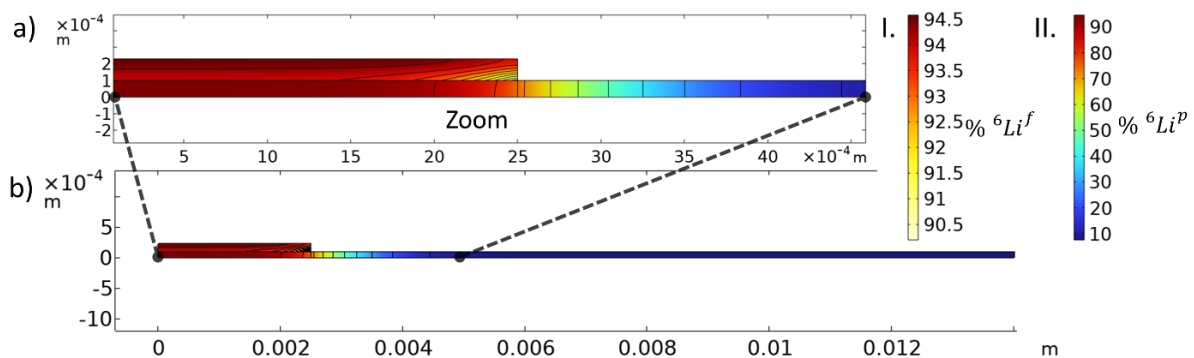


Figure III-16. a) Enlargement of b) allowing to focus on lithium isotopic abundance variations into the ${}^6\text{Li}$ -foil and at the interface with the polymer electrolyte. b) Final enrichment in ${}^6\text{Li}$ of each material composing the *in-plane* device were modelled after $120\ \text{h}$ of contact time at $60^\circ\ \text{C}$. Black lines correspond to isovalue lines. The scale I. applies to the ${}^6\text{Li}$ -foil and the scale II. applies to the polymer electrolyte.

Thanks to numerical simulation, Figure III-16 describes the final enrichment in ${}^6\text{Li}$ of each material composing the *in-plane* device after $120\ \text{h}$ of contact time at $60^\circ\ \text{C}$. It should be noted that coloured scales are different in each domain, otherwise no contrast would be seen. It is clear on Figure III-16.a that the polymer electrolyte area localised under the ${}^6\text{Li}$ -foil is highly enriched in ${}^6\text{Li}$. The lithium isotopic abundance gradient along the polymer electrolyte is highlighted by the isovalue black lines. It was previously mentioned that at some point ($3.69\ \text{mm}$) the lithium natural isotopic abundance was reached. Figure III-16.a is an enlargement to examine the ${}^6\text{Li}$ abundance variations at the ${}^6\text{Li}$ -foil/polymer electrolyte interface. The final ${}^6\text{Li}$ -foil enrichment in ${}^6\text{Li}$ might be more difficult to explain. The bottom right corner of the ${}^6\text{Li}$ -foil was less enriched in ${}^6\text{Li}$. This can be explained by the geometry and the diffusive effect of the polymer electrolyte. It is easier to understand ${}^6\text{Li}$ abundance variations in the device (Figure III-16) by presented ${}^6\text{Li}$ concentration evolution in the ${}^6\text{Li}$ -foil over time (Figure III-17).

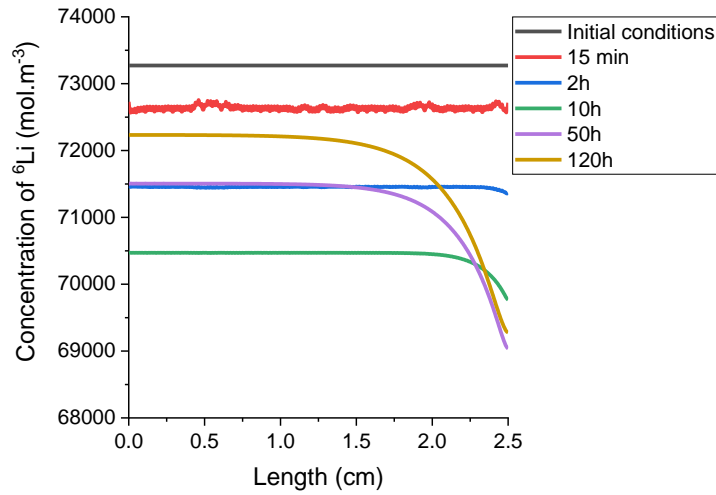


Figure III-17. Modelling of ${}^6\text{Li}$ concentration variations at the interface between the ${}^6\text{Li}$ -foil and the polymer electrolyte.

The initial concentration of ${}^6\text{Li}$ is calculated by the following Equation III-13

$$c_0^f({}^6\text{Li}) = 0.954 \times c_0^f \quad \text{III-13}$$

According to Equation III-13, $c_0^f({}^6\text{Li})$ was equal to $73,272 \text{ mol. m}^3$. The black line on Figure III-17 illustrates the initial conditions. Then, by increasing the contact time to 15 min, 2 h or 10 h, the ${}^6\text{Li}$ concentration is decreasing in the ${}^6\text{Li}$ -foil, meaning that ${}^6\text{Li}$ is diffusing from the foil to the polymer electrolyte through the interface. Thus, ${}^6\text{Li}$ -foil is enriching the polymer electrolyte in ${}^6\text{Li}$. Simultaneously, ${}^6\text{Li}$ diffusion occurs along the polymer electrolyte from the left to the right, inducing a ${}^6\text{Li}$ gradient previously discussed. ${}^6\text{Li}$ diffusion along the polymer electrolyte is dependent of the transfer frequency at the interface between both materials. Furthermore, Figure III-17 allows to notice that the ${}^6\text{Li}$ -foil is more enriched in ${}^7\text{Li}$ on its bottom right corner than on its bottom left corner. This phenomenon appears after few hours of contact time. On Figure III-17, it was unexpected that ${}^6\text{Li}$ concentration in ${}^6\text{Li}$ -foil was higher after 50 h of contact time compared to 10 h of contact time. An explanation is that the ${}^6\text{Li}$ -foil starts to be enriched in ${}^6\text{Li}$ at the interface because around the interface the polymer electrolyte was more enriched in ${}^6\text{Li}$ than the ${}^6\text{Li}$ -foil. Such case can occur due to the spontaneous transfer at the interface ($2.0 \times 10^{-9} \text{ s}^{-1}$), which is quicker than the ${}^6\text{Li}$ diffusion through the polymer electrolyte ($1.6 \times 10^{-12} \text{ m}^2. \text{ s}^{-1}$). Furthermore, while there are ${}^6\text{Li}^+$ ions exchanges with ${}^7\text{Li}^+$ ions from the ${}^6\text{Li}$ -foil to the polymer electrolyte, lithium self-diffusion being relatively slow in the ${}^6\text{Li}$ -foil ($10^{-14} \text{ m}^2. \text{ s}^{-1}$), it cannot compensate ${}^6\text{Li}^+$ ions, which are going out of the ${}^6\text{Li}$ -foil. Thus, the polymer electrolyte was more enriched in ${}^6\text{Li}$ under the ${}^6\text{Li}$ -foil compared to the enrichment in ${}^6\text{Li}$ of the surface of the ${}^6\text{Li}$ -foil in contact with the polymer electrolyte. All these conditions induce an enrichment in ${}^6\text{Li}$ of the ${}^6\text{Li}$ -foil at the interface.

The polymer electrolyte is more enriched in ${}^7\text{Li}$ under the bottom right corner. Thus, it induces ${}^7\text{Li}^+$ exchanges from the polymer electrolyte to the ${}^6\text{Li}$ -foil, leading to locally decrease the ${}^6\text{Li}$ concentration into the ${}^6\text{Li}$ -foil. It explains the yellow area on the bottom right corner of the ${}^6\text{Li}$ -foil (Figure III-16.b).

As a reminder, the enrichment in ${}^6\text{Li}$ of polymer electrolyte analysed by ToF-SIMS and high-resolution ssNMR were estimated at 11.8% and 13.1% in ${}^6\text{Li}$, respectively. Here, modelling provides another estimation of the polymer electrolyte enrichment in ${}^6\text{Li}$ (Figure III-18).

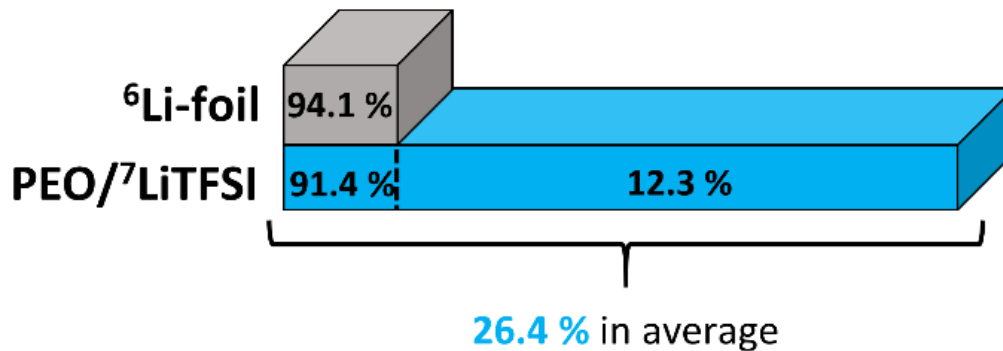


Figure III-18. Final average enrichment in ${}^6\text{Li}$ of each material or part of the material were modelled on the in-plane configuration schematic after 120 h of contact time at 60° C.

The final average enrichment in ${}^6\text{Li}$ of the characterised part of the electrolyte was estimated at 12.3% in ${}^6\text{Li}$ by modelling (Figure III-18). This value is in-between the ones obtained by ToF-SIMS and high-resolution ssNMR. The model is once again reinforced by the experimental results. Furthermore, the polymer electrolyte average enrichment under the ${}^6\text{Li}$ -foil was estimated at 91.4% in ${}^6\text{Li}$ by modelling (Figure III-18), whereas it was not characterised experimentally. Regarding the numerical simulation, the global polymer electrolyte enrichment is estimated at 26.4% in ${}^6\text{Li}$. Furthermore, the ${}^6\text{Li}$ -foil final enrichment was estimated at 94.1% in ${}^6\text{Li}$. Thus, it has been slightly enriched in ${}^7\text{Li}$ by comparing to values on Figure III-11. The ultimate equilibrium state would be to obtain both materials at the same lithium isotopic abundance. Regarding numerical simulations, it would require more than 5 years at 60° C to reach this equilibrium state in such configuration (Figure III-19).

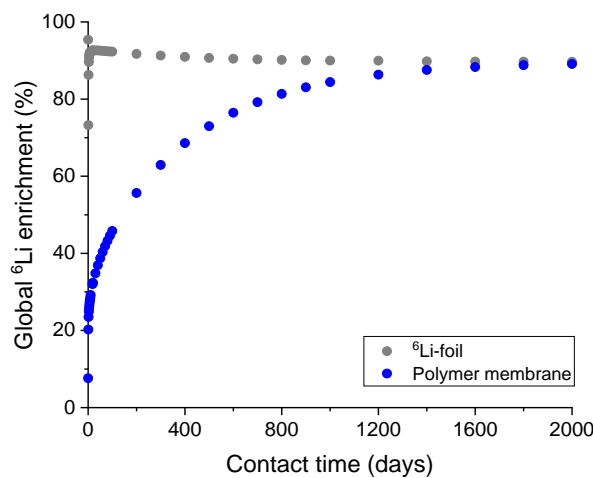


Figure III-19. Evolution of the global ${}^6\text{Li}$ enrichment of the polymer electrolyte (blue) and of the ${}^6\text{Li}$ -foil (grey).

Numerical simulations estimated that after more than 5 years (2000 days) of contact time, the polymer electrolyte and the ${}^6\text{Li}$ -foil lithium isotopic abundance would be equal (Figure III-19). Experiments involved significantly shorter contact times.

Combining ToF-SIMS, high-resolution ssNMR and modelling approaches is a strength. Firstly, experimental characterisations are complementary because surface and bulk of the polymer electrolyte were characterised. Then, unlike ToF-SIMS or high-resolution ssNMR *ex situ* characterisations, numerical simulations provide access to continuous information on lithium exchange dynamics through the whole device. Furthermore, numerical simulations are faster to run than experiments. They last only few minutes. To conclude, these results are helpful to better understand lithium mobility in a polymer membrane such as PEO containing LiTFSI.

Conclusion

Lithium exchanges were characterised at 60° C between a ⁶Li-foil enriched at 95.4% in ⁶Li, and a PEO membrane containing LiTFSI as lithium salt at lithium natural isotopic abundance (7.6% in ⁶Li). Furthermore, lithium self-diffusion through the ⁶Li-foil and the polymer electrolyte were also determined at 60° C. Lithium isotopic concentration differences led to spontaneous lithium exchanges between both materials. ToF-SIMS and high-resolution ssNMR are the two complementary advanced characterisation techniques carried out. ToF-SIMS provides local chemical information of the polymer electrolyte surface. Thus, lithium isotopic abundance profiles along the polymer electrolyte could be obtained by tracking ⁶Li⁺ and ⁷Li⁺ intensities. On another side, high-resolution ssNMR could give access to the global enrichment in ⁶Li of the polymer electrolyte bulk. Furthermore, lithium quantification could be performed, which was not the case in ToF-SIMS. Finally, a model describing lithium exchanges based on lithium isotopic labelling was built and helped to interpret experimental data. Lithium self-diffusion coefficient in the ⁶Li-foil ($D_{6Li}^f = 10^{-14} \text{ m}^2 \cdot \text{s}^{-1}$) and lithium self-diffusion coefficient in the polymer electrolyte ($D_{6Li^+}^p = 1.6 \times 10^{-12} \text{ m}^2 \cdot \text{s}^{-1}$) were determined by fitting ToF-SIMS results with numerical simulations. They are coherent with reported values. Spontaneous exchanges of lithium were modelled at the ⁶Li-foil/PEO interface by assuming electroneutrality conservation. A transfer frequency ($\nu = 2 \times 10^{-9} \text{ s}^{-1}$) translates lithium exchange dynamics at the interface. Furthermore, the average enrichment in ⁶Li of the polymer electrolyte obtained by modelling matches with the ones estimated by high-resolution ssNMR and by ToF-SIMS. This study highlights that using modelling tools is necessary to enhance the full exploitation of such experimental data. A numerical model enabled to mathematise lithium exchanges between solid materials and to determine their corresponding lithium self-diffusion. Furthermore, lithium isotopic abundance in depth under the ⁶Li-foil was provided, whereas it could not be obtained experimentally. Lithium diffusion is a continuous phenomenon. However, ToF-SIMS experiments were performed only after specific contact time, whereas modelling can give access to lithium behaviour over time in whole the device. Numerical simulations offer a deeper understanding of lithium diffusion phenomena occurring in solid materials, such as PEO/LiTFSI, a polymer electrolyte dedicated to solid-state batteries. The developed model can be adapted for other materials, by modifying the polymer properties for instance.

The same strategies will be applied on various electrolyte configurations to better understand lithium diffusion mechanisms during the application of potentiostatic or galvanostatic steps. ToF-SIMS and high-resolution ssNMR characterisations demonstrated that lithium exchanges occur at 60° C between a ⁶Li-foil enriched at 95.4% in ⁶Li and a polymer electrolyte at lithium natural isotopic abundance (7.6% in ⁶Li). Thus, these dynamics have to be taken into account in the following studies. Within the progression of the thesis work, the model will be adapted to simulate lithium diffusion while applying an electrical stress. These results will be discussed in detail in chapter IV and in chapter V.

Chapter IV. Lithium dynamics through an *in-plane* and a *sandwich* device

The rules governing the dependence of lithium exchange dynamics with temperature were stated in chapter III. Here, the developed ToF-SIMS and ssNMR methodologies will be applied to investigate lithium migration through two different devices. An *in-plane* and a *sandwich* configuration will be studied after applying an electrical stress. Both devices are containing SSE materials. Firstly, lithium migration through polymer electrolyte in an *in-plane* configuration is studied after applying a constant voltage. Keeping the same configuration studied in chapter III will help to distinguish various processes involved in lithium dynamics. Then, lithium migration is tracked in another device containing a composite electrolyte. Such configuration was called "*sandwich*" due to its geometry. Indeed, an ionic conductive ceramic pellet is placed in-between two polymer electrolyte layers. It will facilitate the characterisation of lithium behaviour in each material and at their interfaces.

Numerical models describing lithium dynamics under an electrical stress are used to deeper understand lithium behaviour through the whole studied devices. A conventional model based on mixing theory and a more advanced model allowing to implement lithium isotopic tracing are used. Simulated lithium isotope dynamics results will be compared with experimental results.

IV.1. Lithium diffusion through the *in-plane* device under voltage

1.1. Description of the *in-plane* device assembly

Lithium exchanges at 60° C were previously characterised in an *in-plane* device between a lithium foil enriched in ${}^6\text{Li}$ (${}^6\text{Li}$ -foil) and a polymer electrolyte containing a lithium salt at lithium natural isotopic abundance (chapter III). The same *in-plane* configuration used to characterise lithium exchange dynamics was maintained in order to facilitate data comparison between both devices. As lithium exchange dynamics at 60° C were already fully characterised in the previous chapter, it will allow separating and distinguishing additional contributions coming from an applied voltage. Polymer electrolyte and Li electrodes are described in Appendix A-IV-1. *Polymer electrolyte and Li electrodes preparation.*

The *in-plane* configuration is composed of a polymer electrolyte and two lithium foils. Both lithium foils are placed on the surface of both the polymer electrolyte extremities (Figure IV-1).

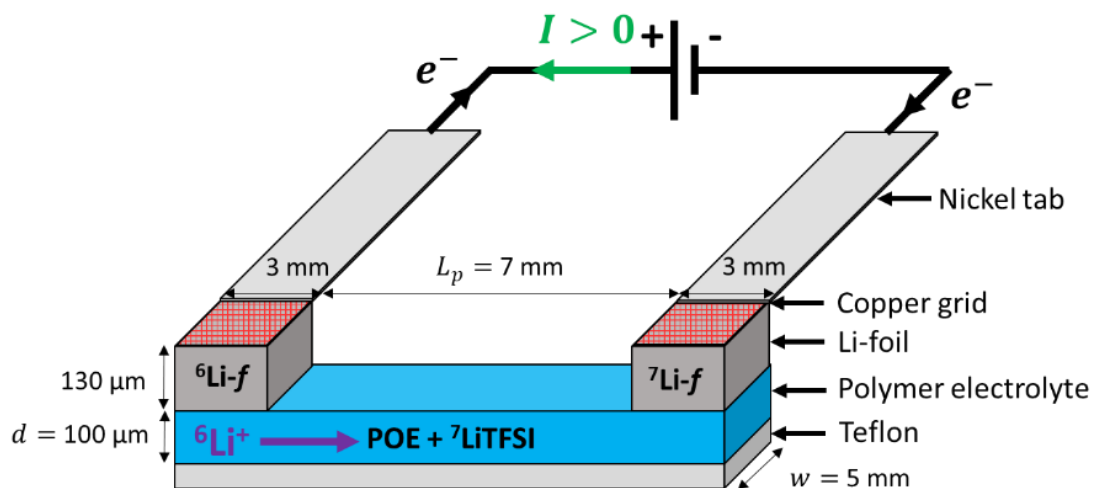


Figure IV-1. Schematic of the *in-plane* configuration composed of a ${}^6\text{Li}$ -foil and a ${}^7\text{Li}$ -foil stuck on the surface at each polymer electrolyte extremity. An external electric circuit connects them. The green arrow indicates the current direction, and the purple arrow indicates the ${}^6\text{Li}^+$ ions migration direction, which is opposite to the electrons flux.

The *in-plane* configuration was assembled in a dry room. A ${}^6\text{Li}$ -foil ($5 \times 3 \text{ mm}^2$) enriched at 95.4% in ${}^6\text{Li}$ was stuck onto one extremity, and a ${}^7\text{Li}$ -foil at lithium natural isotopic abundance, having the same dimensions was stuck onto the opposite extremity. Such configuration has already been studied by Jeanne-Brou *et al.* [135] The Li-foils were separated by 7 mm space leading to an important resistance between two electrodes. The device was sealed under vacuum at 100 mbar into an airtight packaging. Then, it was placed in an oven at 60 °C. A particular attention was paid to protect the polymer electrolyte from moisture and mechanical damages thanks to a specific sealed packaging.

The polymer electrolyte initially contains only LiTFSI at lithium natural isotopic abundance. It is proposed to follow specifically the diffusion of ${}^6\text{Li}$ isotope to distinguish lithium already present in the electrolyte from the one added during the test. Consequently, a ${}^6\text{Li}$ -foil was connected as the positive electrode and a ${}^7\text{Li}$ -foil as the negative electrode. A positive voltage was then applied to initiate the ${}^6\text{Li}^+$ migration through the device. Indeed, the electron flow goes from the negative electrode to the positive electrode, inducing a lithium ions flow in the reverse way in order to balance charges (Figure IV-1). According this schematised device, it was assumed that 95.4% of the injected lithium was composed of ${}^6\text{Li}$ isotope. Figure IV-2 illustrates the first and the second packaging.

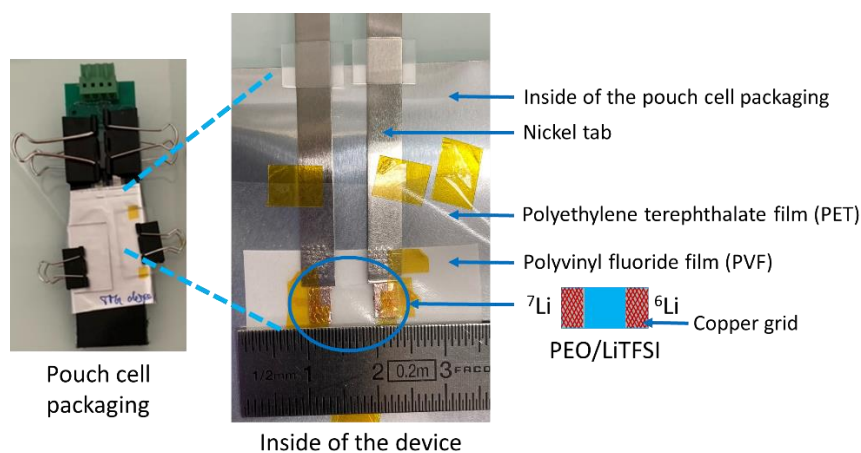


Figure IV-2. Pictures of the in-plane device and description of the various components.

The electrochemical tests were performed out of the dry room. Thus, the device had to be sealed in an airtight packaging (Figure IV-2). The packaging is made of coffee bag commonly used to seal pouch cells. However, the polymer electrolyte sticks on its packaging, while performing experiments at 60°C . Thus, strategies have been found to avoid polymer electrolyte degradation while opening the packaging. The polymer electrolyte was placed on a $56\text{-}\mu\text{m}$ polyvinyl fluoride film (PVF, TMR20SM3, DuPont™ Tedlar®) to easily take it out of the packaging after the heating and electrochemical sequences, (Figure IV-2). The polymer electrolyte was prone to stick to this film instead of sticking to the packaging. Thus, polymer electrolyte was left on this rigid film, facilitating electrolyte handling. Additionally, another film was needed to prevent the top of the polymer electrolyte to stick to the packaging. A $24\text{-}\mu\text{m}$ protective film of polyethylene terephthalate (PET, Hostaphan® RNK 2PRK) was put on top (Figure IV-2). The main advantage of this film is that it can be easily removed without causing any damage to the polymer electrolyte. Regarding provided data by the supplier this film was coated with silicone. The supplier ensures that there is no risk of silicon migration from the film to the studied polymer electrolyte because the silicone was highly polymerised. Several films have been tested before selecting a PET film.

To conclude, thanks to both films (PET and PVF), a way to take out the electrolyte without destroying it or altering its surface has been found. Notice that only non-conductive films have been selected to avoid any short-circuits.

1.2. Electrochemical results

a. Electrochemical impedance spectroscopy (EIS) characterisation

Electrochemical impedance spectroscopy (EIS) was carried out to determine ionic conductivity of six identical *in-plane* devices at 60° C before and after applying a constant voltage of 0.25 V during either 24 h, 48 h or 72 h. Figure IV-3 presents the Nyquist plots obtained by performing EIS before (initial) and after (final) applying an external electrical stress on the devices.

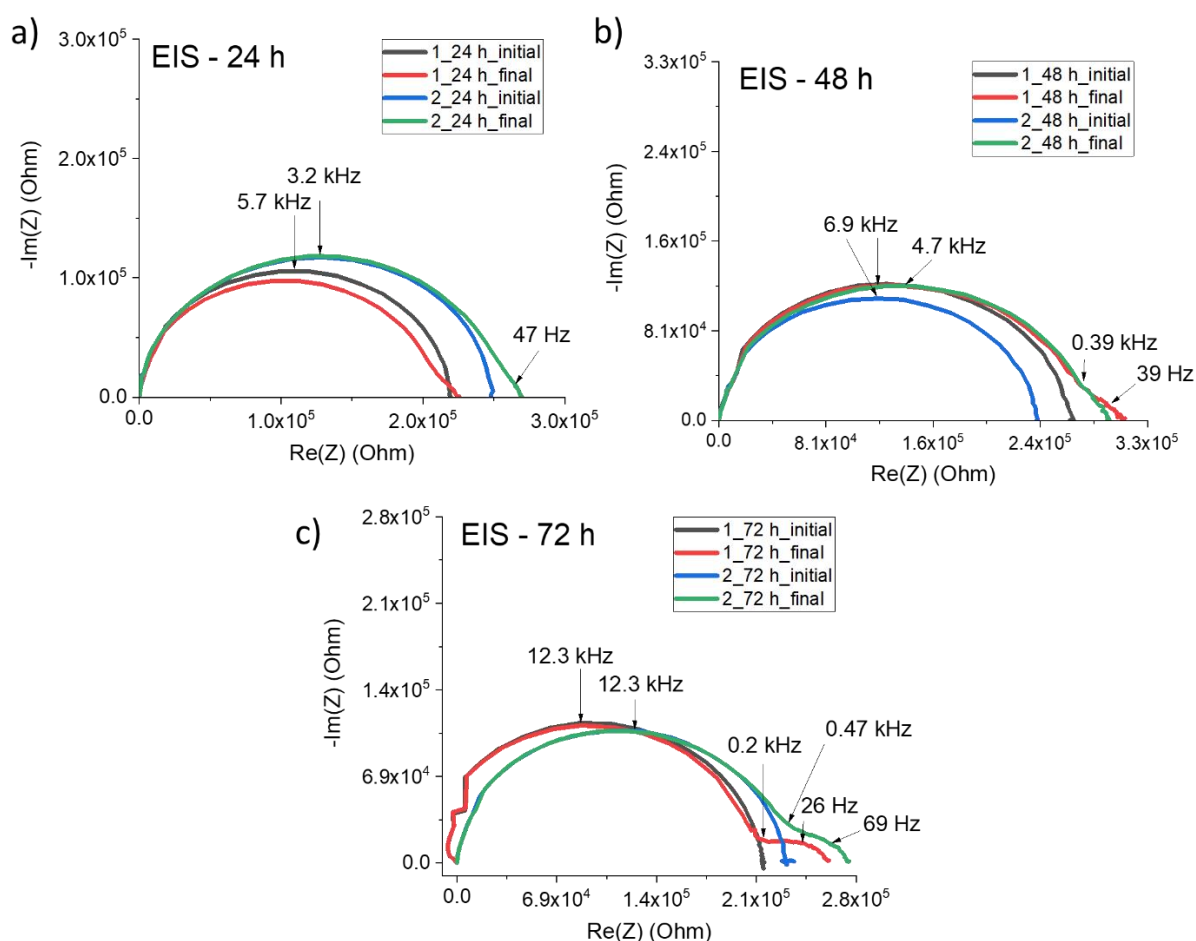


Figure IV-3. Nyquist plots obtained by performing EIS on *in-plane* devices before (black and blue curves), and after (red and green curves) a chronoamperometry sequence ($E = 0.25$ V) of either 24 h (a), 48 h (b) or 72 h (c).

The EIS technique allows to estimate the resistance of the material used to calculate the ionic conductivity. Interface modifications can be detected by comparing initial EIS with those obtained after the experiment (Figure IV-3). The surface alteration seems to have increased after applying a constant voltage at 60° C. Jeanne-Brou *et al.* studied a device having the same design. [135]

The ionic conductivity of such device ($\sigma_{in-plane}$) was given by the following Equation IV-1,

$$\sigma_{in-plane} = \frac{L_p}{R_{el} \cdot w \cdot d} \quad \text{IV-1}$$

with L_p (cm), the length between the two electrodes, R_{el} (Ω), the resistance of the electrolyte, w (cm), the width of the polymer electrolyte, and d (cm), the thickness of the polymer electrolyte. Parameters related to dimensions were introduced on Figure IV-1.

Here, L_p , w , and d are equal to 0.7, 0.5, and 0.01 cm respectively. After 1 h at 60° C, the average resistance (R_{el}) of the six devices presented on Figure IV-3 was estimated at $232,902 \pm 17,325 \Omega$ by performing a serie of EIS on the six devices. This leads to a $\sigma_{in-plane}$ average of $6.0 \times 10^{-4} \pm 0.5 \times 10^{-4} S \cdot cm^{-1}$. At the end of the chronoamperometry sequence, an open circuit-voltage (OCV) step of 10 min allows devices to return at their equilibrium state. Then, the average R_{el} was again estimated by performing an EIS. R_{el} slightly increased up to $238,931 \pm 28,931 \Omega$. Thus, the average $\sigma_{in-plane}$ slightly decreased to $4.5 \times 10^{-4} \pm 0.7 \times 10^{-4} S \cdot cm^{-1}$.

The ionic conductivity of the polymer electrolyte was also estimated by performing EIS on Li/Li symmetric coin cell in CR2032 format (Figure IV-4).

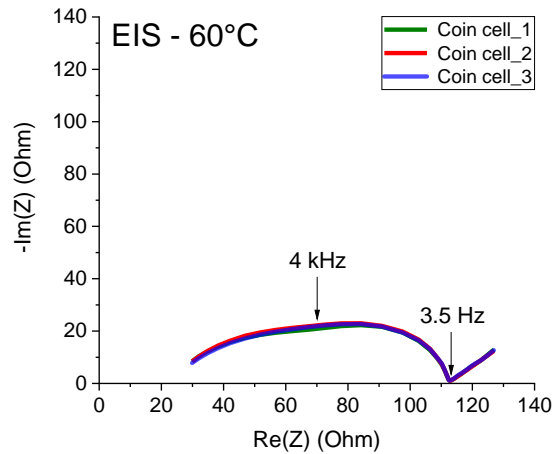


Figure IV-4. Nyquist plots obtained at 60° C by performing EIS on three Li/Li symmetric coin cells containing the polymer electrolyte made of PEO+LiTFSI.

On Figure IV-4, the three Nyquist plots obtained at 60° C are superimposable. The average R_{el} was estimated at $22.0 \pm 0.5 \Omega$. The ionic conductivity ($\sigma_{coin cell}$) was determined by using the conventional Equation IV-2 already mentioned in chapter II.

$$\sigma_{coin cell} = \frac{d}{R_{el} \cdot S} \quad \text{IV-2}$$

with S (cm²), the surface of the polymer electrolyte. An ionic conductivity of $6.4 \times 10^{-4} \pm 0.2 \times 10^{-4} S \cdot cm^{-1}$ was estimated at 60° C in the Li/Li symmetric coin cell. This value is close compared to the one obtained by performing EIS on the *in-plane* device.

The ionic conductivity is an intrinsic property of a material. As the ionic conductivity depends on the thickness, it would be relevant to estimate the thickness modifications during the storage at 60° C, which is just below the polymer melting point which is 65° C. [24]

The determination of the electrical equivalent circuit of each device is presented in Appendix A-IV-2. *Determination of the electrical equivalent circuit of each device.*

b. Chronoamperometry (CA) sequence

A chronoamperometry (CA) sequence was applied on the devices. The voltage was set at 0.25 V. It was applied during either 24 h, 48 h or 72 h. The CA sequence was performed at 60° C. Previously, lithium self-diffusion through a similar *in-plane* device was detected at 60° C (chapter III). Thus, a non-tested device was systematically introduced simultaneously as a reference in the oven to have a reference sample allowing to distinguish lithium migration induced by an electrical stress from lithium self-diffusion at 60° C. Figure IV-5 presents the results of a CA sequence performed on an *in-plane* device by applying a constant voltage of 0.25 V during 24 h.

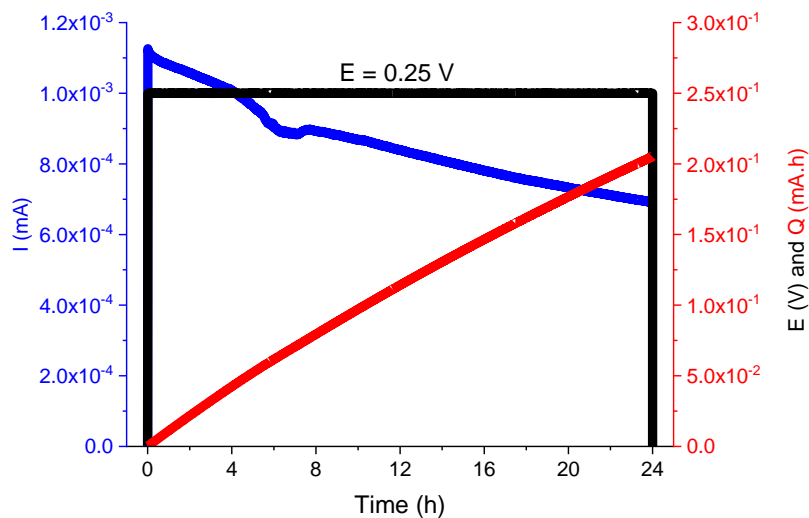


Figure IV-5. Example of a chronoamperometry (CA) sequence with $E = 0.25 \text{ V}$ applied during 24 h. Voltage crenel (in black) applied between two lithium electrodes of an *in-plane* device. The current response I (blue) and the charged capacity Q (red).

On Figure IV-5, the applied voltage corresponds to the black crenel. The blue curve is the resulting current variation and the red curve indicates the charged capacity determined over time. It provides an estimation on the amount of exchanged lithium.

Here, the CA sequence was performed instead of chronopotentiometry (CP) sequence because, due to the huge polarisation, the cut-off voltage was quickly reached with a CP sequence. Applying a CP sequence does not allow to maintain the voltage in the range of the electrochemical stability window of the polymer electrolyte during several days.

The evolution of the current as function of time is presented on Figure IV-6. Furthermore, the specific capacity could be determined, leading to an estimation of the amount of the exchanged lithium (Figure IV-6).

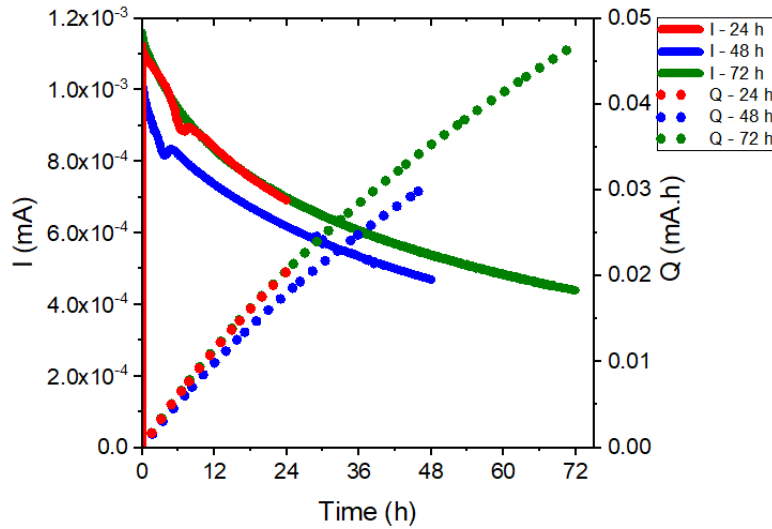


Figure IV-6. Evolution of the current I (left axis) and specific capacity Q (right axis) as a function of time. Three devices were tested by applying a constant voltage of 0.25 V during 24 h (red curves), 48 h (blue curves), and 72 h (green curves).

On Figure IV-6, electrochemical results are presented for three *in-plane* devices after applying a constant voltage of 0.25 V during 24 h (red curves), 48 h (blue curves) or 72 h (green curves). It is important to notice that applying a constant voltage during 48 h instead of 24 h will not double the amount of inserted lithium into the polymer electrolyte. The specific capacity Q ($\text{A} \cdot \text{h}$) is determined with the following Equation IV-3,

$$Q = I \cdot t \quad \text{IV-3}$$

with $I(\text{A})$, the current and $t(\text{h})$, the time of the CA sequence. The amount of exchanged lithium, $n_{\text{Li}}^{\text{ex}}$ (mol), is expressed by the following Equation IV-4,

$$n_{\text{Li}}^{\text{ex}} = \frac{3600 \times Q}{F} \quad \text{IV-4}$$

with F , the Faraday constant ($F = 96,485\text{ C} \cdot \text{mol}^{-1}$). Then, a ratio of exchanged lithium compared to the amount of lithium originally contained in the polymer electrolyte, $\%n_{\text{Li}}$ (%), can be estimated by using the following Equation IV-5,

$$\%n_{\text{Li}} = \frac{n_{\text{Li}}^{\text{ex}}}{n_{\text{Li}}(\text{polymer})} \cdot 100 \quad \text{IV-5}$$

with $n_{\text{Li}}(\text{polymer})$ (mol), the amount of lithium contained into the polymer electrolyte. Table IV-1 sums up the estimated specific capacity, and the absolute and relative amount of exchanged lithium of each device.

Table IV-1. Specific capacity, amount of exchanged lithium, and the corresponding percentage estimated for each in-plane device. For each time stored at 60°C, the sample in which more lithium has diffused was characterised. They are highlighted in green.

Devices	Q ($\mu A \cdot h$)	n_{Li} (μmol)	$\%n_{Li}$ (%)
1_24 h	21	0.8	10
2_24 h	18	0.7	9
1_48 h	28	1.1	14
2_48 h	31	1.2	16
1_72 h	47	1.8	24
2-72 h	46	1.7	23

Experimental characterisations were performed on *in-plane* devices highlighted in green (1_24 h, 2_48 h and 1_72 h). Applying a constant voltage during 24 h, 48 h or 72 h allowed reaching a specific capacity of 21, 31, and 47 $\mu A \cdot h$, respectively (Table IV-1). This corresponds to 0.8, 1.2, and 1.8 μmol of exchanged lithium, respectively. It represents 10, 16, and 24% of exchanged lithium compared to lithium contained in the polymer electrolyte.

More samples should be characterised to improve reproducibility. Other experiments were performed by applying 0.5 V and 1 V to increase the amount of moved lithium. However, applying higher voltage exacerbate the polarisation related to the distance of 7 mm standing in-between both electrodes.

After electrochemical characterisations, devices were dismantled in a dry room to take out the polymer electrolyte. Samples were transferred to ToF-SIMS and ssNMR spectrometers by using airtight transfer systems.

1.3. Advanced characterisations based on lithium isotopic tracing

Samples cannot be characterised by ToF-SIMS after high-resolution ssNMR analyses because of sample preparation, which consists of compacting them into inserts. Therefore, ToF-SIMS characterisations were performed first. The methodologies described in chapter II were followed. According to previous results (Appendix A-III-1. *Lithium self-diffusion at room temperature (25° C)*), it was assumed that the contact time at room temperature between a ^6Li -foil enriched in ^6Li and a polymer electrolyte at lithium natural isotopic abundance does not affect the final ^6Li abundance estimation. Indeed, lithium isotopic exchanges do not occur at room temperature or are too low to be detected.

ToF-SIMS and high-resolution ssNMR characterisation results on of three *in-plane* devices during various time at 60°C (1_24 h, 2_48 h and 1_72 h) are presented and compared in the next sections.

a. ToF-SIMS characterisations

The device was designed in order to easily have access to the polymer electrolyte surface. As the electrode were separated by 7 mm, ToF-SIMS analyses between both Li-foils can easily be performed (Figure IV-7).

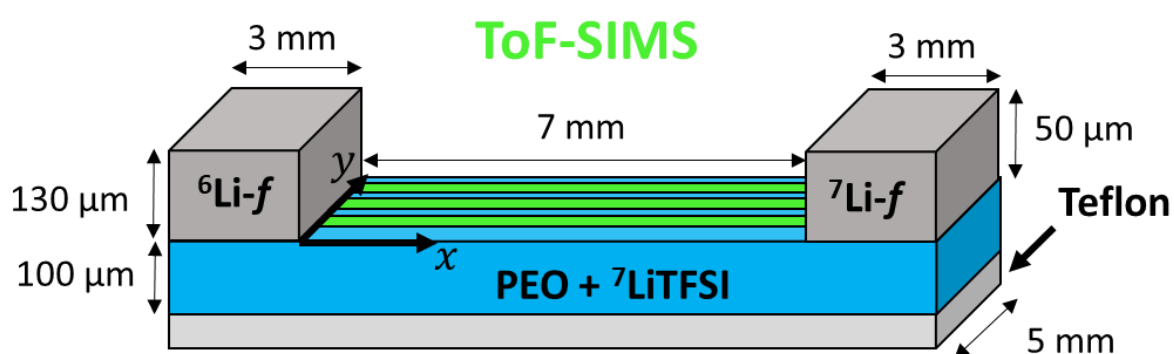


Figure IV-7. Schematic of the *in-plane* device highlighted the areas analysed by ToF-SIMS.

ToF-SIMS analyses were carried out on the polymer electrolyte surface standing between the two electrodes. The analysed surfaces were indicated in green on Figure IV-7. Several analyses were performed on a same electrolyte to check reproducibility by tracking potential variations in the *y* axis. The same two-dimensional large area (2DLA) acquisition mode described in chapter III was used to scan the surface of the electrolyte from the ^6Li -foil to the ^7Li -foil. Sample preparation after dissembling for ToF-SIMS characterisations are thoroughly explained on Figure IV-8.

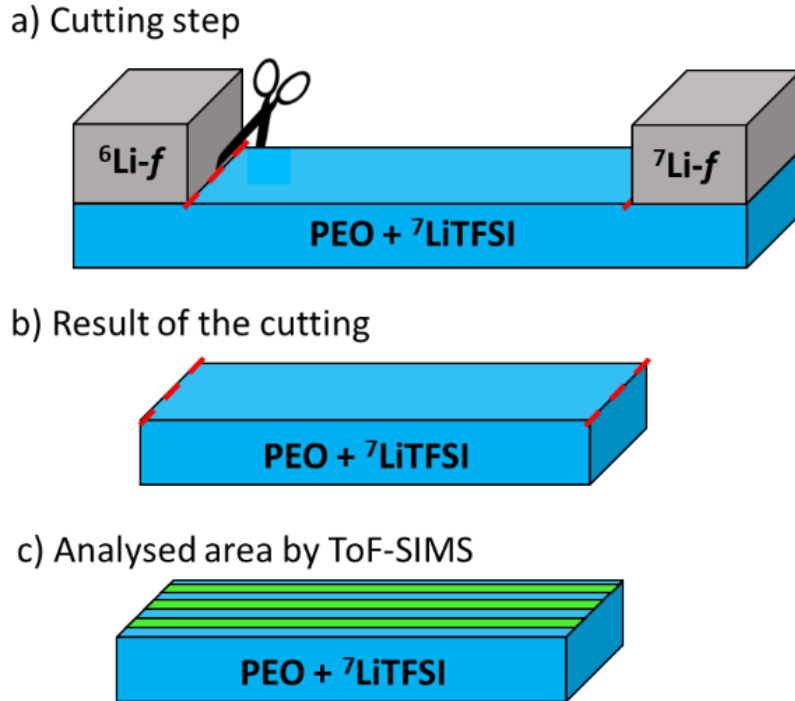


Figure IV-8. Sample preparation for ToF-SIMS characterisations of the polymer electrolyte composing the in-plane device.

Both electrodes and polymer electrolyte layer under were removed (Figure IV-8.a to b). As previously explained in chapter III, it allows avoiding any shading effect due to the thickness of the Li-foils. Molecular fragments were mapped after applying a constant voltage 0.25 V various times at 60°C . The Poisson correction was applied on all ToF-SIMS results presented in this chapter. According to the methodology developed in chapter II, accurate estimation of lithium isotopic abundances can be obtained. ${}^6\text{Li}^+$ ions migration was characterised after applying a constant voltage of 0.25 V during various time at 60°C (Figure IV-9).

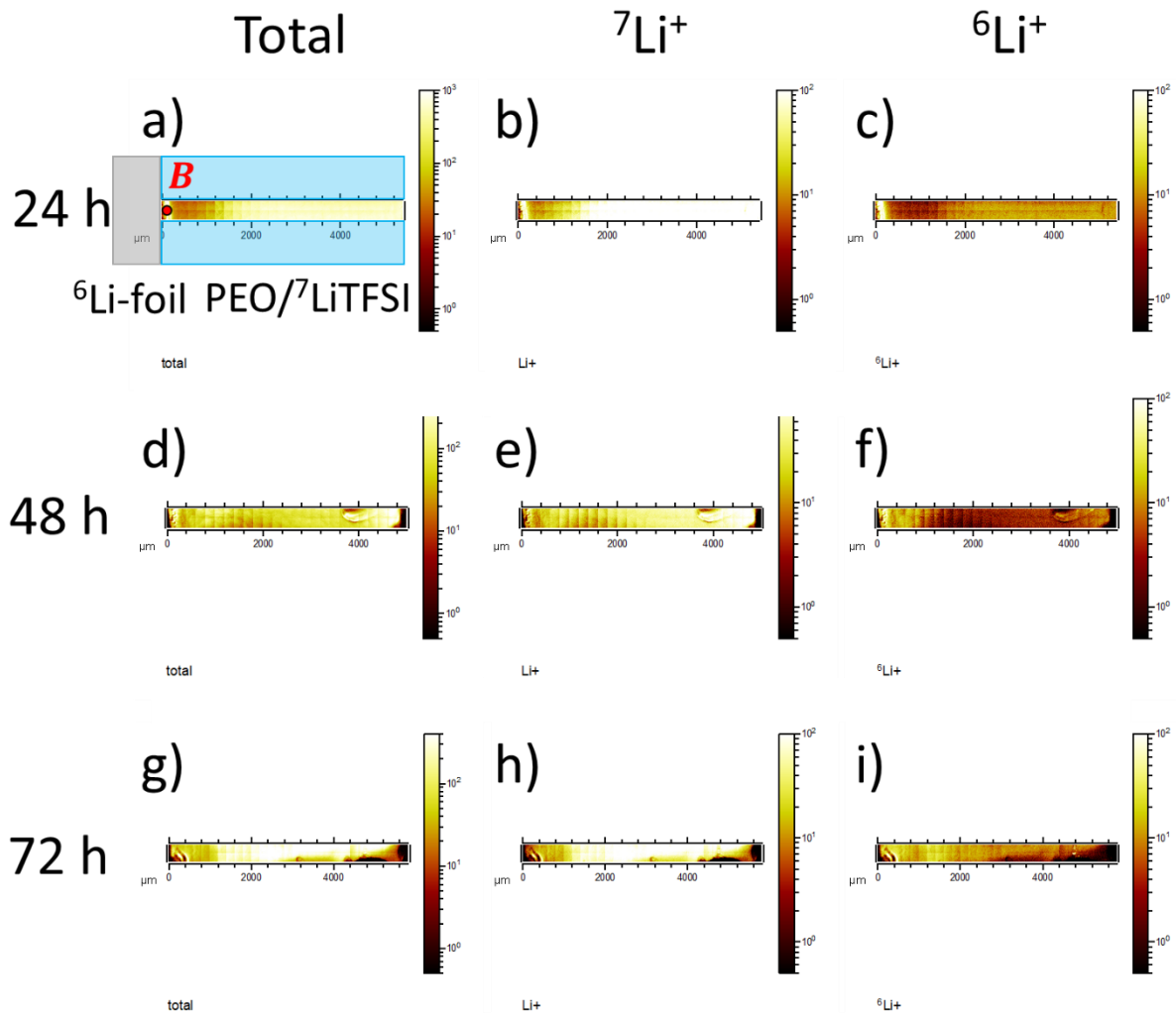


Figure IV-9. Characterisation of ${}^6\text{Li}^+$ ions migration at 60°C after applying a constant voltage of 0.25 V by performing ToF-SIMS 2DLA scan on the surface of three polymer electrolytes from B ($x_B = 0\ \mu\text{m}$). Intensity of all the detected molecular fragments (total), ${}^7\text{Li}^+$ and ${}^6\text{Li}^+$ are represented on three different images after 24 h (a, b, c), 48 h (d, e, f), and 72 h (g, h, i).

Figure IV-9 presents the obtained images with the 2DLA scan mode along polymer electrolyte started from B (red point) after applying a constant voltage of 0.25 V during either 24 h (Figure IV-9.a, b, c), 48 h (Figure IV-9.d, e, f) or 72 h (Figure IV-9.g, h, i) at 60°C . The intensity of the ${}^7\text{Li}^+$ molecular fragment seems homogeneous along the polymer electrolyte. However, on images representing the ${}^6\text{Li}^+$ intensity, variations can be observed (Figure IV-9.c, f, i). On Figure IV-9.c, next to B , the ${}^6\text{Li}^+$ intensity is clearly higher than in the rest of the electrolyte. ${}^6\text{Li}^+$ ions migrate further along the polymer electrolyte when a constant voltage of 0.25 V is applied over a longer time. However, from these images it is difficult to provide accurate conclusions. Therefore, images were processed to obtain lithium migration mappings as a function of the distance from the ${}^6\text{Li}$ -foil (B). Figure IV-10 presents the ${}^6\text{Li}^+$ ions migration profiles obtained by combining ${}^6\text{Li}^+$ and ${}^7\text{Li}^+$ mappings after applying a constant voltage of 0.25 V at 60°C during various times.

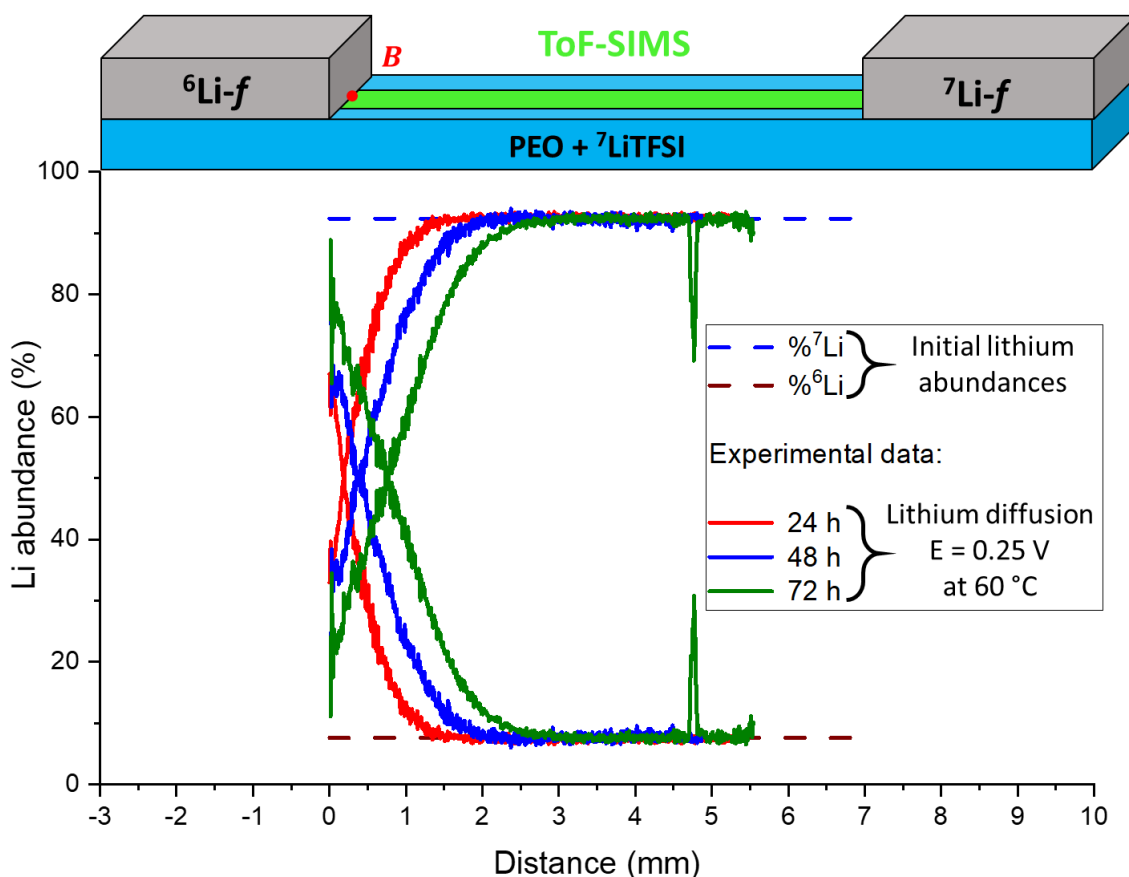


Figure IV-10. ToF-SIMS characterisation of lithium isotopic abundance profiles along the polymer electrolyte at 60° C under 0.25 V. Three tested times were studied: 24 h, 48 h, and 72 h.

Figure IV-10 was obtained by processing images presented on Figure IV-9 using the developed ToF-SIMS methodology presented in chapter II.

Lithium isotopic abundances were estimated as a function of the distance from *B*. To save acquisition time, the polymer electrolyte surfaces were not always characterised until the other extremity if the lithium natural isotopic abundance plateaux were already reached. On Figure IV-10, it is obvious that increasing the time of the CA sequence at 60° C induces a further lithium migration through the polymer electrolyte. Indeed, ${}^6\text{Li}^+$ ions significantly enrich the first 1.4 mm, 2.5 mm, and 3 mm of the polymer electrolyte after applying a constant voltage of 0.25 V during 24 h, 48 h and 72 h, respectively.

Temperature and the applied CA sequence effects cannot be distinguished on these profiles. Both effects participate additionally to the ${}^6\text{Li}^+$ ions diffusion profiles obtained by ToF-SIMS.

Using reference samples may help to distinguish lithium self-diffusion and lithium migration. As previously mentioned, non-tested samples were systematically introduced

simultaneously in the oven. ToF-SIMS 2DLA performed on these reference samples are presented on Figure IV-11.

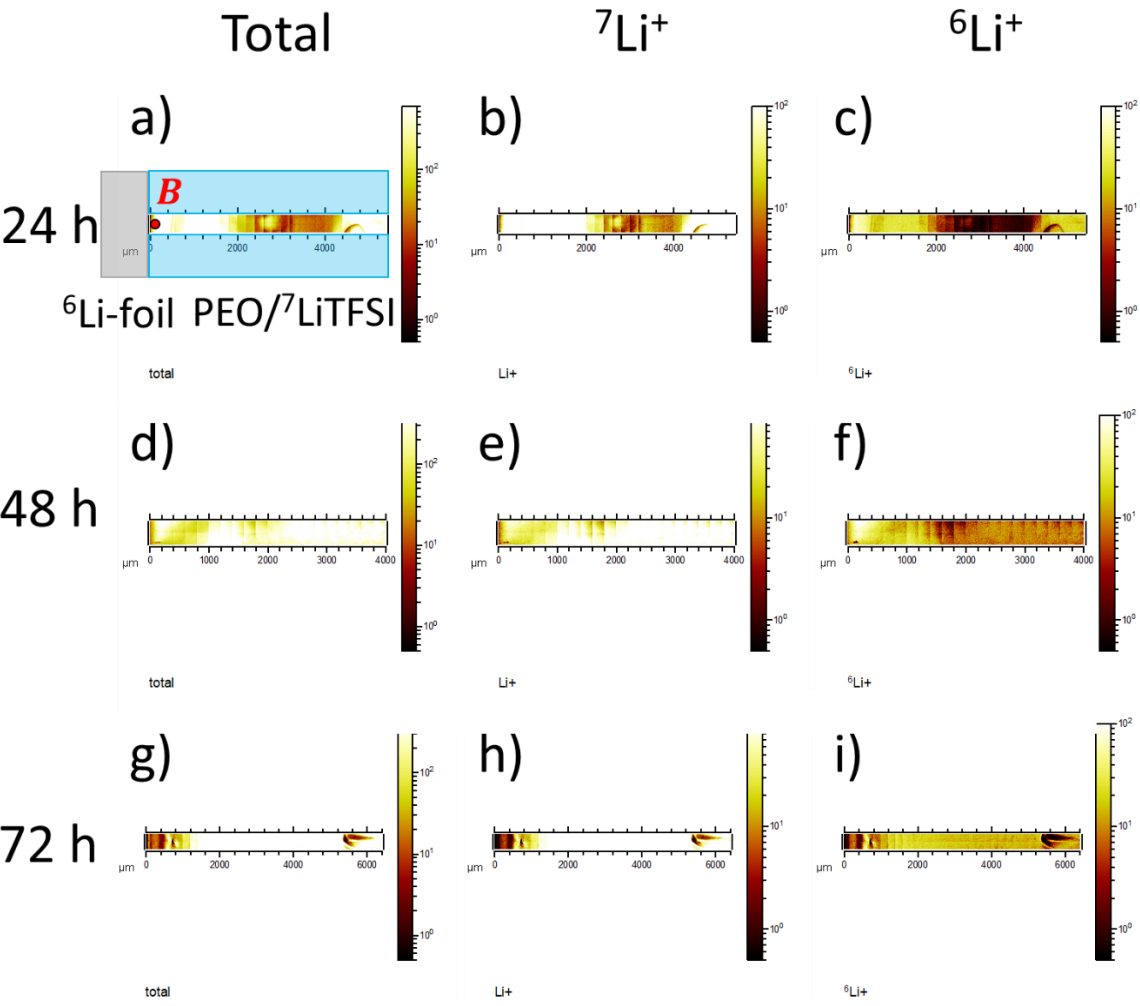


Figure IV-11. Characterisation of lithium self-diffusion at 60° C by performing ToF-SIMS 2DLA scan on the surface of polymer electrolytes from B ($x_B = 0 \mu m$). Intensity of all the detected molecular fragments (total), $^7Li^+$ and $^6Li^+$ are represented on three different images after 24 h (a, b, c), after 48 h (d, e, f) and after 72 h (g, h, i).

Results presented on Figure IV-11 were processed to obtain lithium self-diffusion profiles over time. Furthermore, they were compared with lithium dynamics profiles under a voltage of 0.25 V at 60° C (Figure IV-12).

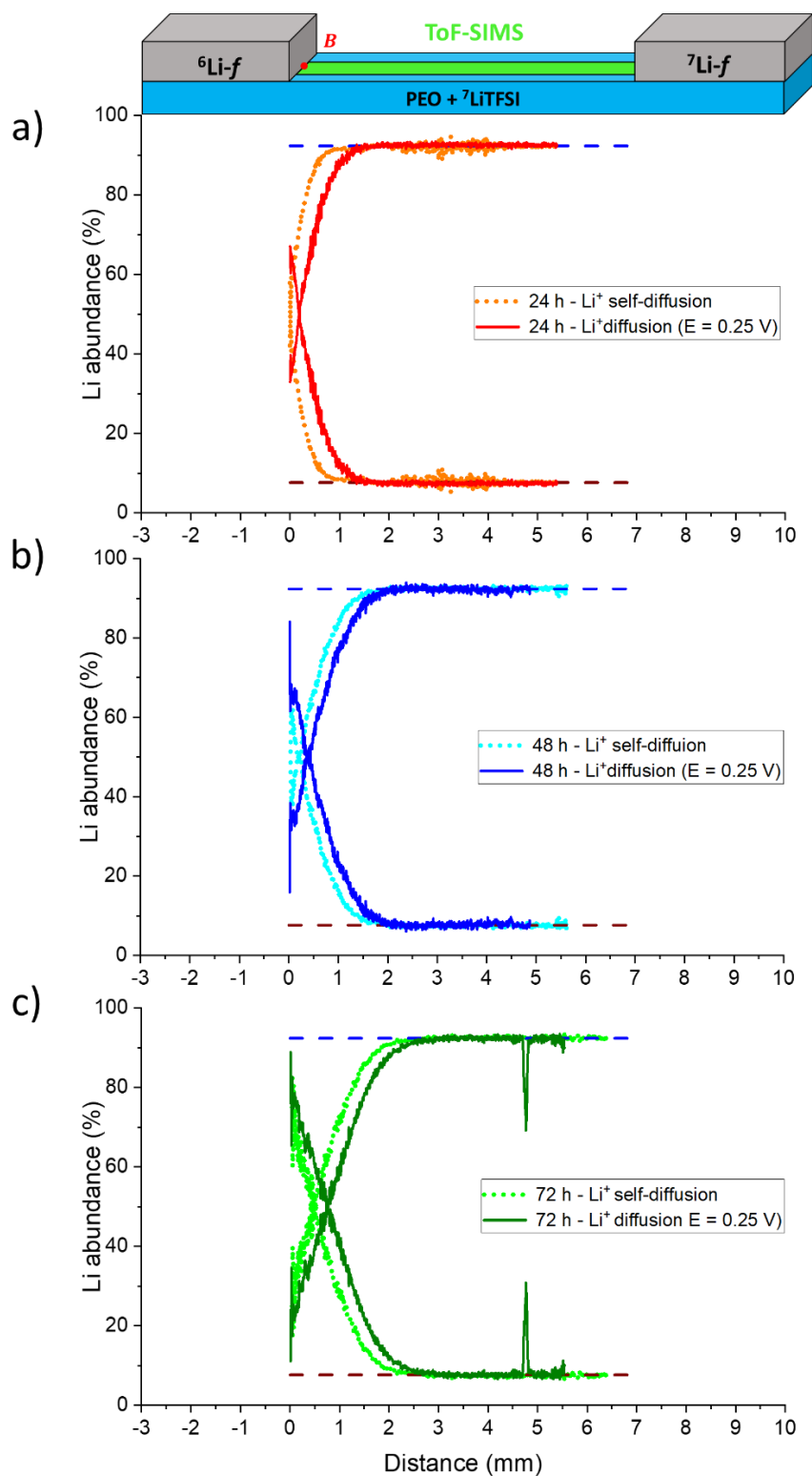


Figure IV-12. ToF-SIMS characterisation of lithium isotopic abundance profiles as a function of the distance from the ${}^6\text{Li}$ -foil (B). Comparison between lithium self-diffusion (dotted lines) induced at 60°C and lithium migration due to the application of a constant voltage of 0.25 V (solid lines) after, a) 24 h, b) 48 h, and c) 72 h at 60°C .

Figure IV-12 was obtained by processing images presented on Figure IV-11 using the developed ToF-SIMS methodology presented in chapter II.

The 2DLA scans on the surface allow the determination of lithium isotopic abundance in the polymer electrolyte as a function of the distance from the ${}^6\text{Li}$ -foil. Figure IV-12.a, Figure IV-12.b and Figure IV-12.c present results obtained after only storing or also testing *in-plane* devices during 24 h, 48 h and 72 h at 60° C, respectively. There is a difference between lithium self-diffusion (dotted lines) induced only at 60° C, and lithium migration due to the application of a constant voltage of 0.25 V (solid lines). Lithium migration front under voltage is detected further from the interface compared with lithium self-diffusion front. Indeed, lithium self-diffusion at 60° C induced ${}^6\text{Li}^+$ ions diffusion through only the first 1 mm (dotted orange curve), 1.6 mm (dotted light-blue curve), and 2.5 mm (dotted light-green curve) after 24 h, 48 h and 72 h, respectively. The ${}^6\text{Li}^+$ ions diffusion profiles obtained after applying a constant voltage of 0.25 V led to further ${}^6\text{Li}^+$ ions diffusion. On Figure IV-12.a, Figure IV-12.b, and Figure IV-12.c, this shift is highlighted. It is due to the application of a 0.25 V voltage acting as an additional driving force.

To sum up, using reference samples stored at 60° C without applying any electrical stress can allow to detect a further lithium diffusion after applying an electrical stress on the *in-plane* devices compared with the only ones stored at 60° C. However, distinguishing precisely lithium self-diffusion and lithium migration processes from Figure IV-12 is difficult. Modelling is mandatory to describe each contribution (lithium self-diffusion and lithium migration) playing a role in lithium dynamics. Numerical simulations presented thereafter (section 1.4) will allow a more accurate description of lithium dynamics processes.

b. High-resolution ssNMR characterisations

The polymer electrolytes, already analysed by ToF-SIMS, were introduced in 4 mm inserts. Then, inserts were placed in rotors to perform high-resolution ssNMR analyses. ${}^6\text{Li}$ abundance is estimated by using the developed high-resolution ssNMR methodology presented in chapter II. Acquisitions were performed in quantitative conditions. ${}^6\text{Li}$ and ${}^7\text{Li}$ spectra were compared by using a reference polymer electrolyte at lithium natural isotopic abundance. This reference sample was characterised in the same conditions as the studied polymer electrolytes.

On Figure IV-13, Figure IV-14, and Figure IV-15, lithium self-diffusion through *in-plane* devices was compared with lithium migration after applying a constant voltage of 0.25 V.

On the following high-resolution ssNMR spectra, the absolute integral values were normalised by the amount of material contained in each probed insert. It allows to easily compare absolute integral values obtained in the same acquisition conditions. Notice that asterisks indicate spinning sidebands on each ${}^7\text{Li}$ spectrum. Their intensities are negligible compared to the isotropic peak, but they have to be considered according to the presented methodology in chapter II.

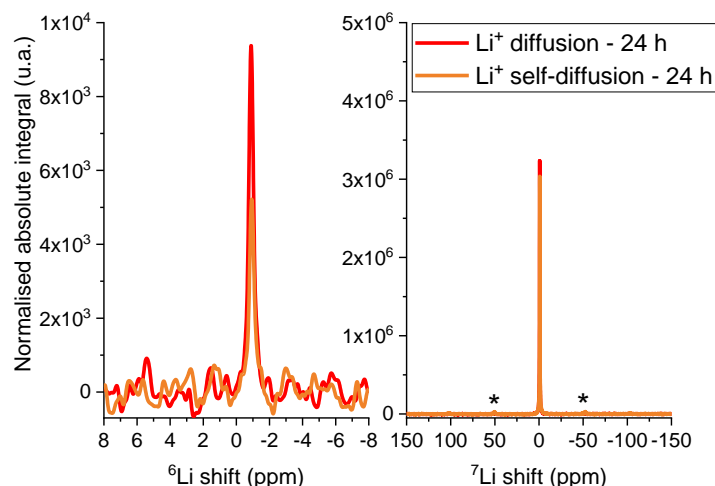


Figure IV-13. ${}^6\text{Li}$ (left) and ${}^7\text{Li}$ (right) high-resolution ssNMR spectra of polymer electrolytes stored at 60°C during 24 h. Comparison between lithium self-diffusion (orange spectra) with lithium migration due to the application of 0.25 V during 24 h. (red spectra).

While an *in-plane* device underwent the described CA sequence, another one was stored during 24 h at 60°C . Figure IV-13 presents the high-resolution ssNMR spectra obtained by probing both polymer electrolytes. ${}^6\text{Li}$ absolute integral value has more or less doubled after the CA sequence compared to the amount of ${}^6\text{Li}$ contained in the device only stored at 60°C during 24 h. On the contrary, ${}^7\text{Li}$ absolute integral is slightly higher for the device only stored at 60°C . Thus, lithium self-diffusion dynamics are detected by ssNMR. According to the methodology presented in chapter II, a normalisation factor S was determined to combine ${}^6\text{Li}$ and ${}^7\text{Li}$ spectra. A ${}^6\text{Li}$ abundance estimation of 11% was obtained for the only stored device at 60°C . Furthermore, lithium migration led to an even higher ${}^6\text{Li}$ abundance estimation. It was increased up to 21% of ${}^6\text{Li}$. Thus, lithium migration could be characterised in addition of lithium self-diffusion.

Other experiments were carried out during 48 h (Figure IV-14) and 72 h (Figure IV-15) in order to estimate the effect of the stored time at 60°C and the CA sequence time on lithium dynamics.

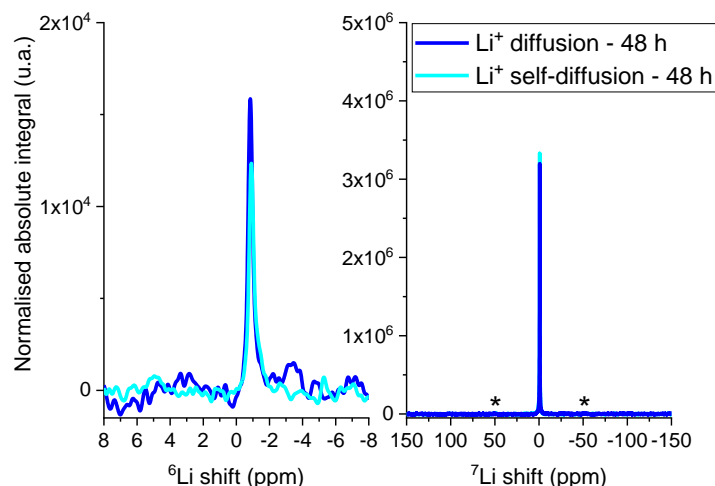


Figure IV-14. ${}^6\text{Li}$ (left) and ${}^7\text{Li}$ (right) high-resolution ssNMR spectra of polymer electrolytes stored at 60°C during 48 h. Comparison between lithium self-diffusion (light-blue spectra) with lithium migration due to the application of 0.25 V during 48 h. (blue spectra).

Figure IV-14 presents the high-resolution ssNMR spectra obtained by probing two polymer electrolytes. ${}^6\text{Li}$ absolute integral value is higher after applying a constant voltage of 0.25 V during 48 h compared to the amount of ${}^6\text{Li}$ contained in the device only stored at 60°C during 48 h. ${}^7\text{Li}$ absolute integral is still slightly higher for the device only stored at 60°C . Lithium self-diffusion led to a ${}^6\text{Li}$ abundance estimation of 23% in such conditions. Furthermore, lithium migration after a CA sequence led to a ${}^6\text{Li}$ abundance estimation of 33% of ${}^6\text{Li}$.

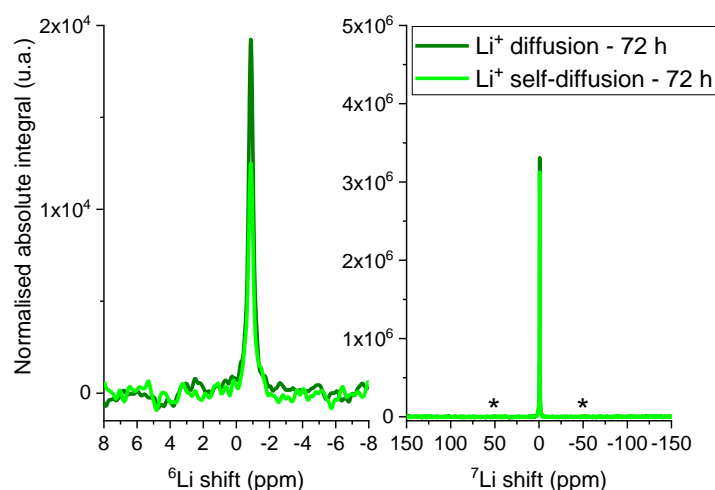


Figure IV-15. ${}^6\text{Li}$ (left) and ${}^7\text{Li}$ (right) high-resolution ssNMR spectra of polymer electrolytes stored at 60°C during 72 h. Comparison between lithium self-diffusion (light-green spectra) with lithium migration due to the application of 0.25 V during 72 h (green spectra).

Figure IV-15 presents the high-resolution ssNMR spectra obtained by probing two polymer electrolytes. ${}^6\text{Li}$ absolute integral value is still higher after applying a constant voltage of 0.25 V during 72 h at 60° C compared to the amount of ${}^6\text{Li}$ contained in the device only stored at 60° C during 72 h . ${}^7\text{Li}$ absolute integral is again slightly higher for the device only stored at 60° C . Lithium self-diffusion led to a ${}^6\text{Li}$ abundance estimation of 28% in such conditions. Furthermore, lithium migration after a CA led to a ${}^6\text{Li}$ abundance estimation of 41% of ${}^6\text{Li}$. Figure IV-16 is a superimposition of all ${}^6\text{Li}$ high-resolution ssNMR spectra of non-tested or tested devices.

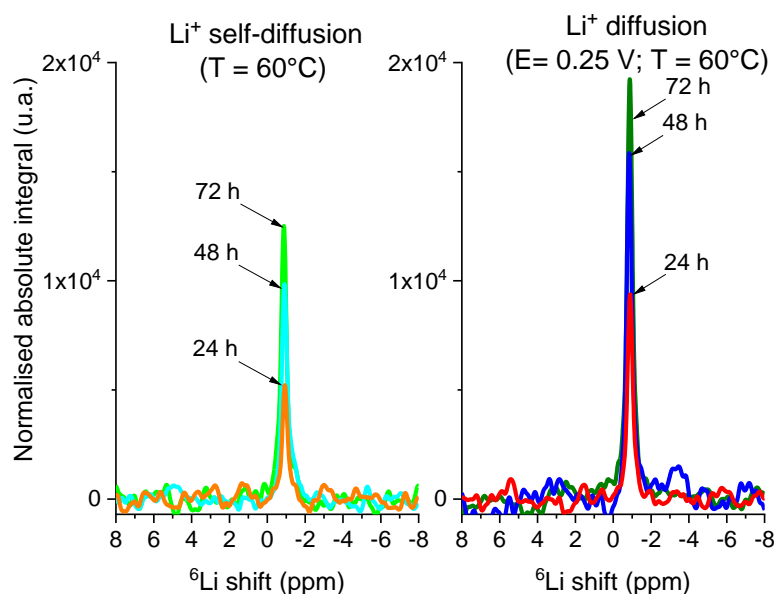


Figure IV-16. ${}^6\text{Li}$ high-resolution ssNMR spectra of polymer electrolytes storing at 60° C during 24 h , 48 h or 72 h . Comparison of isotropic peak intensities between lithium self-diffusion (left, non-tested devices) with lithium migration after applying a constant voltage of 0.25 V at 60° C (right, tested devices).

Figure IV-16 clearly illustrates that ${}^6\text{Li}$ abundance increases with a longer stored time at 60° C . Furthermore, a greater rise of the ${}^6\text{Li}$ abundance was obtained by applying a constant voltage of 0.25 V on the *in-plane* device at 60° C . The results of the respective ${}^6\text{Li}$ abundance are reported in Table IV-2.

Table IV-2. ${}^6\text{Li}$ abundances of the *in-plane* devices estimated by high-resolution ssNMR. Some samples were only stored at 60° C , and others have undergone a CA sequence with a constant voltage of 0.25 V at 60° C during 24 h , 48 h or 72 h .

Conditions	${}^6\text{Li}$ abundance (%)		
	24 h	48 h	72 h
Only stored at 60° C	11 ± 2	23 ± 2	28 ± 2
Stored at 60° C and $E = 0.25\text{ V}$	21 ± 2	33 ± 2	41 ± 2

Table IV-2 sums up ${}^6\text{Li}$ abundances determined by high-resolution ssNMR of the *in-plane* devices as a function of the storing time at 60° C and the CA sequence duration ($E = 0.25\text{ V}$).

Firstly, self-diffusion effect is still detected. Indeed, after 24 *h* of storing time at 60° C, the ${}^6\text{Li}$ abundance is estimated at 11% in the polymer electrolyte. This enrichment increases with the storing time. Levels of 23 and 28% in ${}^6\text{Li}$ are reached after 48 *h* and 72 *h* of storing time, respectively. The polymer electrolyte domain located under the ${}^6\text{Li}$ -foil was not analysed and thus not considered for lithium quantification, even if it is the richest part in ${}^6\text{Li}$ of the polymer electrolyte. Furthermore, lithium migration after applying a voltage of 0.25 *V* is high enough to be detectable. Indeed, ssNMR uncertainty has been estimated at 2%. ${}^6\text{Li}$ abundance variations between lithium self-diffusion at 60° C and lithium migration after a CA sequence can be detected. After applying a constant voltage of 0.25 *V* during 24 *h* at 60° C, the polymer electrolyte is enriched at 21% in ${}^6\text{Li}$. Enrichments of 33 and 41% in ${}^6\text{Li}$ are reached after 48 *h* and 72 *h* of tested time, respectively.

Equation IV-6 allows the discrimination of the various origins of ${}^6\text{Li}$ ($\% {}^6\text{Li}_{estimated}$):

$$\% {}^6\text{Li}_{estimated} = \% {}^6\text{Li}_{initial\ abundance} + \% {}^6\text{Li}_{self-diffusion} + \% {}^6\text{Li}_{migration} \quad \text{IV-6}$$

with $\% {}^6\text{Li}_{initial\ abundance}$, the ${}^6\text{Li}$ initial abundance which is the ${}^6\text{Li}$ natural abundance (7.6% of ${}^6\text{Li}$) in most of the cases, $\% {}^6\text{Li}_{self-diffusion}$, the enrichment in ${}^6\text{Li}$ due to self-diffusion process described in chapter III, and $\% {}^6\text{Li}_{migration}$, the enrichment in ${}^6\text{Li}$ under an electrical stress, which is the studied process in this chapter. According the Equation IV-6, the three contributions can be distinguished and are reported in Table IV-3.

Table IV-3. Dissociation of the contributions leading to the estimated ${}^6\text{Li}$ abundance

Contributions	${}^6\text{Li}$ abundance (%)		
	24 <i>h</i>	48 <i>h</i>	72 <i>h</i>
$\% {}^6\text{Li}_{initial\ abundance}$ (%)	7.6 ± 0.1	7.6 ± 0.1	7.6 ± 0.1
$\% {}^6\text{Li}_{self-diffusion}$ (%)	3.2 ± 2	15.9 ± 2	20.2 ± 2
$\% {}^6\text{Li}_{migration}$ (%)	9.9 ± 2	21.9 ± 2	29.9 ± 2

ToF-SIMS and high-resolution ssNMR analyses highlighted the effect of applying a voltage on lithium dynamics. However, dissociated experimentally this process from the effect of the temperature is difficult. A modelling approach was carried out in order to better understand the effect of the applied voltage. The goal was to model lithium mobility through polymer electrolyte under voltage. Lithium dynamics occurring at 60° C were already modelled in chapter III. Here, lithium isotopes dynamics under voltage at 60° C are modelled.

1.4. A modelling approach to better understand lithium dynamics

Some modelling tools have been specifically developed in parallel of this PhD in the modelling laboratory of the French Atomic Energy and Alternative Energies Commission (CEA). The goal is to simulate lithium dynamics. Numerical simulations are implemented to extract more information from my experimental results and to provide additional information on lithium dynamics through a polymer electrolyte. Volume fraction and diffusion coefficient can be determined for each component for instance. Intermediate steps are required before building an appropriate model of lithium dynamics taking into account lithium isotopic exchanges through the *in-plane* device (Figure IV-1). The various steps are discussed in the next section throughout the presented geometries.

a. Description of the geometries and involved dynamics

The model is able to reproduce common electrochemical experiments performed in battery field such as EIS and CA sequence. Firstly, a *sandwich* geometry is simulated to determine the ionic conductivity of the polymer electrolyte (σ_p) at 60° C. Furthermore, charge transfer dynamics at the interface while applying a constant voltage are modelled (Figure IV-17).

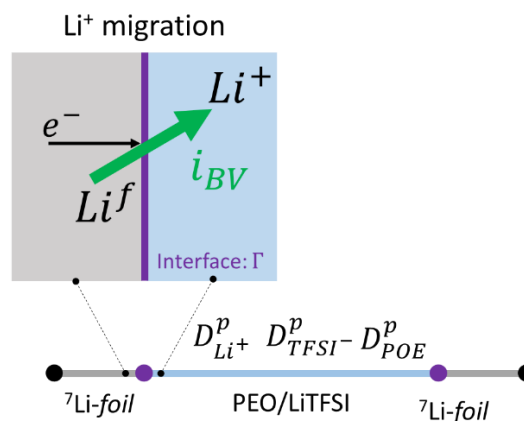


Figure IV-17. Schematic of the 1D geometry which is composed of a polymer electrolyte layer in-between two lithium electrodes. Zoom on lithium migration at the interface. D_i^p are the diffusion coefficients of each species ($i = Li^+$; TFSI⁻, PEO) in the polymer electrolyte. i_{BV} represents the exchange current at the Li-foil/polymer interface.

On Figure IV-17, the one-dimensional (1D) geometry is used to model lithium dynamics into a *sandwich* containing a polymer electrolyte layer in-between two lithium electrodes. EIS and CA sequence of 30 *min* will be performed experimentally and modelled. Butler-Volmer (BV) equations are required to describe lithium migration and to describe lithium exchanges while applying a constant voltage. The electrochemical response of the system is modelled. The polymer electrolyte ionic conductivity (σ_p) and the exchange current at the interface (i_{BV}) will be extracted from these experiments.

Then, the determined parameters will be applied on a more complex geometry in order to compare ToF-SIMS results with simulated ones. The *in-plane* geometry is presented on Figure IV-18.

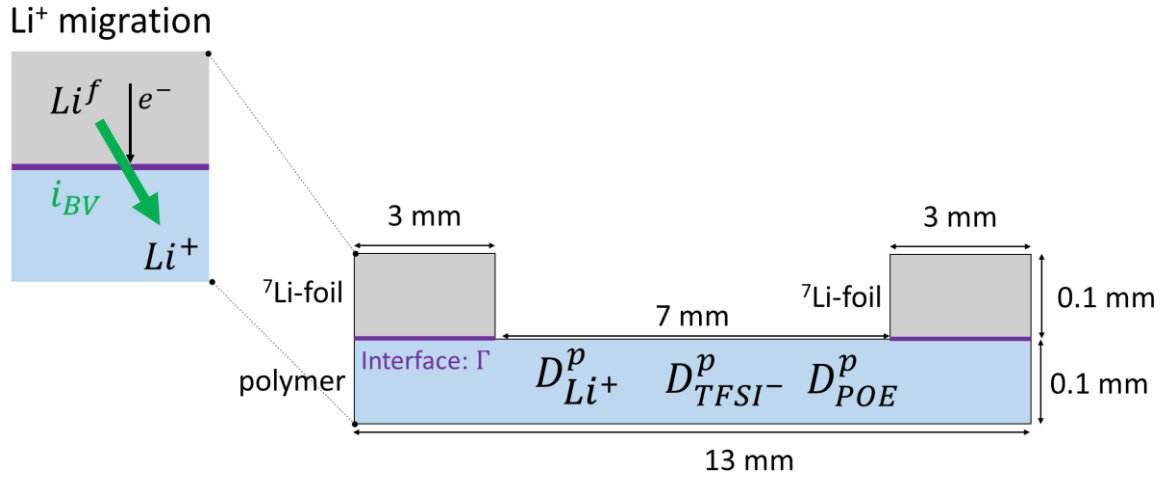


Figure IV-18. Schematic of the 2D in-plane geometry and its associated parameters. Zoom on lithium migration at the interfaces. D_i^p are the diffusion coefficient of each species ($i = \text{Li}^+$; TFSI⁻, PEO) in the polymer electrolyte. i_{BV} represents the exchange current at the interface.

This geometry was already investigated in chapter III. Other parameters such as lithium volume fraction has to be modelled. In this chapter, the 2D models are developed from the presented one in chapter III. Here, ${}^7\text{Li}$ -electrodes are added on each extremity of the polymer electrolyte (Figure IV-18). It allows applying a constant voltage on the device. The used device to study lithium dynamics is presented on Figure IV-18. Dimensions were defined according to the ones of the experiments. Fick's second law was still used to describe lithium self-diffusion at 60° C.

Finally, a ^7Li -electrode is replaced by a ^6Li -electrode in order to perform lithium isotopic tracing experiments (Figure IV-19).

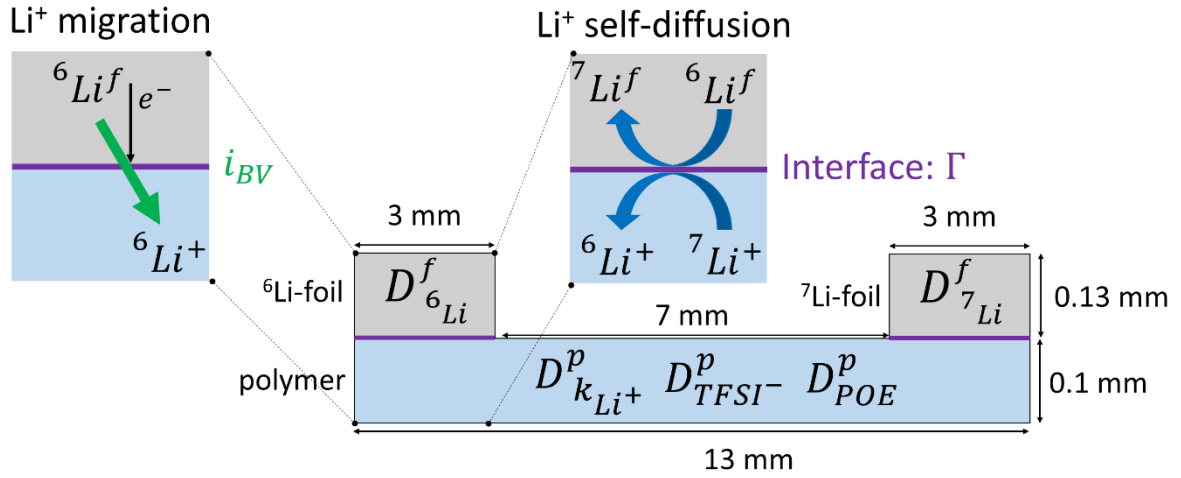


Figure IV-19. Schematic of the 2D in-plane geometry involving a ^6Li -foil enriched at 95.4% in ^6Li and its associated defined parameters. Zoom on lithium migration and lithium self-diffusion at the interfaces. D_i^p are the diffusion coefficients of each species ($i = \text{Li}^+$; TFSI $^-$, PEO) in the polymer electrolyte. i_{BV} represents the exchange current at the interface.

The use of a ^6Li -electrode at the positive electrode will provide more detailed information on lithium dynamics into the polymer electrolyte (Figure IV-19).

Notice that only the main parameters were mentioned on the schematic. Geometries are implemented in COMSOL Multiphysics to study lithium dynamics. The models are using either a generalised mixing model (GMM) based on thermodynamics of mixing equations or an isotopic mixing model (IMM). The IMM is based on the GMM, but it is taking into account lithium isotopic tracing.

b. Use of the generalised mixing model (GMM)

- Description of the general mixing model

The variation in lithium ion concentration is typically simulated using a Nernst-Planck equation [136],

$$\frac{\partial c_{\text{Li}}}{\partial t} = \nabla \cdot D_{\text{Li}} \left(\nabla c_{\text{Li}} + \frac{c_{\text{Li}}}{V_0} \nabla V \right) \quad \text{IV-7}$$

with D_{Li} ($\text{m}^2 \cdot \text{s}^{-1}$) the lithium diffusion coefficient, c_{Li} (mol), the lithium concentration, and V (V), the applied voltage. More details are provided in Appendix A-IV-3. *Présentation du modèle utilisé.*

The first term corresponds to the driving force associated with the presence of a concentration gradient in the electrolyte. Second one arises from the driving force induced by an electric potential gradient. This equation is an approximation of a more general mixing law, based on the electrochemical potential gradient of the electrolyte components.

In order to understand the polymer electrolyte dynamics, a model based on the theory of polymers in solution is proposed in this work. Thus, notice that it is based on existing theory. The GMM used in the following numerical simulations is based on the thermodynamics of mixing. Here, a ternary system composed of Li^+ , TFSI^- , and PEO, is modelled. The following equation-system I presented in Table IV-4 has to be solved. More details are provided in Appendix A-IV-4. *Simplification du modèle de mélange.*

Table IV-4. Summary of the equation-system I used into the generalised mixing model (GMM) and the meaning of each equation.

Equation	Origin	
$\frac{\partial \phi_{\text{Li}^+}}{\partial t} = -\nabla \cdot \underline{J}_{\text{Li}^+} + S_{\text{Li}^+}$	Continuity equation	I
$\phi_{\text{TFSI}^-} = \frac{\Omega_{\text{TFSI}^-}}{\Omega_{\text{Li}^+}} \phi_{\text{Li}^+}$	Deduced from electroneutrality	
$\phi_{\text{PEO}} = 1 - \phi_{\text{Li}^+} \left(1 + \frac{\Omega_{\text{TFSI}^-}}{\Omega_{\text{Li}^+}} \right)$	Volume fraction conservation	
$\underline{J}_{\text{Li}^+} = - \sum_j \Lambda_{\text{Li}^+j}^{\text{th}} \nabla \left(\frac{\partial \Delta \bar{G}}{\partial \phi_j} \right) - q \frac{\Lambda_{\text{Li}^+}^{\text{V}}}{\Omega_{\text{Li}^+}} \nabla V$	Li^+ flux	
$\underline{J}_{\text{TFSI}^-} = - \sum_j \Lambda_{\text{TFSI}^-j}^{\text{th}} \nabla \left(\frac{\partial \Delta \bar{G}}{\partial \phi_j} \right) - q \frac{\Lambda_{\text{TFSI}^-}^{\text{V}}}{\Omega_{\text{TFSI}^-}} \nabla V$	TFSI^- flux	
$\nabla \cdot \left[q \sum_j \left(\frac{\Lambda_{\text{Li}^+j}^{\text{th}}}{\Omega_{\text{Li}^+}} - \frac{\Lambda_{\text{TFSI}^-j}^{\text{th}}}{\Omega_{\text{TFSI}^-}} \right) \nabla \left(\frac{\partial \Delta \bar{G}}{\partial \phi_j} \right) + \sigma \nabla V \right] = 0$ $\sigma = q^2 \left(\frac{\Lambda_{\text{Li}^+}^{\text{V}}}{\Omega_{\text{Li}^+}^2} - \frac{\Lambda_{\text{TFSI}^-}^{\text{V}}}{\Omega_{\text{TFSI}^-}^2} \right)$	Charge conservation	

Note: j stands for the components of the ternary system, Li^+ , TFSI^- , and PEO.

To summarise, the equation system I consists of solving the volume fraction ϕ of the three components (Li^+ , TFSI^- , and PEO) by integrating the volume fraction, the flux, the charge, and the electroneutrality conservation. These four conservation properties are solved in all location and at every time step.

Table IV-5 sums up all the set parameters that were set to describe lithium diffusion from a Li-foil to a polymer electrolyte.

Table IV-5. Set parameters describing lithium diffusion phenomena while applying a constant voltage on the in-plane device at 60° C. Parameters are implemented into the generalised mixing model (GMM).

Material	Set parameters	Numerical value	Unit
Li-foil	Conductivity (σ_{Li-f})	1×10^7	$S \cdot m^{-1}$
Li-foil/polymer electrolyte	Symetric coefficient (α)	0.5	/
polymer electrolyte	Salt concentration (C_{LiTFSI})	1,250	$mol \cdot m^{-3}$
	Lithium self-diffusion coefficient ($D_{Li^+}^p$)	1.6×10^{-12}	$m^2 \cdot s^{-1}$
	LiTFSI volume fraction (ϕ_{LiTFSI})	0.27	/
	PEO volume fraction (ϕ_{PEO})	$1 - \phi_{LiTFSI}$	/
	Effective charge of 6Li or 7Li (Z_{Li})	1	/
	Effective charge of TFSI (Z_{TFSI})	-1	/
	Effective charge of PEO (Z_{PEO})	0	/

All the parameters presented in Table IV-5 were set. They were either set from literature, determined from the experiments or set thanks to the model presented in chapter III. Different combinations of the parameters are not discussed in this report because some parameters depend on the model itself, which can be modified.

Boundary conditions have to be taken into account, such as the Butler-Volmer equation expressed as the following Equation IV-8, [136]

$$i_{BV} = i_0 \cdot \phi_{Li}^{0.5} \cdot \left\{ \exp\left(\alpha \frac{\eta_{Li}}{V_0}\right) - \exp\left[-(1 - \alpha) \frac{\eta_{Li}}{V_0}\right] \right\} \quad IV-8$$

with i_0 (s^{-1}), the Butler-Volmer transfer coefficient, which is similar to the spontaneous transfer frequency (ν) determined in chapter III, α , the charge transfert, $V_0 = \frac{RT}{F}$ (V), an electric potential constant, and $\eta_{Li}(V)$ the activation overpotential defined as the following Equation IV-9,

$$\eta_{Li} = V_s - V \quad IV-9$$

with $V_s(V)$, the calculated electric potential in the lithium foil domain. It is extremely close to the applied potential value, and $V(V)$, the electric potential in the polymer electrolyte.

Lithium dynamics into the lithium foil domain and at the interface with the polymer electrolyte domain are simulated based on the Equation IV-10,

$$\nabla \cdot \sigma_{Li-f} \nabla V_s = 0 \quad \text{IV-10}$$

with $\sigma_{Li-f} (S \cdot m^{-1})$ the conductivity into the lithium metal. In addition of the Butler-Volmer current, a capacitive current (i_{capa}) is also modelled. It is defined as the following Equation IV-11,

$$i_{capa} = Capa \frac{\partial \eta_{Li}}{\partial t} \quad \text{IV-11}$$

with $Capa (F \cdot m^2)$, the electric capacity

The total current at the interface is the sum of the two contributions occurring at the interface. Thus, the measured exchange current at the interface ($i_{interface}$) is expressed as the following Equation IV-12,

$$i_{interface} = i_{BV} + i_{capa} \quad \text{IV-12}$$

The $i_{interface}$ corresponds to the current recorded during a CA sequence.

Set parameters were presented in Table IV-5, whereas parameters that can be adjusted to better fit experimental data are listed in Table IV-6.

Table IV-6. Adjusted parameters describing lithium diffusion phenomena while applying a constant voltage on the in-plane device at 60° C. Parameters are implemented into the general mixing model (GMM).

Material	Adjusted parameters	Numerical value	Unit
Li-foil/Polymer Interface	Exchange current (i_{BV})	21.5	$A \cdot m^{-2}$
	Capacity (Capa)	0.02	$F \cdot m^2$
	Ionic conductivity (σ_p)	0.064	$S \cdot m^{-1}$
polymer electrolyte	PEO self-diffusion coefficient (D_{PEO}^p)	$10^{-6} \times D_{Li^+}^p$	$m^2 \cdot s^{-1}$
	TFSI self-diffusion coefficient ($D_{TFSI^-}^p$)	$\frac{\sigma RT}{F^2 C} - D_{Li^+}^p$	$m^2 \cdot s^{-1}$
	Volume fraction of Li (ϕ_{Li})	0.02	/
	TFSI volume fraction (ϕ_{TFSI})	$0.27 - \phi_{Li}$	/

Notice that parameters related to the Li-foil are all set in the GMM.

Table IV-7 sums up equations allowing to determine the component volume fraction.

Table IV-7. Effective volume parameter Ω_i determination for each component i ($i = Li^+$; TFSI, PEO)

Effective volume parameter	Value	Unit
Ω_{Li}	$\frac{\phi_{Li}}{C_{LiTFSI} \cdot N_A}$	m^3
Ω_{LiTFSI}	$\frac{\phi_{LiTFSI}}{C_{LiTFSI} \cdot N_A}$	m^3
Ω_{PEO}	$10^3 \times \Omega_{Li}$	m^3

The effective volumes are either determined for ϕ_{Li} and ϕ_{LiTFSI} or estimated in the case of the polymer (Table IV-7). They have an effect on the Gibbs free energy density, which is expressed by the following Equation IV-13,

$$\Delta \bar{G} = -T\Delta S + \Delta U \quad \text{IV-13}$$

with ΔS the density entropy variation, defined as the following Equation IV-14,

$$\Delta S = -k_B \left(\frac{\phi_{Li}}{\Omega_{Li}} \ln \phi_{Li} + \frac{\phi_{TFSI}}{\Omega_{TFSI}} \ln \phi_{TFSI} + \frac{\phi_{PEO}}{\Omega_{PEO}} \ln \phi_{PEO} \right) \quad \text{IV-14}$$

with ΔU , the internal energy variation, defined as the following Equation IV-15,

$$\Delta U = \chi_{Li,TFSI} \phi_{Li} \phi_{TFSI} + \chi_{Li,PEO} \phi_{Li} \phi_{PEO} + \chi_{TFSI,PEO} \phi_{PEO} \phi_{TFSI} \quad \text{IV-15}$$

with $\chi_{Li,TFSI}$ ($J \cdot m^{-3}$) the Flory interaction parameters of the internal energy. [137] Their values are defined in Table IV-8.

Table IV-8. Flory interaction parameters of the internal energy $\chi_{i,j}$

Flory interaction parameters	Value	Unit
$\chi_{Li,TFSI}$	$500/\Omega_{PEO}$	$J \cdot m^{-3}$
$\chi_{Li,PEO}$	$2000/\Omega_{PEO}$	$J \cdot m^{-3}$
$\chi_{TFSI,PEO}$	$-2000/\Omega_{PEO}$	$J \cdot m^{-3}$

The estimation of the effective volume parameters can be modified as a function of the Flory interaction parameters of the internal energy (Table IV-8).

Equation IV-14 and Equation IV-15 highlight that the density entropy variation ΔS is weighted by the effective volume parameters, while the internal energy variation ΔU is weighted by the Flory interaction parameters.

To conclude, in order to fit the experimental data, around ten independent parameters have to be tuned and three variables have to be solved such as V_s , the calculated electric potential in the lithium foil domain, V , the electric potential in the polymer electrolyte and ϕ_{Li} , the lithium volume fraction into the polymer electrolyte. Notice that all parameters and variables have a physical meaning.

The GMM is used in the following section to perform numerical simulations that will be compared to experimental results. Parameters listed in Table IV-5 were set and parametric studies allowed to optimise the parameters presented in Table IV-6, Table IV-7, and Table IV-8. The following simulated results were obtained with the specific presented set of parameters.

- Simulated results confronted to the experimental results

EIS results are simulated by applying frequencies between 10^6 and 10^{-6} Hz on a sandwich coin cell composed of a polymer electrolyte between two lithium electrodes (Figure IV-17). This range is wide compared to the experimental one (from 7 MHz to 100 mHz). Results from numerical simulations are compared with experimental data on Figure IV-20.

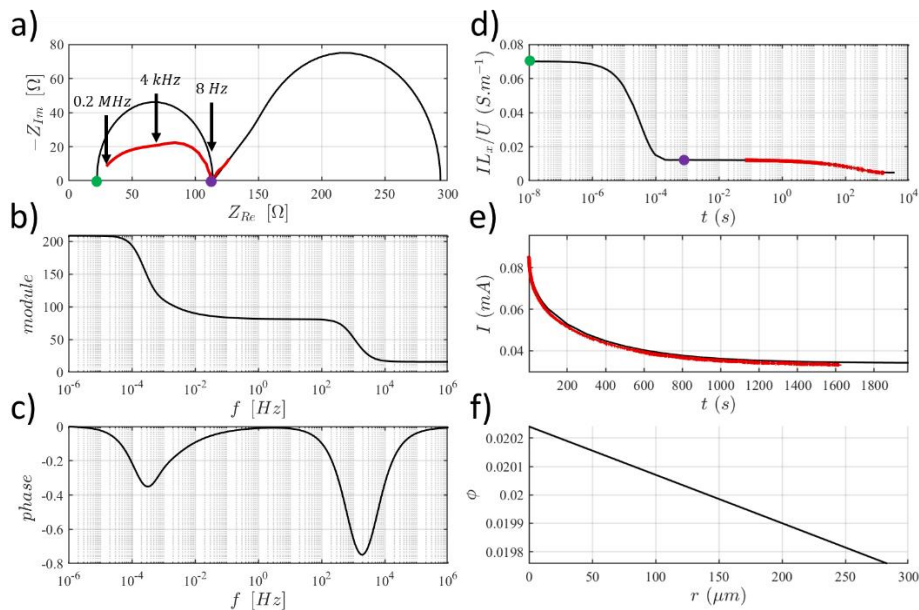


Figure IV-20. a) EIS spectra recorded between 10^6 and 10^{-6} Hz on a polymer electrolyte in between two Li-foils at $60^\circ C$, with b) the corresponding module, and with c) the corresponding phase. d) and e) Current response during the Bruce-Vincent experiment while applying a chronoamperometry (CA) sequence during 30 min, comparison between experimental data (red curves) and simulated results (black curves), f) Lithium gradient into the polymer electrolyte.

On Figure IV-20, the bulk resistance of the polymer electrolyte (R_{el}) and the interface resistance (R_i) can be determined at the green and purple point, respectively (Figure IV-20.a

and Figure IV-20.d). The green and purple points placed on Figure IV-20.a correspond to the two plateaus present on Figure IV-20.d. The Nyquist plot (Figure IV-20.a) provides information on resistances at the high frequency regime, whereas the current profile offers information on diffusion phenomena at the low frequency regime. The module and the phase are plotted on Figure IV-20.b and Figure IV-20.c. A characteristic frequency was measured at 4 kHz experimentally and simulated at 2 kHz in the high frequency regime. Furthermore, Figure IV-20.d allows to compare the evolution of the current response during the Bruce-Vincent experiment. Figure IV-20.f presents the gradient profile of lithium volume fraction. From the EIS the ionic conductivity was set at $6.4 \times 10^{-2}\text{ S} \cdot \text{m}^{-1}$ (cf. green point). The i_{BV} current was set at $21.5\text{ A} \cdot \text{m}^{-2}$ from the CA sequence. The i_0 current is determined from the obtained plateau. The experimental EIS was performed with a lower range of frequencies. Thus, just the beginning of the Warburg diffusion can be seen. Notice that the model well estimates Z_{Re} , whereas other contributions should be added in the model in order to enhance the fitted of Z_{im} .

To conclude, the determined ionic conductivity of the polymer electrolyte, σ_p , and the exchange current, i_0 , are then set in the model describing lithium dynamics through the *in-plane* geometry. A CA sequence was carried out during 72 h by applying a constant voltage of 0.25 V on the *in-plane* geometry (Figure IV-18). The results are presented on Figure IV-21.

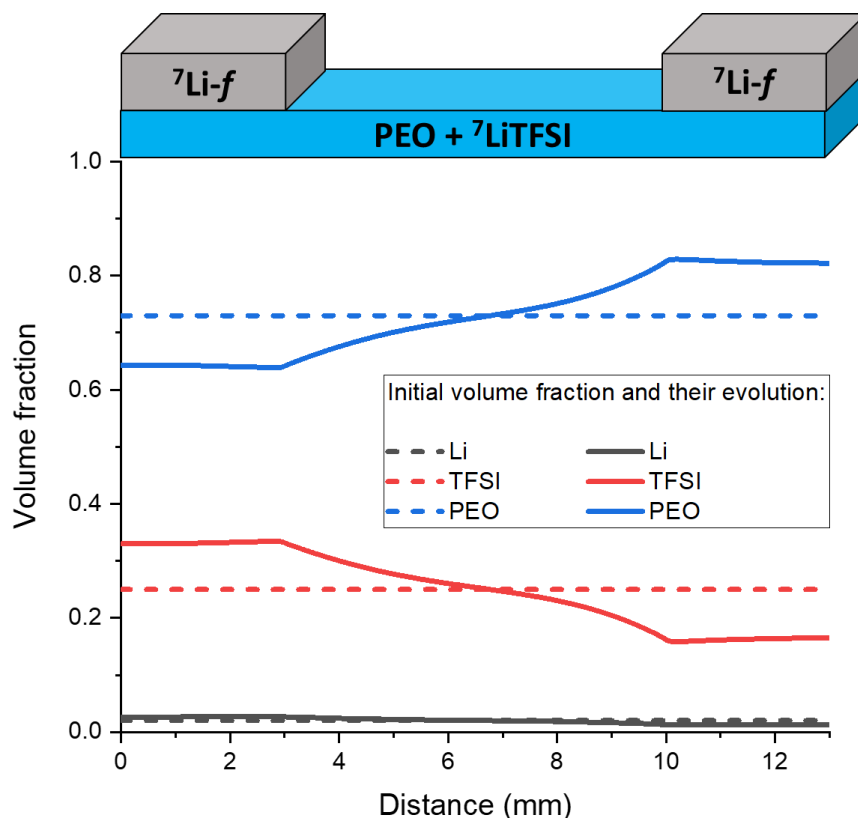


Figure IV-21. Volume fraction distribution into the *in-plane* device after a CA sequence of 72 h . The lithium, TFSI, and PEO volume fraction are represented in black, red and blue, respectively.

A slight increase of lithium concentration occurs under the lithium foil electrically connected to the positive electrode. It induces a higher variation of the PEO and TFSI volume fractions (Figure IV-21). Indeed, as the conservation of the electroneutrality is set (cf.

Table IV-4). Adding lithium into the polymer electrolyte induces TFSI diffusion under the lithium foil, and PEO diffuses in the other direction. Non-negligible variations of the TFSI and PEO volume fraction are simulated. A strength of the GMM is to take into account all components volume fractions which are related one to each other.

Here, lithium dynamics into the *in-plane* device were described with the help of the GMM. The same *in-plane* geometry will be now studied, but as presented on Figure IV-19, the positive ^7Li -electrode is replaced by a ^6Li -electrode. It will allow to carry out lithium isotopic tracing experiments. Therefore, the GMM can no longer be used. An IMM will be used because it can take into account the distinction of lithium isotopes.

c. Use of an isotopic mixing model (IMM)

- Description of the isotopic mixing model (IMM)

The IMM used in the following numerical simulations is based on the thermodynamics of mixing. Here, a quaternary system composed of $^6\text{Li}^+$, $^7\text{Li}^+$, TFSI $^-$, and PEO, is modelled. All the parameters related to lithium ions are duplicated in order to be attributed either to the ^6Li or to the ^7Li isotope.

When lithium ions are separated in two groups, $^6\text{Li}^+$ and $^7\text{Li}^+$, having the same effective volume and charge ($\Omega_{^6\text{Li}^+} = \Omega_{^7\text{Li}^+} = \Omega_{\text{Li}^+}$, $Z_{^6\text{Li}^+} = Z_{^7\text{Li}^+} = Z_{\text{Li}^+}$), the following equation-system II presented in Table IV-9 has to be solved.

Table IV-9. Summary of the equation-system II used into the isotopic mixing model (IMM) and the meaning of each equation.

Equation	Origin	II
$\frac{\partial \phi_{{}^6\text{Li}^+}}{\partial t} = -\underline{\nabla} \cdot \underline{J}_{{}^6\text{Li}^+} + S_{{}^6\text{Li}^+}$	${}^6\text{Li}^+$ continuity equation	
$\frac{\partial \phi_{{}^7\text{Li}^+}}{\partial t} = -\underline{\nabla} \cdot \underline{J}_{{}^7\text{Li}^+} + S_{{}^7\text{Li}^+}$	${}^7\text{Li}^+$ continuity equation	
$\phi_{\text{TFSI}^-} = \frac{\Omega_{\text{TFSI}^-}}{\Omega_{\text{Li}^+}} (\phi_{{}^6\text{Li}^+} + \phi_{{}^7\text{Li}^+})$	Deduced from electroneutrality	
$\phi_{\text{PEO}} = 1 - (\phi_{{}^6\text{Li}^+} + \phi_{{}^7\text{Li}^+}) \left(1 + \frac{\Omega_{\text{TFSI}^-}}{\Omega_{\text{Li}^+}}\right)$	Volume fraction conservation	
$\underline{J}_{{}^6\text{Li}^+} = -\sum_j \Lambda_{{}^6\text{Li}^+j}^{\text{th}} \underline{\nabla} \left(\frac{\partial \Delta \bar{G}}{\partial \phi_j}\right) - q \frac{\Lambda_{{}^6\text{Li}^+}^{\text{V}}}{\Omega_{\text{Li}^+}} \underline{\nabla} V$	${}^6\text{Li}^+$ flux	
$\underline{J}_{{}^7\text{Li}^+} = -\sum_j \Lambda_{{}^7\text{Li}^+j}^{\text{th}} \underline{\nabla} \left(\frac{\partial \Delta \bar{G}}{\partial \phi_j}\right) - q \frac{\Lambda_{{}^7\text{Li}^+}^{\text{V}}}{\Omega_{\text{Li}^+}} \underline{\nabla} V$	${}^7\text{Li}^+$ flux	
$\underline{J}_{\text{TFSI}^-} = -\sum_j \Lambda_{\text{TFSI}^-j}^{\text{th}} \underline{\nabla} \left(\frac{\partial \Delta \bar{G}}{\partial \phi_j}\right) - q \frac{\Lambda_{\text{TFSI}^-}^{\text{V}}}{\Omega_{\text{TFSI}^-}} \underline{\nabla} V$	TFSI ⁻ flux	
$\underline{\nabla} \cdot \left[q \sum_j \left(\frac{\Lambda_{{}^6\text{Li}^+j}^{\text{th}}}{\Omega_{\text{Li}^+}} + \frac{\Lambda_{{}^7\text{Li}^+j}^{\text{th}}}{\Omega_{\text{Li}^+}} - \frac{\Lambda_{\text{TFSI}^-j}^{\text{th}}}{\Omega_{\text{TFSI}^-}} \right) \underline{\nabla} \left(\frac{\partial \Delta \bar{G}}{\partial \phi_j}\right) + \sigma \underline{\nabla} V \right] = 0$ $\sigma = q^2 \left(\frac{\Lambda_{{}^6\text{Li}^+}^{\text{V}}}{\Omega_{\text{Li}^+}^2} + \frac{\Lambda_{{}^7\text{Li}^+}^{\text{V}}}{\Omega_{\text{Li}^+}^2} - \frac{\Lambda_{\text{TFSI}^-}^{\text{V}}}{\Omega_{\text{TFSI}^-}^2} \right)$	Charge conservation	

Note: j stands for the components of the quaternary system, ${}^6\text{Li}^+$, ${}^7\text{Li}^+$, TFSI⁻, and PEO.

In the IMM, parameters are added related to the distinction of the lithium isotope populations. Both lithium self-diffusion into components and lithium exchanges at the interfaces are modelled. ${}^6\text{Li}$ -foil/polymer and polymer/ ${}^7\text{Li}$ -foil interfaces are taken into account. Thus, Butler-Volmer equations are also modified in order to involve the distinction between both lithium isotopes.

A continuity equation in lithium metal is added (Equation IV-16) and the flux of each lithium isotope is considered (Flux equation in Table IV-9), taking into account the theory of mixtures. Table IV-10 sums up all the set parameters that were set to describe lithium isotopic diffusion from a Li-foil to a polymer electrolyte.

Table IV-10. Set parameters describing lithium diffusion while applying a constant voltage on the in-plane device at 60° C. Parameters are implemented into the isotopic mixing model (IMM).

Material	Set parameters	Numerical value	Unit
⁶ Li-foil	Lithium isotopic abundance (% ⁶ Li)	95.4	%
	⁶ Li self-diffusion coefficient (D_{6Li}^f)	10 ⁻¹⁴	m ² · s ⁻¹
	Lithium concentration (C_{Li-f})	76,805	mol · m ⁻³
Polymer electrolyte	⁶ Li isotopic abundance (% ⁶ Li)	7.6	%
⁷ Li-foil	⁶ Li isotopic abundance (% ⁶ Li)	7.6	%
	⁶ Li self-diffusion coefficient (D_{6Li}^f)	10 ⁻¹⁴	m ² · s ⁻¹
	Lithium concentration (C_{Li-f})	76,805	mol · m ⁻³

As presented in chapter III, it is now necessary to consider the lithium isotopic mixture in materials. The GMM is upgraded to model an isotopic mixture system by following the mathematics of mixture thermodynamics (Equation IV-16 and Equation IV-17), based on the resolution of the Gibbs energy density of the mixture.

$$\frac{\partial \phi_{6Li,m}}{\partial t} = -\underline{\nabla} \cdot \underline{J}_{6Li,m} + S_{6Li,m} \quad \text{IV-16}$$

$$\underline{J}_{6Li,m} = -\Lambda \underline{\nabla} \left(\frac{\partial G}{\partial \phi_{6Li,m}} \right) \quad \text{IV-17}$$

Lithium isotopic distinction has also an effect on the Gibbs free energy density. Its expressed as previously detail in Equation IV-13. In the IMM, the density entropy variation (ΔS) is defined as the following Equation IV-18,

$$\Delta S = -k_B \left(\frac{\phi_{6Li^+}}{\Omega_{6Li^+}} \ln \phi_{6Li^+} + \frac{\phi_{7Li^+}}{\Omega_{7Li^+}} \ln \phi_{7Li^+} + \frac{\phi_{TFSI}}{\Omega_{TFSI}} \ln \phi_{TFSI} + \frac{\phi_{PEO}}{\Omega_{PEO}} \ln \phi_{PEO} \right) \quad \text{IV-18}$$

And the internal energy variation (ΔU) is defined as the following Equation IV-19,

$$\begin{aligned} \Delta U = & \chi_{6Li^+,TFSI} \phi_{6Li^+} \phi_{TFSI} + \chi_{6Li^+,PEO} \phi_{6Li^+} \phi_{PEO} \\ & + \chi_{7Li^+,TFSI} \phi_{7Li^+} \phi_{TFSI} + \chi_{7Li^+,PEO} \phi_{7Li^+} \phi_{PEO} + \chi_{TFSI,PEO} \phi_{PEO} \phi_{TFSI} \\ & + \chi_{6Li^+,7Li^+} \phi_{6Li^+} \phi_{7Li^+} + \chi_{7Li^+,6Li^+} \phi_{7Li^+} \phi_{6Li^+} \end{aligned} \quad \text{IV-19}$$

Notice that additional Flory interaction parameters appear due to lithium isotope distinction, but equalities are mentioned in Table IV-11.

Table IV-11. Flory interaction parameters of the internal energy.

Flory interaction parameters	Value	Unit
$\chi_{{}^6\text{Li}^+, {}^7\text{Li}^+} = \chi_{{}^7\text{Li}^+, {}^6\text{Li}^+}$	0	$J \cdot m^{-3}$
$\chi_{{}^6\text{Li}^+, TFSI} = \chi_{{}^7\text{Li}^+, TFSI}$	$500/\Omega_{PEO}$	$J \cdot m^{-3}$
$\chi_{{}^6\text{Li}^+, PEO} = \chi_{{}^7\text{Li}^+, PEO}$	$2000/\Omega_{PEO}$	$J \cdot m^{-3}$
$\chi_{TFSI, PEO}$	$-2000/\Omega_{PEO}$	$J \cdot m^{-3}$

Boundary conditions are duplicated in the case of lithium isotopic labelling have to be taken into account. The Butler-Volmer equations applied at the Li-foil/polymer electrolyte were decomposed as presented in the following Equation IV-20 and Equation IV-21,

$$i_{BV, {}^6\text{Li}} = i_0 \left\{ \phi_{{}^6\text{Li}, m} \phi_{{}^7\text{Li}} \exp\left(\alpha \frac{\eta_{\text{Li}}}{V_0}\right) - \phi_{{}^6\text{Li}} \phi_{{}^7\text{Li}, m} \exp\left[-(1 - \alpha) \frac{\eta_{\text{Li}}}{V_0}\right] \right\} \quad \text{IV-20}$$

$$i_{BV, {}^7\text{Li}} = i_0 \left\{ \phi_{{}^6\text{Li}} \phi_{{}^7\text{Li}, m} \exp\left(\alpha \frac{\eta_{\text{Li}}}{V_0}\right) - \phi_{{}^6\text{Li}, m} \phi_{{}^7\text{Li}} \exp\left[-(1 - \alpha) \frac{\eta_{\text{Li}}}{V_0}\right] \right\} \quad \text{IV-21}$$

Thus, the global i_{BV} is expressed by the following Equation IV-22,

$$i_{BV} = i_{BV, {}^6\text{Li}} + i_{BV, {}^7\text{Li}} \quad \text{IV-22}$$

According to Equations IV-20, IV-21 and IV-22, the final expression of the exchange current at the interface i_{BV} is expressed by the following Equation IV-23,

$$i_{BV} = i_0 \left(\phi_{{}^6\text{Li}, m} \phi_{{}^7\text{Li}} + \phi_{{}^6\text{Li}} \phi_{{}^7\text{Li}, m} \right) \left\{ \exp\left(\alpha \frac{\eta_{\text{Li}}}{V_0}\right) - \exp\left[-(1 - \alpha) \frac{\eta_{\text{Li}}}{V_0}\right] \right\} \quad \text{IV-23}$$

Notice that if η_{Li} is null, the i_{BV} is null. Thus, formula would be equivalent to the model described in chapter III, where lithium dynamics are studied without applying any electrical stress. Indeed, a general case is presented here, whereas in chapter III a simplified case was modelled assuming low lithium concentrations.

Notice that a strength of the IMM is that there are obviously new parameters, but most of them are set from literature or from the experimental data. Furthermore, the previously tuned parameters obtained with the GMM were set identical in the IMM.

To conclude, in order to fit the experimental data five variables have to be solved such as V_s , V , both lithium isotopes volume fractions into the polymer electrolyte $\phi_{6Li^+}^p$ and $\phi_{7Li^+}^p$, and only the ${}^6Li^+$ volume fraction into the lithium foil, ϕ_{6Li}^f . The ϕ_{7Li}^f depends on ϕ_{6Li}^f ($\phi_{7Li}^f = 1 - \phi_{6Li}^f$ in the Li-foils).

The IMM is used in the following section to perform numerical simulations that will be compared to experimental results. Parameters used into the GMM are involved. However, some of them have been adjusted according to Table IV-9, Table IV-10 and Table IV-11. The following simulated results were obtained with the specific mentioned set of parameters.

- Simulated results confronted to the experimental results

Numerical simulations are run with the new IMM. Figure IV-22 compares lithium volume fraction variations into the polymer electrolyte according to the used model, and at various times.

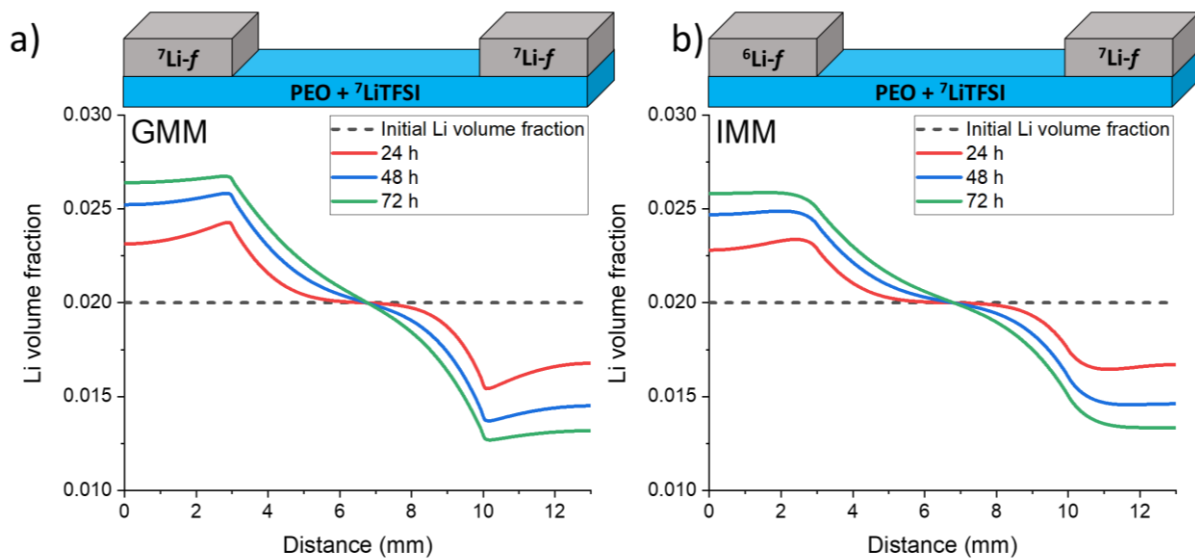


Figure IV-22. Simulated lithium volume fraction variations into the polymer electrolyte after applying a CA sequence of 24 h (red), 48 h (blue) and 72 h (green) by using either the GMM (a) or by using the IMM (b).

On Figure IV-22, the initial lithium volume fraction is represented by the dotted black line at 0.020. Figure IV-22.a presents intermediate results. Before involving isotopic tracing, the GMM was tested. A lithium gradient can be observed into the polymer electrolyte. In addition, the amount of lithium added into the system increases with the CA sequence time because of lithium exchange dynamics. Then, the same numerical simulations were run with the IMM. Both models led to the same lithium volume fraction variation trends. The IMM provides softer lithium volume fraction variations. It may be due to the way that Butler-Volmer

equations are written. It was confirmed that model modifications between the GMM and the IMM do not affect the final results. Thus, more detailed studies are conducting on the simulated results obtained by the IMM, which is able to distinguishing ^6Li and ^7Li isotopes.

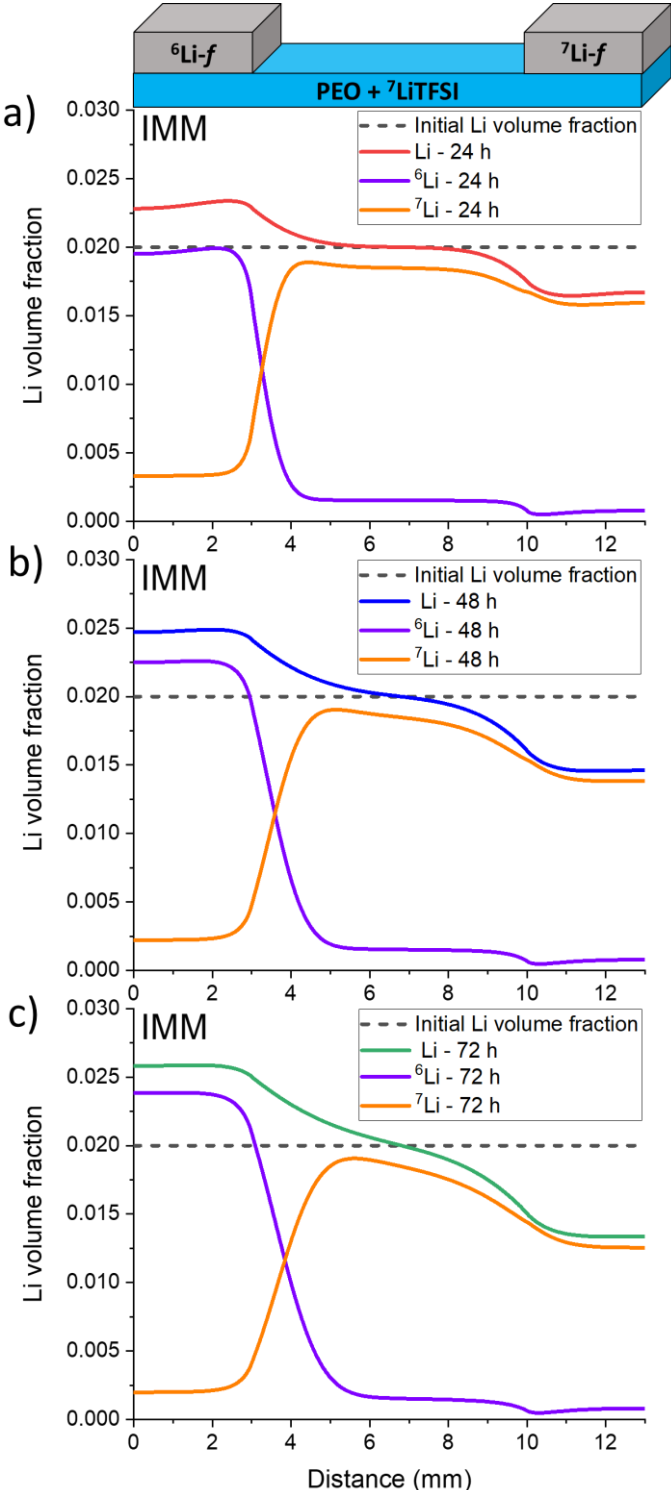


Figure IV-23. Lithium isotopic volume fraction variations into the polymer electrolyte contained in the in-plane device after applying a constant voltage of 0.25 V during a) 24 h, b) 48 h, and c) 72 h. ^6Li volume fraction variation corresponds to the purple curves and ^7Li volume fraction variation corresponds to the orange curves.

The following Equation IV-24 was applied to determine ${}^6\text{Li}$ abundance ($\%{}^6\text{Li}$) from the lithium isotopic volume fraction.

$$\%{}^6\text{Li} = \frac{\phi_{{}^6\text{Li}}}{\phi_{{}^6\text{Li}} + \phi_{{}^7\text{Li}}} \quad \text{IV-24}$$

Therefore, simulated results can be compared with ToF-SIMS results. Indeed, the lithium isotopic abundance profiles along the polymer electrolyte are presented on Figure IV-24.

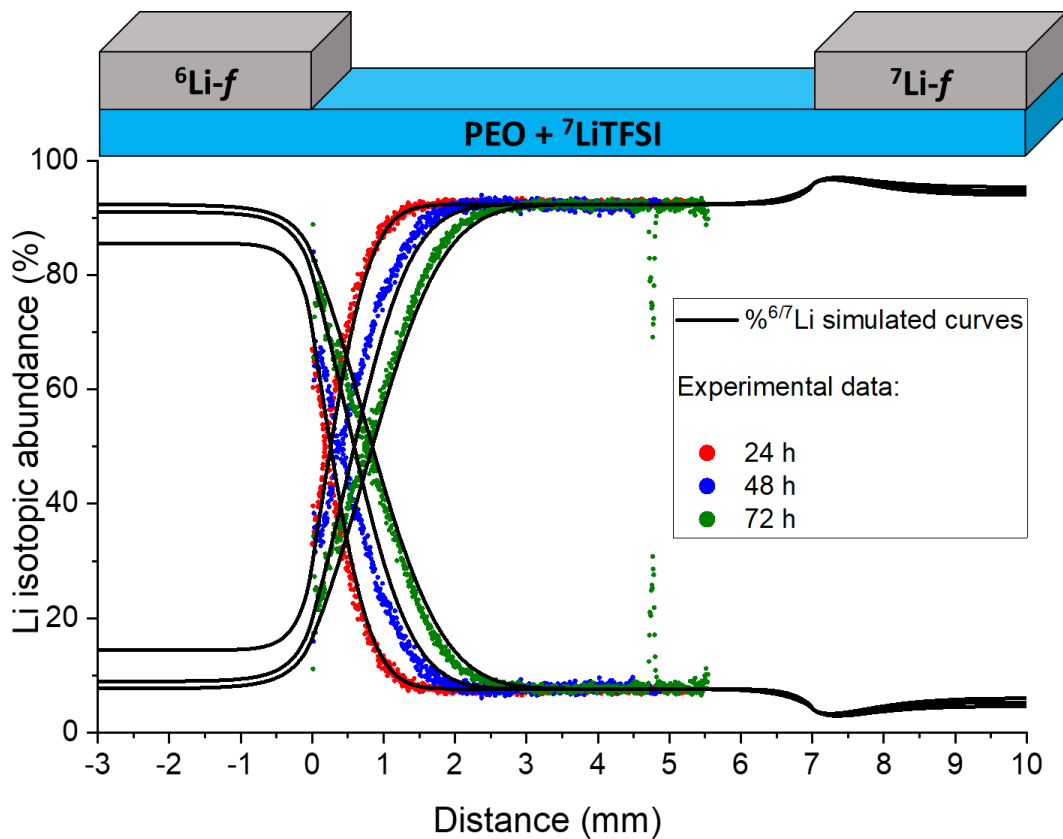


Figure IV-24. Comparison of lithium isotopic abundance profiles after applying a constant voltage of 0.25 V at 60 °C on a polymer electrolyte determined by ToF-SIMS (coloured dotted curves) and simulated (solid black curves) at three various contact times of 24 h, 48 h, and 72 h. Each analysis was performed on different samples.

First lithium dynamics simulated are presented on Figure IV-24. They were obtained after applying a constant voltage of 0.25 V at 60 °C on a polymer electrolyte. Simulated curves correspond to the solid black curves at three various contact times of 24 h, 48 h, and 72 h. They can be compared to ToF-SIMS results (coloured dotted curves). Experimental data and simulated results match with the selected set of parameters used in the IMM. Therefore, the using isotopic Butler-Volmer equations seem to be adequate.

A strength of the model is to provide information of lithium behaviour under the Li-foils. The ${}^6\text{Li}$ abundance increases under the ${}^6\text{Li}$ -foil while the CA sequence time also increases. Furthermore, a local ${}^7\text{Li}$ enrichment occurs just under the ${}^7\text{Li}$ -foil. It may be explained by ${}^7\text{Li}$ plating on the lithium negative electrode (${}^7\text{Li}$ -foil). On Figure IV-23, it was observed that under the ${}^7\text{Li}$ -foil both lithium isotopes concentrations decrease. According to Equation IV-24 a small variation of the ${}^6\text{Li}$ volume has a huge impact of the estimated ${}^6\text{Li}$ abundance. This prediction could be investigated experimentally.

As previously mentioned in section 1.3, reference samples were only stored at 60°C during various times. Thus, only spontaneous lithium exchanges were simulated by setting the external applied voltage at 0 V in the IMM. Results are presented on Figure IV-25.

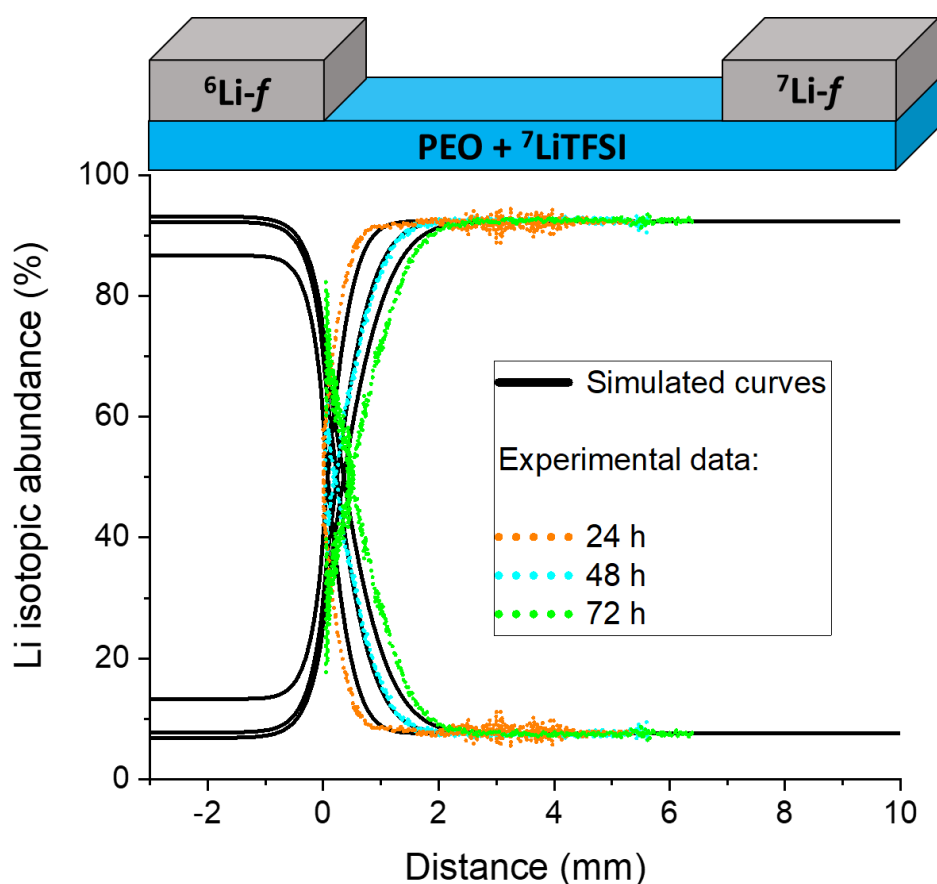


Figure IV-25. Comparison of lithium isotopic abundance profiles at 60°C on a polymer electrolyte determined by ToF-SIMS (coloured dotted curves) and simulated (solid black curves) at three various contact times of 24 h, 48 h, and 72 h. Each analysis was performed on different samples.

On Figure IV-25, the experimental and simulated results after storing the *in-plane* device 48 h at 60°C are identical. However, the obtained results after 24 h and 72 h differ. This shift was investigated on Figure IV-26.

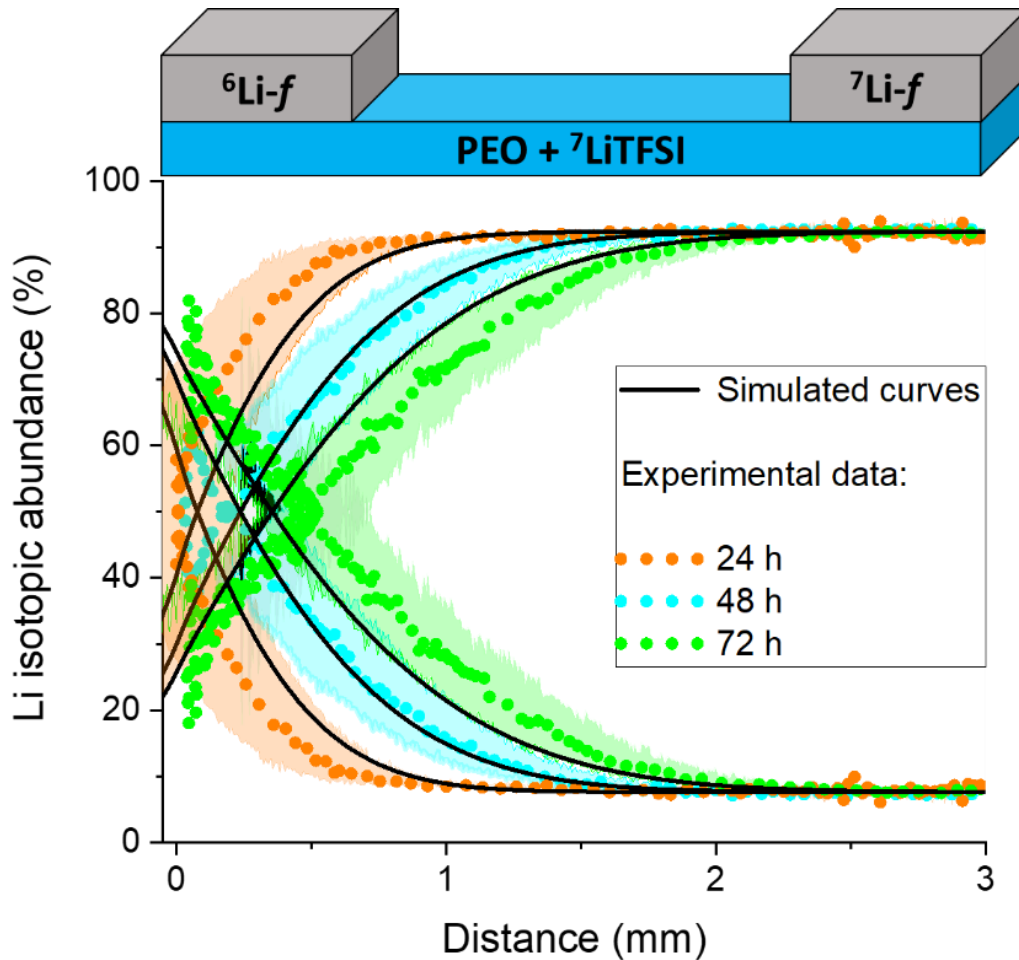


Figure IV-26. Enlargement of Figure IV-25 from 0 to 3 mm. The effect of a 0.2 mm lateral shift on the ${}^6\text{Li}$ -foil position is represented by the coloured areas.

On Figure IV-26 an enlargement of Figure IV-25 from 0 to 3 mm is presented. It illustrates the effect of a 0.2 mm lateral shift on the ${}^6\text{Li}$ -foil position. Such low difference may explain the observed lithium isotopic abundance variations. The geometry parameters are crucial. An error of 0.2 mm leads to significant variations regarding lithium isotopic abundance (Figure IV-26).

Variations between numerical simulations and experimental results on Figure IV-24 may be explained by the simulated current response while applying a constant voltage of 0.25 V (Figure IV-27).

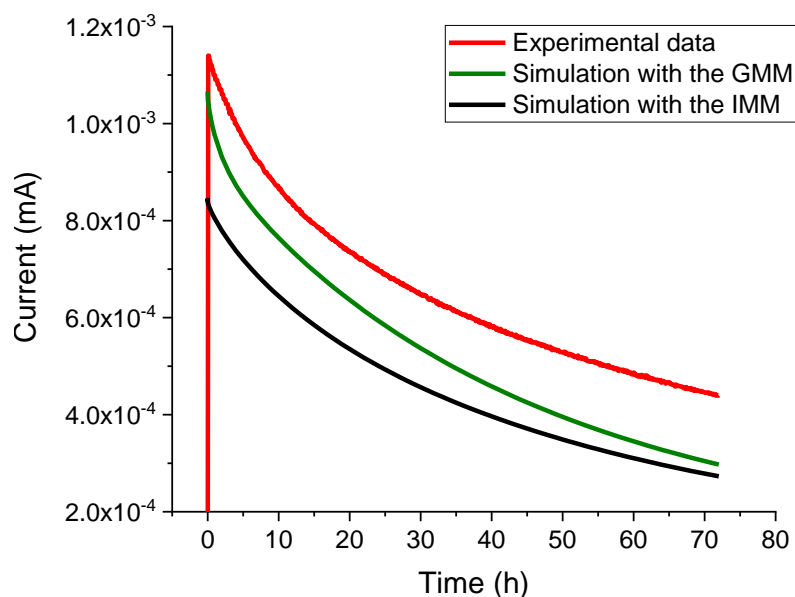


Figure IV-27. Resulting current profiles while applying a constant voltage of 0.25 V on the *in-plane* device during 72 h: current profile obtained experimentally (red curve), current profile simulated by the GMM (green curve), and current profile simulated by the IMM (black curve).

On Figure IV-27, the resulting current profile obtained while applying a constant voltage of 0.25 V on the *in-plane* device during 72 h is represented in red. Both GMM and IMM were used to simulate the current profile. They are represented in green and in black, respectively. The current response has the same trend. However, the initial measured current is 100 nA or 300 nA higher than the initial simulated current with the GMM or the IMM, respectively. Therefore, parameters set in the IMM can be discussed and may be adjusted to enhance the current response fit as well as the ToF-SIMS fits.

Furthermore, the *in-plane* geometry induces curved electric field lines, which are difficult to accurately model (Figure IV-28).



Figure IV-28. Schematic of the electric field lines simulated into the polymer electrolyte of the *in-plane* configuration.

Another explanation of differences between the experiments and the model was found in literature. In our work, we assumed that lithium diffusion coefficient into the polymer electrolyte is the same whatever the geometry studied. However, Jeanne-Brou *et al.* demonstrated that the ionic conductivity of a polymer electrolyte composed of PEO and LiTFSI can differ according to the diffusion direction studied. [135] In other words, lithium diffusion coefficient may be different in a *through-plane* geometry (corresponding to a *sandwich* system) compared to an *in-plane* geometry. Jeanne-Brou *et al.* determined an anisotropic

conductivity ratio of 1.8 corresponding to an *in-plane* and a *through-plane* conductivity of $1.0 \times 10^{-3} \text{ S} \cdot \text{cm}^{-1}$ and $5.7 \times 10^{-4} \text{ S} \cdot \text{cm}^{-1}$, respectively. [135] Thus, the lithium self-diffusion coefficient may also be tuned.

Finally, the applied pressure on the devices may affect contacts at the interface and thus the quality of lithium exchanges between materials. The applied pressure value might also influence lithium dynamics and lithium ionic conductivity.

An alternative set of parameters can be investigated in order to accurately fit the obtained current profiles while maintaining correct fittings of the ToF-SIMS results. Parameters such D_{TFSI} , Flory interaction parameters (χ) as well as the polymer electrolyte properties can be modified. Furthermore, the lithium salt concentration of 1.25 M may also be adjusted. Indeed, it was estimated by weighing masses. Thus, an uncertainty should be attributed. Furthermore, if a part of lithium is blocked into section of the polymer electrolyte or non-solvated, it may affect the final results because in the model all lithium ions are moving. The choice of the parameters presented in Table IV-5 and in Table IV-10 can be improved. Therefore, it could provide another valid set of parameters leading to better fit of both current profile and ToF-SIMS profile. Initial lithium salt and volume fractions will for instance influence the determination of the other parameters.

Lithium dynamics were studied in detail at the interface between a Li-foil and a polymer electrolyte. ToF-SIMS characterisations, high-resolution ssNMR characterisations and even modelling were used to investigate lithium exchanges between materials. The same methodologies will be applied on another configuration in order to understand lithium dynamics at the interface between a polymer electrolyte layer and an ionic conductive ceramic pellet. A configuration called *sandwich* is investigated in the following section.

IV.2. Lithium dynamics through the *sandwich* device under electrical current

2.1. Description of the *sandwich* device

The *sandwich* device is composed of an ionic conductive ceramic pellet in-between two polymer electrolyte layers. It is schematised on Figure IV-29. As described in chapter II, the used $\text{Li}_{6.4}\text{La}_3\text{Zr}_{1.4}\text{Ta}_{0.6}\text{O}_{12}$ (Ta-doped LLZO, LLZTO) ceramic pellet was commercially available, and the polymer electrolyte was prepared with a lithium salt at lithium natural isotopic abundance. Disks with a diameter of 14 mm were punched in the polymer electrolyte. Disks of a ^6Li -foil and a ^7Li -foil were used as positive and negative electrode, respectively. The goal of such design is to facilitate lithium behaviour characterisations at the interface between a polymer electrolyte layer and a ceramic pellet.

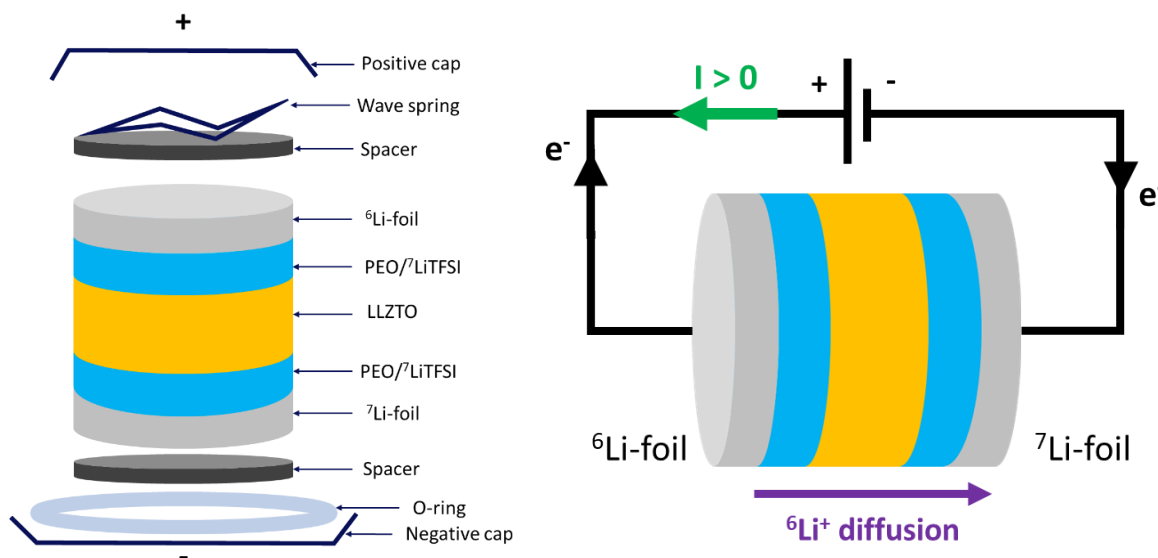


Figure IV-29. Schematic of the sandwich device composed of a ceramic pellet in-between two layers of polymer electrolyte assembled in a coin cell. A ${}^6\text{Li}$ -foil and a ${}^7\text{Li}$ -foil were placed on both sides of the sandwich, forcing ${}^6\text{Li}^+$ ions to flow through all the layers of the SSE. The green arrow indicates the current direction and the purple arrow indicates the ${}^6\text{Li}^+$ ions migration direction.

Coin cells were assembled in a dry room. Components required to assemble a coin cell are mentioned on Figure IV-29. Coin cells were sealed in a glovebox under argon atmosphere. The applied pressure was about 1 bar. The ceramic pellet and the polymer electrolyte thickness of each device S1, S2 and S3 are mentioned in Table IV-12.

Table IV-12. Thickness of the polymer electrolyte layers (${}^6\text{Li}$ side and ${}^7\text{Li}$ side) and the ceramic pellet as a function of the studied device. Test conditions (current density and test time) are indicated.

Device n°	PEO/LiTFSI ${}^6\text{Li}$ side (μm)	LLZTO (μm)	PEO/LiTFSI ${}^7\text{Li}$ side (μm)	Current density ($\mu\text{A} \cdot \text{cm}^{-2}$)	Test time at 60°C (h)
S1	96	731	101	50	48
S2	101	741	80	50	86
S3	62	738	62	39	90

Thickness values presented in Table IV-12 will be taken into account to estimate the ionic conductivity of a sandwich device. They will also be used to model lithium dynamics in such device.

2.2. Electrochemical results

a. Electrochemical impedance spectroscopy (EIS) characterisation

Here, the distance between the two lithium foils (d) is determined by the following Equation IV-25,

$$d = t_{\text{polymer-}^6\text{Li side}} + t_{\text{ceramic}} + t_{\text{polymer-}^7\text{Li side}} \quad \text{IV-25}$$

with t_i (μm), the thickness of the layer i . d was estimated at 928 and 922 μm for $S1$ and $S2$, respectively. EIS measurements were performed at 60° C before applying any electrochemical tests (Figure IV-30).

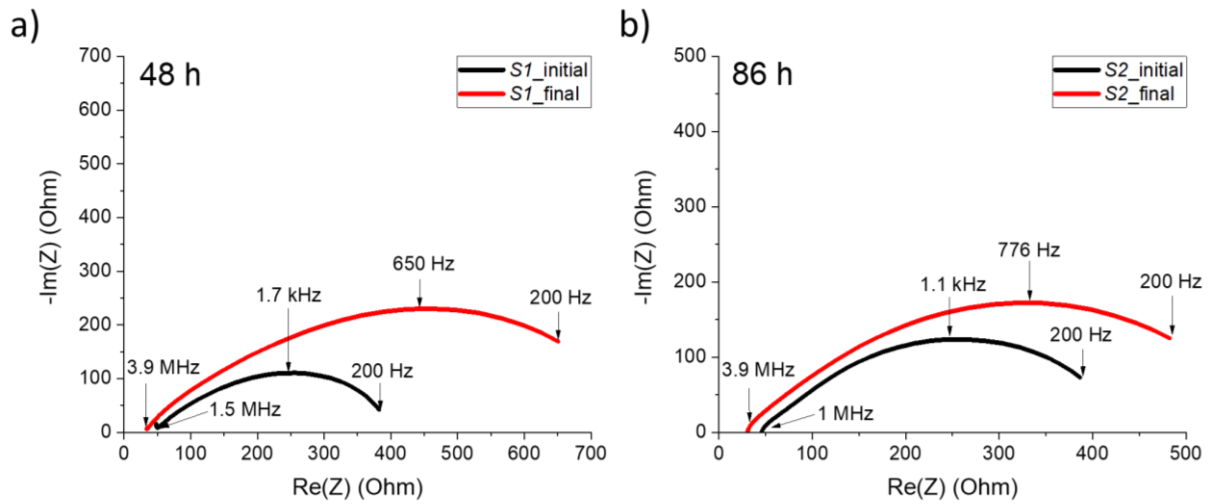


Figure IV-30. Nyquist plots obtained by performing EIS on $S1$ (a) and on $S2$ (b) before (black curves) and after (red curves) applying a constant current density of $50 \mu\text{A} \cdot \text{cm}^2$ during either 48 h (a) or 86 h (b).

After applying the first EIS (black curves), the resistances were estimated at 46 ± 3 and $34 \pm 3 \Omega$ for $S1$ (Figure IV-30.a) and $S2$ (Figure IV-30.b), respectively. From these resistances and the various thicknesses reported in Table IV-12, the ionic conductivities of $S1$ and $S2$ were estimated at 1.3×10^{-3} and $1.7 \times 10^{-3} \text{ S} \cdot \text{cm}^{-1}$ at 60° C, respectively. They are higher than the one estimated for the pure PEO assembled in the same configuration ($6.5 \times 10^{-4} \text{ S} \cdot \text{cm}^{-1}$). The ionic conductivity enhancement is due the ceramic pellet integration.

An EIS experiment was also performed at 60° C after applying a current density of $50 \mu\text{A} \cdot \text{cm}^{-2}$ on both devices (red curve). The resistance was estimated at 31 ± 3 and $27 \pm 3 \Omega$ for $S1$ (Figure IV-30.a) and $S2$ (Figure IV-30.b), respectively. Thus, ionic conductivities of $2.0 \times 10^{-3} \text{ S} \cdot \text{cm}^{-1}$ and $2.3 \times 10^{-3} \text{ S} \cdot \text{cm}^{-1}$ were estimated for $S1$ and $S2$, respectively. The determination of the electrical equivalent circuit of each device is presented in Appendix A-IV-2. *Determination of the electrical equivalent circuit of each device.*

b. A chronopotentiometry (CP) sequence

After the initial EIS, a chronopotentiometry (CP) sequence with a constant current density of $50 \mu\text{A} \cdot \text{cm}^{-2}$ was applied on S1 and S2 during either 48 h (Figure IV-31) or 86 h (Figure IV-32). The CP sequence was performed at 60°C . The time effect affects the amount of exchanged lithium.

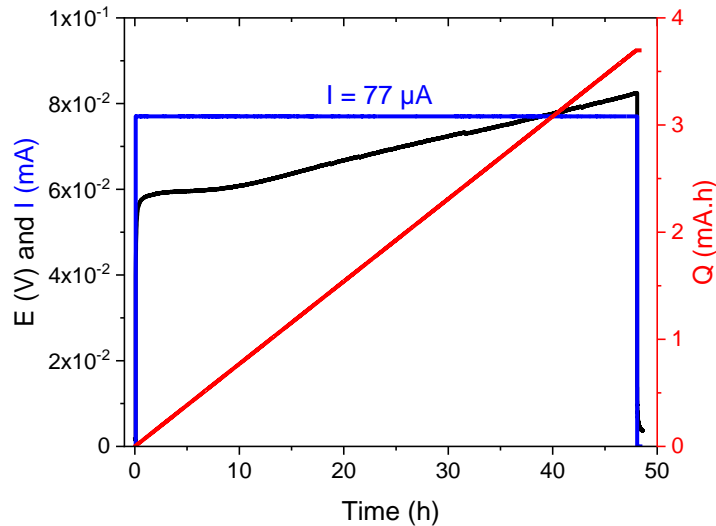


Figure IV-31. Evolution of the voltage as a function of time (black line) due to the applied electrical stress (CP with $I = 77 \mu\text{A}$, blue line) during 48 h on the sandwich device. The specific capacity was determined as a function of time (red line).

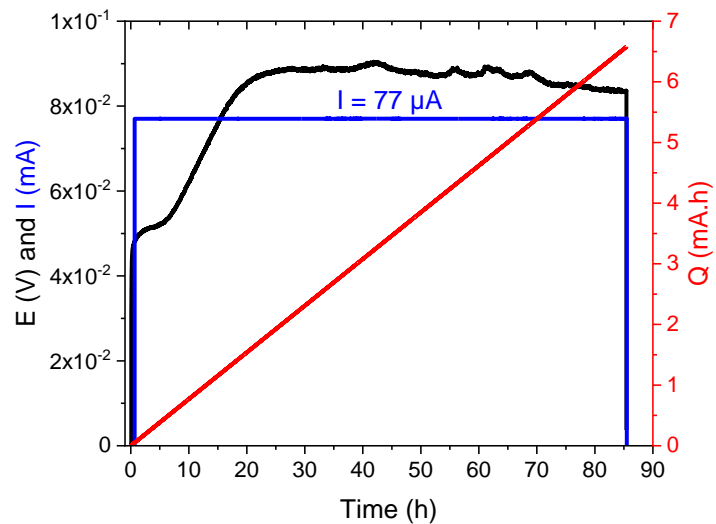


Figure IV-32. Evolution of the voltage as a function of time (black line) due to the applied in electrical stress (CP with $I = 77 \mu\text{A}$, blue line) during 86 h on the sandwich device. The specific capacity was determined as a function of time (red line).

On Figure IV-31 and Figure IV-32, the application of a constant current (I) is represented by the blue crenel. The evolution of the voltage (E) is recorded as a function of time (black curve), and the specific capacity (Q) is determined (red line). As the current is

constant, the evolution of Q is linear. A constant current of $77 \mu A$ was applied in order to control the current density during the entire chronopotentiometry sequence. Regarding the surface of 1.5 cm^2 , it corresponds to a current density of $50 \mu A \cdot \text{cm}^{-2}$. The specific capacity measured electrochemically provides a first estimation of the amount of exchanged lithium. Specific capacities of 3.7 and $6.6 \text{ mA} \cdot \text{h}$ were determined after a CP sequence of 48 h and 86 h , respectively.

2.3. Advanced characterisations based on lithium isotopic tracing

a. ToF-SIMS characterisations

The main challenge was to gain access to the buried interfaces. *Sandwich* devices were taken out of coin cells by using a coin cell disassembling tool (from Hohsen®) in a glovebox.

The various interfaces were characterised by performing ToF-SIMS two-dimensional measurements. To ensure their accessibility, Li-foils and polymer electrolytes were successively removed manually from the *sandwich* device (Figure IV-33).

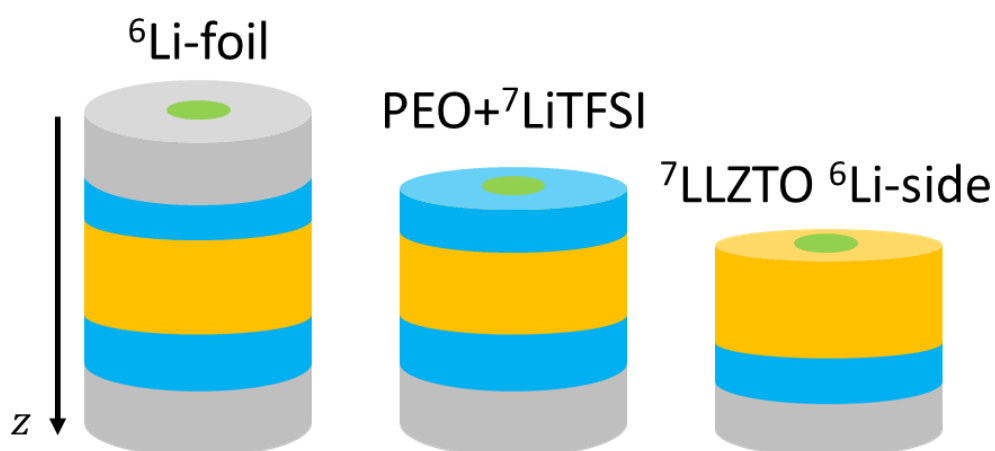


Figure IV-33. *Sandwich* device preparation for ToF-SIMS characterisation of each interface. Green areas represent the analysed surface.


As few micrometres of the polymer electrolytes were stuck on the Li-foils, the z coordinate of the analysis could not be properly estimated. The z coordinate corresponds to the position along the axis between both lithium electrodes. Then, the polymer electrolytes were analysed by ToF SIMS on both sides of the ceramic after peeling and scraping. Thus, lithium isotopic abundances could be determined at the various *sandwich* interfaces. Green areas on Figure IV-33 stand for the characterised surfaces.

As described in chapter I, three-dimensional ToF-SIMS analyses can be performed. However, sputtering materials without inducing any additional degradation is slow.

Furthermore, artefacts such as peak slitting can appear on the mass spectrum by sputtering deeply into such materials. If the distance from the sample surface to the analyser increases more than $20\ \mu\text{m}$ during the analysis, the same molecular fragments will take more time to reach the detector as the distance has increased. Thus, the detector will detect them as heavier molecular fragments. ToF-SIMS technique is not dedicated to sputter thick materials. Table IV-13 confronts ToF-SIMS results of both *sandwich* devices, *S1* and *S2*.

Table IV-13. ToF-SIMS estimations of ${}^6\text{Li}$ abundances of both Li-foils and at the four interfaces of a sandwich device after applying a constant current density of $50\ \mu\text{A} \cdot \text{cm}^{-2}$ during either 48 h (*S1*) or 86 h (*S2*).

Material	% ${}^6\text{Li}$ estimated by ToF-SIMS (%)	
	<i>S1</i> (48 h)	<i>S2</i> (86 h)
${}^6\text{Li}$ -foil	95.4 ± 1	95.4 ± 1
P_1 : PEO+ ${}^7\text{LiTFSI}$	65 ± 1	82 ± 1
LLZTO - ${}^6\text{Li}$ side	24 ± 1	53 ± 1
LLZTO ${}^7\text{Li}$ side	10 ± 1	23 ± 1
P_2 : PEO+ ${}^7\text{LiTFSI}$	9 ± 1	15 ± 1
${}^7\text{Li}$ -foil	7.8 ± 1	7.8 ± 1



Firstly, ${}^6\text{Li}$ abundance of both Li-foils were determined at 7.8 and 95.4% (Table IV-13). These values are in agreement with the provided information by the supplier (7.6 and 95.4% of ${}^6\text{Li}$, respectively).

The surface of the polymer electrolyte under the ${}^6\text{Li}$ -foil (P_1) of *S1* was enriched at 65% of ${}^6\text{Li}$. The top of the ceramic (LLZTO- ${}^6\text{Li}$ side) was enriched at 24% of ${}^6\text{Li}$, while the bottom of the ceramic (LLZTO- ${}^7\text{Li}$ side) was enriched at 10% of ${}^6\text{Li}$. These new results confirm that lithium can migrate from the polymer electrolyte to the ceramic pellet. Finally, the surface of the polymer electrolyte under the ${}^7\text{Li}$ -foil (P_2) of *S1* was also enriched at 9% in ${}^6\text{Li}$. Thus, it demonstrates that ${}^6\text{Li}^+$ ions migrate through the whole device. Furthermore, the ${}^6\text{Li}$ abundance decreases along the z axis, from the ${}^6\text{Li}$ -foil to the ${}^7\text{Li}$ -foil. The same conclusion was obtained by characterising *S2*. Higher enrichments in ${}^6\text{Li}$ were expected because more lithium amount was exchanged according the charged capacity. The surface of the polymer electrolyte under the ${}^6\text{Li}$ -foil was enriched at 82% of ${}^6\text{Li}$. The top of the ceramic (LLZTO- ${}^6\text{Li}$ side) was enriched at 53% of ${}^6\text{Li}$, while the bottom of the ceramic (LLZTO- ${}^7\text{Li}$ side) was enriched at 23% of ${}^6\text{Li}$. Finally, the surface of the polymer electrolyte under the ${}^7\text{Li}$ -foil was also enriched at 15% in ${}^6\text{Li}$. To conclude, ${}^6\text{Li}$ abundance increases with the specific capacity and lithium was able to cross all layers in such *sandwich* device.

Having access to lithium isotopic abundance variations inside each layer would be an additional key information. Figure IV-34 presents pictures of a sample holder on which *sandwich* cross sections of *sandwich* devices are stuck vertically. Cross sections were obtained by manually breaking the *sandwich* devices.

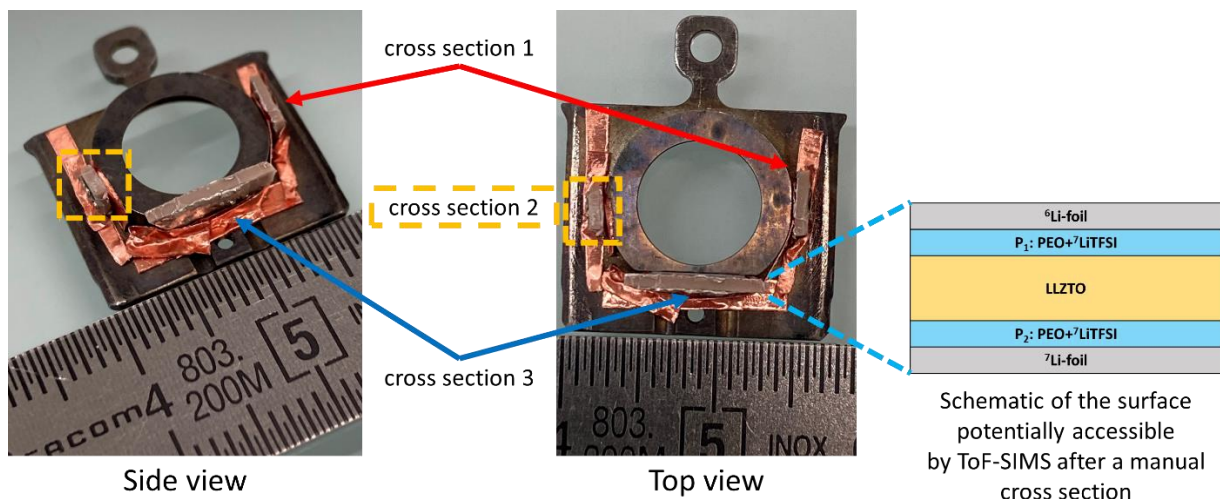


Figure IV-34. Pictures of sandwich cross sections placed on the used sample holder.

The flattest cross sections were selected to be characterised. They were vertically attached to a specific sample holder, which allows the use of an airtight suitcase to protect samples during transfers from the dry room to the analysis chamber of the spectrometer. The positioning of the cross section was crucial because non-planar surface is prone to characterisation artefacts. There is room for enhancement of the setup presented on Figure IV-34. Indeed, obtaining planar surfaces was difficult. An optimised sample holder should allow to easily stick samples in vertical position. Figure IV-35 illustrates the first results.

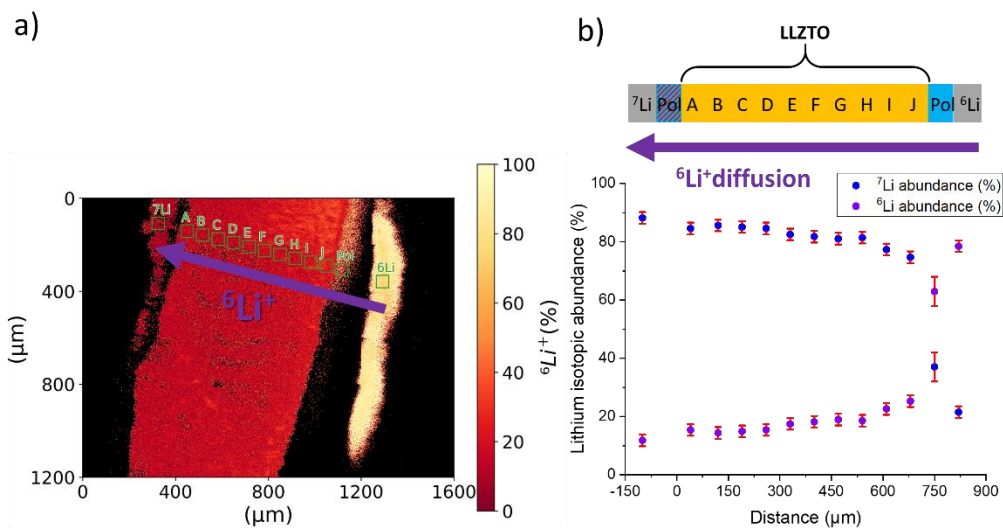


Figure IV-35. ToF-SIMS characterisation of lithium isotopic abundances along the scanned axis of a cross section of S3 after applying a constant current density of $39 \mu A \cdot cm^{-2}$ during 90 h at $60^\circ C$: a) 6Li abundance mapping on the cross section b) Average of 6Li abundance determination in each selected area. Uncertainties were estimated at 2%.

On Figure IV-35, the image was obtained by determining 6Li abundance in each pixel. Data were processed by using a specifically developed Python code. According to the analysed axis, the 7Li -foil and the 6Li -foil have a 6Li abundance of 9.7 and 84.2%, respectively, after applying a constant current density of $39 \mu A \cdot cm^{-2}$ during 90 h at $60^\circ C$. (Figure IV-35). These

results slightly differ from the expected abundances for the Li-foils. This small deviation could be explained by a slight contamination during sample preparation coming from the polymer electrolyte layer. The polymer electrolyte in-between a ${}^6\text{Li}$ -foil and a ceramic pellet was enriched at 53.6% in ${}^6\text{Li}$. Analysing cross sections can lead to estimate the evolution of lithium isotopic abundance through a thick ceramic pellet. ${}^6\text{Li}$ abundance of the ceramic pellet decreased from 24 to 14.5% in ${}^6\text{Li}$. Thus, lithium migration seems to be a continuous process in the ceramic pellet. The thin polymer electrolyte in-between the ceramic pellet and the ${}^7\text{Li}$ -foil was not detected and appears as a dark zone on Figure IV-35. The manual way to prepare the cross section can induce the roughness of the cross section. Therefore, it is more difficult to analyse the cross sections. As already mentioned, sample preparation should be investigated. Some *sandwich* devices were fractured into liquid nitrogen at -196°C in order to facilitate the breaking process. However, it did not work. As a workaround, it was considered to polish the cross sections. However, a standard polishing approach may lead to a mixing of all the atoms at the surface and to create artefacts. Cryo-Focused Ion Beam Scanning Electron Microscopy (FIB-SEM) cross section may be a way to obtain flat surfaces by minimising their alteration. However, it cannot be performed on such thick ceramic pellets, but only on smaller sections.

Figure IV-35 illustrates one of the only analyse in which a polymer electrolyte cross section was slightly detected. Indeed, in most cases, polymer electrolytes were not detected due to slicing and planarity issues. However, the polymer electrolyte was too thin to allow detection of any variations along its cross section.

On Figure IV-36.a, only the cross section of a ceramic pellet was characterised after applying a constant current density of $50\ \mu\text{A} \cdot \text{cm}^{-2}$ during 48 h at 60°C .

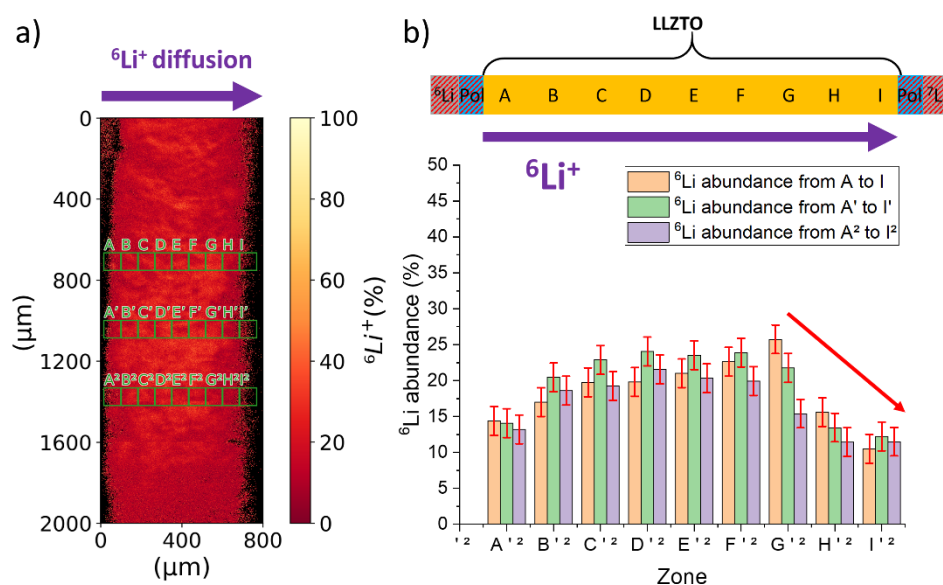


Figure IV-36. ToF-SIMS characterisation of lithium isotopic abundances along the cross section of S1 after applying a constant current density of $50\ \mu\text{A} \cdot \text{cm}^{-2}$ during 48 h at 60°C : a) ${}^6\text{Li}$ abundance mapping on the cross section b) Average of ${}^6\text{Li}$ abundance determination in each selected area. Uncertainties were estimated at 2%. The red arrow indicates the ${}^6\text{Li}$ abundance gradient.

On Figure IV-36.a, only the cross section of the ceramic pellet contained in S1 was characterised. Polymer electrolyte cross sections were not accessible. ${}^6\text{Li}$ abundances were determined on the ceramic cross section along three parallel lines following the ${}^6\text{Li}^+$ ions migration direction (purple arrow on Figure IV-36.a): from A to I, from A' to I' and from A² to I². The estimated ${}^6\text{Li}$ abundance of each zone is reported on Figure IV-36.b. On the ${}^6\text{Li}$ -foil side (A), ${}^6\text{Li}$ abundance was estimated at 14% in average. A higher ${}^6\text{Li}$ abundance estimation would be expected compared with the previous ${}^6\text{Li}$ abundance surface estimation of 24% (Table IV-13).

${}^6\text{Li}$ abundance was estimated at 11% on the ${}^7\text{Li}$ -foil side (H), which is in agreement with the ToF-SIMS surface characterisation results of 10% (Table IV-13). Furthermore, the ${}^6\text{Li}$ abundance decreases close to the ${}^7\text{Li}$ -foil. It is indicated by the red arrow on Figure IV-36.b. It may be explained by the fact that ${}^6\text{Li}^+$ ions diffuse from the ${}^6\text{Li}$ -foil to the ${}^7\text{Li}$ -foil. Thus, a higher ${}^6\text{Li}$ enrichment is expected close to the ${}^6\text{Li}$ -foil. No clear ${}^6\text{Li}$ abundance gradient is obtained in the ceramic (Figure IV-36.b). On the contrary, an average ${}^6\text{Li}$ abundance of 21% was estimated in the middle of the ceramic (from B to G).

After applying a constant current density, lithium isotopes may still reorganise in the ceramic pellet. The constant ${}^6\text{Li}$ abundance in the middle of the ceramic pellet suggests that a homogenisation may occur. If this assumption is confirmed, freezing sample after applying the electrochemical test could be a way to avoid any unwanted Li^+ ions self-diffusion into the device, even after stopping the applying constant current density and the heating.

On Figure IV-37, only the cross section of the ceramic pellet contained in S2 was characterised. Here, a longer CP was applied compared to S1. Thus, higher ${}^6\text{Li}$ enrichments are expected.

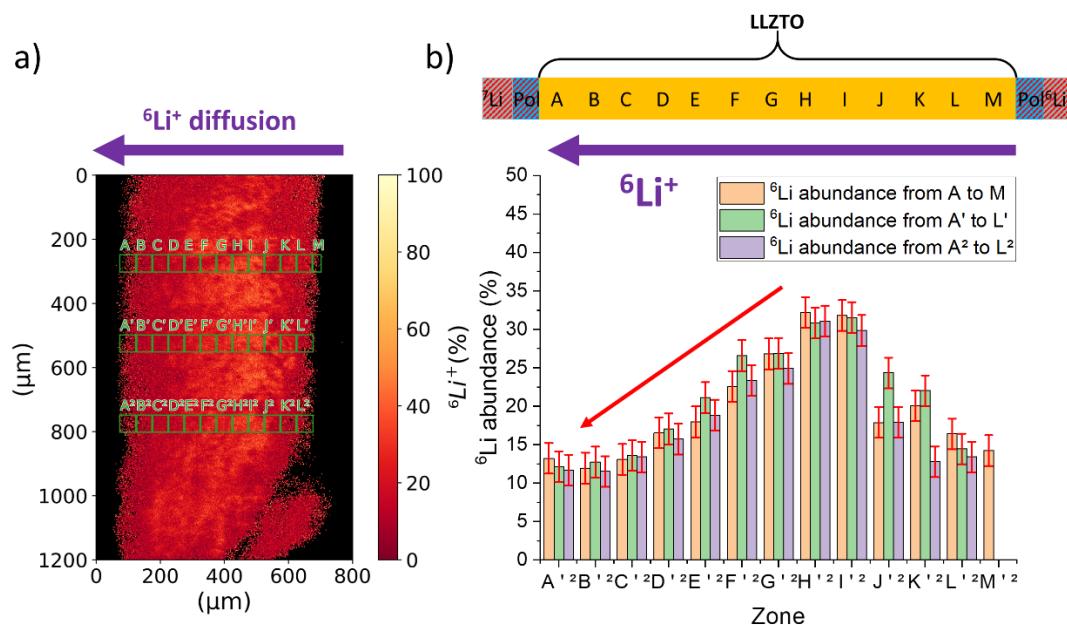


Figure IV-37. ToF-SIMS characterisation of lithium isotopic abundance along the cross section of S2 after applying a constant current density of $50 \mu\text{A} \cdot \text{cm}^{-2}$ during 86 h at 60°C : a) ${}^6\text{Li}$ abundance mapping on the cross section b) Average of ${}^6\text{Li}$ abundance determination in each selected area. Uncertainties were estimated at 2%. The red arrow indicates the ${}^6\text{Li}$ abundance gradient.

^6Li abundances were determined on the ceramic cross section along three parallel lines following the $^6\text{Li}^+$ ions migration direction (purple arrow on Figure IV-37.a): from M to A, from M' to A' and from M² to A². The estimated ^6Li abundance of each zone is reported on Figure IV-37.b. Here, the ^6Li abundance gradient is more pronounced from I to B (compared to S1 analyses), but still not present through all the ceramic pellet thickness. The red arrow on Figure IV-37 indicates the ^6Li abundance gradient. On the ^6Li -foil side (L) higher ^6Li abundances would be expected. Indeed, only 15% of ^6Li was detected by averaging characterisation of L, M, L', and L², whereas 53% of ^6Li were estimated by characterising the surface of the ceramic pellet (Table IV-13).

b. High-resolution ssNMR characterisations

To prepare samples, the ceramic pellet was crushed and an insert was filled with the obtained powder. Only few milligrams of polymer electrolytes were collected due to the low thickness of the layers. Thus, polymer electrolyte layers were mixed with potassium bromide (KBr) powder to obtain properly and fully filled inserts. Indeed, inserts have to be homogeneously filled to avoid any rotation issue as rotor are spinning very fast (10,000 Hz). Small movements of the materials in the inserts can unbalance them. Three inserts were prepared to characterise the three layers composing the *sandwich*, namely the polymer electrolyte on top of the ceramic pellet (P₁), the interlayer ceramic pellet, and the polymer electrolyte under the ceramic pellet (P₂). Thus, the ceramic pellet and both polymer electrolytes (P₁ and P₂) were characterised separately. The contamination by the polymer electrolyte of the ceramic insert cannot be excluded as the polymer is sticky. However, it is not an issue because their chemical shift is different. Li-foils were not analysed by high-resolution ssNMR.

On Figure IV-38, Figure IV-39, and Figure IV-40, lithium dynamics through *sandwich* devices was compared according to the duration of the CP sequence. Furthermore, ^6Li abundance of each layer was estimated to better understand lithium diffusion mechanisms. Normalising the absolute integral values by the amount of material contained in each insert allows to easily compare the absolute integral values obtained in the same acquisition conditions. Sidebands are indicated by asterisks on each ^7Li spectrum. They appear on both sides of the isotropic signal and are separated by 10,000 Hz.

^6Li and ^7Li were probed to estimate lithium isotopic abundances by following the methodology described in chapter II. Figure IV-38 represents high-resolution ssNMR spectra obtained by probing ^6Li and ^7Li nuclei in the polymer electrolyte between the ^6Li -foil and the ceramic pellet contained in the *sandwich* device (P₁).

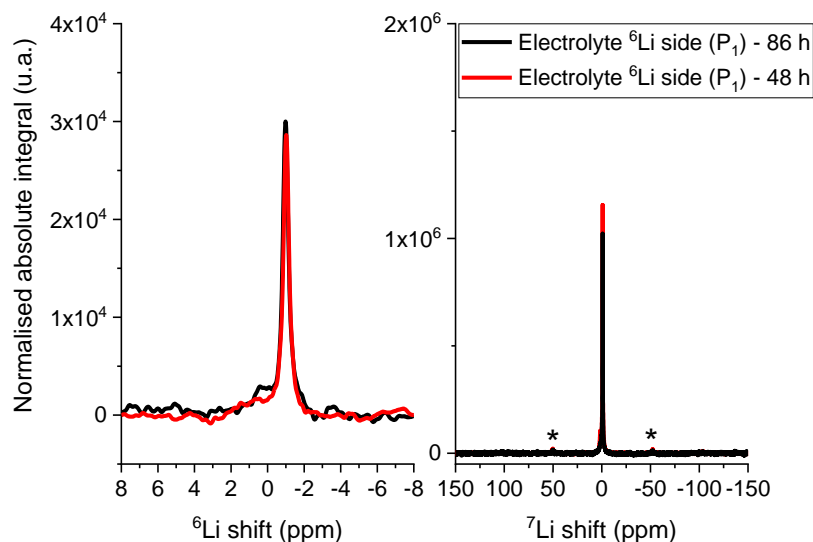


Figure IV-38. ${}^6\text{Li}$ (left) and ${}^7\text{Li}$ (right) high-resolution ssNMR spectra of the polymer electrolyte between the ${}^6\text{Li}$ -foil and the ceramic pellet (P_1) after applying a current density of $50 \mu\text{A} \cdot \text{cm}^{-2}$ on a sandwich device during either 48 h (red line) or 86 h (black line). Sidebands are indicated by asterisks.

On Figure IV-38, P_1 was characterised after applying a current density of $50 \mu\text{A} \cdot \text{cm}^{-2}$ during either after 48 h (red line) or after 86 h (black line) at 60°C . ${}^6\text{Li}$ abundance in P_1 was estimated at 62% in S1 and at 73% in S2.

Figure IV-39 represents high-resolution ssNMR spectra obtained by probing ${}^6\text{Li}$ and ${}^7\text{Li}$ nuclei in the ceramic pellet contained in the sandwich device.

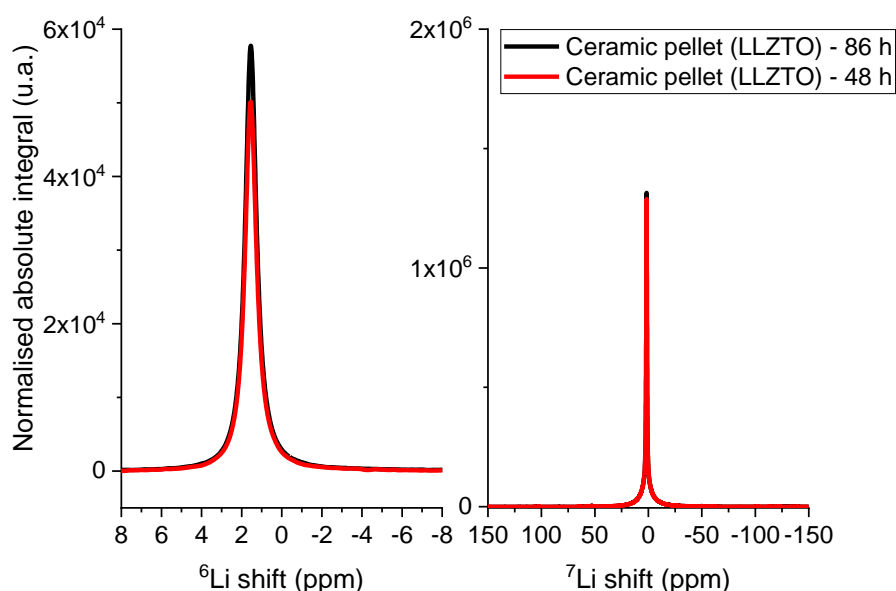


Figure IV-39. ${}^6\text{Li}$ (left) and ${}^7\text{Li}$ (right) high-resolution ssNMR spectra of the ceramic pellet after applying a current density of $50 \mu\text{A} \cdot \text{cm}^{-2}$ on a sandwich device during either 48 h (red line) or 86 h (black line).

On Figure IV-39, the ceramic pellet was characterised after applying a current density of $50 \mu\text{A} \cdot \text{cm}^{-2}$ during either after 48 h (red line) or after 86 h (black line) at 60°C . ^6Li abundance in LLZTO was estimated at 28% in $S1$ and at 30% in $S2$.

Figure IV-40 represents high-resolution ssNMR spectra obtained by probing ^6Li and ^7Li nuclei in the polymer electrolyte between the ceramic pellet and the ^7Li -foil contained in the sandwich device (P_2).

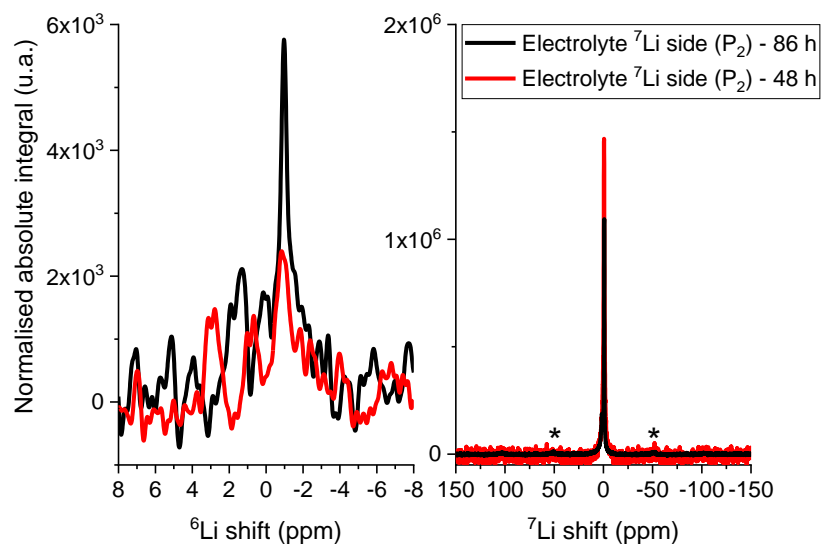


Figure IV-40. ^6Li (left) and ^7Li (right) high-resolution ssNMR spectra of the polymer electrolyte between the ceramic pellet and the ^7Li -foil (P_2) after applying a current density of $50 \mu\text{A} \cdot \text{cm}^{-2}$ on a sandwich device during either 48 h (red line) or 86 h (black line). Sidebands are indicated by asterisks.

On Figure IV-40, P_2 was characterised after applying a current density of $50 \mu\text{A} \cdot \text{cm}^{-2}$ during either after 48 h (red line) or after 86 h (black line) at 60°C . ^6Li abundance in P_2 was estimated at 18% in $S1$ and at 29% in $S2$.

Results from Figure IV-38, Figure IV-39, and Figure IV-40 are summed up in Table IV-14.

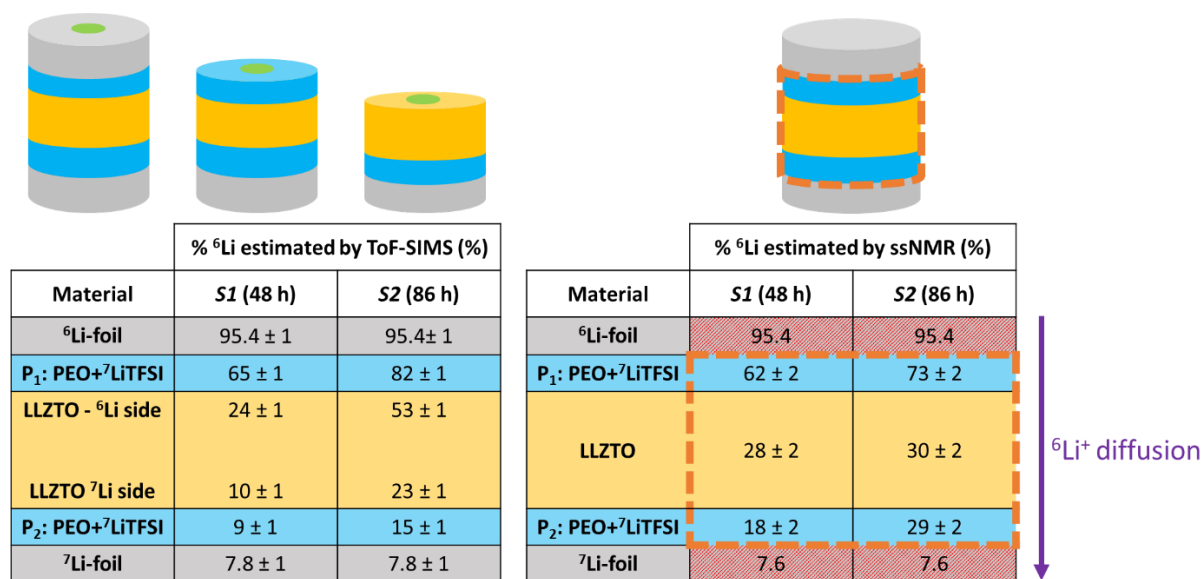
Table IV-14. High-resolution ssNMR global estimations of ${}^6\text{Li}$ abundances of the three layers composing S1 and S2. Theoretical ${}^6\text{Li}$ abundances of Li-foils are indicated, but not determined experimentally.

Material	% ${}^6\text{Li}$ estimated by ssNMR (%)	
	S1 (48 h)	S2 (86 h)
${}^6\text{Li}$ -foil	95.4	95.4
P ₁ : PEO+ ${}^7\text{LiTFSI}$	62 ± 2	73 ± 2
LLZTO	28 ± 2	30 ± 2
P ₂ : PEO+ ${}^7\text{LiTFSI}$	18 ± 2	29 ± 2
${}^7\text{Li}$ -foil	7.6	7.6

↓ ${}^6\text{Li}^+$ diffusion

Table IV-14 highlights that in each SSE layer the ${}^6\text{Li}$ abundance is higher when the duration of the CP sequence increases. It is obvious in the polymer electrolyte layer: 62% < 73% in P₁, and 18% < 29% in P₂. However, ${}^6\text{Li}$ abundances estimated in the ceramic pellet are relatively equivalent because the methodology provides abundances with an uncertainty of 2%. Thus, ${}^6\text{Li}$ abundance of the ceramic pellets seems identical in both cases. High-resolution ssNMR characterisation provides average values. Here, the ceramic pellets are thick compared to polymer electrolyte layers. It could be possible that the same average value is obtained with relatively different ${}^6\text{Li}$ abundance distributions into the ceramic pellet. Table IV-15 confronts ${}^6\text{Li}$ abundance estimations of layers composing S1 and S2 by ToF-SIMS and by high-resolution ssNMR.

Table IV-15. ${}^6\text{Li}$ abundances estimations by ToF-SIMS and by high-resolution ssNMR after having applied a constant current density of $50 \mu\text{A} \cdot \text{cm}^{-2}$ during 48 h on S1 and during 86 h on S2.



The main result is that in both cases (S1 and S2), P₂ ${}^6\text{Li}$ abundance is higher than lithium natural isotopic abundance in ${}^6\text{Li}$. It is a proof that lithium migrates through all the layers during the CP sequence in such device. Applying a constant current density of $50 \mu\text{A} \cdot \text{cm}^{-2}$ during 48 h on S1 led to lower ${}^6\text{Li}$ enrichments of the SSE layers compared to applying a constant current density of $50 \mu\text{A} \cdot \text{cm}^{-2}$ during 86 h on S2 (Table IV-8).

More specifically, in the case of S1, P1 was enriched at 65% of ${}^6\text{Li}$ on its surface (ToF-SIMS) and at 62% by considering the whole electrolyte thickness (ssNMR). ToF-SIMS and high-resolution ssNMR estimations are in agreement. Furthermore, the higher enrichment of the surface of the polymer electrolyte in direct contact with the ${}^6\text{Li}$ -foil compared to the bulk is coherent due to the lithium migration direction. Then, the ceramic enrichment was estimated at 28% of ${}^6\text{Li}$ by high-resolution ssNMR. This corresponds to the average ${}^6\text{Li}$ -enrichment of the ceramic pellet. It is not in between the ToF SIMS boundaries 10 and 24%. However, it might be tricky to compare surface and bulk analyses for relatively thick layer compared to the polymer layer thickness. Modelling could offer the opportunity to further investigate these results in order to estimate lithium dynamics through the ceramic for instance. Finally, P₂ was enriched at 9% of ${}^6\text{Li}$ on its surface (ToF SIMS) and at 18% by considering the whole electrolyte (ssNMR). The high-resolution ssNMR estimation is twice higher the ToF-SIMS one. However, the lesser enrichment of the surface of the polymer electrolyte in direct contact with the ${}^7\text{Li}$ -foil than the bulk is also coherent and expected.

To some degree the same conclusions were obtained by characterising S2. P₁ was enriched at 82% of ${}^6\text{Li}$ on its surface (ToF-SIMS) and at 74% by considering the whole electrolyte (ssNMR). The ceramic enrichment was estimated at 30% of ${}^6\text{Li}$ by high-resolution ssNMR. This average is, in this case, in-between ToF-SIMS estimations of 23 and 53%, for the bottom and the top of the ceramic pellet. ToF-SIMS surface and cross section characterisations confirm that the ceramic pellet contained into S2 is locally more enriched in ${}^6\text{Li}$ than the one

containing in *S1*. However, it was not clearly understandable by high-resolution ssNMR. Finally, P_2 was enriched at 15% of ${}^6\text{Li}$ on its surface (ToF SIMS) and at 29% by considering the whole polymer electrolyte layer (ssNMR).

To conclude, the observed trends by ToF SIMS and by high-resolution ssNMR characterisations are coherent. ${}^6\text{Li}$ abundance decreases by moving away from the ${}^6\text{Li}$ -foil. It confirms that lithium migration seems to be a continuous process. Additionally, according to electrochemical measurements, the amount of exchanged lithium was doubled between *S1* and *S2*, and a ${}^6\text{Li}$ abundance increase was detected by ToF-SIMS and ssNMR characterisations. However, ${}^6\text{Li}$ abundance estimated in *S2* layers is not twice the ones estimated in the *S1* layers. An explanation is that lithium self-diffusion also occurs at 60° C and it modifies the detected ${}^6\text{Li}$ abundance.

Characterising *sandwich* devices highlights the relevance of tracking lithium through polymer and ceramic electrolytes by combining ToF-SIMS and high-resolution ssNMR. Furthermore, characterisations proved that lithium ions migrate between each interface. Numerical simulations are mandatory to better understand lithium diffusion parameters involved. Following the example of *in-plane* device, the *sandwich* device has been modelled based on the same isotopic mixing model (IMM). The model presented in section 1.4.c is updated in order to simulate also lithium dynamics at the interface between polymer electrolyte layers and the ionic conductive ceramic pellet.

2.4. Modelling approach to better understand lithium dynamics

a. Description of the *sandwich* geometry

Numerical simulations could allow to deeper understand ${}^6\text{Li}^+$ ions migration through the ceramic pellet and at its interfaces in direct contact with polymer electrolyte layers. A lithium diffusion coefficient through the ceramic will be estimated and compared with literature. Furthermore, lithium behaviour at the interface between a polymer electrolyte and a ceramic pellet will be mathematised. An exchange current at the interface between both materials will be determined by confronted experimental and simulation results.

A one-dimension (1D) model has been developed to simulate lithium diffusion through a *sandwich* device. Thickness of the various layers were taken into account. Figure IV-41 illustrates the considered geometry.

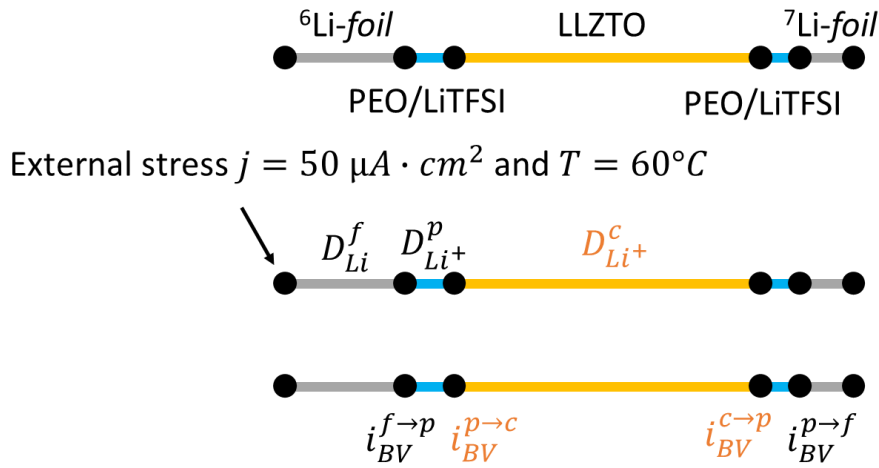


Figure IV-41. Schematic of the one-dimensional and main parameters such as the constant current density, j , lithium diffusion coefficient in i , D_i , and the exchange current at the various interface, i_{BV} .

b. Use of an isotopic mixing model (IMM)

- Description of the isotopic mixing model (IMM)

Exactly the same parameters, related to Li-foils and to the polymer electrolyte (described in section 1.4.c), are used. Here, additional parameters related to the ceramic pellet presence are discussed in Table IV-16.

Table IV-16. Set and optimised parameters describing lithium diffusion through ceramic pellet while applying a constant current density.

Material	Parameters	Numerical value	Unit
Polymer/Ceramic Interface	The exchange current ($i_{BV\ cer}$)	250	$A \cdot m^{-2}$
	Lithium isotopic abundance in LLZTO (% 6Li)	7.6	%
Ceramic (LLZTO)	Lithium concentration (C_{Li}^{cer})	5000	$mol \cdot m^{-3}$
	LLZTO volume fraction (ϕ_{cer})	$1 - \phi_{void} - \phi_{6Li^+} - \phi_{7Li^+}$	/
	Void volume fraction (ϕ_{void})	0.001	/
	Ionic conductivity LLZTO (σ_{cer})	$5 \times \sigma_p$	$S \cdot m^{-1}$
	${}^6Li^+$ diffusion coefficient ($D_{6Li^+}^{cer}$)	Equation IV-26	$m^2 \cdot s^{-1}$
	${}^7Li^+$ diffusion coefficient ($D_{7Li^+}^{cer}$)	$D_{6Li^+}^{LLZTO}$	$m^2 \cdot s^{-1}$
	Effective charge of Li (Z_{cer})	1	/
Effective volume ($\Omega_{6Li^+} = \Omega_{7Li^+}$)	Ω_{Li}	m^3	

Set and optimised parameters related to the addition of the ceramic pellet are listed in Table IV-16.

An IMM is defined, including lithium isotopes presence, structural vacancies (voids) enabling lithium mobility, and a representation of the ceramic structure as negatively charged and static, ensuring electroneutrality. Here, the ${}^6\text{Li}^+$ diffusion coefficient into the ceramic pellet, $D_{6\text{Li}^+}^{cer}$, is determined by the following Equation IV-26,

$$D_{6\text{Li}^+}^{cer} = \left(\frac{\Omega_{6\text{Li}^+}}{q} \right)^2 \frac{\sigma_{cer} k_B T}{\Omega_{6\text{Li}^+} (\phi_{6\text{Li}^+} + \phi_{7\text{Li}^+}) (\phi_{Void} + \phi_{cer})} \quad \text{IV-26}$$

with $\Omega_{i\text{Li}^+} (m^3)$, the effective volume of the $i\text{Li}$ isotope, $\sigma_{cer} (S \cdot cm)$, the ionic conductivity of the ceramic and ϕ_i , the volume fractions of voids, ceramic or lithium isotopes.

The lithium concentration in the ceramic pellet, $C_{Li}^{cer} (\text{mol} \cdot m^{-3})$, is expressed by the following Equation IV-27,

$$C_{Li}^{cer} = \frac{(\phi_{6\text{Li}^+} + \phi_{7\text{Li}^+})}{\Omega_{6\text{Li}^+} \cdot N_A} \quad \text{IV-27}$$

More details are provided in Appendix A-IV-5. *Conductivité céramique dans le modèle sandwich*. Therefore, the diffusion coefficient $D_{6\text{Li}^+}^{cer}$ can also be expressed by the following Equation IV-28,

$$D_{6\text{Li}^+}^{cer} = \left(\frac{1}{F} \right)^2 \frac{\sigma_{cer} RT}{C_{Li}^{cer} (1 - \Omega_{6\text{Li}^+} C_{Li}^{cer} N_A)} \quad \text{IV-28}$$

According to the set parameters, with a C_{Li}^{cer} of $5000 \text{ mol} \cdot m^{-3}$, and with an ionic conductivity 5 times higher than the polymer electrolyte, the $D_{6\text{Li}^+}^{cer}$ is estimated at $3.3 \times 10^{-11} m^2 \cdot s^{-1}$.

The lithium concentration in the ceramic pellet, C_{Li}^{cer} , the ceramic ionic conductivity, σ_{cer} , and the Butler-Volmer transfer coefficient at the polymer/ceramic interface, $i_{0\text{ref cer}}$, can be tuned in order to enhance numerical simulation results. Notice that $i_{0\text{ref cer}}$ is analogous to the spontaneous transfer frequency, ν , determined in chapter III. The $i_{0\text{ref cer}}$ takes also into account the application of a constant current density.

Boundary conditions in the case of lithium isotopic labelling have to be taken into account. The Butler-Volmer equations applied at the polymer electrolyte/ceramic interface were decomposed as presented in the following Equation IV-29 and Equation IV-30,

$$i_{BV, \epsilon_{Li}} = i_{0 \text{ ref cer}} \left\{ \phi_{\epsilon_{Li,m}} \phi_{\gamma_{Li}} \exp\left(\alpha \frac{\eta_{Li}}{V_0}\right) - \phi_{\epsilon_{Li}} \phi_{\gamma_{Li,m}} \exp\left[-(1 - \alpha) \frac{\eta_{Li,cer}}{V_0}\right] \right\} \quad \text{IV-29}$$

$$i_{BV, \gamma_{Li}} = i_{0 \text{ ref cer}} \left\{ \phi_{\epsilon_{Li}} \phi_{\gamma_{Li,m}} \exp\left(\alpha \frac{\eta_{Li}}{V_0}\right) - \phi_{\epsilon_{Li,m}} \phi_{\gamma_{Li}} \exp\left[-(1 - \alpha) \frac{\eta_{Li,cer}}{V_0}\right] \right\} \quad \text{IV-30}$$

with $\eta_{Li,cer}$ (V) the activation overpotential defined as the following Equation IV-31,

$$\eta_{Li,cer} = V - V_{cer} \quad \text{IV-31}$$

with V_{cer} (V), the calculated electric potential in the ceramic domain from the following equation, and V (V), the electric potential in the polymer electrolyte.

Lithium dynamics into the ceramic pellet domain and at the interface with the polymer electrolyte domain are simulated based on the Equation IV-32,

$$\nabla \cdot \sigma_{cer} \nabla V_{cer} = 0 \quad \text{IV-32}$$

with σ_{cer} ($S \cdot m^{-1}$) the ionic conductivity into the ceramic.

Here, the IMM, takes into account the presence of an ionic conductive ceramic pellet. It is used in the following section to perform numerical simulations, which will be compared to experimental results. The following simulated results were obtained with the specific polymer electrolyte parameters already set in the 1.4 section and with the presented parameters listed in Table IV-16 related to the addition of the ceramic pellet.

- Simulated results confronted to the experimental ones

Numerical simulations are run with the IMM. Figure IV-42 presents lithium volume fraction variations in each component after applying a constant current density of $50 \mu A \cdot cm^{-2}$ during 86 h at 60° C on a *sandwich* device.

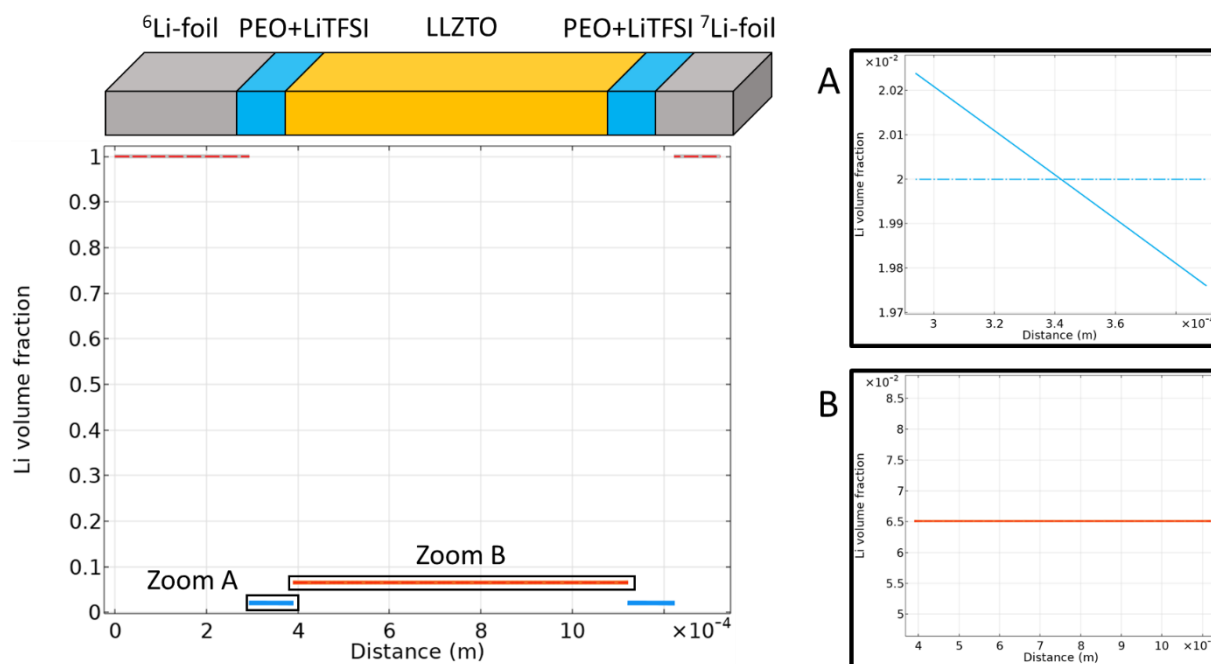


Figure IV-42. Lithium volume fraction in each component simulated after applying a constant current density of $50 \mu\text{A} \cdot \text{cm}^{-2}$ during 86 h at 60°C on a sandwich device. Grey, blue and orange lines correspond respectively to the Li-foils, the polymer electrolyte layers and the ceramic pellet. Zoom A on the lithium volume fraction of the polymer electrolyte reveals a lithium gradient. Zoom B on the lithium volume fraction of the ceramic pellet reveals no lithium gradient.

On Figure IV-42, the zoom A on the lithium volume fraction of the polymer electrolyte reveals a lithium gradient, whereas the zoom B on the lithium volume fraction of the ceramic pellet reveals no lithium gradient. Thus, it confirms the conservation of the electroneutrality. It can be explained by the fact that the counter ion (TFSI^-) is mobile into the polymer membrane, whereas the ceramic skeleton containing the negative charges does not move. Notice that lithium gradient is identical in both polymer electrolyte layers.

As previously explained, the IMM offers the possibility to distinguish both lithium isotopes. Thus, lithium volume fraction of each lithium isotope can be observed after a CP sequence of 48 h (Figure IV-43.a) or 86 h (Figure IV-43.b).

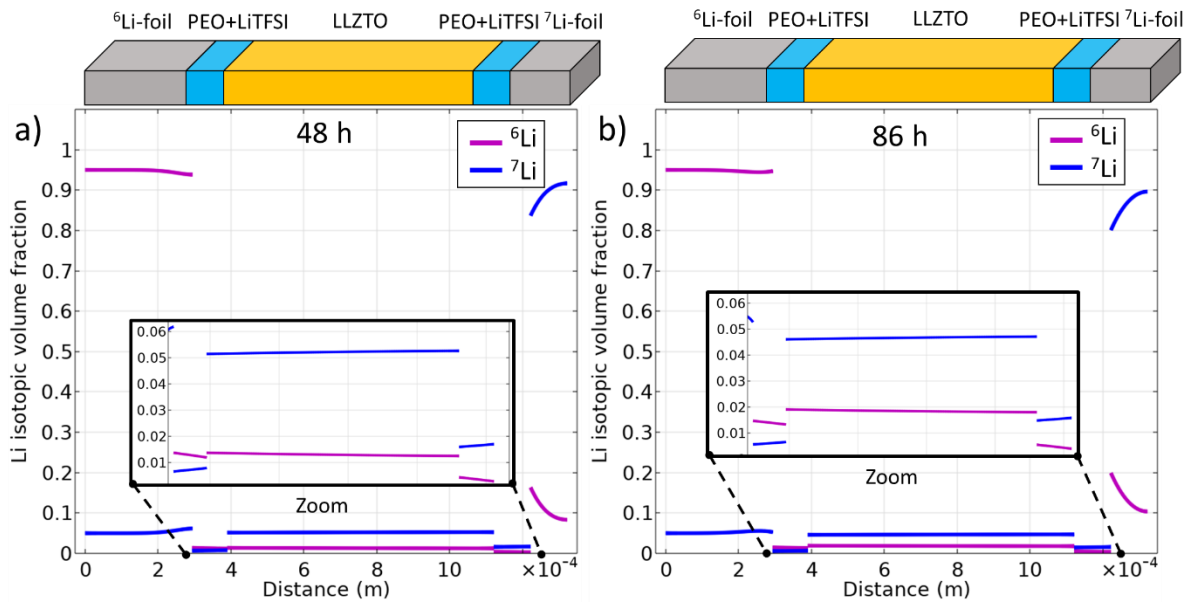


Figure IV-43. Lithium isotopic volume fraction variations in each component simulated after applying a constant current density of $50 \mu\text{A} \cdot \text{cm}^{-2}$ on a sandwich device during either a) 48 h or b) 86 h at 60°C . ${}^6\text{Li}$ and ${}^7\text{Li}$ volume fractions are represented in purple and in blue, respectively.

Lithium isotopic volume fraction variations in each component simulated after applying a constant current density of $50 \mu\text{A} \cdot \text{cm}^{-2}$ on a sandwich device during either 48 h or 86 h at 60°C are presented on Figure IV-43.a and on Figure IV-43.b, respectively. Looking at the zooms, ${}^6\text{Li}$ volume fraction of the ceramic pellet has increased from 0.015 to 0.020 by increasing the CP sequence time from 48 h to 86 h. In order to better interpret these variations, lithium isotopic abundances are determined from Figure IV-43.

On Figure IV-44, ${}^6\text{Li}$ abundances are determined from simulated lithium isotopic volume fractions (Figure IV-43) by applying the Equation IV-24.

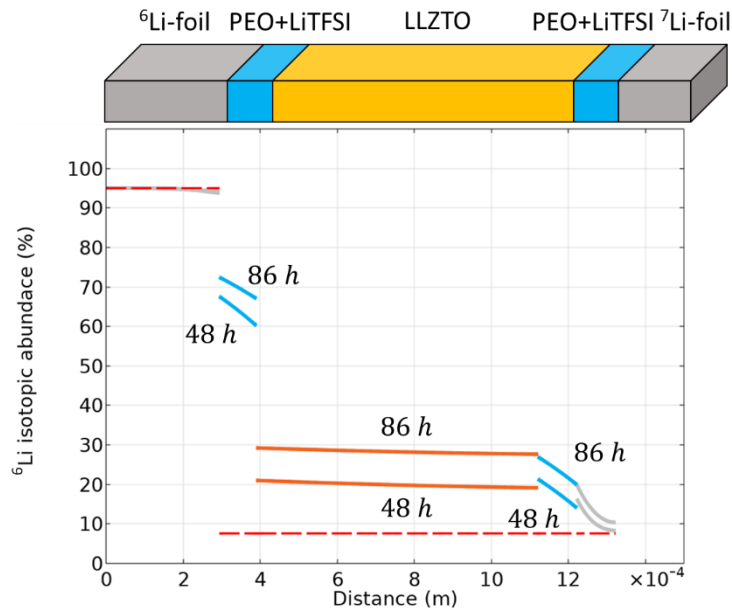


Figure IV-44. ${}^6\text{Li}$ abundance variations in each component simulated after applying a constant current density of $50 \mu\text{A} \cdot \text{cm}^{-2}$ on a sandwich device during either a) 48 h or b) 86 h at 60°C .

Figure IV-44 presents simulated results that could be obtained by ToF-SIMS assuming an ideal sample preparation that can provide clear cross section without damaging the sample. Furthermore, an overlap of ceramic cross section by stick polymer electrolyte must be avoided. The cryogenic of the sample may be a solution. Performing the cross-section should not modify the detected lithium isotopic abundance.

Table IV-17 summarises the simulated ${}^6\text{Li}$ abundances at each interface of a *sandwich* device after applying a constant current density of $50 \mu\text{A} \cdot \text{cm}^{-2}$ during 48 h (S1) and 86 h (S2). Furthermore, lithium gradient into materials is also detected by modelling. It is sharper into the polymer electrolyte than the one simulated into the ceramic pellet.

Thanks to the IMM applied to describe lithium isotopes dynamics into the *sandwich* device, the lithium self-diffusion coefficient into the ceramic pellet, $D_{6\text{Li}^+}^{\text{LLZTO}}$, could be estimated at $3.3 \times 10^{-11} \text{m}^2 \cdot \text{s}^{-1}$ at 60°C .

Table IV-17. Simulated ${}^6\text{Li}$ abundances at each interface of a sandwich device after applying a constant current density of $50 \mu\text{A} \cdot \text{cm}^{-2}$ during 48 h (S1) and 86 h (S2).

Material	Surface % ${}^6\text{Li}$ estimated by modelling (%)	
	S1 (48 h)	S2 (86 h)
${}^6\text{Li}$ -foil	95.4	95.4
P ₁ : PEO+ ${}^7\text{LiTFSI}$	68	72
LLZTO - ${}^6\text{Li}$ side	21	29
LLZTO ${}^7\text{Li}$ side	19	28
P ₂ : PEO+ ${}^7\text{LiTFSI}$	14	20
${}^7\text{Li}$ -foil	7.6	7.6

↓ ${}^6\text{Li}^+$ diffusion

Tendencies are relevant in Table IV-17. ${}^6\text{Li}$ abundance is decreasing from the ${}^6\text{Li}$ -foil to the ${}^7\text{Li}$ -foil. As the polymer electrolyte layer, P₂, is enriched in ${}^6\text{Li}$ it is a proof by modelling that ${}^6\text{Li}^+$ ions have diffused through all the layers. Furthermore, ${}^6\text{Li}$ abundances obtained from numerical simulations are lower after applying a constant current density of $50 \mu\text{A} \cdot \text{cm}^{-2}$ during 48 h (S1) compared with results obtained after 86 h (S2). Simulated results presented in Table IV-17 are compared with ToF-SIMS analyses (cf. section 2.3.a) because they both refer to ${}^6\text{Li}$ abundances at various interfaces.

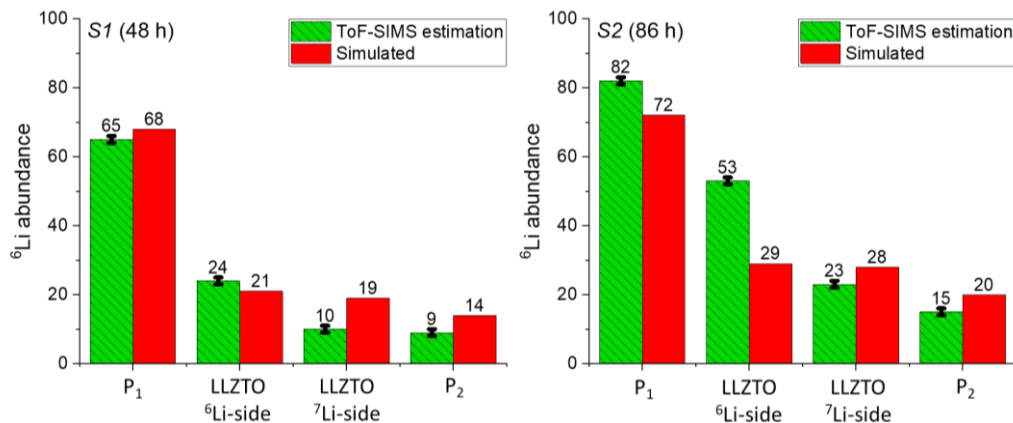


Figure IV-45. Comparison between surface ${}^6\text{Li}$ abundances estimated by ToF-SIMS (green bars) and global simulated ${}^6\text{Li}$ abundances (red bars). Back bars correspond to ToF-SIMS uncertainties of 1%.

On Figure IV-45, simulated ${}^6\text{Li}$ abundances at the interface (red bars) are compared with ToF-SIMS surface analyses (green bars) in both sandwich devices. Simulated ${}^6\text{Li}$ abundance on polymer electrolytes (P₁ and P₂) are close to the one estimated by ToF-SIMS. Looking at ${}^6\text{Li}$ abundance of the ceramic pellet there are differences. Indeed, a sharper ${}^6\text{Li}$ abundance gradient is estimated into the ceramic pellet by ToF-SIMS compared with the simulated one. According to ToF-SIMS analyses there is a gap of 14% between the ${}^6\text{Li}$ abundance on the ${}^6\text{Li}$ side and on the ${}^7\text{Li}$ side in S1 device (Figure IV-36). This gap is even higher (30%) in the case of the S2 device (Figure IV-37), whereas numerical simulations provide a gap of 2 and 1% in S1 and S2 devices, respectively. Thus, the set parameters describing lithium dynamics into the ceramic pellet must be adjusted.

Numerical simulations can also provide global ${}^6\text{Li}$ abundances in each component after applying a constant current density of $50 \mu\text{A} \cdot \text{cm}^{-2}$ during 48 h (S1) and 86 h (S2). These results are summarised in Table IV-18.

Table IV-18. Simulated global ${}^6\text{Li}$ abundances of the three layers composing S1 and S2 such as P₁, LLZTO (ceramic) and P₂.

Material	Global % ${}^6\text{Li}$ estimated by modelling (%)	
	S1 (48 h)	S2 (86 h)
P ₁ : PEO+ ⁷ LiTFSI	64	70
LLZTO	20	28
P ₂ : PEO+ ⁷ LiTFSI	18	24

↓ ${}^6\text{Li}^+$ diffusion

Simulated results presented in Table IV-18 provide global ${}^6\text{Li}$ abundance simulated in each component. They can be compared with ${}^6\text{Li}$ abundance estimations obtained by high-resolution ssNMR characterisations (Figure IV-46).

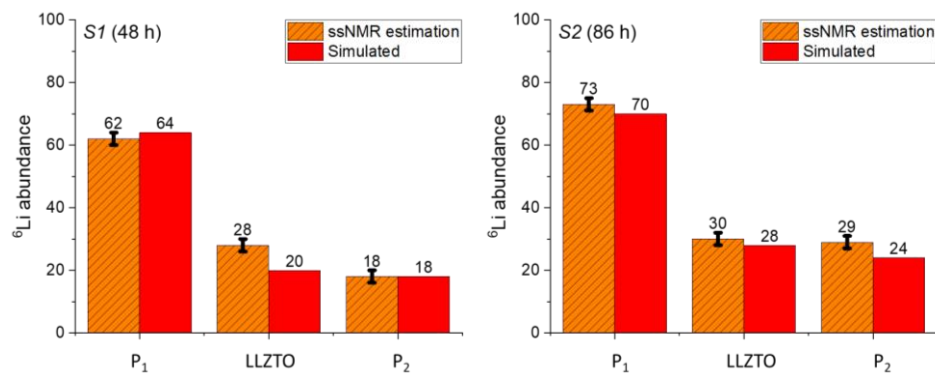


Figure IV-46. Comparison between global ${}^6\text{Li}$ abundances estimated by high-resolution ssNMR (orange bars) and simulated (red bars). Back bars correspond to ssNMR uncertainties of 2%.

On Figure IV-46, global ${}^6\text{Li}$ abundances estimated by modelling (red bars) are compared with the ones obtained by high-resolution ssNMR surface analyses (green bars) of both sandwich devices. They are close. Indeed, except for P₂ of the S2 device, in other polymer electrolyte layers the ${}^6\text{Li}$ abundance differ by a maximum of 3%, which is non-significant compared to the ssNMR uncertainty of 2%.

Regarding global ${}^6\text{Li}$ abundance into the ceramic pellet, results match well in the case of S2, whereas numerical simulations underestimate the global ${}^6\text{Li}$ abundance compared to the one estimated by high-resolution ssNMR. A way to solve this issue may be to consider two lithium populations according to the type of site they are occupying into the ceramic, either tetrahedral or octahedral site. As lithium ions mainly move through the tetrahedral sites into the LLZTO structure, lithium global dynamic may change. The way lithium dynamics is modelled into the ceramic pellet can be modified because part of the lithium is not involved into the migration.

Conclusion

Two configurations were thoroughly studied to investigate lithium dynamics while applying either a CA or a CP sequence. Lithium self-diffusion and lithium migration were revealed for the *in-plane* configuration after applying a CA sequence (constant voltage of 0.25 V), with the help of data obtained in chapter III.

Lithium dynamics were also characterised in *sandwich* devices after applying a constant current density of $50 \mu\text{A} \cdot \text{cm}^{-2}$. Such specific geometry was designed to probe the various interfaces (Li/polymer and polymer/ceramic) by using ToF-SIMS. Each layer of the device can also easily be analysed by high-resolution ssNMR. One significant result is that the polymer electrolyte under the ceramic pellet is enriched in ^6Li , which is a clear evidence of lithium diffusion through the whole device. Moreover, cross section characterisations were performed by ToF-SIMS. They confirm that lithium migration is a continuous process. Lithium isotopic homogenisation seems to occur partially in the time between the electrochemical test and the analysis.

The setup improvements could be achieved by freezing the sample straight after the electrochemical test to mitigate lithium diffusion prior to sample analysis. In addition, cross section preparation appears to be a critical parameter.

Both studied configurations, *in-plane* and *sandwich*, were modelled and experimental results were used as input data. The IMM, based on mixing thermodynamics and taking into account lithium isotopic exchanges, was specifically developed. Numerical simulations provided additional information on lithium dynamics in the whole device. The IMM was also adapted to take into account the ceramic pellet integration in the *sandwich* device. The lithium self-diffusion coefficient into the ceramic pellet could be estimated at $3.3 \times 10^{-11} \text{m}^2 \cdot \text{s}^{-1}$ at 60° C.

These devices (*in-plane*, *sandwich*) have been designed in our work as model systems in order to develop robust methodologies and numerical models for the study of lithium isotopic abundance spatial distribution and its determination in the bulk of materials or at interfaces. To explore further, it is entirely logical to approach a genuinely commercially viable composite SSE, which is promising in battery applications. Thus, in the last chapter, a *dispersion* configuration will be studied in detail. It is composed of ionic conductive ceramic particles embedded in a polymer electrolyte matrix.

Chapter V. Lithium dynamics through a composite solid-state electrolyte: A ceramic dispersion in a polymer matrix

Lithium dynamics were studied in chapter IV by working on two devices having specific geometries: the *in-plane* device and the *sandwich* device. The goal was to facilitate the determination of numerical parameters such as lithium self-diffusion coefficients in each material composing the SSE and lithium exchange frequencies at the interfaces between two materials. However, these geometries do not reflect the targeted ones and composites with viable geometry have to be optimised in order to be competitive with existing liquid electrolytes. Indeed, they present high resistance compared to liquid electrolytes. It is mainly due to the distance between both lithium electrodes, low ionic conductivity of the polymer electrolyte and high polymer/ceramic interfacial resistance. Here, lithium dynamics are investigated through a configuration named *dispersion* that has promising perspectives in battery applications. The configuration is composed of a polymer electrolyte matrix containing an ionic conductive ceramic dispersion. Such design is widely reported in literature. [21], [44], [46] The developed ToF-SIMS and high-resolution ssNMR methodologies are applied on this increasingly intricate device. Additionally, a collaboration initiated with Orsay Physics company will allow to investigate the suitability of orthogonal ToF-SIMS (o-ToF-SIMS) characterisation approach to obtain a better lateral resolution for our purposes. In the end, lithium ions pathways can be proposed from these various studies.

V.1. Lithium dynamics through a composite solid-state electrolyte

5.1. Description of the *dispersion* device

The *dispersion* device is composed of ionic ceramic particles dispersed into a polymer electrolyte matrix. It is schematised on Figure V-1.

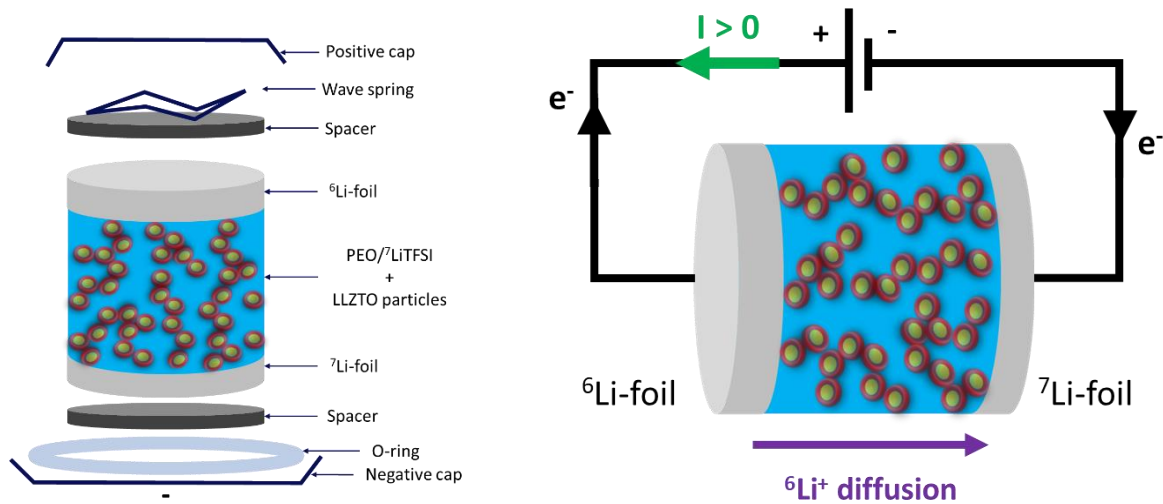


Figure V-1. Schematic of the composite SSE composed of a polymer electrolyte (PEO/LiTFSI) containing 20 vol% submicronic ceramic particles (LLZTO) assembled in a coin cell. A ⁶Li-foil and a ⁷Li-foil were used as positive and negative electrode, respectively, allowing ⁶Li⁺ ions migration through the device while applying an electrical stress.

The composite SSE was investigated because such composite electrolyte could be implemented in commercial solid-state batteries. As described in chapter II, the used $\text{Li}_{6.4}\text{La}_3\text{Zr}_{1.4}\text{Ta}_{0.6}\text{O}_{12}$ (Ta-doped LLZO, LLZTO) submicronic ceramic particles are commercially available, and the polymer electrolyte was prepared with a lithium salt at lithium natural isotopic abundance. Dispersion preparation is described in chapter II. As a reminder, the composite SSE is containing 20 vol% of ceramic particles, corresponding to 52.7 wt%. The assembly step is identical to the *sandwich* device. A ⁶Li-foil and ⁷Li-foil disks are used as positive and negative electrode, respectively. Coin cells were assembled in a dry room (Figure V-1), and sealed in a glovebox under inert atmosphere. The applied pressure was of 1 bar. Device dimensions (C1, C2, C3, and C4) and their respective test conditions are mentioned in Table V-1.

Table V-1. Thickness of the composite SSE as a function of the studied device.

Device	Composite SSE: PEO/LiTFSI + LLZTO particles (μm)	Current density ($\mu\text{A} \cdot \text{cm}^{-2}$)	Test time at 60° C (h)
C1	183	0	0
C2	171	0	100
C3	216	50	100
C4	161	50	50

C1 was not tested. It is used as reference in the whole chapter (Table V-1). C2 was not connected to a potentiostat, but it was assembled in coin cell and stored during 100 h at 60° C. A constant current density of $50 \mu\text{A} \cdot \text{cm}^{-2}$ was applied on C3 and C4 during 100 h and 50 h at 60° C, respectively. Firstly, the effect of the temperature will be investigated by comparing C1 and C2. Then, the effect of the applied current density will be investigated by comparing C2, C3 and C4.

5.2. Electrochemical results

a. Electrochemical impedance spectroscopy (EIS) characterisation

Figure V-2 presents the Nyquist plots obtained by performing an EIS on C3 and C4.

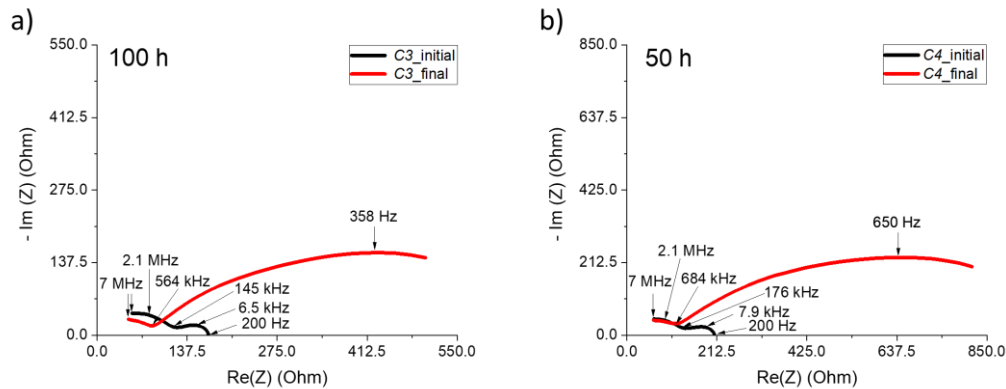


Figure V-2. Nyquist plots obtained by performing EIS on C3 (a) and C4 (b) before (black curves) and after (red curves) applying a constant current density of $50 \mu\text{A} \cdot \text{cm}^{-2}$ during either 100 h (a) or only 50 h (b).

On Figure V-2 black curves represent EIS performed before applying a CP sequence on both devices. The red curves correspond to EIS performed at the end of the CP sequence.

The applied CP sequence is described in the following section. Table V-2 sums up the resistances obtained by Zfit module of the EC lab software.

Table V-2. Electrolyte resistance obtained before and after applying a CP sequence on the C3 and C4 during 100 h and 50 h, respectively.

Device (CP sequence time)	Initial resistance (Ω)	Final resistance (Ω)
C3 (100 h)	11 ± 3	12 ± 3
C4 (50 h)	28 ± 3	29 ± 3

The resistance contribution attributed to the bulk electrolyte is reported in Table V-2. At 60°C , the global ionic conductivity of the composite SSE ($\sigma_{composite}$) was of $6.3 \times 10^{-4} \pm 3.4 \times 10^{-4} \text{ S} \cdot \text{cm}^{-1}$. This value is close the determined ionic conductivity into the pure polymer electrolyte ($6.4 \times 10^{-4} \text{ S} \cdot \text{cm}^{-1}$). Addition of ceramic particles does not increase the global ionic conductivity of the whole system. The second resistance contribution is attributed to the interfaces between the Li-foils and the composite SSE. The determination of the electrical equivalent circuit is presented in Appendix A-V-1. *Determination of the electrical equivalent circuit of each device.*

b. A chronopotentiometry (CP) sequence

A chronopotentiometry (CP) sequence with a constant current density of $50 \mu\text{A} \cdot \text{cm}^{-2}$ was applied after the initial EIS on two *dispersion* devices, during either 50 h (Figure V-3) or 100 h (Figure V-4). Two levels of charge capacity could be investigated.

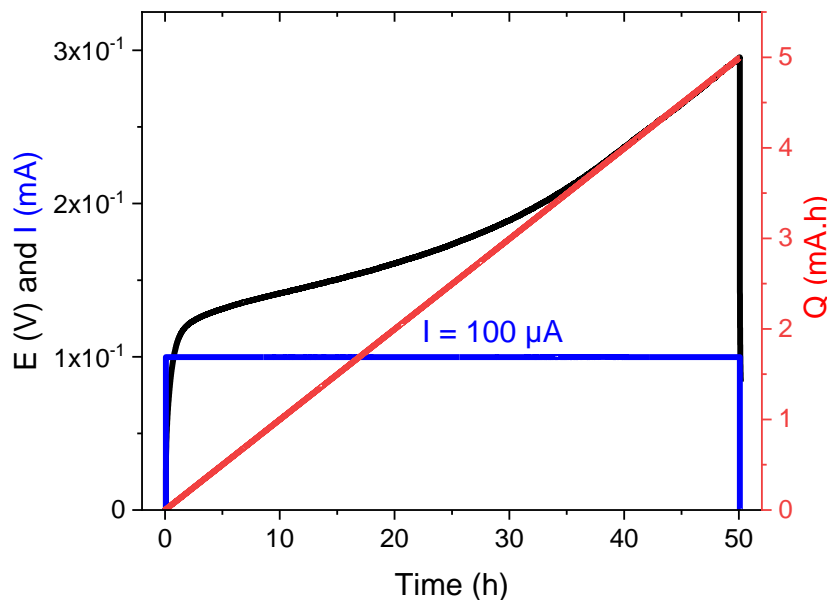


Figure V-3. Evolution of the voltage (black line) and charged capacity (red line) as a function of time due to the applied electrical stress (CP sequence with $I = 100 \mu\text{A}$, blue line) on the dispersion configuration during 50 h (C4).

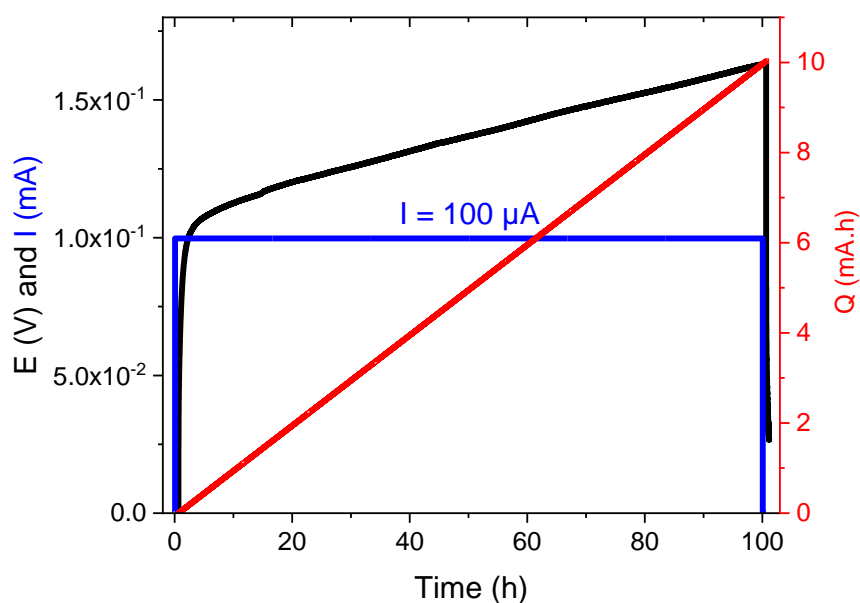


Figure V-4. Evolution of the voltage (black line) and charged capacity (red line) as a function of time due to the applied electrical stress (CP sequence with $I = 100 \mu\text{A}$, blue line) on the dispersion configuration during 100 h (C3).

A current of $100 \mu\text{A}$ was applied, corresponding to a current density of $50 \mu\text{A} \cdot \text{cm}^{-2}$ during either 50 or 100 h at 60°C . The evolution of the voltage was recorded as the function of the time (Figure V-4). The specific capacity was calculated as a function of time. Coin cells were taken out of the oven straight after the end of the electrochemical test to carefully take into account lithium isotopic exchange dynamics occurring at 60°C . Lithium dynamics were also characterised after 100 h at 60°C without undergoing any electric driving force.

On Figure V-3 and Figure V-4, the application of a constant current (I) is represented by the blue crenel. The evolution of the voltage (E) is recorded as a function of time (black curve), and the charged capacity (Q) is calculated (red line). As the current is constant, the evolution of Q is linear. A constant current of $100 \mu\text{A}$ was applied in order to control the current density during the entire CP sequence. Regarding the surface of 2cm^2 , it corresponds to a current density of $50 \mu\text{A} \cdot \text{cm}^{-2}$. The specific capacity measured electrochemically offers a first estimation of the amount of exchanged lithium. Specific capacities of 5 and $10 \text{mA} \cdot \text{h}$ were calculated after a CP sequence of 50 h and 100 h, respectively.

5.3. Advanced characterisations

a. High-resolution ssNMR characterisations

Coin cells were disassembled in a glovebox. The Li-foils were peeled off from the composite SSEs. Then, samples were transferred to the dry room in order to fill inserts. The mass of each composite SSE ($m_{composite}$) was weighed. Lithium amount in each component was estimated according to the composite SSE preparation mentioned in chapter II. All masses and lithium amounts are reported in Table V-3.

Table V-3. Mass of the composite SSE contained in each insert ($m_{composite}$) was weighed and the corresponding amount of lithium in each material $n_{Li}^{polymer}$ and $n_{Li}^{ceramic}$, and the total amount of lithium (n_{Li}^{total}) were calculated.

Composite SSE	Insert containing the composite SSE	$m_{composite}$ (mg)	$n_{Li}^{polymer}$ (mol)	$n_{Li}^{ceramic}$ (mol)	n_{Li}^{total} (mol)
C1	At lithium natural isotopic abundance	34.85	1.6×10^{-5}	1.3×10^{-4}	1.5×10^{-4}
C2	After 100 h at 60° C	30.97	1.5×10^{-5}	1.2×10^{-4}	1.3×10^{-4}
C3	After a CP sequence during 100 h at 60° C	36.10	1.7×10^{-5}	1.4×10^{-4}	1.5×10^{-4}
C4	After a CP sequence during 50 h at 60° C	34.10	1.6×10^{-5}	1.3×10^{-4}	1.5×10^{-4}

Inserts contain a maximum of 1.5×10^{-4} mol of lithium, which is a low amount (Table V-3). Lithium confined in the ceramic particles ($n_{Li}^{ceramic}$) has a different chemical environment from lithium incorporated in the polymer electrolyte ($n_{Li}^{polymer}$). [46] Acquisition parameters have to be adapted to obtain enough signal. The gain was set at the maximum (101), and the numbers of scans were set at 32 and 64 for 6Li and 7Li , respectively. To be quantitative, the longest D_1 value between the polymer and the ceramic particles have to be applied, as they were both present in the samples. The ceramic parameters were selected to record lithium spectra to be quantitative and to get well-defined contributions for lithium contained in ceramic particles as well as lithium contained in polymer electrolyte. Thus, D_1 was set at 500 s to record 7Li spectra and at 230 s to record 6Li spectra. Increasing the number of scans could increase the signal/noise ratio, but also the acquisition time. The acquisition time of 6Li and 7Li high-resolution ssNMR spectra already last 2 h 04 and 1 h 14 in these conditions, respectively. All spectra were acquired with an 11.744 T magnetic field, and rotors were spun at 10 kHz at magic angle (54.7°).

The methodology developed in chapter II was used. Figure V-5 presents the high-resolution ssNMR spectra acquired using specific settings allowing to perform experiments on composite SSEs, providing accurate results on lithium isotopic abundance.

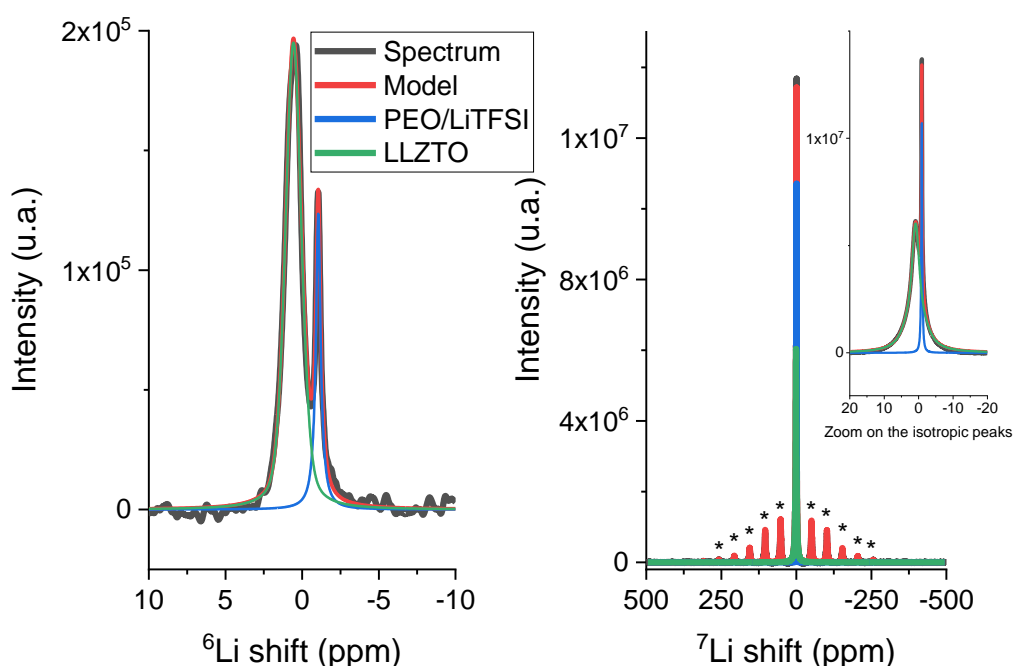


Figure V-5. ${}^6\text{Li}$ and ${}^7\text{Li}$ high-resolution ssNMR spectra of the composite SSE at lithium natural isotopic abundance (C1, reference). Asterisks indicate spinning sidebands.

C1 is at lithium natural isotopic abundance. Therefore, it was used as a reference sample to determine ${}^6\text{Li}$ abundances of composite SSEs C2, C3, and C4. To combine ${}^6\text{Li}$ and ${}^7\text{Li}$ high-resolution ssNMR spectra, it is mandatory to determine a global normalisation factor (S_{global}). [16] It was calculated from each ${}^6\text{Li}$ and ${}^7\text{Li}$ absolute integrals obtained by characterising the composite SSE at lithium natural isotopic abundance (C1). These high-resolution ssNMR spectra are presented on Figure V-5. The determination of the integrals requires systematic process. ${}^6\text{Li}$ and ${}^7\text{Li}$ spectra are integrated using TopSpin software over a range of 20 ppm and 700 ppm centred at 0 ppm, respectively. An enlargement of the ${}^7\text{Li}$ isotropic peaks of ceramic particles and polymer is also presented. The green contributions stand for the lithium inside ceramic particles (LLZTO), and the blue ones for the lithium contained into the polymer electrolyte (PEO/LiTFSI). They result from spectrum deconvolutions of the experimental spectrum (black) using the Dmfit software. The red curve corresponds to the calculated spectra obtained with Dmfit (Model) by summing the polymer (blue) and the ceramic particles (green) contributions.

As a first approximation, no contribution distinction between the polymer electrolyte and the ceramic particles contribution was carried out. Thus, a S_{global} was estimated at 23.1 by combining both ${}^6\text{Li}$ and ${}^7\text{Li}$ spectra of C1. This factor is used to calculate ${}^6\text{Li}$ abundance of C2, C3, and C4.

Figure V-6, Figure V-7, and Figure V-8 represent ${}^6\text{Li}$ and ${}^7\text{Li}$ high-resolution ssNMR spectra obtained by probing C2, C3, and C4, respectively.

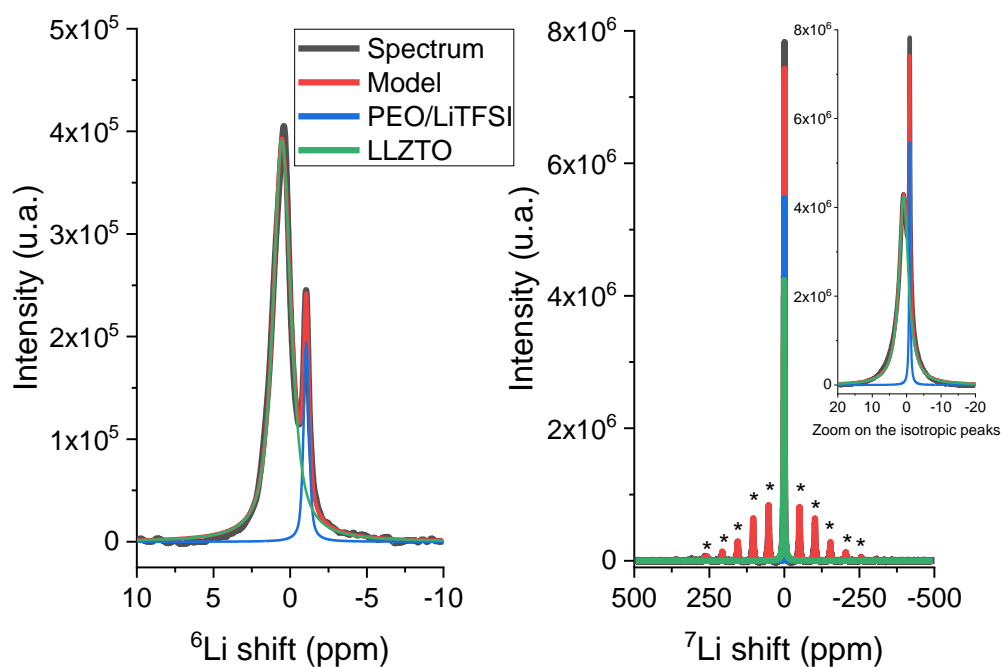


Figure V-6. ${}^6\text{Li}$ and ${}^7\text{Li}$ high-resolution ssNMR spectra of the composite SSE after 100 h at 60°C (C2). Asterisks indicate spinning sidebands.

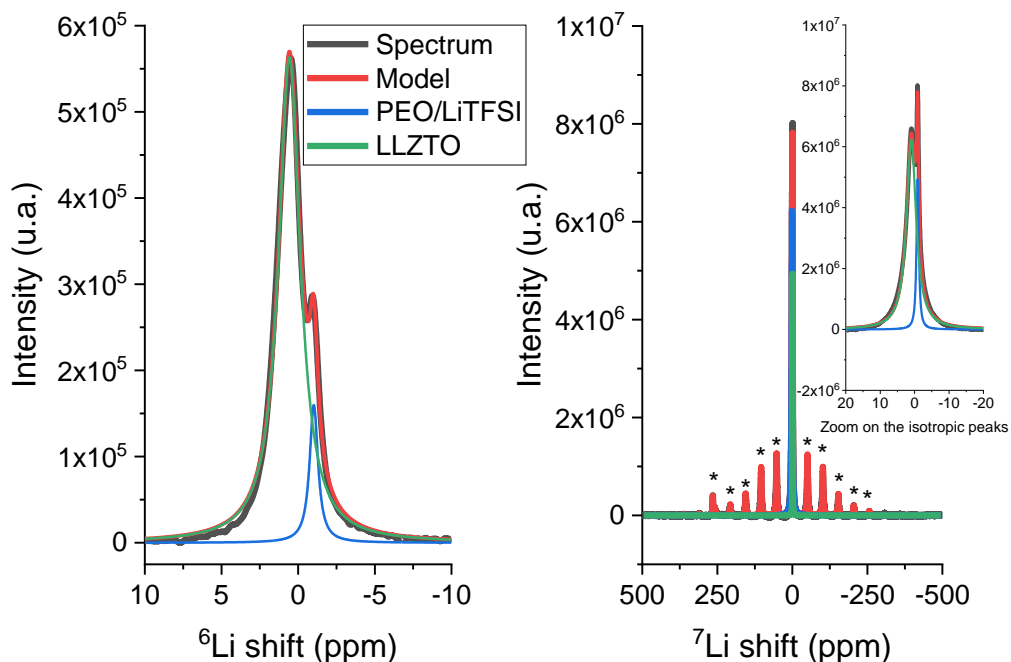


Figure V-7. ${}^6\text{Li}$ and ${}^7\text{Li}$ high-resolution ssNMR spectra of the composite SSE after applying a constant current density of $50\ \mu\text{A} \cdot \text{cm}^{-2}$ during 100 h at 60°C (C3). Asterisks indicate spinning sidebands.

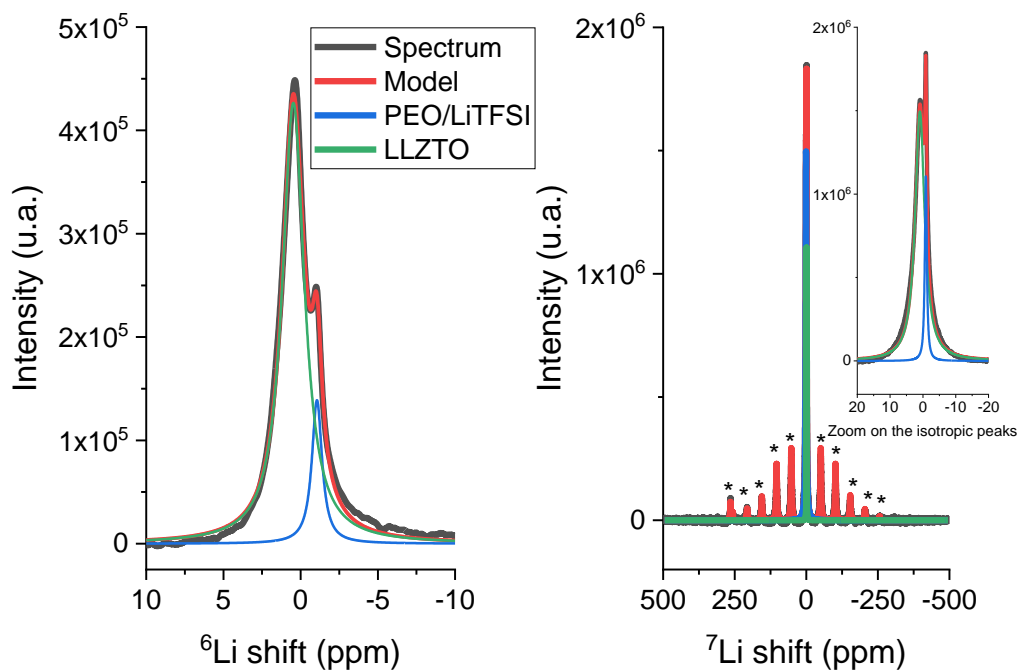


Figure V-8. ${}^6\text{Li}$ and ${}^7\text{Li}$ high-resolution ssNMR spectra of the composite SSE after applying a constant current density of $50 \mu\text{A} \cdot \text{cm}^{-2}$ during 50 h at 60°C (C4). Asterisks indicate spinning sidebands.

High-resolution ssNMR spectra presented on Figure V-6, Figure V-7, and Figure V-8 were processed in the same way as the reference sample, C1. Phase adjustment and baseline correction were identical for instance. Additionally, all integrals were obtained by applying the same spectral limits as those used on C1 spectra. Legend colours are identical to facilitate comparison between spectra. Finally, a new isotropic contribution was detected on the ${}^7\text{Li}$ spectrum of composite SSEs C2, C3 and C4 at 265 ppm. On Figure V-9, an enlargement allows to observe the new isotropic peak fitted by the purple dotted line.

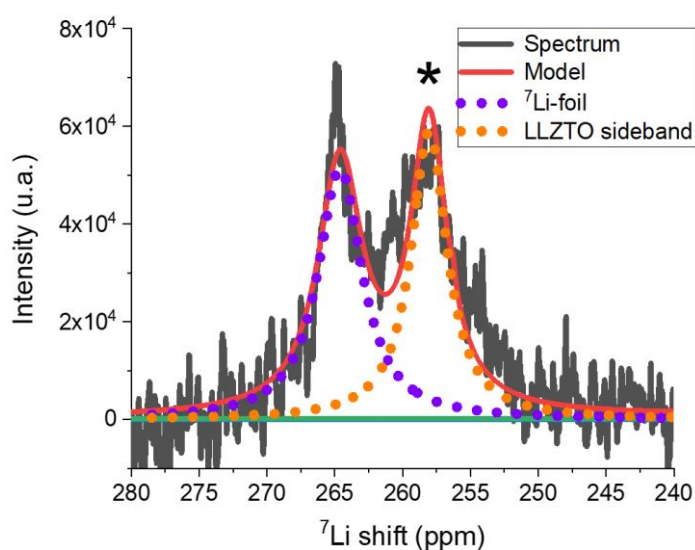


Figure V-9. Enlargement of the ${}^7\text{Li}$ high-resolution ssNMR spectrum of C2 highlighting the detection of the ${}^7\text{Li}$ -foil contribution at 265 ppm. Asterisk indicates a LLZTO spinning sideband.

Based on literature, this new isotropic peak can be assigned to metallic lithium. [138] [139] [140] Its detection is explained by the little scraps of lithium metal remaining at the surface of the composite SSEs. The isotropic peak of metallic lithium overlaps one spinning sideband of the ceramic particles represented by an orange dotted line on Figure V-9. An overestimation of ^7Li may lead to an underestimation of the ^6Li abundance. Thus, by using the Dmfit software, both contributions were deconvoluted, allowing to subtract the absolute integral of metallic lithium contribution from the global absolute integral. According to deconvolution performed on Dmfit, the metallic lithium contribution represents only 0.7%, 1.8%, and 2.0% of the ^7Li absolute integral of C2, C3, and C4, respectively. Thanks to this data processing, the Li-foils contribution presence does not affect ^6Li abundance estimation of composite SSEs. The signal of the Li-foils was not detected on the ^6Li spectra because the studied chemical shift window is narrower: $[-196.3 ; 196.3]$ ppm.

^6Li abundances of C2, C3, and C4 were estimated by combining the ^6Li and ^7Li absolute integrals determined on Figure V-6, Figure V-7, and Figure V-8, respectively, thanks to the S_{global} of 23.1. Table V-4 sums up global ^6Li abundance ($\% ^6\text{Li}_{\text{global}}$) of the composite SSEs.

Table V-4. Global ^6Li abundance estimations ($\% ^6\text{Li}_{\text{global}}$) of the composite SSEs C2, C3, and C4, by using S_{global} .

Composite SSE	$\% ^6\text{Li}_{\text{global}}$ (%)
At lithium natural isotopic abundance (C1, reference)	7.6 ± 0.5
After 100 h at 60° C (C2)	35.7 ± 2.0
After a CP sequence during 100 h at 60° C (C3)	56.0 ± 2.0
After a CP sequence during 50 h at 60° C (C4)	52.5 ± 2.0

Results presented in Table V-4 led to a global estimation of the lithium isotopic abundances induced after heating and after applying a CP sequence at 60° C. The composite SSE C2 was enriched up to 35.7% of ^6Li after 100 h at 60° C (Table V-4). The applied pressure due to the spring in the coin cell (about 1 bar) also may help to keep intimate contact at the interfaces. Applying a current density of $50 \mu\text{A} \cdot \text{cm}^{-2}$ led to an increase of the enrichment up to 56.0% of ^6Li (C3). The applied current density during 100 h at 60° C contributed to an increase of the ^6Li abundance by 21.7%. A last experiment was carried out by applying the same current density only during 50 h at 60° C on C4. ^6Li abundance was estimated at 52.5% of ^6Li . Only half of each composite SSE was analysed, it can affect the results if lithium diffusion pathways are not homogeneous in the whole sample.

Two distinct materials are present in each sample. Consequently, it becomes exciting to differentiate ^6Li abundance of the ceramic particles and of the polymer electrolyte by processing data differently. It may help to trace lithium diffusion pathways in such a complex device. On the ^6Li spectrum (Figure V-5), both contributions were detected at 0.4 ppm for the ceramic particles, and at -1.0 ppm for the polymer electrolyte. On the ^7Li spectrum, both contributions were detected, at 0.9 and -0.9 ppm, for the ceramic particles and the polymer electrolyte, respectively. The absolute integrals percentage of each contribution can thus be determined by using Dmift. Peaks assignment was based on literature. [141] [142] Same

trends arise from these works. However, chemical shifts differences may be due to the influence of the specific matrix present in our study.

In such case, the global normalisation factor S_{global} cannot be used anymore, and new S factors have to be determined to combine ${}^6\text{Li}$ and ${}^7\text{Li}$ absolute integrals of the polymer electrolyte or the ceramic particle contributions. Therefore, as a first approximation, normalisation factors were estimated from high-resolution ssNMR characterisations of the pure reference materials (only polymer electrolyte or only ceramic particles) obtained with the same acquisition conditions applied to characterise the composite SSEs. The normalisation factor of the polymer ($S_{polymer}^{pure}$) and that of the ceramic particles ($S_{ceramic}^{pure}$) were determined to be 21.1 and 35.7, respectively. Figure V-10 presents a summary of the estimated ${}^6\text{Li}$ abundance of both materials (polymer and ceramic particles) by combining ${}^6\text{Li}$ and ${}^7\text{Li}$ absolute integrals with either $S_{polymer}^{pure}$ or $S_{ceramic}^{pure}$, respectively.

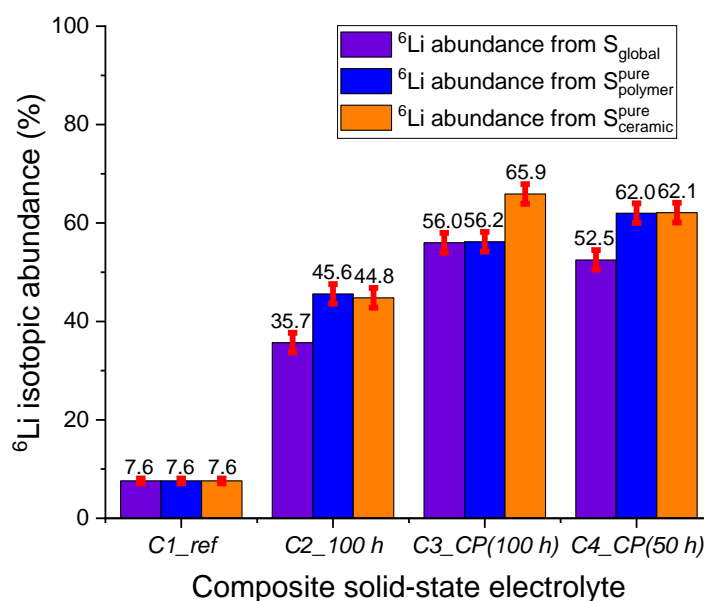


Figure V-10. ${}^6\text{Li}$ abundance estimations of composite SSEs C2, C3, and C4 by using $S_{polymer}^{pure}$ (blue bars) and $S_{ceramic}^{pure}$ (orange bar) obtained from the pure materials and C1 as reference sample. Comparison with global estimations sum up in Table V-4 (purple bar). Uncertainties are estimated at 0.5% on the reference sample and at 2.0% on the others.

On Figure V-10, ${}^6\text{Li}$ abundance of composite SSEs C2, C3, and C4 are estimated by using $S_{polymer}^{pure}$ (blue bars) and $S_{ceramic}^{pure}$ (orange bar) obtained from the pure materials and C1 as reference sample. Uncertainties are estimated at 0.5% on the reference sample and at 2.0% on the others. ${}^6\text{Li}$ abundances obtained in each domain were higher compared to the ${}^6\text{Li}$ global estimation already presented Table V-4 (purple bar). Thus, results are not correct because ${}^6\text{Li}$ abundance of both contributions was overestimated. To solve this issue, an alternative way to process data is suggested. A normalisation factor S is still calculated for each material, but instead of using pure references, the deconvolution of the ${}^6\text{Li}$ and ${}^7\text{Li}$ spectra obtained from the composite SSE C1 (Figure V-5) are used. Lithium chemical environment should be the same in the analysed samples and in the reference sample, C1. Thus, the response to the 90° pulse may depend only of the lithium isotopic abundance, considering identical, the acquisition parameters between the reference sample analysis and the analysis of samples with unknown

lithium abundance. [16] New normalisation factors for the polymer ($S_{polymer}^{composite}$) and for the ceramic particles ($S_{ceramics}^{composite}$) were estimated at 9.0 and 26.5, respectively. A $S^{composite}$ can be calculated by weighted S factors of each material ($S_{polymer}^{composite}$ and $S_{ceramics}^{composite}$) by the full width at half maximum (FWHM) percentage of the peak contribution. Weighting by FWHM is relevant because, it was found that S factors are affected by the dynamics of the different types of lithium (related to their chemical environment) in a given sample. The origin of this problem arises from the effective spin-spin relaxation time (T_2^*) differences that can be observed for different NMR signals inside the same sample. T_2^* is describing the transverse relaxation. [143] As a matter of fact, shorter T_2^* may underestimate the signal intensity under magic angle spinning (MAS) conditions. This weighting process is a way to take into account the effects of various T_2 differences in high-resolution ssNMR. [144] Equation V-1 was established in order to compare S factors of various materials.

$$S^{composite} = S_{polymer}^{composite} \times \frac{FWHM_{polymer}}{FWHM_{polymer} + FWHM_{ceramics}} + S_{ceramic}^{composite} \times \frac{FWHM_{ceramics}}{FWHM_{polymer} + FWHM_{ceramics}} \quad V-1$$

with S_i , the normalisation factor of the domain i composing the composite SSE, and $FWHM_i$, the full width at half maximum of the i contribution. $FWHM_{polymer}$ and $FWHM_{ceramics}$ were determined with Origin 2020. They were estimated at 0.37 and 1.24 ppm, respectively. With these values, a $S^{composite}$ of 22.5 was calculated. $S^{composite}$ is close to S_{global} (23.1) implying that the width of the peaks affects the normalisation factor. That is why a normalisation factor has to be calculated for each studied matrix. Thus, 6Li abundance can be accurately estimated in both domains, by using their respective normalisation factor (Figure V-11).

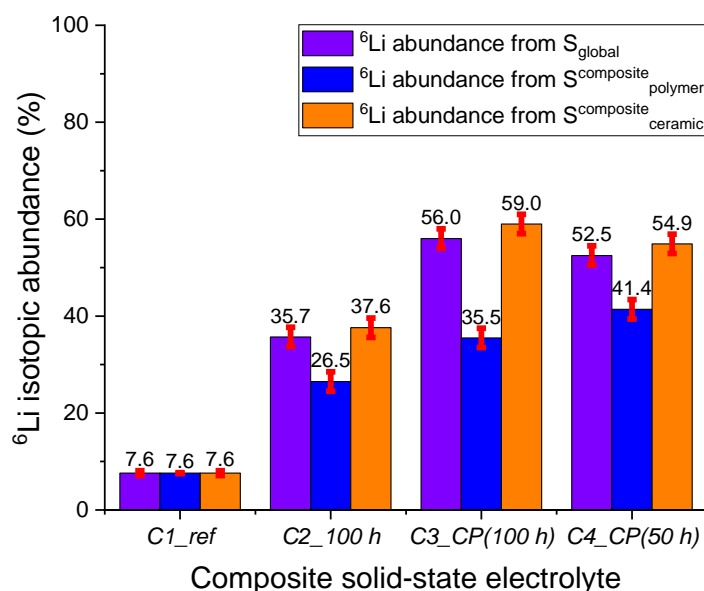


Figure V-11. 6Li abundance estimations of composite SSEs C2, C3, and C4 by using $S_{polymer}^{composite}$ (blue bars) and $S_{ceramics}^{composite}$ (orange bar) obtained from the composite SSE C1 as reference. Comparison with global estimations sum up in Table V-4 (purple bar). Uncertainties are estimated at 0.5% on the reference sample and at 2.0% on the others.

On Figure V-11, the estimated ${}^6\text{Li}$ abundances are summarised. The ceramic particles are more enriched in ${}^6\text{Li}$ than the polymer electrolyte in C2, C3 and C4. Thus, ${}^6\text{Li}^+$ ions seem to diffuse preferentially through the ceramic. After 100 h at 60° C, the polymer electrolyte was enriched at 26.5% of ${}^6\text{Li}$ against 37.6% of ${}^6\text{Li}$ in the ceramic particles. Then, applying a current density of $50 \mu\text{A} \cdot \text{cm}^{-2}$ during 100 h led to an increase of the enrichment up to 35.5% of ${}^6\text{Li}$ in the polymer electrolyte and up to 59.0% in the ceramic particles. Finally, applying a current density of $50 \mu\text{A} \cdot \text{cm}^{-2}$ during 50 h led to an increase of the enrichment up to 41.4% of ${}^6\text{Li}$ in the polymer electrolyte and 54.9% in the ceramic particles.

In order to better interpret the obtained results, the average ${}^6\text{Li}$ abundance of a composite SSE ($\% {}^6\text{Li}_{average}^{composite}$) is calculated with the following Equation V-2,

$$\begin{aligned} \% {}^6\text{Li}_{average}^{composite} &= \% {}^6\text{Li}_{polymer} \times \% {}^{mol}_{polymer} + \% {}^6\text{Li}_{ceramics} \times \% {}^{mol}_{ceramics} \\ &= \% {}^6\text{Li}_{polymer} \times \frac{n_{polymer}(\text{Li})}{n_{polymer}(\text{Li}) + n_{ceramics}(\text{Li})} + \% {}^6\text{Li}_{ceramics} \times \frac{n_{ceramics}(\text{Li})}{n_{polymer}(\text{Li}) + n_{ceramics}(\text{Li})} \quad \text{V-2} \end{aligned}$$

with $\% {}^6\text{Li}_i$ the ${}^6\text{Li}$ abundance of the material i , and $n_i(\text{Li})$ the mole of lithium in the material i .

The $\% {}^6\text{Li}_{average}^{composite}$ determined from both contributions must match with the global ${}^6\text{Li}$ abundance of a composite SSE ($\% {}^6\text{Li}_{global}^{composite}$). Note that the ${}^6\text{Li}$ abundances of each material was weighted by the percentage of lithium moles contained in each material ($\% {}^{mol}_i$) in order to provide accurate result. Table V-5 sums up and confronts the ${}^6\text{Li}$ abundance averages obtained by Equation V-2, and the determined global ${}^6\text{Li}$ abundances.

Table V-5. Comparison of ${}^6\text{Li}$ abundances estimated by using $S_{polymer}^{composite}$ and $S_{ceramics}^{composite}$ with the global estimation of the ${}^6\text{Li}$ abundance estimated by using S_{global} .

Composite SSE	$\% {}^6\text{Li}_{average}^{composite}$ (%)	$\% {}^6\text{Li}_{global}^{composite}$ (%)
At lithium natural isotopic abundance (C1, reference)	7.6 ± 0.5	7.6 ± 0.5
After 100 h at 60° C (C2)	36.0 ± 2.0	35.7 ± 2.0
After a CP sequence during 100 h at 60° C (C3)	55.9 ± 2.0	56.0 ± 2.0
After a CP sequence during 50 h at 60° C (C4)	52.7 ± 2.0	52.5 ± 2.0

In Table V-5, the $\% {}^6\text{Li}_{average}^{composite}$ are close to the $\% {}^6\text{Li}_{global}^{composite}$. Regarding Equation V-2, the composite SSE C2 is enriched at 36.0% of ${}^6\text{Li}$ after 100 h at 60° C. The composite SSE C3 is enriched at 55.9% of ${}^6\text{Li}$ after applying a constant current density of $50 \mu\text{A} \cdot \text{cm}^{-2}$ during 100 h. The composite SSE C4 is enriched at 52.7% of ${}^6\text{Li}$ after applying a constant current density of $50 \mu\text{A} \cdot \text{cm}^{-2}$ during 50 h.

Taking into account uncertainties of 2%, the global and the average abundances of each material match. It confirms the relevance of the developed methodology to perform ${}^6\text{Li}$

and ^7Li isotope abundance estimation using high-resolution ssNMR, involving specific acquisition parameters and advanced data processing.

The fact these high-resolution ssNMR analyses allow the determination lithium amount was verified. Figure V-12 reports the amount of lithium estimated by high-resolution ssNMR in the polymer electrolyte ($n_{\text{polymer}}^{\text{ssNMR}}$) and in the ceramic particles ($n_{\text{ceramics}}^{\text{ssNMR}}$).

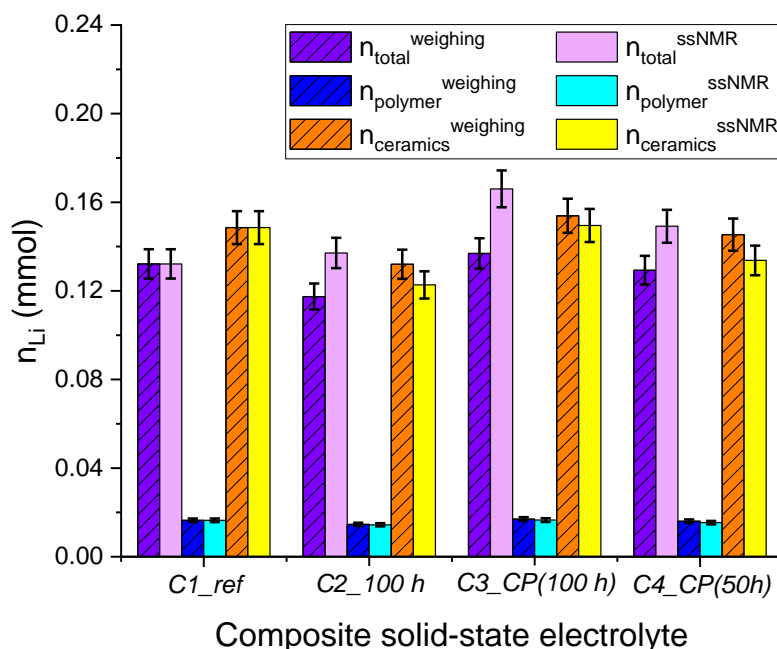


Figure V-12. Lithium amount (n^{ssNMR}) was determined by ssNMR in C2, C3 and C4. Comparison of lithium amounts in the whole composite SSEs ($n_{\text{total}}^{\text{ssNMR}}$), specifically in the polymer electrolyte ($n_{\text{polymer}}^{\text{ssNMR}}$) and specifically in the ceramic particles ($n_{\text{ceramics}}^{\text{ssNMR}}$), estimated by weighing (purple, blue, and orange hatched bars) and by high-resolution ssNMR (pink, light blue, and yellow bars). Sample C1 was used as reference sample. Uncertainties are estimated at 5% on the determination of the lithium amount.

On Figure V-12, the total amount of lithium estimated by weighing the composite SSE present in each insert ($n_{\text{total}}^{\text{weighing}}$) corresponds to the purple bars. It is compared to the total amount of lithium estimated by high-resolution ssNMR ($n_{\text{total}}^{\text{ssNMR}}$) represents by the pink bars. Sample C1 was used as a reference sample, and the n^{weighing} values were set regarding the composite SSE preparation and the probed weight of each insert (Table V-3). The estimations of $n_{\text{total}}^{\text{ssNMR}}$ are slightly overestimated compared to $n_{\text{total}}^{\text{weighing}}$. Through more detailed high-resolution ssNMR analyses, lithium from the polymer electrolyte (blue and light-blue bars) is distinguished from the one contained into the ceramic particles (orange and yellow bars). Notice that lithium is 27 times lower in the polymer electrolyte than in ceramic particles due to their respective initial lithium concentration of 1.25 M and 33.81 M.

To conclude, high-resolution ssNMR characterisations led to global estimations of ^6Li abundance in the whole composite SSEs C2, C3, and C4. Furthermore, distinction between lithium contained into the polymer electrolyte and into the ceramic particles allow to determine a ^6Li abundance for each domain. $^6\text{Li}^+$ ions seem to diffuse more into the ceramic particles. It would be a strength to confirm this hypothesis at the local scale. Indeed, as

high-resolution ssNMR characterises sample bulk, it is not possible to affirm that in a composite SSE area, ceramic particles are more enriched in ${}^6\text{Li}$ than the polymer electrolyte. However, advanced surface characterisation techniques with a high lateral resolution may provide some keys in order to better understand Li^+ ions diffusion dynamics in composite SSEs.

b. ToF-SIMS characterisations

ION-TOF ToF-SIMS 5 spectrometer has a standard lateral resolution of a few micrometres by using an analyser mode with high mass resolution. [64] Analyser modes set to enhance lateral resolution also exist. They allow to obtain a lateral resolution lower than $100/200\text{ nm}$ but to the detriment of the mass resolution. [64] However, an “Extractor Delay” mode developed by ION-TOF can increase the lateral resolution down to 100 nm without losing much on the mass resolution. [145] This mode was used to attempt discerning the ceramic particles having a diameter between 400 and 600 nm . No molecular fragment corresponding to the ceramic was detected by performing only surface analyses, confirming that particles are deeply embedded in the polymer matrix. To reach them, it is mandatory to achieve a controlled sputtering of the composite SSE surface. A crater of $300 \times 300\ \mu\text{m}^2$ was sputtered by using a gas cluster ion beam (GCIB) composed of $\text{Ar}_{1500}\ 15\text{ keV}$ ($I = 10,70\text{ nA}$) during 1 h . Then, an analysis of $80 \times 80\ \mu\text{m}^2$ was performed in the crater centre. Ceramic particles were revealed thanks to the sputtering step. Figure V-13 is an example of a $5 \times 5\ \mu\text{m}^2$ enlargement of such ceramic particle after a sputtering step by GCIB.

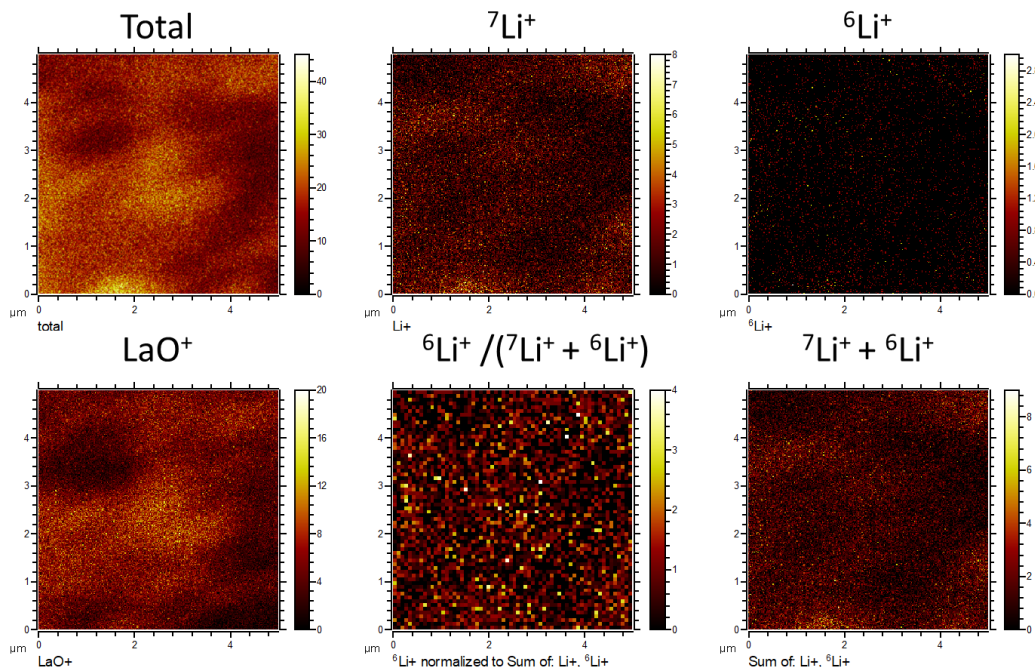


Figure V-13. ToF-SIMS analyses of the composite SSE at lithium natural isotopic abundance.

On Figure V-13, the presence of the ceramic particles was confirmed by the detection of the LaO^+ molecular fragment characteristic from the LLZTO ceramic particles. Furthermore, data processing revealed an abundance of 94.2% in ^7Li on the particles. This value is awaited because the composite SSE is at lithium natural isotopic abundance. However, the lateral resolution was not high enough to access the interfaces between the ceramic particles and the polymer electrolyte. Furthermore, polymer electrolyte abrasion is not perfect. Thus, while studying enriched samples, ^6Li abundance determination of the ceramic particles can be affected by the one of the polymer electrolyte. Here, lateral resolution may be affected by the sputtering methodology. Revealing ceramic particles was difficult.

To conclude, in such conditions, lateral resolution of these ToF-SIMS characterisations was not high enough to properly probe ceramic particles contained into a polymer electrolyte. Therefore, with the help of Orsay Physics company another characterisation technique, orthogonal ToF-SIMS, is performed in order to obtain a better lateral resolution while probing the chemistry and lithium isotopic abundance of ceramic particles embedded in a polymer electrolyte.

c. Orthogonal ToF-SIMS characterisation coupled with focused ion beam scanning electron microscopy (FIB-SEM) characterisations

- *Description of an orthogonal ToF-SIMS (o-ToF-SIMS) coupled with FIB-SEM*

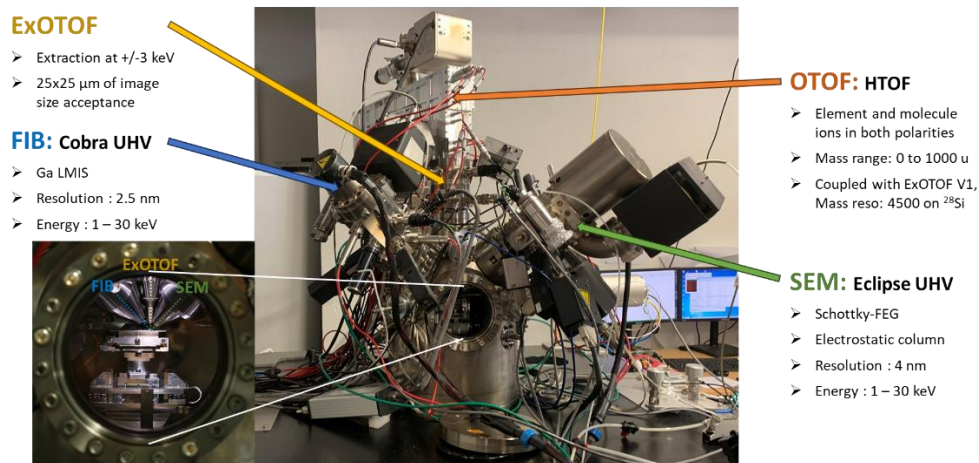


Figure V-14. Equipment used by Orsay Physics to perform orthogonal ToF-SIMS coupled with FIB-SEM. (from Orsay Physic)

Orsay Physics company owns the advanced equipment presented on Figure V-14. This instrument allows to combine FIB-SEM analyses with SIMS characterisations. However, until now, samples are exposed to air between the FIB cross section and o-ToF-SIMS analysis. However, risks that lithium isotopic abundance could be impacted on the sample surface are low. Furthermore, a transfer under inert atmosphere could be possible by using a sealed transfer vessel or using a specific stage allowing to modify the inclination of the sample into the analysis chamber.

Figure V-15 presents the principle of an orthogonal ToF-SIMS (o-ToF-SIMS).

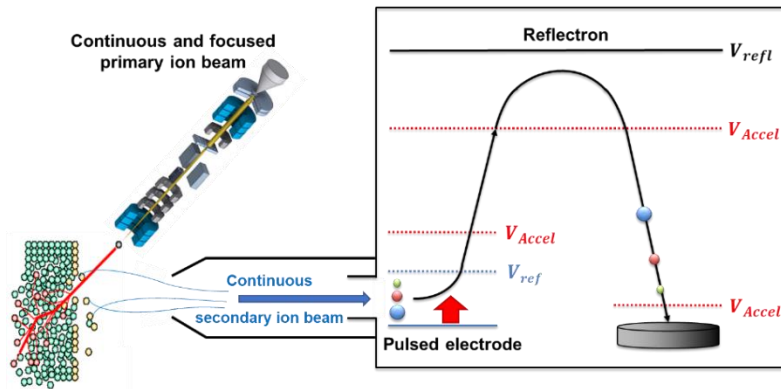


Figure V-15. Schematic of the orthogonal ToF-SIMS principle. (from Orsay Physic)

The o-ToF-SIMS principle is based on the ToF-SIMS principle previously described in chapter I, but there are some non-negligible differences. The key advantage of the o-ToF-SIMS technique compared with the ToF-SIMS lies in the use of a continuous and focused primary ion beam, while it is pulsed in the case of standard ToF-SIMS (Figure V-15). [146] [147] While the continuous primary ion beam continuously sputters the sample surface, secondary ions are collected by an optic column and transferred into the mass spectrometer. Once inside the mass spectrometer, the secondary ions are accelerated orthogonally through the reflectron by a pulsed electrode. [146] This pulse provides a precise starting time of the time-of-flight measurement without disturbing the primary ion beam. [148] As a result, the o-ToF-SIMS technique allows high lateral resolution, while keeping a high mass resolution. [148] Almorici *et al.* could reach a lateral resolution lower than 30 nm by upgrading an o-ToF-SIMS with a new optic of secondary ion extraction designed to improve transmission and mass resolution. [147] Furthermore, a high mass resolution of 4,500 was also obtained by characterising ^{28}Si by o-ToF-SIMS. [147] Thus, the o-ToF-SIMS technique can easily distinguish lithium isotopes. These assets are investigated to determine if o-ToF-SIMS can also allow accurate lithium isotopic abundance estimation, and if it can provide precise ^6Li abundance mapping thanks to its high lateral resolution.

The major drawback lies in the low duty cycle on collected secondary ions due to the pulsation of the secondary ion beam. The duty cycle is the filling time of the pulsed cell before the pulsation of a considered species divided by the time of flight after the pulsation of the same species. Therefore, the duty cycle depends on the mass of the considered secondary ion and on the mass range selected. For instance, the duty cycle is around 30% for heaviest masses and a few percent for lightest masses, with a mass range of 150 u. [147] The time between two pulses is called the cycle time. It is set to allow the heaviest ion detection. A low duty cycle only lengthens the conventional ToF-SIMS analysis time, while it additionally leads to a signal loss of the lightest secondary ions during o-ToF-SIMS acquisition. However, as lithium has one of the highest ionisation yields, the signal loss on small masses is not a problem for our study.

To sum up, such characterisation technique provides high lateral resolution without altering the high mass resolution. Indeed, as the primary ion beam is continuous, no bunching step is required. Thus, no lateral dispersion is induced.

- *Determination of lithium isotopic abundances by o-ToF-SIMS*

Polymer electrolytes composed of a PEO polymer membrane containing LiTFSI as lithium salt were prepared with various ${}^6\text{Li}$ abundance as described in chapter II. They are analysed by o-ToF-SIMS to assess if this advanced characterisation technique can provide accurate estimations of lithium isotopic abundance. Table V-6 sums up the expected lithium isotopic abundances of four polymer electrolytes obtained based on mass calculations.

Table V-6. Polymer membranes made of PEO and containing LiTFSI at 1.2 M, with various expected lithium isotopic abundances.

Polymer electrolyte	% ${}^7\text{Li}$ (%)	% ${}^6\text{Li}$ (%)	Used salts
A (reference sample)	92.4 ± 0.1	7.6 ± 0.1	${}^7\text{LiTFSI}$
B	66.2 ± 0.1	33.8 ± 0.1	${}^7\text{LiTFSI}$ and ${}^6\text{LiTFSI}$
C	35.2 ± 0.1	64.8 ± 0.1	${}^7\text{LiTFSI}$ and ${}^6\text{LiTFSI}$
D	4.6 ± 0.1	95.4 ± 0.1	${}^6\text{LiTFSI}$

Firstly, ToF-SIMS characterisations were performed on the four polymer electrolytes, based on the developed methodology presented in chapter II. Lithium isotopic abundances of polymer electrolytes were estimated in each case. Then, polymer electrolytes were characterised by o-ToF-SIMS. Notice that o-ToF-SIMS measurements and data treatment were carried out by Orsay Physics collaborators.

The o-ToF-SIMS analyses were performed on an area of $10 \times 10 \mu\text{m}^2$. A Ga^+ ion beam with an energy of 30 kV and a current of 1 pA was used. 500 frames were milled to obtain depth-averaged information. The analysed area can be observed in the centre of Figure V-16.a and Figure V-16.b by performing scanning electron microscope (SEM) after the o-ToF-SIMS analyses. Figure V-16 illustrates the surface state after o-ToF-SIMS analyses on A and D.

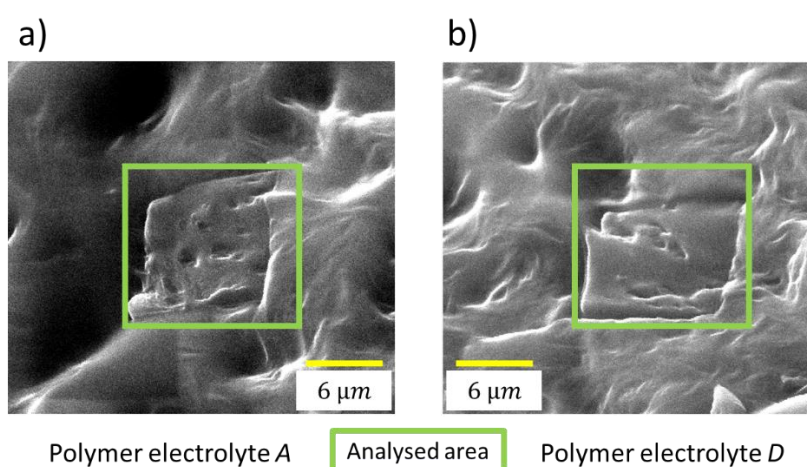


Figure V-16. SEM images of polymer electrolytes A and D after o-ToF-SIMS analyses. The green squares indicate the analysed areas.

Regarding SEM images on Figure V-16, polymer electrolyte surfaces seem rough. However, the o-ToF-SIMS technique is much less dependent on the roughness of the sample than conventional ToF-SIMS. Therefore, the roughness observed on these SEM images induces no problem for our measurements. [74] On Figure V-17, the ${}^6\text{Li}^+$ and ${}^7\text{Li}^+$ peak intensities obtained on the mass spectrum of the polymer electrolyte A are presented.

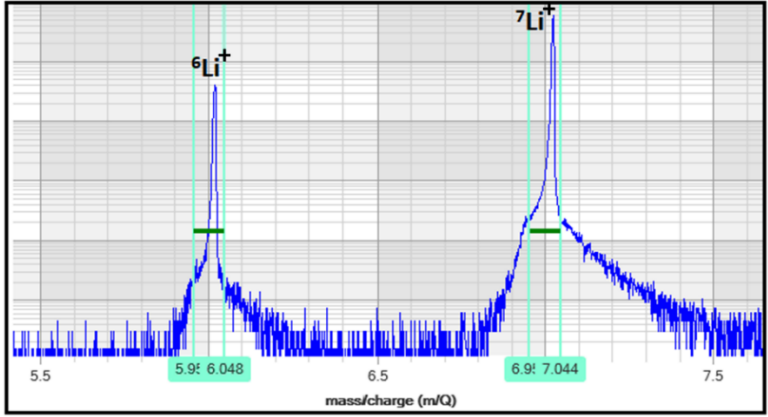


Figure V-17. ${}^6\text{Li}^+$ and ${}^7\text{Li}^+$ mass peaks on the mass spectrum of the polymer electrolyte A.

The mass spectrum on Figure V-17 confirms and illustrates that lithium isotopes can be separated. ${}^7\text{Li}$ abundance was estimated by o-ToF-SIMS thanks to the same equation as presented in the ToF-SIMS methodology, involving ${}^6\text{Li}^+$ and ${}^7\text{Li}^+$ signal intensities.

On Figure V-18, ToF-SIMS and o-ToF-SIMS results are both compared. They are also confronted to the expected ${}^7\text{Li}$ abundances.

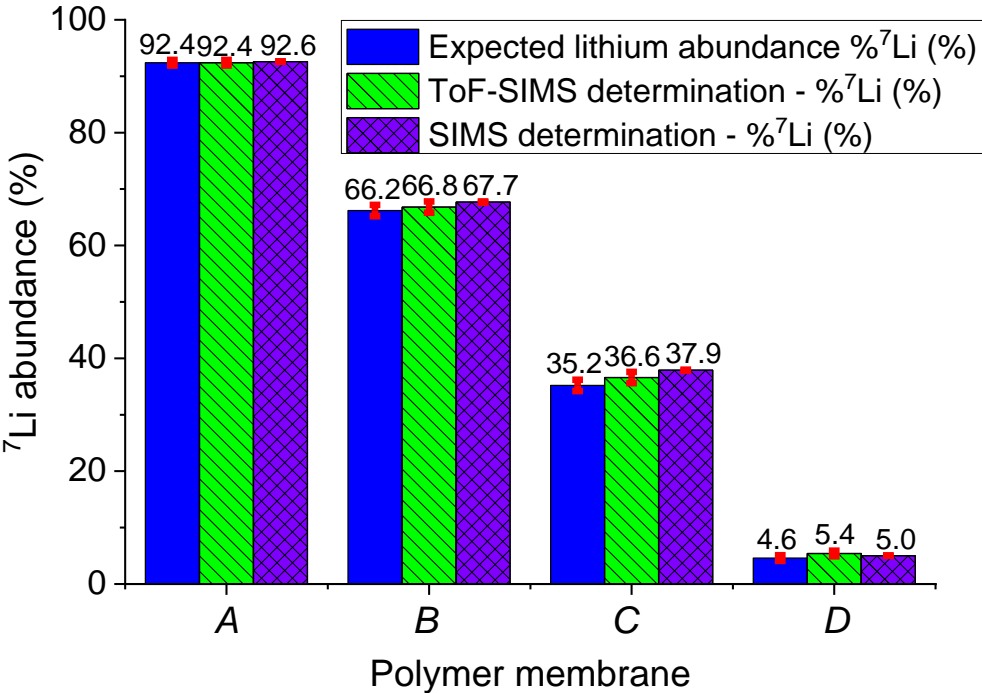


Figure V-18. Comparison of expected lithium isotopic abundances of polymer membranes (blue bars) with the ones determined by ToF-SIMS (green bars), and the ones determined by o-ToF-SIMS (purple bars). Red bars represent uncertainties.

ToF-SIMS results (green bars) and o-ToF-SIMS results (purple bars) are confronted on Figure V-18. Blue bars represent the expected ${}^7\text{Li}$ abundances determined by weighting the lithium salts. ToF-SIMS characterisations of polymer electrolytes *A*, *B*, *C* and *D* lead to ${}^7\text{Li}$ abundance estimations of $92.4 \pm 0.5\%$, $66.8 \pm 1\%$, $36.6 \pm 1\%$ and $5.4 \pm 0.5\%$, respectively. Considering the uncertainties indicated in red, ToF-SIMS results are accurate compared to the expected ${}^7\text{Li}$ abundances. Furthermore, o-ToF-SIMS characterisations also provide relevant results. ${}^7\text{Li}$ abundances of polymer electrolytes *A*, *B*, *C* and *D* were estimated at $92.6 \pm 0.03\%$, $67.7 \pm 0.1\%$, $37.9 \pm 0.1\%$ and $5.0 \pm 0.03\%$ of ${}^7\text{Li}$, respectively. Notice that o-ToF-SIMS uncertainties are ten times lower than the ToF-SIMS ones. Uncertainties of ${}^7\text{Li}$ abundance estimations of polymer electrolytes *B* and *C* are higher than those of polymer electrolytes *A* and *D*, for both techniques. This is due to the mixing salts step, which slightly increases the uncertainty on the lithium isotopic abundance estimation. The main trend is that ${}^7\text{Li}$ abundances are slightly overestimated, but still close to the expected lithium isotopic abundance. Thus, as for ToF-SIMS, o-ToF-SIMS technique can be performed to accurately estimate lithium isotopic abundance of lithiated sample, and to track lithium diffusion in various conditions.

- *Application to the study of lithium dynamics in composite SSEs*

Exactly the same four composite SSEs characterised by high-resolution ssNMR in section 5.3.a are analysed by o-ToF-SIMS. Their preparation was described in section 5.1. Preliminary steps were required in order to access the depth of the composite material. Cross sections were milled by performing FIB-SEM. They allow to reveal ceramic particles contained into the polymer electrolyte matrix. FIB cross sections have already been characterised by o-ToF-SIMS in literature. Lorinčík *et al.* performed orthogonal ToF-SIMS and energy dispersive X-ray spectroscopy (EDX) analyses on FIB-SEM cross sections to quantify rare Earth elements, such as Er^{3+} , and Yb^{3+} , which are doping optical fibres. [149] SEM images on Figure V-19 illustrate a FIB cross section carried out on the composite SSE C3.

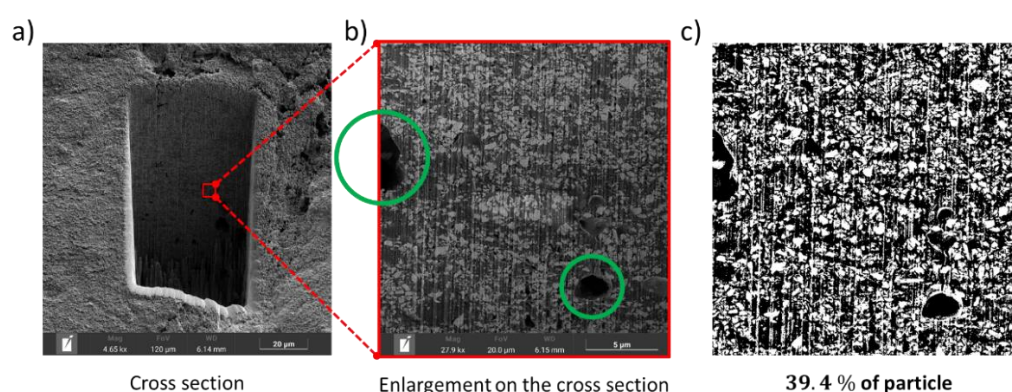


Figure V-19. a) FIB-SEM cross section on C3 with 30 keV and 30 nA. b) Enlargement of the FIB-SEM cross section. Voids are indicated by green circles c) Determination of the surface occupied by the ceramic particles.

FIB cross sections were performed on each sample by using a gallium FIB at 30 keV. Figure V-19.a offers a large view of the FIB-SEM cross section carried out on C3, and Figure V-19.b presents an enlargement of it. Curtaining artefacts can be observed due to heterogeneity density of the milled section. Furthermore, presence of voids can be detected on SEM images (green circles on Figure V-19.b). It is most probably due to the electrolyte porosity occurring during its preparation. The mixing step may incorporate air into the polymer electrolyte. Additionally, solvent evaporation has to be slow in order to obtain a homogenous membrane. Porosity will affect lithium ions pathways. However, voids volume density seems low. Figure V-19.b was processed in order to obtain Figure V-19.c. It is estimated that ceramic particles are recovering 39.4% of the surface according to 2D images. Percolation paths may exist in such conditions. However, this value is overestimated because the used threshold technique to estimate this percentage is affected by curtaining effects. Some particles are in contact, but tomography FIB-SEM may be required in order to quantify it.

Table V-7 confronts the ^6Li abundances estimations obtained by characterising the four studied samples by either high-resolution ssNMR (section 5.3.a) or by o-ToF-SIMS. The o-ToF-SIMS analyses were performed on the top of the FIB cross sections, near the side which was in direct contact with the ^6Li -foil. The analysis position was at 20 or 30 μm in depth from the surface (Figure V-20.a).

Table V-7. Global ${}^6\text{Li}$ abundance of the composite SSEs, which have undergone various tests.

Composite SSE	$\% {}^6\text{Li}_{\text{global}}^{\text{NMR}}$ (%)	$\% {}^6\text{Li}_{\text{surface}}^{\text{o-ToF-SIMS}}$ (%)
At lithium natural isotopic abundance (C1, reference)	7.6 ± 0.5	7.4 ± 0.1
After 100 h at 60° C (C2)	35.7 ± 2.0	58.4 ± 0.1
After a CP sequence during 100 h at 60° C (C3)	56.0 ± 2.0	44.2 ± 0.1
After a CP sequence during 50 h at 60° C (C4)	52.5 ± 2.0	76.0 ± 0.1

In Table V-7, ${}^6\text{Li}$ abundance of C1 is accurately estimated at 7.4% by o-ToF-SIMS. It is close to the expected 7.6% of ${}^6\text{Li}$. This estimation confirms that o-ToF-SIMS technique can be used with confidence to determine ${}^6\text{Li}$ abundance in a complex sample. In Table V-7, ${}^6\text{Li}$ abundances determined by o-ToF-SIMS are based on an average of two or three measured areas. ${}^6\text{Li}$ abundances were estimated at 58.4, 44.2 and 76.0% for C2, C3, and C4, respectively.

${}^6\text{Li}$ abundances estimated by o-ToF-SIMS differ from the ones obtained by high-resolution ssNMR. They are higher for C2 and C4. This may be attributed to the fact that high-resolution ssNMR technique probes the whole sample. Whereas o-ToF-SIMS technique focuses on a narrow area on the FIB-SEM cross section (Figure V-20.a). Therefore, it is consistent that close to the ${}^6\text{Li}$ -foil, the ${}^6\text{Li}$ abundance is higher than the ${}^6\text{Li}$ average of the whole sample. A higher ${}^6\text{Li}$ abundance would be expected for C3. More precisely, a higher ${}^6\text{Li}$ abundance than what was estimated for C4 would be expected according to the applied electrochemical test. The local ${}^6\text{Li}$ abundance may not be representative of the whole surface of the tested sample. Another possible explanation is that the composite SSE side in contact with the ${}^7\text{Li}$ -foil may be characterised, instead of the side in contact with the ${}^6\text{Li}$ -foil. In such case, these results would be coherent because the estimated ${}^6\text{Li}$ abundance is lower than the bulk estimation obtained by high-resolution ssNMR. Characterising again this sample is mandatory to strengthen the conclusions of this work.

Comparison of lithium isotopic abundances has also been achieved between the ceramic particles, the polymer electrolyte and also at their interface. The methodology to distinguish each domain is explained. Firstly, FIB-SEM cross sections were performed with an energy of 30 keV to reveal the ceramic particles. Results are presented on Figure V-20.

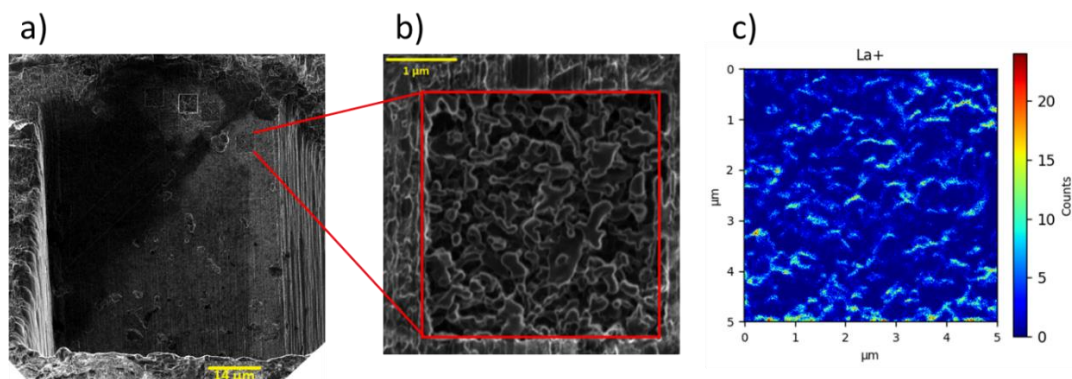


Figure V-20. a) SEM image of the FIB cross section carried out with an energy of 30 keV. b) Enlargement of the analysed area by o-ToF-SIMS (contained in the red square). c) o-ToF-SIMS analysis revealing the presence of the lanthanum molecular fragment (La^+).

SEM image presented on Figure V-20.a shows the obtained FIB cross section. The planar face was then characterised by o-ToF-SIMS. Figure V-20.b presents the analysed area by o-ToF-SIMS, and Figure V-20.c the mapping of the lanthanum molecular fragment (La^+) presence in this area. Characterising composite materials is difficult due to their different sputter yield. These results provide an idea of the sputtering rate of the polymer electrolyte and of the ceramic particles. The correlation between the SEM image taken after the o-ToF-SIMS analysis and La^+ mapping reveals a much lower sputtering rate for the ceramic particles than for the polymer electrolyte. Indeed, ceramic particles are detected on the surface, meaning that the polymer electrolyte has been removed all around the ceramic particles. Knowing the sputtering rate of a material is a crucial information to perform o-ToF-SIMS analyses. From these results, acquisition settings were optimised in order to reduce polymer electrolyte degradation during the acquisition by decreasing the FIB beam current. The various steps to obtain ^6Li abundance mappings from o-ToF-SIMS analyses are discussed on Figure V-21.

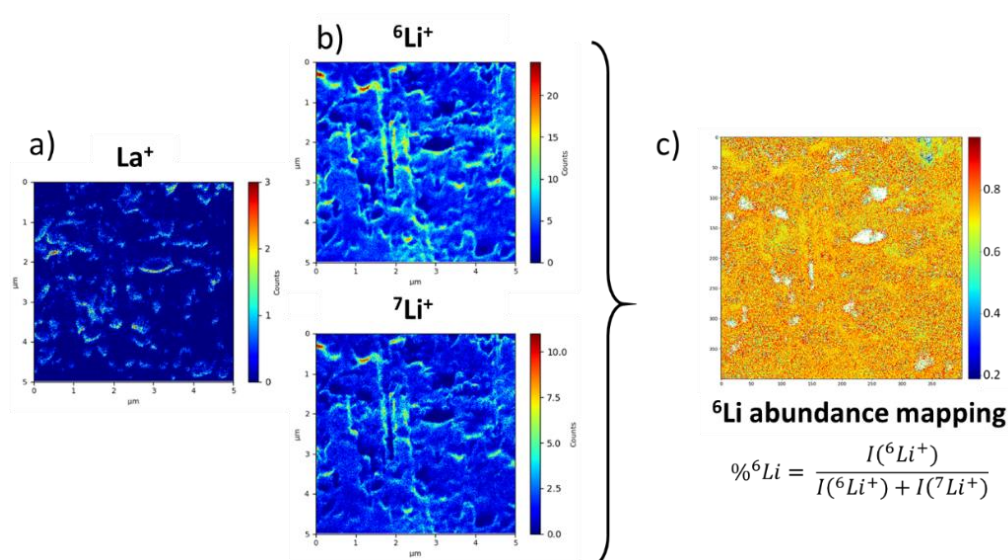


Figure V-21. o-ToF-SIMS analysis on C4 revealed the presence and the localisation of a) La^+ and of b) $^6\text{Li}^+$ and $^7\text{Li}^+$. c) ^6Li abundance mapping by combining $^6\text{Li}^+$ and $^7\text{Li}^+$ intensities.

The chemical composition of the surface can be characterised by o-ToF-SIMS. The molecular fragment La^+ is characteristic from the used LLZTO ceramic particles (Figure V-21.a). ^6Li abundance is mapped (Figure V-21.c) from the analysis of $^6\text{Li}^+$ and $^7\text{Li}^+$ intensities (Figure V-21.b). Notice that topographic visible effects on lithium isotope mappings are removed on the ^6Li abundance mapping, since it results from a division. Here, acquisition settings are chosen to optimise characterisation of the extreme surface, and to avoid any over-sputtering of the polymer electrolyte. From the ^6Li abundance mapping, the global ^6Li abundance can then be estimated for each sample.

Finally, white areas on the ^6Li abundance mapping seem to match with the ceramic particles location by superimposing it with the La^+ mapping. White pixels forming these white areas do not indicate a ^6Li abundance, but a lack of signal to calculate the lithium isotopic abundance (Figure V-21.c). Thus, a low sputtering rate of ceramic particles compared to the

polymer electrolyte is confirmed. Therefore, pixels corresponding to the ceramic particles can be distinguished from pixels corresponding to the polymer electrolyte matrix. This is why ${}^6\text{Li}$ abundance can be specifically determined for each domain. Various masks were used to specifically select a domain. From a ${}^6\text{Li}$ abundance mapping presented on Figure V-22.a, a segmentation program on Python allows to distinguish three domains: the ceramic particles (Figure V-22.b), the polymer electrolyte matrix (Figure V-22.c), and the edge of the ceramic particles (Figure V-22.d).

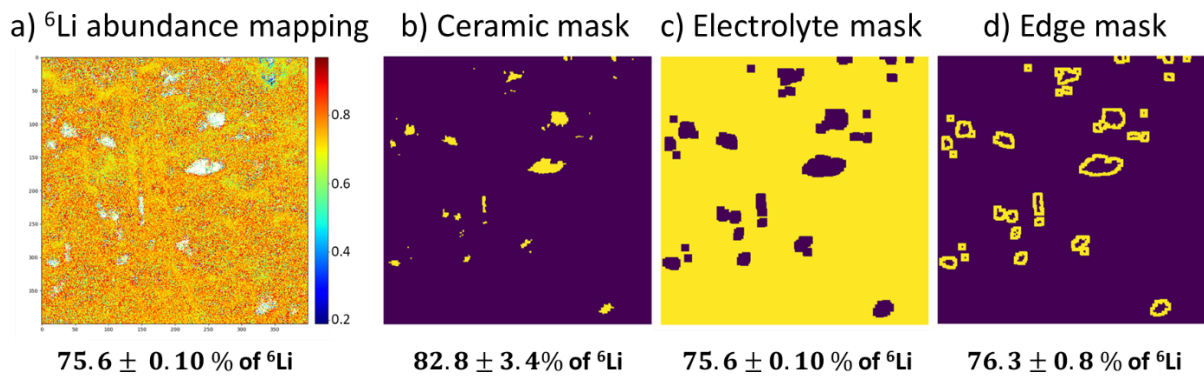


Figure V-22.a) ${}^6\text{Li}$ abundance mapping obtained by o-ToF-SIMS characterisations of C4. Segmentation results of: the ceramic particles (b), the polymer electrolyte matrix (c), and the edge of the ceramic particles (d). The selected domains are filled in yellow. Average ${}^6\text{Li}$ abundance of the considered domain is indicated below each image.

On Figure V-22, ${}^6\text{Li}$ abundance was estimated for each domain and compared. ${}^6\text{Li}$ abundance is equal to $75.6 \pm 0.10\%$ in average (Figure V-22.a). Thanks to the segmentation, more detailed information was obtained. ${}^6\text{Li}$ abundance was estimated at $82.8 \pm 3.4\%$ in the ceramic particles, at $75.6 \pm 0.10\%$ in the polymer electrolyte, and at $76.3 \pm 0.80\%$ at the edges of the ceramic particles. ${}^6\text{Li}$ abundance is higher in ceramic particles than in polymer electrolyte. Furthermore, the ${}^6\text{Li}$ abundance value at the edge is in-between. ${}^6\text{Li}^+$ ions have diffused in both materials regarding to their high ${}^6\text{Li}$ abundance. However, ${}^6\text{Li}^+$ ions seem to diffuse preferentially through the ceramic particles.

A strength of the o-ToF-SIMS technique is its high lateral resolution allowing to detect submicronic ceramic particles and their edges (Figure V-22.d). On Figure V-23, enlargements of the ${}^6\text{Li}$ abundance mapping is presented.

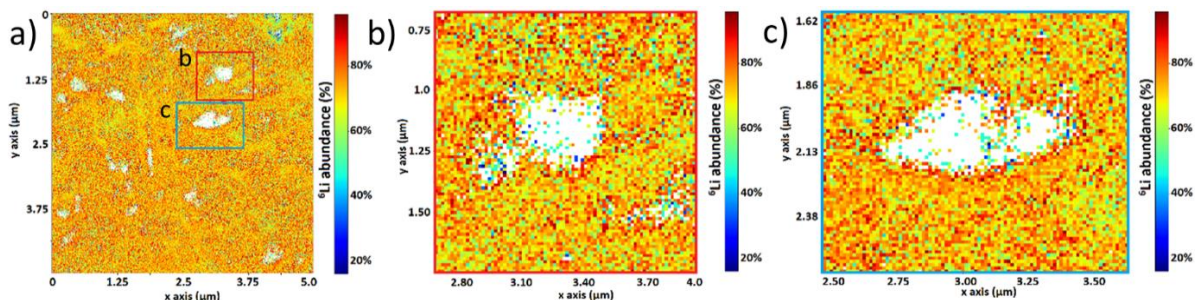


Figure V-23.a) ${}^6\text{Li}$ abundance mapping obtained by o-ToF-SIMS characterisations of C4 after FIB cross section with 30 keV and 4 pA , b) Enlargement of the area circle in red, c) Enlargement of the area circle in blue.

Enlargements of the ^6Li abundance mappings presented on Figure V-23.b and Figure V-23.c highlight that ceramic domains are mostly composed of white pixels. It means that not enough signal is detected to calculate ^6Li abundance for the white pixels. This explains a higher uncertainty of 3.4% (compared to the other domains). The polymer electrolyte is much better detected than the ceramic particles in such acquisition conditions. Tests were performed to acquire more signal intensity from the ceramic particles and they led to polymer electrolyte degradation (Figure V-20).

The segmentation protocol was performed on various areas analysed on each sample (C1, C2, C3 and C4). Various segmentation results are presented in Appendix A-V-2. *Segmentation results on each composite electrolyte.* Figure V-24 summarises some o-ToF-SIMS analyses performed by Orsay Physics company.

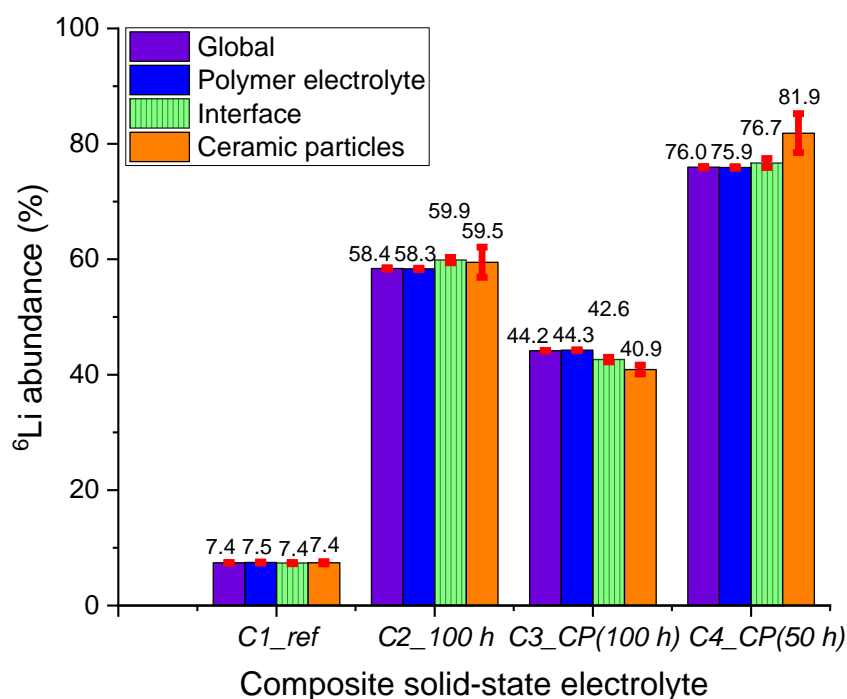


Figure V-24. ^6Li isotopic abundance as a function of the studied domain in each device.

On Figure V-24, the purple bars represent the global ^6Li abundance of each composite SSE. Blue, green, and orange bars correspond to the ^6Li abundance of the polymer electrolyte, the ceramic particle edges, and the ceramic particles, respectively. The average ^6Li abundance was estimated at 7.4% in C1, which is close to the expected 7.6% of ^6Li . It is consistent, as this sample is at lithium natural isotopic abundance. ^6Li abundance was also estimated around 7.4% in each domain. No variation was expected as no heating and no electrochemical step was applied on C1.

Regarding results on C2 and C4, it seems that lithium ions diffuse preferentially into ceramic particles, compared to the polymer electrolyte (Figure V-24). Indeed, ceramic particles ^6Li abundance is estimated at 59.5 and 81.9%, whereas the polymer electrolyte around has a ^6Li abundance of 58.3 and 75.9%, respectively. ^6Li abundance of the polymer

electrolyte is lower than the ceramic particles one, but still high compared to lithium natural isotopic abundance. ${}^6\text{Li}^+$ ions also diffuse through the polymer electrolyte. Lithium diffusion pathways through the ceramic particles might not be present in the whole composite SSE. The existence of ceramic particles percolation pathways was not precisely investigated in this study. It would be relevant, though difficult, to achieve ceramic percolation characterisation through the whole composite SSE depth. Notice that the ${}^6\text{Li}$ abundance of the interface between both domains (edges of ceramic particles) has an intermediate value in all cases, except for *C2* in which it is slightly higher than the ceramic particles ${}^6\text{Li}$ abundance. Following the trend highlighted in Table V-7, o-TOF-SIMS analyses on *C3* should provide the highest ${}^6\text{Li}$ abundance. A similar trend is found on Figure V-24. This confirms that the opposite face of the polymer electrolyte may have been analysed.

5.4. Perspectives

Further investigations can be carried out on composite SSEs. Performing ToF-SIMS and o-ToF-SIMS depth profiling analyses using a 3D analysis mode may be possible. However, it can be difficult to obtain accurate results while working on composite samples. Indeed, composite materials often induce a significant difference in abrasion between the different chemical phases. Thus, obtained data are a mixing of information from different depths processed on the same SIMS image. Thus, ^6Li abundance of the ceramic particles would be mixed with the one of the polymer electrolyte around. Cryogenic conditions could avoid any undesirable damage induced by the primary ion beam. Furthermore, while performing experiment at room temperature, degradation products can be created, depending the selected acquisition mode. [62] Most of the battery materials are composites. To characterise several materials having various properties, such as a melting of polymer partly filling the electrode pores cryogenic acquisition conditions are required in order to keep material integrity during the acquisition. [62]

X-ray tomography is a non-destructive characterisation technique, which provides 3D images of the probed sample. [150] The reconstructed volume can be in the order of submillimetre. X-ray tomography may allow to determine if ceramic particles are percolating or not and if diffusion pathways exist through ceramic particles into the polymer electrolyte matrix. As mentioned in chapter I, Zheng and Hu demonstrated that ceramic percolation affects lithium diffusion pathways and thus the ionic conductivity of the whole system. [46] Yufuit *et al.* performed X-ray computed tomography in order to determine the origin of Li-ion polymer battery failure. [151] EIS only warned them about a decline of battery performances. However, thanks to X-ray computed tomography, they detected deformations due to formation of gas increasing the pressure into the cell. Thus, post-mortem analysis allowed to determine the origin of the short circuits. Méry *at al.* also mentioned that X-ray microtomography combined with numerical simulation could be a powerful tool to determine porosity through a ceramic pellet. [152]

New investigations on composite SSEs can be carried out by combining both experimental characterisations and theoretical calculation methodologies. [153] Regarding the modelling approach, tools such as monte carlo, Vogel–Tammann–Fulcher (VTF) or density functional theory (DFT) may be required. [153] Kim *et al.* demonstrated by electrochemical characterisations and modelling that modifying the LLZTO surface by adding an Ag/Ag-C interlayer electrochemical performances could be enhanced. [154] The system worked over 800 cycles (charge/discharge), instead of only 2. Furthermore, resistance was also decreased. They used density functional theory (DFT) calculation to simulate lithium behaviour at the atomic scale. *Ab initio* molecular dynamics simulations were also carried out in order to describe interface modifications. Based on the mentioned numerical tools, it could also be relevant to model lithium dynamics through a dispersion of ceramic particles in a polymer electrolyte.

Conclusion

A composite SSE made of a polymer electrolyte matrix containing a dispersion of ionic conductive ceramic particles was studied in this chapter. This last device has the most representative design regarding what could be implemented in commercial solid-state batteries. Such SSEs aim at combining advantages of each material. However, it presents a lower ionic conductivity than liquid electrolyte. Thus, investigating specifically lithium diffusion may lead to better understand lithium dynamics through the device. High-resolution ssNMR characterisations highlighted that the choice of the reference sample is crucial in order to obtain accurate ${}^6\text{Li}$ abundance estimations. The reference sample needs to have a similar matrix compared to the one of the analysed samples. High-resolution ssNMR characterisations provide a global estimation of ${}^6\text{Li}$ abundance in the whole composite SSE. Applying a CP sequence on a *dispersion* device at 60°C induces ${}^6\text{Li}$ abundance variations in the composite SSE. Additionally, the ability to distinguish lithium contained in the polymer electrolyte from the one in ceramic particles allows to determine that ${}^6\text{Li}^+$ ions seem to diffuse preferentially through the ceramic particles. ToF-SIMS technique does not have a high enough lateral resolution to carry out precise analysis of such submicrometric ceramic particles. However, o-ToF-SIMS characterisations performed by Orsay Physics company provide accurate estimations of ${}^6\text{Li}$ abundance in composite SSEs at the local scale. Moreover, these analyses are in agreement with high-resolution ssNMR characterisations. Indeed, a higher ${}^6\text{Li}$ abundance was estimated in the ceramic particles, close to the ${}^6\text{Li}$ -foil, compared to the ${}^6\text{Li}$ abundance estimated in the polymer electrolyte matrix around.

Further investigations can be carried out. Performing 3D analysis such as X-ray tomography can offer additional information on ceramic particles distribution into the polymer electrolyte matrix. Even if chemical analyses are not possible, morphology information may explain preferential Li^+ ions pathways. Determining if the LLZTO ceramic particles are percolating is a crucial information because it can influence Li^+ ions pathways. Additionally, several compositions could be investigated to further estimate the influence of the ceramic particle content on the Li^+ ions diffusion pathways. An optimum could be determined. Finally, a modelling approach could also help to describe and to understand lithium dynamics in such complex *dispersion* configuration.

General conclusion and perspectives

Energy transition plans to reduce greenhouse gas emissions are involving the development of secondary batteries. Li-ion technology is already widely used in our daily lives. Furthermore, banning internal combustion engines from vehicles by 2035 requires significant technological improvements in terms of energy density, safety, cycle life and fast charging. In such context, all-solid-state batteries can be a relevant alternative to conventional Li-ion technology. They are supposed to improve safety, due to the replacement of the liquid electrolyte by a SSE. Additionally, the implementation of a SSE opens the way to the use of lithium metal as the negative electrode, which can provide a theoretical capacity of $3,860 \text{ mAh} \cdot \text{g}^{-1}$, further enhancing the energy density. However, critical issues (cited above as technological improvements to achieve) have to be solved before integrating SSEs into commercial batteries.

The ultimate objective of this PhD work was to understand lithium mobility in a composite polymer-ceramic SSE. Well-known materials can be used as a SSE, such as a blend of PEO, submicrometric ceramic particles of LLZTO, and LiTFSI as the lithium salt. In order to understand lithium dynamics within such a complex device, first studies were typically achieved on simpler systems to gradually gather all the necessary information and build robust methodologies.

In particular, the latter are based on lithium isotopic tracing. This consists in using a material enriched in ${}^6\text{Li}$. This approach is mandatory because as lithium enters in the composition of the various battery components, isotopic tracing allows to identify lithium isotopes in the whole device as a function of their initial position in the studied system. Combined with ToF-SIMS and high-resolution ssNMR characterisations, lithium isotopic labelling can reveal crucial information on lithium dynamics. A surface chemical analysis by ToF-SIMS allows to determine ${}^6\text{Li}$ abundance from intensities of ${}^6\text{Li}^+$ and ${}^7\text{Li}^+$ fragments at submicrometric scale. On the other hand, by probing the chemical environments of ${}^6\text{Li}$ and ${}^7\text{Li}$ nuclei by ssNMR allows to estimate ${}^6\text{Li}$ abundance in bulk by combining ${}^6\text{Li}$ and ${}^7\text{Li}$ absolute integrals. Furthermore, lithium quantification is possible by using ssNMR. Thanks to lithium isotopic tracing it was demonstrated that lithium isotopic exchanges occur at the Li-metal/polymer interface at 60°C , whereas no diffusion was detected at room temperature. Li^+ ions migration was also investigated through composite SSE. Additionally, numerical simulations obtained from isotopic mixing models are also one of the fundamental pillars of this research. Indeed, an innovative synergy between experiments and modelling was created in order to characterise lithium dynamics, including lithium self-diffusion into SSE, lithium migration through SSE, and lithium isotopic exchanges at the various interfaces: Li-metal/polymer and polymer/ceramic.

A precise estimation of lithium isotopic abundance is mandatory to follow ${}^6\text{Li}^+$ ions diffusion or migration in its environment. ToF-SIMS and high-resolution ssNMR methodologies were thus developed to accurately determine lithium isotopic abundance in either region (surface or bulk) of a lithiated (or delithiated) material. Polymer electrolytes with various ${}^6\text{Li}$ abundances were prepared to carry out such experiments. It was demonstrated that ToF-SIMS and high-resolution ssNMR characterisations can provide a lithium isotopic abundance estimation with an uncertainty of 1% and 2%, respectively. To achieve such high precision, acquisition conditions as well as data processing steps have been deeply optimised.

Furthermore, the methodologies developed are based on quite complementary information: ToF-SIMS analyses provide a local characterisation of the surface, offering a chemical information, while lithium high-resolution ssNMR characterisations provide a global information on lithium chemical environments. These methodologies could then be applied with a high degree of confidence to characterise different configurations of solid-state electrolytes (SSEs).

Previous studies in literature demonstrated the existence of spontaneous lithium isotopic exchanges. In our case, lithium exchange dynamics were investigated at 60° C between a ${}^6\text{Li}$ -foil enriched at 95.4% in ${}^6\text{Li}$, and a PEO membrane containing LiTFSI as lithium salt at lithium natural isotopic abundance (7.6% in ${}^6\text{Li}$). Specific configurations were set up in order to ease their characterisations by ToF-SIMS and high-resolution ssNMR. Numerical simulations were also performed, based on an isotopic mixing model and relevant hypotheses. Lithium self-diffusion and lithium migration through a polymer electrolyte and an ionic conductive ceramic electrolyte were thoroughly studied when an electrical stress was applied. Furthermore, these simpler geometries also ease the use of numerical models. The modelling approach offers better data interpretation by providing lithium isotopic concentration variations into devices, while experimental results provided input parameters required for simulations.

Studies of the *in-plane* configuration allowed the determination of lithium self-diffusion coefficient in the ${}^6\text{Li}$ -foil ($D_{6\text{Li}}^f = 10^{-14} \text{ m}^2 \cdot \text{s}^{-1}$), lithium self-diffusion coefficient in the polymer electrolyte ($D_{6\text{Li}^+}^p = 1.6 \times 10^{-12} \text{ m}^2 \cdot \text{s}^{-1}$) and a specific parameter, named lithium “transfer frequency” at the interface ($\nu = 2 \times 10^{-9} \text{ s}^{-1}$), by fitting ToF-SIMS results with numerical simulations. Furthermore, the average enrichment in ${}^6\text{Li}$ of the polymer electrolyte obtained by modelling match with those estimated by high-resolution ssNMR. This study highlights that using modelling tools is a critical step to enhance the full exploitation of such experimental data. Additionally, a constant voltage of 0.25 V was applied at 60° C, which induces lithium migration. Both effects could be distinguished by combining ToF-SIMS, ssNMR and a modelling approach.

In a second step, a *sandwich* configuration was studied in order to facilitate lithium isotopic tracing at the polymer/ceramic interface. All the previous parameters of lithium dynamics through the polymer electrolyte previously determined, were known from the previous study (*in-plane* configuration). Thus, only lithium dynamics through the ionic conductive ceramic pellet, and lithium behaviour at the polymer/ceramic interface, were unknown at this point. Lithium dynamics were studied by ToF-SIMS, ssNMR, and modelling in such configuration after applying a constant current density of $50 \mu\text{A} \cdot \text{cm}^{-2}$. Lithium self-diffusion coefficient in the ceramic pellet was determined at $3 \times 10^{-11} \text{ m}^2 \cdot \text{s}^{-1}$. However, lithium mobility in the ionic conductive ceramic pellet could not be perfectly understood.

Finally, a *dispersion* configuration made of a composite SSE was studied. In this case, lithium dynamics were characterised by high-resolution ssNMR and orthogonal ToF-SIMS after applying a constant current density of $50 \mu\text{A} \cdot \text{cm}^{-2}$. This device is the most representative of what could be implemented in commercial solid-state batteries. High-resolution ssNMR as well as o-ToF-SIMS characterisations can both allow the estimation of lithium isotopic abundance of each component of the composite material. In accordance with global

high-resolution ssNMR analyses and local o-ToF-SIMS analyses, it appears that ${}^6\text{Li}^+$ ions seem to diffuse preferentially through the ceramic particles. Ceramic particle percolation should be investigated because it may significantly modify lithium diffusion pathways. Furthermore, Orsay Physics company demonstrated that the orthogonal ToF-SIMS characterisation technique can provide high lateral resolution for such systems, while ToF-SIMS reaches its lateral resolution limits.

All these results, obtained by an extensive use of lithium isotopic tracing, illustrate the strengths of the methodologies presented in this work. They provide new keys to a better understanding of Li^+ ions pathways in these complex devices. Models based on lithium isotopic tracing and characterisation techniques such as ToF-SIMS, o-ToF-SIMS and high-resolution ssNMR might be adapted and applied to investigate other lithiated materials. Only preliminary experiments will be required on reference samples having the same matrix and known lithium isotopic abundance. Along this work, we highlighted the importance of the reference sample choice, especially in high-resolution ssNMR, in order to accurately estimate the ${}^6\text{Li}$ abundance. The models can be adapted for other materials, by tuning materials properties and geometries. In this sense, modelling the *dispersion* configuration could also be carried out and compared with high-resolution ssNMR and o-ToF-SIMS results. Numerical simulations can also quickly provide lithium isotopic concentration in the whole composite SSE.

High-resolution ssNMR spectroscopy is a powerful technique to investigate lithium dynamics in SSEs for solid-state batteries. [155] Indeed, this advanced characterisation technique can be used to determine key parameters related to lithium dynamics such as diffusion coefficient, ionic jump rates, and transference number. [155] Furthermore, other ssNMR sequence could be investigated such as ${}^6\text{Li}$ - ${}^6\text{Li}$ 2D exchange spectroscopy (EXSY) sequence, which can provide information on lithium exchange dynamics between two different phases. [156] Finally, operando NMR might be investigated to monitor lithium dynamics into composite materials during charge or discharge cycles. However, NMR spectra under static conditions lead to a drastic loss of resolution and subsequently loss of information regarding lithium due to the appearance of anisotropic interactions (e.g. chemical shifts, dipolar or quadrupolar).

Initial orthogonal ToF-SIMS analyses were conducting in collaboration with Orsay physics company. It would be relevant to continue developing such studies in order to enhance composite material characterisations at the submicrometer scale. In parallel, in order to go even further than o-ToF-SIMS, the combination of Helium Ion Microscopy and Secondary Ion Mass Spectrometry techniques (HIM-SIMS) developed in 2015 could also be performed. It provides a lateral resolution of below 20 nm , which is one of the smallest lateral resolutions achievable instrumentally. [157] Ceramic particles contained into the polymer electrolyte matrix could be easily detected and effect of particle size may be investigated.

References

- [1] B. Greening, T. Braunschweig, R. Wood, and M. Freer, 'Batteries and beyond: Multi-vector energy storage as a tool to decarbonise energy services', *Front. Energy Res.*, vol. 10, p. 1109997, Jan. 2023, doi: 10.3389/fenrg.2022.1109997.
- [2] Y. Wu and L. Zhang, 'Can the development of electric vehicles reduce the emission of air pollutants and greenhouse gases in developing countries?', *Transportation Research Part D: Transport and Environment*, vol. 51, pp. 129–145, Mar. 2017, doi: 10.1016/j.trd.2016.12.007.
- [3] J. Ma *et al.*, 'The 2021 battery technology roadmap', *J. Phys. D: Appl. Phys.*, vol. 54, no. 18, p. 183001, Apr. 2021, doi: 10.1088/1361-6463/abd353.
- [4] M. S. Whittingham, 'Intercalation chemistry and energy storage', *Journal of Solid State Chemistry*, vol. 29, no. 3, pp. 303–310, Sep. 1979, doi: 10.1016/0022-4596(79)90187-7.
- [5] K. Mizushima, P. C. Jones, P. J. Wiseman, and J. B. Goodenough, 'LiCoO₂ (0 < x < 1): A new cathode material for batteries of high energy density', vol. 15, no. 6, doi: 10.1016/0025-5408(80)90012-4.
- [6] J. Janek and W. G. Zeier, 'A solid future for battery development', *Nat Energy*, vol. 1, no. 9, p. 16141, Sep. 2016, doi: 10.1038/nenergy.2016.141.
- [7] W. Lai and F. Ciucci, 'Mathematical modeling of porous battery electrodes-Revisit of Newman's model', *Electrochimica Acta*, vol. 56, no. 11, pp. 4369–4377, 2011, doi: 10.1016/j.electacta.2011.01.012.
- [8] S. A. Pervez, M. A. Cambaz, V. Thangadurai, and M. Fichtner, 'Interface in Solid-State Lithium Battery: Challenges, Progress, and Outlook', *ACS Appl. Mater. Interfaces*, vol. 11, no. 25, pp. 22029–22050, Jun. 2019, doi: 10.1021/acsami.9b02675.
- [9] S. Martinet, 'Nouvelles générations de batteries des véhicules électriques et hybrides', *Innovations technologiques*, May 2012, doi: 10.51257/a-v1-in203.
- [10] D. Linden and T. B. Reddy, *Handbook of batteries*, vol. 33, no. 04. 2013. doi: 10.5860/choice.33-2144.
- [11] J. B. Goodenough and Y. Kim, 'Challenges for Rechargeable Li Batteries', *Chem. Mater.*, vol. 22, no. 3, pp. 587–603, Feb. 2010, doi: 10.1021/cm901452z.
- [12] F. Sangines *et al.*, 'Long term lithium availability and electric mobility: What can we learn from resource assessment?', *Journal of Geochemical Exploration*, vol. 249, p. 107212, Jun. 2023, doi: 10.1016/j.gexplo.2023.107212.
- [13] M. Winter, B. Barnett, and K. Xu, 'Before Li Ion Batteries', *Chem. Rev.*, vol. 118, no. 23, pp. 11433–11456, Dec. 2018, doi: 10.1021/acs.chemrev.8b00422.
- [14] X. Shen, H. Liu, X.-B. Cheng, C. Yan, and J.-Q. Huang, 'Beyond lithium ion batteries: Higher energy density battery systems based on lithium metal anodes', *Energy Storage Materials*, vol. 12, pp. 161–175, May 2018, doi: 10.1016/j.ensm.2017.12.002.
- [15] M. Berthault, J. Santos-Peña, D. Lemordant, and E. De Vito, 'Dynamics of the ⁶Li/⁷Li Exchange at a Graphite–Solid Electrolyte Interphase: A Time of Flight–Secondary Ion Mass Spectrometry Study', *J. Phys. Chem. C*, vol. 125, no. 11, pp. 6026–6033, Mar. 2021, doi: 10.1021/acs.jpcc.0c10398.
- [16] M. Berthault *et al.*, 'Lithium isotope tracing in silicon-based electrodes using solid-state MAS NMR: a powerful comprehensive tool for the characterization of lithium batteries', *Phys. Chem. Chem. Phys.*, p. 10.1039.D3CP02646A, 2023, doi: 10.1039/D3CP02646A.

- [17] Z. Li *et al.*, 'Ionic Conduction in Composite Polymer Electrolytes: Case of PEO:Ga-LLZO Composites', *ACS Appl. Mater. Interfaces*, vol. 11, no. 1, pp. 784–791, Jan. 2019, doi: 10.1021/acsami.8b17279.
- [18] M. Winter and J. O. Besenhard, 'Wiederaufladbare Batterien', *Chem. Unserer Zeit*, vol. 33, no. 5, pp. 252–266, Oct. 1999, doi: 10.1002/ciuz.19990330503.
- [19] R. Bouchet and T. N. T. Phan, 'Électrolytes polymères pour les batteries au lithium métal', *Innovations technologiques*, Feb. 2015, doi: 10.51257/a-v1-re234.
- [20] Q. Li *et al.*, 'Electro-plating and stripping behavior on lithium metal electrode with ordered three-dimensional structure', *Nano Energy*, vol. 45, pp. 463–470, Mar. 2018, doi: 10.1016/j.nanoen.2018.01.019.
- [21] J. Zhang *et al.*, 'Flexible and ion-conducting membrane electrolytes for solid-state lithium batteries: Dispersion of garnet nanoparticles in insulating polyethylene oxide', *Nano Energy*, vol. 28, pp. 447–454, Oct. 2016, doi: 10.1016/j.nanoen.2016.09.002.
- [22] F. Zheng, 'Review on solid electrolytes for all-solid-state lithium-ion batteries', *Journal of Power Sources*, p. 16, 2018, doi: 10.1016/j.jpowsour.2018.04.022.
- [23] J.-Y. Sanchez, F. Alloin, D. Benrabah, and R. Arnaud, 'Polymer and salt selection for lithium polymer batteries', *Journal of Power Sources*, vol. 68, no. 1, pp. 43–51, Sep. 1997, doi: 10.1016/S0378-7753(97)02573-1.
- [24] R. Bouchet and T. N. T. Phan, 'Électrolytes polymères pour les batteries au lithium métal', *Innovations technologiques*, Feb. 2015, doi: 10.51257/a-v1-re234.
- [25] W. H. Meyer, 'Polymer Electrolytes for Lithium-Ion Batteries', *Adv. Mater.*, vol. 10, no. 6, pp. 439–448, Apr. 1998, doi: 10.1002/(SICI)1521-4095(199804)10:6<439::AID-ADMA439>3.0.CO;2-I.
- [26] Z. Xue, D. He, and X. Xie, 'Poly(ethylene oxide)-based electrolytes for lithium-ion batteries', *J. Mater. Chem. A*, vol. 3, no. 38, pp. 19218–19253, 2015, doi: 10.1039/C5TA03471J.
- [27] S. A. Pervez, P. Ganjeh-Anzabi, U. Farooq, M. Trifkovic, E. P. L. Roberts, and V. Thangadurai, 'Fabrication of a Dendrite-Free all Solid-State Li Metal Battery via Polymer Composite/Garnet/Polymer Composite Layered Electrolyte', *Adv. Mater. Interfaces*, p. 1900186, May 2019, doi: 10.1002/admi.201900186.
- [28] M. Ebadi, L. T. Costa, C. M. Araujo, and D. Brandell, 'Modelling the Polymer Electrolyte/Li-Metal Interface by Molecular Dynamics simulations', *Electrochimica Acta*, vol. 234, pp. 43–51, Apr. 2017, doi: 10.1016/j.electacta.2017.03.030.
- [29] J. Feng, L. Wang, Y. Chen, P. Wang, H. Zhang, and X. He, 'PEO based polymer-ceramic hybrid solid electrolytes: a review', *Nano Convergence*, vol. 8, no. 1, p. 2, Dec. 2021, doi: 10.1186/s40580-020-00252-5.
- [30] P. V. Wright, 'Electrical conductivity in ionic complexes of poly(ethylene oxide)', *Brit. Poly. J.*, vol. 7, no. 5, pp. 319–327, Sep. 1975, doi: 10.1002/pi.4980070505.
- [31] J. Mindemark, M. J. Lacey, T. Bowden, and D. Brandell, 'Beyond PEO—Alternative host materials for Li⁺-conducting solid polymer electrolytes', *Progress in Polymer Science*, vol. 81, pp. 114–143, Jun. 2018, doi: 10.1016/j.progpolymsci.2017.12.004.
- [32] N. A. Stolwijk, C. Heddier, M. Reschke, M. Wiencierz, J. Bokeloh, and G. Wilde, 'Salt-Concentration Dependence of the Glass Transition Temperature in PEO–NaI and PEO–LiTFSI Polymer Electrolytes', *Macromolecules*, vol. 46, no. 21, pp. 8580–8588, Nov. 2013, doi: 10.1021/ma401686r.

- [33] Z. Zhang *et al.*, 'An advanced construction strategy of all-solid-state lithium batteries with excellent interfacial compatibility and ultralong cycle life', *J. Mater. Chem. A*, vol. 5, no. 32, pp. 16984–16993, 2017, doi: 10.1039/C7TA04320A.
- [34] X. Huang, Y. Lu, Z. Song, T. Xiu, M. E. Badding, and Z. Wen, 'Preparation of dense Ta-LLZO/MgO composite Li-ion solid electrolyte: Sintering, microstructure, performance and the role of MgO', *Journal of Energy Chemistry*, vol. 39, pp. 8–16, Dec. 2019, doi: 10.1016/j.jechem.2019.01.013.
- [35] Y. Gao *et al.*, 'Amorphous Dual-Layer Coating: Enabling High Li-Ion Conductivity of Non-Sintered Garnet-Type Solid Electrolyte', *Adv Funct Materials*, vol. 31, no. 15, p. 2009692, Apr. 2021, doi: 10.1002/adfm.202009692.
- [36] Y. Zhu, X. He, and Y. Mo, 'First principles study on electrochemical and chemical stability of solid electrolyte–electrode interfaces in all-solid-state Li-ion batteries', *J. Mater. Chem. A*, vol. 4, no. 9, pp. 3253–3266, 2016, doi: 10.1039/C5TA08574H.
- [37] A. J. Samson, K. Hofstetter, S. Bag, and V. Thangadurai, 'A bird's-eye view of Li-stuffed garnet-type $\text{Li}_7\text{La}_3\text{Zr}_2\text{O}_{12}$ ceramic electrolytes for advanced all-solid-state Li batteries', *Energy Environ. Sci.*, vol. 12, no. 10, pp. 2957–2975, 2019, doi: 10.1039/C9EE01548E.
- [38] B. Liu *et al.*, 'Garnet Solid Electrolyte Protected Li-Metal Batteries', *ACS Appl. Mater. Interfaces*, vol. 9, no. 22, pp. 18809–18815, Jun. 2017, doi: 10.1021/acsami.7b03887.
- [39] W. Luo *et al.*, 'Transition from Superlithiophobicity to Superlithiophilicity of Garnet Solid-State Electrolyte', *J. Am. Chem. Soc.*, vol. 138, no. 37, pp. 12258–12262, Sep. 2016, doi: 10.1021/jacs.6b06777.
- [40] V. Thangadurai, H. Kaack, and W. J. F. Weppner, 'Novel Fast Lithium Ion Conduction in Garnet-Type $\text{Li}_5\text{La}_3\text{M}_2\text{O}_{12}$ (M = Nb, Ta)', *Journal of the American Ceramic Society*, vol. 86, no. 3, pp. 437–440, Mar. 2003, doi: 10.1111/j.1151-2916.2003.tb03318.x.
- [41] A. K. Baral, S. Narayanan, F. Ramezanipour, and V. Thangadurai, 'Evaluation of fundamental transport properties of Li-excess garnet-type $\text{Li}_{5+2x}\text{La}_3\text{Ta}_2-x\text{YxO}_{12}$ (x = 0.25, 0.5 and 0.75) electrolytes using AC impedance and dielectric spectroscopy', *Phys. Chem. Chem. Phys.*, vol. 16, no. 23, p. 11356, 2014, doi: 10.1039/c4cp00418c.
- [42] C. Wang *et al.*, 'Conformal, Nanoscale ZnO Surface Modification of Garnet-Based Solid-State Electrolyte for Lithium Metal Anodes', *Nano Lett.*, vol. 17, no. 1, pp. 565–571, Jan. 2017, doi: 10.1021/acs.nanolett.6b04695.
- [43] R. Dubey *et al.*, 'Building a Better Li-Garnet Solid Electrolyte/Metallic Li Interface with Antimony', *Advanced Energy Materials*, vol. 11, no. 39, p. 2102086, Oct. 2021, doi: 10.1002/aenm.202102086.
- [44] A. Gupta and J. Sakamoto, 'Controlling Ionic Transport through the PEO-LiTFSI/LLZTO Interface', *Electrochem. Soc. Interface*, vol. 28, no. 2, pp. 63–69, 2019, doi: 10.1149/2.F06192if.
- [45] S. Li *et al.*, 'Progress and Perspective of Ceramic/Polymer Composite Solid Electrolytes for Lithium Batteries', *Adv. Sci.*, vol. 5, no. 9, p. 22, 2020, doi: 10.1002/advs.201903088.
- [46] J. Zheng and Y.-Y. Hu, 'New Insights into the Compositional Dependence of Li-Ion Transport in Polymer–Ceramic Composite Electrolytes', *ACS Appl. Mater. Interfaces*, vol. 10, no. 4, pp. 4113–4120, Jan. 2018, doi: 10.1021/acsami.7b17301.
- [47] X. Fu *et al.*, 'Probing the Fast Lithium-Ion Transport in Small-Molecule Solid Polymer Electrolytes by Solid-State NMR', *Macromolecules*, vol. 53, no. 22, pp. 10078–10085, Nov. 2020, doi: 10.1021/acs.macromol.0c01521.

- [48] J. Zheng, M. Tang, and Y.-Y. Hu, 'Lithium Ion Pathway within $\text{Li}_7\text{La}_3\text{Zr}_2\text{O}_{12}$ - Polyethylene Oxide Composite Electrolytes', *Angew. Chem. Int. Ed.*, vol. 55, no. 40, pp. 12538–12542, Sep. 2016, doi: 10.1002/anie.201607539.
- [49] L. Chen, Y. Li, S.-P. Li, L.-Z. Fan, C.-W. Nan, and J. B. Goodenough, 'PEO/garnet composite electrolytes for solid-state lithium batteries: From "ceramic-in-polymer" to "polymer-in-ceramic"', *Nano Energy*, vol. 46, pp. 176–184, Apr. 2018, doi: 10.1016/j.nanoen.2017.12.037.
- [50] R. Murugan, V. Thangadurai, and W. Weppner, 'Fast Lithium Ion Conduction in Garnet-Type $\text{Li}_7\text{La}_3\text{Zr}_2\text{O}_{12}$ ', *Angew. Chem. Int. Ed.*, vol. 46, no. 41, pp. 7778–7781, Oct. 2007, doi: 10.1002/anie.200701144.
- [51] H. Liu *et al.*, 'Effects of Antisite Defects on Li Diffusion in LiFePO_4 Revealed by Li Isotope Exchange', *J. Phys. Chem. C*, vol. 121, no. 22, pp. 12025–12036, Jun. 2017, doi: 10.1021/acs.jpcc.7b02819.
- [52] A.-M. Desautly *et al.*, 'Tracing the origin of lithium in Li-ion batteries using lithium isotopes', *Nat Commun*, vol. 13, no. 1, p. 4172, Jul. 2022, doi: 10.1038/s41467-022-31850-y.
- [53] G. D. FLEZSCH, A. R. ANDERSON, and H. J. SVEC, 'A secondary isotopic standard for $^6\text{Li}/\text{Li}$ determinations', vol. 12, pp. 265–272, May 1973, doi: 10.1016/0020-7381(73)80043-9.
- [54] S. Penniston-Dorland, X.-M. Liu, and R. L. Rudnick, 'Lithium Isotope Geochemistry', *Reviews in Mineralogy and Geochemistry*, vol. 82, no. 1, pp. 165–217, 2017, doi: 10.2138/rmg.2017.82.6.
- [55] E. A. Bonnin and S. O. Rizzoli, 'Novel Secondary Ion Mass Spectrometry Methods for the Examination of Metabolic Effects at the Cellular and Subcellular Levels', *Front. Behav. Neurosci.*, vol. 14, p. 124, Jul. 2020, doi: 10.3389/fnbeh.2020.00124.
- [56] E. Darque-Ceretti, M. Aucouturier, and P. LEHUÉDÉ, 'Spectrométrie de masse d'ions secondaires : SIMS et ToF-SIMS - Principes et appareillages', *Techniques d'analyse*, Dec. 2014, doi: 10.51257/a-v4-p2618.
- [57] J. S. Becker and H.-J. Dietze, 'Inorganic trace analysis by mass spectrometry', *Spectrochimica Acta Part B: Atomic Spectroscopy*, vol. 53, no. 11, pp. 1475–1506, Oct. 1998, doi: 10.1016/S0584-8547(98)00110-4.
- [58] F. J. M. Rutten, D. Briggs, J. Henderson, and M. J. Roe, 'THE APPLICATION OF TIME-OF-FLIGHT SECONDARY ION MASS SPECTROMETRY (ToF-SIMS) TO THE CHARACTERIZATION OF OPAQUE ANCIENT GLASSES*', *Archaeometry*, vol. 51, no. 6, pp. 966–986, Dec. 2009, doi: 10.1111/j.1475-4754.2008.00445.x.
- [59] J. J. Thomson, 'Rays of Positive Electricity', *Phil. Mag.*, vol. 20, no. 118, pp. 752–767, 1910, doi: 10.1080/14786441008636962.
- [60] C. Trouiller, 'ToF-SIMS Applications in Microelectronics: Quantification of Organic Surface Contamination', in *AIP Conference Proceedings*, Richardson, Texas (USA): AIP, 2005, pp. 584–588. doi: 10.1063/1.2063022.
- [61] T. Stephan, 'ToF-SIMS in cosmochemistry', *Planetary and Space Science*, vol. 49, no. 9, pp. 859–906, Aug. 2001, doi: 10.1016/S0032-0633(01)00037-X.
- [62] T. Lombardo *et al.*, 'ToF-SIMS in battery research: Advantages, limitations, and best practices', *Journal of Vacuum Science & Technology A*, vol. 41, no. 5, p. 053207, Sep. 2023, doi: 10.1116/6.0002850.
- [63] J.-W. Park *et al.*, 'Multivariate analysis of ToF-SIMS data for biological applications: Multivariate analysis of ToF-SIMS data', *Surf. Interface Anal.*, vol. 41, no. 8, pp. 694–703, Aug. 2009, doi: 10.1002/sia.3049.

- [64] R. N. S. Sodhi, 'Time-of-flight secondary ion mass spectrometry (TOF-SIMS):—versatility in chemical and imaging surface analysis', *Analyst*, vol. 129, no. 6, pp. 483–487, 2004, doi: 10.1039/B402607C.
- [65] E. Darque-Ceretti, M. Aucouturier, and P. LEHUÉDÉ, 'Spectrométrie de masse d'ions secondaires : SIMS et ToF-SIMS - Principes et appareillages', *Techniques d'analyse*, Dec. 2014, doi: 10.51257/a-v4-p2618.
- [66] G. Holzlechner, M. Kubicek, H. Hutter, and J. Fleig, 'A novel ToF-SIMS operation mode for improved accuracy and lateral resolution of oxygen isotope measurements on oxides', *J. Anal. At. Spectrom.*, vol. 28, no. 7, p. 1080, 2013, doi: 10.1039/c3ja50059d.
- [67] M. Kubicek, G. Holzlechner, A. K. Opitz, S. Larisegger, H. Hutter, and J. Fleig, 'A novel ToF-SIMS operation mode for sub 100nm lateral resolution: Application and performance', *Applied Surface Science*, vol. 289, pp. 407–416, Jan. 2014, doi: 10.1016/j.apsusc.2013.10.177.
- [68] N. Davies, D. E. Weibel, P. Blenkinsopp, N. Lockyer, R. Hill, and J. C. Vickerman, 'Development and experimental application of a gold liquid metal ion source', *Applied Surface Science*, vol. 203–204, pp. 223–227, Jan. 2003, doi: 10.1016/S0169-4332(02)00631-1.
- [69] A. Brown and J. C. Vickerman, 'A comparison of positive and negative ion static SIMS spectra of polymer surfaces', *Surf. Interface Anal.*, vol. 8, no. 2, pp. 75–81, Apr. 1986, doi: 10.1002/sia.740080207.
- [70] E. Darque-Ceretti, M. Aucouturier, and P. Lehuédé, 'Spectrométrie de masse d'ions secondaires : SIMS et ToF-SIMS - Procédures d'analyse et performances', p. 26, 2015, doi: 10.51257/a-v4-p2618.
- [71] R. N. S. Sodhi, 'Time-of-flight secondary ion mass spectrometry (TOF-SIMS):—versatility in chemical and imaging surface analysis', *Analyst*, vol. 129, no. 6, pp. 483–487, 2004, doi: 10.1039/B402607C.
- [72] S. P. Harvey, J. Messinger, K. Zhu, J. M. Luther, and J. J. Berry, 'Investigating the Effects of Chemical Gradients on Performance and Reliability within Perovskite Solar Cells with TOF-SIMS', *Advanced Energy Materials*, vol. 10, no. 26, p. 1903674, Jul. 2020, doi: 10.1002/aenm.201903674.
- [73] A. Henss *et al.*, 'Quantification of calcium content in bone by using ToF-SIMS—a first approach', *Biointerphases*, vol. 8, no. 1, p. 31, Dec. 2013, doi: 10.1186/1559-4106-8-31.
- [74] N. Kuwata, X. Lu, T. Miyazaki, Y. Iwai, T. Tanabe, and J. Kawamura, 'Lithium diffusion coefficient in amorphous lithium phosphate thin films measured by secondary ion mass spectroscopy with isotope exchange methods', *Solid State Ionics*, vol. 294, pp. 59–66, Oct. 2016, doi: 10.1016/j.ssi.2016.06.015.
- [75] S. A. Goudsmit, 'Pauli and nuclear spin', *Physics Today*, vol. 14, no. 6, pp. 18–21, Jun. 1961, doi: 10.1063/1.3057597.
- [76] Y.-X. Xiang, G. Zheng, G. Zhong, D. Wang, R. Fu, and Y. Yang, 'Toward understanding of ion dynamics in highly conductive lithium ion conductors: Some perspectives by solid state NMR techniques', *Solid State Ionics*, vol. 318, pp. 19–26, May 2018, doi: 10.1016/j.ssi.2017.11.025.
- [77] Andrew, E. R., 'Magic angle spinning in solid state n.m.r. spectroscopy', *Phil. Trans. R. Soc. Lond.*, vol. 299, pp. 505–520, Mar. 1981, doi: 10.1098/rsta.1981.0032.
- [78] A. P. M. Kentgens, 'A practical guide to solid-state NMR of half-integer quadrupolar nuclei with some applications to disordered systems', *Geoderma*, vol. 80, no. 3–4, pp. 271–306, Nov. 1997, doi: 10.1016/S0016-7061(97)00056-6.

- [79] I. J. Lowe, 'Free Induction Decays of Rotating Solids', *Phys. Rev. Lett.*, vol. 2, no. 7, pp. 285–287, Apr. 1959, doi: 10.1103/PhysRevLett.2.285.
- [80] Andrew, E. R., A. Bradbury, and Eades R. G, 'Nuclear magnetic resonance spectra in solids: invariance of the second moment under molecular reorientation.', *Arch. Sci.*, vol. 11, no. 223, 1958.
- [81] R. Allabashi, W. Stach, A. de la Escosura-Muñiz, L. Liste-Calleja, and A. Merkoçi, 'ICP-MS: a powerful technique for quantitative determination of gold nanoparticles without previous dissolving', *J Nanopart Res*, vol. 11, no. 8, pp. 2003–2011, Nov. 2009, doi: 10.1007/s11051-008-9561-2.
- [82] H. Paucot and M. Potin-Gautier, 'ICP-MS : couplage plasma induit par haute fréquence – spectrométrie de masse', *Techniques d'analyse*, Jun. 2010, doi: 10.51257/a-v3-p2720.
- [83] C. B. Douthitt, 'The evolution and applications of multicollector ICPMS (MC-ICPMS)', *Anal Bioanal Chem*, vol. 390, no. 2, pp. 437–440, Jan. 2008, doi: 10.1007/s00216-007-1660-x.
- [84] L. K. Steinmann, M. Oeser, I. Horn, H.-M. Seitz, and S. Weyer, '*In situ* high-precision lithium isotope analyses at low concentration levels with femtosecond-LA-MC-ICP-MS', *J. Anal. At. Spectrom.*, vol. 34, no. 7, pp. 1447–1458, 2019, doi: 10.1039/C9JA00088G.
- [85] D. L'Hermite and J.-B. Sirven, 'LIBS : spectrométrie d'émission optique de plasma induit par laser', *Techniques d'analyse*, Jun. 2015, doi: 10.51257/a-v1-p2870.
- [86] K. Touchet, 'Laser-induced breakdown self-reversal isotopic spectrometry for isotopic analysis of lithium', 2020, doi: 10.1016/j.sab.2020.105868.
- [87] D. Gallot-Duval, T. Meyer, C. Quéré, T. Gutel, E. De Vito, and J.-B. Sirven, 'High-resolution isotopic analysis of lithium by micro laser-induced breakdown self-reversal isotopic spectrometry (LIBRIS) for isotopic labelling of lithium in solid-state electrolyte of lithium batteries', *Spectrochimica Acta Part B: Atomic Spectroscopy*, vol. 206, p. 106731, Aug. 2023, doi: 10.1016/j.sab.2023.106731.
- [88] O. Kirstein, U. Garbe, and V. Luzin, 'Kowari - OPAL's New Stress Diffractometer for the Engineering Community: Capabilities and First Results', *MSF*, vol. 652, pp. 86–91, May 2010, doi: 10.4028/www.scientific.net/MSF.652.86.
- [89] C. Muller, 'Diffraction des neutrons : principe, dispositifs expérimentaux et applications', *J. Phys. IV France*, vol. 103, pp. 101–132, Feb. 2003, doi: 10.1051/jp4:20030004.
- [90] Y. Gao *et al.*, 'Classical and Emerging Characterization Techniques for Investigation of Ion Transport Mechanisms in Crystalline Fast Ionic Conductors', *Chem. Rev.*, vol. 120, no. 13, pp. 5954–6008, Jul. 2020, doi: 10.1021/acs.chemrev.9b00747.
- [91] M. Diehl, M. Evertz, M. Winter, and S. Nowak, 'Deciphering the lithium ion movement in lithium ion batteries: determination of the isotopic abundances of ^6Li and ^7Li ', *RSC Adv.*, vol. 9, no. 21, pp. 12055–12062, 2019, doi: 10.1039/C9RA02312G.
- [92] D. Glaros, A. F. LoMonte, K. J. Ellis, S. Yasumura, R. W. Stoenner, and S. H. Cohn, '*In vivo* measurement of lithium in the body by a neutron activation analysis technique', *Med. Phys.*, vol. 13, no. 1, pp. 45–49, Jan. 1986, doi: 10.1118/1.595922.
- [93] V. Balter and N. Vigier, 'Natural variations of lithium isotopes in a mammalian model', *Metallomics*, vol. 6, no. 3, pp. 582–586, 2014, doi: 10.1039/c3mt00295k.
- [94] R. Millot and P. Négrel, 'Lithium isotopes in the Loire River Basin (France): Hydrogeochemical characterizations at two complementary scales', *Applied Geochemistry*, vol. 125, p. 104831, Feb. 2021, doi: 10.1016/j.apgeochem.2020.104831.

- [95] P. Lu and S. J. Harris, 'Lithium transport within the solid electrolyte interphase', *Electrochemistry Communications*, vol. 13, no. 10, pp. 1035–1037, Oct. 2011, doi: 10.1016/j.elecom.2011.06.026.
- [96] S. Shi *et al.*, 'Direct Calculation of Li-Ion Transport in the Solid Electrolyte Interphase', *J. Am. Chem. Soc.*, vol. 134, no. 37, pp. 15476–15487, Sep. 2012, doi: 10.1021/ja305366r.
- [97] Z. Liu, P. Lu, Q. Zhang, X. Xiao, Y. Qi, and L.-Q. Chen, 'A Bottom-Up Formation Mechanism of Solid Electrolyte Interphase Revealed by Isotope-Assisted Time-of-Flight Secondary Ion Mass Spectrometry', *J. Phys. Chem. Lett.*, vol. 9, no. 18, pp. 5508–5514, Sep. 2018, doi: 10.1021/acs.jpcclett.8b02350.
- [98] E. Hüger, L. Dörrer, and H. Schmidt, 'Permeation, Solubility, Diffusion and Segregation of Lithium in Amorphous Silicon Layers', *Chem. Mater.*, vol. 30, no. 10, pp. 3254–3264, May 2018, doi: 10.1021/acs.chemmater.8b00186.
- [99] E. Hüger, L. Dörrer, R. Yimnirun, J. Jutimoosik, J. Stahn, and A. Paul, 'Lithium permeation within lithium niobate multilayers with ultrathin chromium, silicon and carbon spacer layers', *Phys. Chem. Chem. Phys.*, vol. 20, no. 36, pp. 23233–23243, 2018, doi: 10.1039/C8CP03345E.
- [100] N. Kuwata, G. Hasegawa, D. Maeda, N. Ishigaki, T. Miyazaki, and J. Kawamura, 'Tracer Diffusion Coefficients of Li Ions in $\text{Li}_x\text{Mn}_2\text{O}_4$ Thin Films Observed by Isotope Exchange Secondary Ion Mass Spectrometry', *J. Phys. Chem. C*, vol. 124, no. 42, pp. 22981–22992, Oct. 2020, doi: 10.1021/acs.jpcc.0c06375.
- [101] H. J. Chang *et al.*, 'Investigating Li Microstructure Formation on Li Anodes for Lithium Batteries by in Situ $^6\text{Li}/^7\text{Li}$ NMR and SEM', *J. Phys. Chem. C*, vol. 119, no. 29, pp. 16443–16451, Jul. 2015, doi: 10.1021/acs.jpcc.5b03396.
- [102] K. Morita, K. Ishii, M. Sekiya, Y. Tanaka, and T. Hoshino, 'Effects of applied voltages on Lithium-6 enrichment by electro dialysis with lithium ionic conductor', *Fusion Engineering and Design*, vol. 190, p. 113521, May 2023, doi: 10.1016/j.fusengdes.2023.113521.
- [103] N. I. Schwarzburger, H. Behrens, I. Horn, and M. Binnewies, 'On the Mechanisms of Chemical Intercalation of Lithium in Electrode Materials', *Zeitschrift für Physikalische Chemie*, vol. 231, no. 7–8, pp. 1345–1359, Jul. 2017, doi: 10.1515/zpch-2016-0938.
- [104] T. Meyer, T. Gutel, H. Manzanarez, M. Bardet, and E. De Vito, 'Lithium Self-Diffusion in a Polymer Electrolyte for Solid-State Batteries: ToF-SIMS/ssNMR Correlative Characterization and Modeling Based on Lithium Isotopic Labeling', *ACS Appl. Mater. Interfaces*, vol. 15, no. 37, pp. 44268–44279, Sep. 2023, doi: 10.1021/acsami.3c08829.
- [105] C. Chauvin, F. Alloin, P. Judeinstein, D. Foscallo, and J.-Y. Sanchez, 'Electrochemical and NMR characterizations of mixed polymer electrolytes based on oligoether sulfate and imide salts', *Electrochimica Acta*, vol. 52, no. 3, pp. 1240–1246, Nov. 2006, doi: 10.1016/j.electacta.2006.07.023.
- [106] G. J. Redhammer *et al.*, 'Wet-Environment-Induced Structural Alterations in Single- and Polycrystalline LLZTO Solid Electrolytes Studied by Diffraction Techniques', *ACS Appl. Mater. Interfaces*, vol. 13, no. 1, pp. 350–359, Jan. 2021, doi: 10.1021/acsami.0c16016.
- [107] H. P. Paudel and Y. Duan, 'A First-Principles Density Function Theory Study of Tritium Diffusion in Li_2ZrO_3 : Application for Producing Tritium', *J. Phys. Chem. C*, vol. 122, no. 50, pp. 28447–28459, Dec. 2018, doi: 10.1021/acs.jpcc.8b05810.
- [108] Y. Wang and W. Lai, 'High Ionic Conductivity Lithium Garnet Oxides of $\text{Li}_{7-x}\text{La}_3\text{Zr}_2-x\text{Ta}_x\text{O}_{12}$ Compositions', *Electrochem. Solid-State Lett.*, vol. 15, no. 5, p. A68, 2012, doi: 10.1149/2.024205esl.

- [109] J. Awaka, N. Kijima, H. Hayakawa, and J. Akimoto, 'Synthesis and structure analysis of tetragonal $\text{Li}_7\text{La}_3\text{Zr}_2\text{O}_{12}$ with the garnet-related type structure', *Journal of Solid State Chemistry*, vol. 182, no. 8, pp. 2046–2052, Aug. 2009, doi: 10.1016/j.jssc.2009.05.020.
- [110] Y. Cao, Y.-Q. Li, and X.-X. Guo, 'Densification and lithium ion conductivity of garnet-type $\text{Li}_{7-x}\text{La}_3\text{Zr}_{2-x}\text{Ta}_x\text{O}_{12}$ ($x = 0.25$) solid electrolytes', *Chinese Phys. B*, vol. 22, no. 7, p. 078201, Jul. 2013, doi: 10.1088/1674-1056/22/7/078201.
- [111] C. Guo *et al.*, 'Grafting of Lithiophilic and Electron-Blocking Interlayer for Garnet-Based Solid-State Li Metal Batteries via One-Step Anhydrous Poly-Phosphoric Acid Post-Treatment', *Adv Funct Materials*, vol. 33, no. 10, p. 2213443, Mar. 2023, doi: 10.1002/adfm.202213443.
- [112] H. Xie *et al.*, 'Consolidating the grain boundary of the garnet electrolyte LLZTO with Li_3BO_3 for high-performance $\text{LiNi}_{0.8}\text{Co}_{0.1}\text{Mn}_{0.1}\text{O}_2/\text{LiFePO}_4$ hybrid solid batteries', *J. Mater. Chem. A*, vol. 7, no. 36, pp. 20633–20639, 2019, doi: 10.1039/C9TA03263K.
- [113] A. Ch. Lazanas and M. I. Prodromidis, 'Electrochemical Impedance Spectroscopy—A Tutorial', *ACS Meas. Sci. Au*, vol. 3, no. 3, pp. 162–193, Jun. 2023, doi: 10.1021/acsmesuresciau.2c00070.
- [114] R. Bouchet, S. Lascaud, and M. Rosso, 'An EIS Study of the Anode Li/PEO-LiTFSI of a Li Polymer Battery', *J. Electrochem. Soc.*, vol. 150, no. 10, p. A1385, 2003, doi: 10.1149/1.1609997.
- [115] G. Hua-jun, L. Xin-hai, Z. Xin-ming, W. Hong-qiang, W. Zhi-xing, and P. Wen-jie, 'Diffusion coefficient of lithium in artificial graphite, mesocarbon microbeads, and disordered carbon', *New Carbon Materials*, 2007, doi: 10.1016/S1872-5805(07)60006-7.
- [116] C. Schwab *et al.*, 'Bulk and grain boundary Li-diffusion in dense LiMn_2O_4 pellets by means of isotope exchange and ToF-SIMS analysis', *Phys. Chem. Chem. Phys.*, vol. 21, no. 47, pp. 26066–26076, 2019, doi: 10.1039/C9CP05128G.
- [117] R. H. Brugge, R. J. Chater, J. A. Kilner, and A. Aguadero, 'Experimental determination of Li diffusivity in LLZO using isotopic exchange and FIB-SIMS', *J. Phys. Energy*, vol. 3, no. 3, p. 034001, Jul. 2021, doi: 10.1088/2515-7655/abe2f7.
- [118] A. Priebe, T. Xie, G. Bürki, L. Pethö, and J. Michler, 'The matrix effect in TOF-SIMS analysis of two-element inorganic thin films', *J. Anal. At. Spectrom.*, vol. 35, no. 6, pp. 1156–1166, 2020, doi: 10.1039/C9JA00428A.
- [119] T. Stephan, J. Zehnpfenning, and A. Benninghoven, 'Correction of dead time effects in time-of-flight mass spectrometry', *Journal of Vacuum Science & Technology A: Vacuum, Surfaces, and Films*, vol. 12, no. 2, pp. 405–410, Mar. 1994, doi: 10.1116/1.579255.
- [120] M. R. Keenan and V. S. Smentkowski, 'The statistics of ToF-SIMS data revisited and introduction of the empirical Poisson correction: Empirical Poisson correction', *Surf. Interface Anal.*, vol. 48, no. 4, pp. 218–225, Apr. 2016, doi: 10.1002/sia.5955.
- [121] G. H. Gardenier, F. Gui, and J. N. Demas, 'Error Propagation Made Easy—Or at Least Easier', *J. Chem. Educ.*, vol. 88, no. 7, pp. 916–920, Jul. 2011, doi: 10.1021/ed1004307.
- [122] J. Zhang, 'The Calculating Formulae, and Experimental Methods in Error Propagation Analysis', *IEEE Trans. Rel.*, vol. 55, no. 2, pp. 169–181, Jun. 2006, doi: 10.1109/TR.2006.874920.
- [123] P. Kempgens, R. K. Harris, and D. P. Thompson, '6Li and 7Li solid-state NMR spectroscopy of nitrogen ceramic phases', *Solid State Nuclear Magnetic Resonance*, vol. 15, no. 2, pp. 109–118, Nov. 1999, doi: 10.1016/S0926-2040(99)00040-5.
- [124] J.-D. Jeon and S.-Y. Kwak, 'Variable-Temperature ^7Li Solid-State NMR Investigation of Li-Ion Mobility and Its Correlation with Conductivity in Pore-Filling Polymer Electrolytes

- for Secondary Batteries', *Macromolecules*, vol. 39, no. 23, pp. 8027–8034, Nov. 2006, doi: 10.1021/ma061521v.
- [125] G. Foran, N. Verdier, D. Lepage, C. Malveau, N. Dupré, and M. Dollé, 'Use of Solid-State NMR Spectroscopy for the Characterization of Molecular Structure and Dynamics in Solid Polymer and Hybrid Electrolytes', *Polymers*, vol. 13, no. 8, p. 1207, Apr. 2021, doi: 10.3390/polym13081207.
- [126] D. Massiot *et al.*, 'Modelling one- and two-dimensional solid-state NMR spectra', *Magn. Reson. Chem.*, vol. 40, pp. 70–76, Oct. 2001, doi: 10.1002/mrc.984.
- [127] C. H. Cullen, G. J. Ray, and C. M. Szabo, 'A comparison of quantitative nuclear magnetic resonance methods: internal, external, and electronic referencing: Comparison of quantitative NMR methods', *Magn. Reson. Chem.*, p. n/a-n/a, Sep. 2013, doi: 10.1002/mrc.4004.
- [128] Y. Choo, D. M. Halat, I. Villaluenga, K. Timachova, and N. P. Balsara, 'Diffusion and migration in polymer electrolytes', *Progress in Polymer Science*, vol. 103, p. 101220, Apr. 2020, doi: 10.1016/j.progpolymsci.2020.101220.
- [129] 'Gunnarsdóttir et al. - 2020 - Investigating the effect of a fluoroethylene carbo.PDF'.
- [130] A. J. Ilott and A. Jerschow, 'Probing Solid-Electrolyte Interphase (SEI) Growth and Ion Permeability at Undriven Electrolyte–Metal Interfaces Using ^7Li NMR', *J. Phys. Chem. C*, vol. 122, no. 24, pp. 12598–12604, Jun. 2018, doi: 10.1021/acs.jpcc.8b01958.
- [131] R. Messer and F. Noack, 'Nuclear magnetic relaxation by self-diffusion in solid lithium:T 1-frequency dependence', *Appl. Phys.*, vol. 6, no. 1, pp. 79–88, Feb. 1975, doi: 10.1007/BF00883553.
- [132] E. Dologlou, 'Self-diffusion in solid lithium', *Glass Phys Chem*, vol. 36, no. 5, pp. 570–574, Oct. 2010, doi: 10.1134/S1087659610050056.
- [133] C. Chauvin, F. Alloin, P. Judeinstein, D. Foscallo, and J.-Y. Sanchez, 'Electrochemical and NMR characterizations of mixed polymer electrolytes based on oligoether sulfate and imide salts', *Electrochimica Acta*, vol. 52, no. 3, pp. 1240–1246, Nov. 2006, doi: 10.1016/j.electacta.2006.07.023.
- [134] K. Timachova, H. Watanabe, and N. P. Balsara, 'Effect of Molecular Weight and Salt Concentration on Ion Transport and the Transference Number in Polymer Electrolytes', *Macromolecules*, vol. 48, no. 21, pp. 7882–7888, Nov. 2015, doi: 10.1021/acs.macromol.5b01724.
- [135] R. Jeanne-Brou, J. Deseure, T. N. T. Phan, R. Bouchet, and D. Devaux, 'Anisotropic ionic transport properties in solid PEO based electrolytes', *Electrochimica Acta*, vol. 434, p. 141268, Dec. 2022, doi: 10.1016/j.electacta.2022.141268.
- [136] Newman J, Thomas-Alyea KE and Thomas-Alyea KE, *Electrochemical systems.*, John Wiley&Sons. 2012.
- [137] Rubinstein, M. and Colby, R. H., *Polymer Physics*, Oxford University Press. 2003.
- [138] F. Aguesse *et al.*, 'Investigating the Dendritic Growth during Full Cell Cycling of Garnet Electrolyte in Direct Contact with Li Metal', *ACS Appl. Mater. Interfaces*, vol. 9, no. 4, pp. 3808–3816, Feb. 2017, doi: 10.1021/acsami.6b13925.
- [139] Y.-C. Hsieh *et al.*, 'Revealing the Impact of Film-Forming Electrolyte Additives on Lithium Metal Batteries via Solid-State NMR/MRI Analysis', *J. Phys. Chem. C*, vol. 125, no. 1, pp. 252–265, Jan. 2021, doi: 10.1021/acs.jpcc.0c09771.
- [140] A. Marchetti *et al.*, 'Understanding Surface and Interfacial Chemistry in Functional Nanomaterials via Solid-State NMR', *Adv. Mater.*, vol. 29, no. 14, p. 1605895, Apr. 2017, doi: 10.1002/adma.201605895.

- [141] Y. Xu *et al.*, 'Rapid Ion Transport Induced by the Enhanced Interaction in Composite Polymer Electrolyte for All-Solid-State Lithium-Metal Batteries', *J. Phys. Chem. Lett.*, vol. 12, no. 43, pp. 10603–10609, Nov. 2021, doi: 10.1021/acs.jpcllett.1c02701.
- [142] W. Li, C. Sun, J. Jin, Y. Li, C. Chen, and Z. Wen, 'Realization of the Li⁺ domain diffusion effect *via* constructing molecular brushes on the LLZTO surface and its application in all-solid-state lithium batteries', *J. Mater. Chem. A*, vol. 7, no. 48, pp. 27304–27312, 2019, doi: 10.1039/C9TA10400C.
- [143] D. I. Hoult and N. S. Ginsberg, 'The Quantum Origins of the Free Induction Decay Signal and Spin Noise', *Journal of Magnetic Resonance*, vol. 148, no. 1, pp. 182–199, Jan. 2001, doi: 10.1006/jmre.2000.2229.
- [144] F. D. Doty, G. Entzminger, J. Kulkarni, K. Pamarthy, and J. P. Staab, 'Radio frequency coil technology for small-animal MRI', *NMR Biomed.*, vol. 20, no. 3, pp. 304–325, May 2007, doi: 10.1002/nbm.1149.
- [145] Q. P. Vanbellinghen, N. Elie, M. J. Eller, S. Della-Negra, D. Touboul, and A. Brunelle, 'Time-of-flight secondary ion mass spectrometry imaging of biological samples with delayed extraction for high mass and high spatial resolutions', *Rapid Commun. Mass Spectrom.*, vol. 29, no. 13, pp. 1187–1195, Jul. 2015, doi: 10.1002/rcm.7210.
- [146] A. Tempez *et al.*, 'Orthogonal time-of-flight secondary ion mass spectrometric analysis of peptides using large gold clusters as primary ions', *Rapid Commun. Mass Spectrom.*, vol. 18, no. 4, pp. 371–376, Feb. 2004, doi: 10.1002/rcm.1342.
- [147] J. Almoríc *et al.*, 'Implementation of Nanoscale Secondary-Ion Mass Spectrometry Analyses: Application to Ni-Based Superalloys', *Physica Status Solidi (a)*, vol. 219, no. 9, p. 2100414, May 2022, doi: 10.1002/pssa.202100414.
- [148] J. A. Whitby *et al.*, 'High Spatial Resolution Time-of-Flight Secondary Ion Mass Spectrometry for the Masses: A Novel Orthogonal ToF FIB-SIMS Instrument with *In Situ* AFM', *Advances in Materials Science and Engineering*, vol. 2012, pp. 1–13, 2012, doi: 10.1155/2012/180437.
- [149] J. Lorinčík, I. Kašík, J. Vaniš, L. Sedláček, and J. Dluhoš, 'Imaging of dopant distribution in optical fibers with an orthogonal TOF SIMS: Imaging of dopant distribution in optical fibers with TOF SIMS', *Surf. Interface Anal.*, vol. 46, no. S1, pp. 238–240, Nov. 2014, doi: 10.1002/sia.5536.
- [150] P. Pietsch and V. Wood, 'X-Ray Tomography for Lithium Ion Battery Research: A Practical Guide', *Annu. Rev. Mater. Res.*, vol. 47, no. 1, pp. 451–479, Jul. 2017, doi: 10.1146/annurev-matsci-070616-123957.
- [151] V. Yufit, P. Shearing, R. W. Hamilton, P. D. Lee, M. Wu, and N. P. Brandon, 'Investigation of lithium-ion polymer battery cell failure using X-ray computed tomography', *Electrochemistry Communications*, vol. 13, no. 6, pp. 608–610, Jun. 2011, doi: 10.1016/j.elecom.2011.03.022.
- [152] A. Méry, S. Rousselot, D. Lepage, D. Aymé-Perrot, and M. Dollé, 'Limiting Factors Affecting the Ionic Conductivities of LATP/Polymer Hybrid Electrolytes', *Batteries*, vol. 9, no. 2, p. 87, Jan. 2023, doi: 10.3390/batteries9020087.
- [153] X. Yu and A. Manthiram, 'A review of composite polymer-ceramic electrolytes for lithium batteries', *Energy Storage Materials*, vol. 34, pp. 282–300, Jan. 2021, doi: 10.1016/j.ensm.2020.10.006.
- [154] J.-S. Kim *et al.*, 'Surface engineering of inorganic solid-state electrolytes via interlayers strategy for developing long-cycling quasi-all-solid-state lithium batteries', *Nat Commun*, vol. 14, no. 1, p. 782, Feb. 2023, doi: 10.1038/s41467-023-36401-7.

- [155] C. V. Chandran and P. Heitjans, 'Solid-state NMR studies of lithium ion dynamics across materials classes: Review update', in *Annual Reports on NMR Spectroscopy*, vol. 106, Elsevier, 2022, pp. 1–51. doi: 10.1016/bs.arnmr.2022.04.001.
- [156] P. Ranque, J. Zagórski, S. Devaraj, F. Aguesse, and J. M. López del Amo, 'Characterization of the interfacial Li-ion exchange process in a ceramic–polymer composite by solid state NMR', *J. Mater. Chem. A*, vol. 9, no. 33, pp. 17812–17820, 2021, doi: 10.1039/D1TA03720J.
- [157] J.-N. Audinot, P. Philipp, O. De Castro, A. Biesemeier, Q. H. Hoang, and T. Wirtz, 'Highest resolution chemical imaging based on secondary ion mass spectrometry performed on the helium ion microscope', *Rep. Prog. Phys.*, vol. 84, no. 10, p. 105901, Oct. 2021, doi: 10.1088/1361-6633/ac1e32.
- [158] D. Stapel and A. Benninghoven, 'Application of atomic and molecular primary ions for TOF–SIMS analysis of additive containing polymer surfaces', *Applied Surface Science*, vol. 174, no. 3–4, pp. 261–270, Apr. 2001, doi: 10.1016/S0169-4332(01)00173-8.
- [159] G. Nagy and A. V. Walker, 'Enhanced secondary ion emission with a bismuth cluster ion source', *International Journal of Mass Spectrometry*, vol. 262, no. 1–2, pp. 144–153, Apr. 2007, doi: 10.1016/j.ijms.2006.11.003.
- [160] M. P. Seah and I. S. Gilmore, 'Cluster primary ion sputtering: correlations in secondary ion intensities in TOF SIMS', *Surface & Interface Analysis*, vol. 43, no. 1–2, pp. 228–235, Jan. 2011, doi: 10.1002/sia.3491.
- [161] A. Louis-Joseph and P. Lesot, 'Designing and building a low-cost portable FT-NMR spectrometer in 2019: A modern challenge', *Comptes Rendus Chimie*, vol. 22, no. 9–10, pp. 695–711, Sep. 2019, doi: 10.1016/j.crci.2019.07.001.
- [162] Z. Xie *et al.*, 'A sandwich-type composite polymer electrolyte for all-solid-state lithium metal batteries with high areal capacity and cycling stability', *Journal of Membrane Science*, vol. 596, p. 117739, Feb. 2020, doi: 10.1016/j.memsci.2019.117739.
- [163] X. Han *et al.*, 'Negating interfacial impedance in garnet-based solid-state Li metal batteries', *Nature Mater*, vol. 16, no. 5, pp. 572–579, May 2017, doi: 10.1038/nmat4821.
- [164] Z. Wan *et al.*, 'Low Resistance–Integrated All-Solid-State Battery Achieved by $\text{Li}_7\text{La}_3\text{Zr}_2\text{O}_{12}$ Nanowire Upgrading Polyethylene Oxide (PEO) Composite Electrolyte and PEO Cathode Binder', *Adv Funct Materials*, vol. 29, no. 1, p. 1805301, Jan. 2019, doi: 10.1002/adfm.201805301.

A-I-1. Time-of-flight and ionisation yield notions

The time-of-flight corresponds to the flight duration of a secondary ion from the surface of the sample to the detector. Its expression is given by Equation A-I-1

$$t_{TOF} = L \cdot \sqrt{\frac{m}{2 \cdot z \cdot U}} \quad \text{A-I-1}$$

with L the analyser length, m the mass of the ejected molecular fragment and z its charge, and U the potential difference allowing ions extraction. t_{TOF} depends on set intrinsic parameters of the equipment such as L and U , and also on the secondary ion characteristics, m and z . ToF-SIMS technique is based on the mass to charge ratio $\left(\frac{m}{z}\right)$ determination of each detected secondary ion. The $\frac{m}{z}$ ratio can be determined for each pixel from the measured t_{TOF} . Equation A-I-2 is deduced from Equation A-I-1.

$$\frac{m}{z} = 2 \cdot U \cdot \left(\frac{t_{TOF}}{L}\right)^2 \quad \text{A-I-2}$$

Several analyses beams can be used such as Bi^+ , Bi^{2+} or Bi^{3+} at 15 keV. Larger sputtering clusters permit to lower the surface sensitivity. [62] The energy of the beam can also be increased up to 30 keV. By increasing the energy and consequently the current, it results in an improved ionisation yield. The ionisation yield (r_A) is defined by the following Equation A-I-3,

$$r_A = \frac{\text{number of ejected molecular fragments } A^\pm}{\text{number of ejected molecule } A} \quad \text{A-I-3}$$

Several parameters are affecting the ionisation yield, such as the beam energy, [158] the beam nature, [159] the mass of the ejected molecular fragment, [158] and the binding energy of the considered fragment in its environment. [160] The last parameter is commonly called the “matrix effect”. That is why ToF-SIMS characterisation is not quantitative. Indeed, various molecular fragments have different ionisation yield, and an atom is present in various molecular fragments. However, relative quantification may be possible by analysing a reference sample having a known composition and the same matrix as the characterised samples. Moreover, it is assumed that the matrix effects do not have any impact on isotope detection. [74] The intensity of a molecular fragment varies according for instance to the primary ion dose, the ionisation yield and the atom concentration. [65]

A-I-2. Description of NMR pulse sequence and signal acquisition

The objective of this appendix is to provide few keys to understand NMR technique functioning.

NMR technique detects ground state nuclear spin. Thus, NMR can only observe atoms with non-zero ground state nuclear spin because they are magnetic. Probed atom spin will precess around the magnetic field with the resonance frequency. Lithium isotopes can be observed by NMR because their spin is not equal to 0. The ground state nuclei spin of ${}^6\text{Li}$ and ${}^7\text{Li}$ are $I = 1$ and $I = \frac{3}{2}$, respectively. Thus, they can be probed by applied a pulse sequence described on Figure A-I-1.

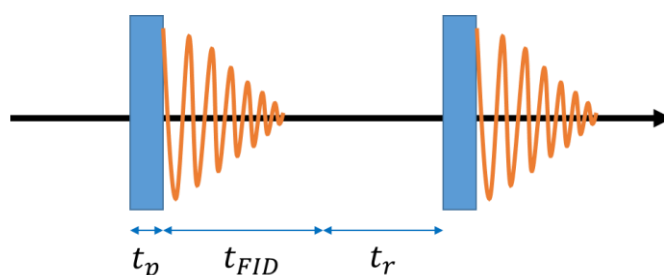


Figure A-I-1. Description of a pulse sequence and the acquisition of the NMR signal.

On Figure A-I-1, the three steps of a pulse sequence are schematised. Firstly, a pulse is applied during few microseconds (t_p). Then, the free induced decay (FID) is recorded during the acquisition time (t_{FID}). Finally, before applying the next pulse, it must wait a certain amount of time called the relaxation delay (t_r). The t_r is required for the longitudinal relaxation to reach its equilibrium state. This time will be investigated to carry out quantitative analyses.

The local environment and the resonance frequency have an impact on the local magnetic field response. On Figure A-I-2 the description of the magnetisation precession after applying a 90° pulse is schematised.

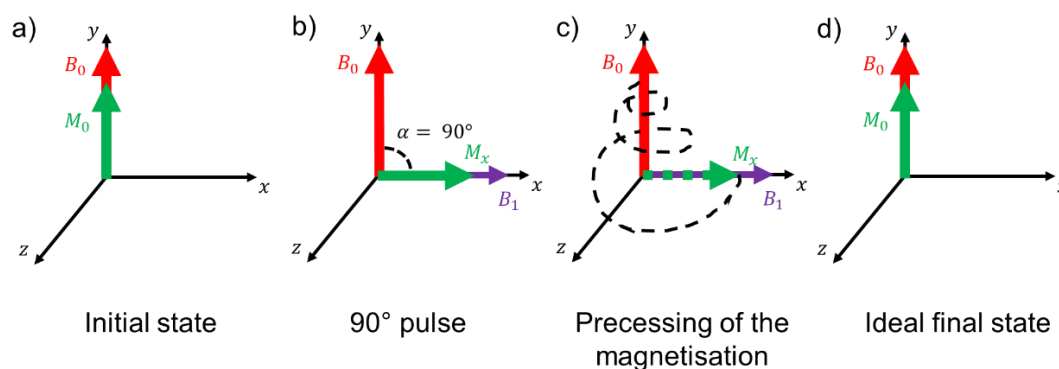


Figure A-I-2. Description of the magnetisation precession after applying a 90° pulse. Figure inspired from Figure 1 presented by Louis-Joseph and Lesot. [161]

On Figure A-I-2.a, the nuclear magnetic moments of a sample are aligned by applying a magnetic field (B_0). B_0 is created by a superconducting magnet. Larmor frequencies (ν) are determined by the following Equation A-I-4,

$$|\nu_0| = \frac{|\gamma|B_0}{2\pi} \quad 0-1$$

with γ , the gyromagnetic ratio (Table A-I-1). The Larmor frequency corresponds to the precession frequency. It is different for isotopes. B_0 is operating at 73.6 and 194.4 MHz Larmor frequencies for ${}^6\text{Li}$ and ${}^7\text{Li}$, respectively (Table A-I-1). The nuclear Larmor frequencies are in the range of radio frequencies, which have a low energy. That is why NMR is a non-destructive technique. The sample is placed in an area where B_0 is homogeneous. Then, on Figure A-I-2.b, the probe can tilt the sample magnetisation away from B_0 by producing a transverse radiofrequency magnetic field (B_1). The probe produces radio frequency field to excite the spins of the probed nucleus. B_1 oscillates at the Larmor frequency. A 90° pulse sequence rotate the magnetisation into an orthogonal plane to B_0 . It corresponds to the (xz) plan. Thus, the magnetic moment is perpendicular to B_0 . When the applied pulse stops, the magnetisation will come back to its equilibrium state (Figure A-I-2.c). The acquisition time (t_{FID}) has to be set regarding the relaxation phenomenon. The recovery to the equilibrium is measured by an NMR console. The NMR console has different roles. Firstly, it creates and amplifies the radiofrequency pulses. Then, NMR signals are detected and transformed into a digital form.

Finally, a computer through dedicated (commercial or homemade) software is necessary to handle the different steps required for the emission and detection of NMR signals and process the digitised NMR signals by applying a Fourier transform and various treatment such as phase adjustment or baseline correction. An NMR spectrum represents the intensity of the detected nucleus as a function of the chemical shift in *ppm*.

Table A-I-1. NMR characteristics of lithium isotopes.

Properties	${}^6\text{Li}$	${}^7\text{Li}$
Spin (S)	1	3/2
Natural isotopic abundance (%)	7.6	92.4
Gyromagnetic ratio (MHz/T)	6.266	16.546
Resonance frequency at 11.74 T (500MHz) (MHz)	73.578	194.317
Quadrupolar moment (m^2)	$-0.0808 \cdot 10^{30}$	$-4.01 \cdot 10^{30}$
Relative sensibility (${}^1\text{H} = 1.00$)	$8.50 \cdot 10^{-3}$	0.29

A-II-1. Composite electrolyte preparation

The aim was to prepare a composite electrolyte containing at least 50 wt% of LLZTO particles. This percentage was set from Zheng and Hu who demonstrated that ceramics percolation may be possible in such conditions. [46]

The question is what is the equivalent ceramic volume percentage?

Table A-II-1 is a summary of the density and the mass of the used materials.

Table A-II-1. Sum up of the set parameters.

	PEO	LiTFSI	LLZTO
$\rho (g \cdot cm^{-3})$	1.20	1.33	5.50
$m (g)$	0.50	0.20	0.78

The volume of the polymer electrolyte (V_p) was estimated by using the following Equation A-II-1,

$$V_p = \frac{m_{poe}}{\rho_{poe}} + \frac{m_{LiTFSI}}{\rho_{LiTFSI}} \quad A-II-1$$

And the volume of the ceramic particles (V_{LLZTO}) was estimated by the following Equation A-II-2,

$$V_p = \frac{m_{LLZTO}}{\rho_{LLZTO}} \quad A-II-2$$

Based on these results, the volume percentage of the ceramic particles ($wt\%_{LLZTO}$) was calculated by applying the following Equation A-II-3,

$$wt\%_{LLZTO} = \frac{V_{LLZTO}}{V_{LLZTO} + V_p} \quad A-II-3$$

Thus, as 0.78 g of LLZTO particles were mixed with 0.7 g of polymer electrolyte (PEO+LiTFSI), it corresponds to 52.7 wt%_{LLZTO} and it represents 20 vol%_{LLZTO}.

A-III-1. Lithium self-diffusion at room temperature (25° C)

Berthault *et al.* studied lithium isotopic exchanges occurring between a liquid electrolyte enriched in ^6Li and a silicon-based electrode. [16] At room temperature such exchanges were relatively fast.

Here, lithium isotopic exchanges are occurring between two solids. ToF-SIMS 2DLA scan was performed on the surface of the device from the ^6Li -foil to the polymer electrolyte, after 24 h of contact time at 25° C (Figure A-III-1).

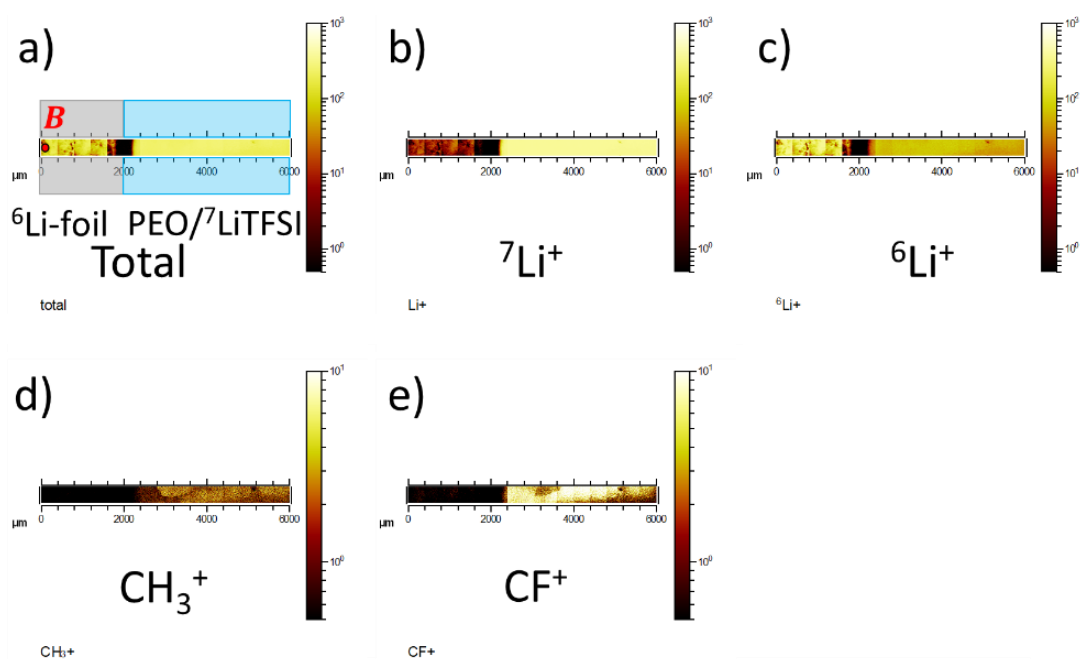


Figure A-III-1. ToF-SIMS 2DLA scan on the surface of the device from the ^6Li -foil to the polymer electrolyte, after 24 h of contact time at 25° C: a) Intensity of all the detected molecular fragments, b) Intensity of $^7\text{Li}^+$, and c) Intensity of $^6\text{Li}^+$ d) Intensity of CH_3^+ intensities, and e) Intensity of CF^+ .

Figure A-III-1.a corresponds to the sum of the intensity of all the detected molecular fragments. Between 1,600 and 2,300 μm no molecular fragment is detected. It is due to the 130 μm -thickness of the ^6Li -foil, creating shading effects. The ^6Li -foil can clearly be detected on Figure A-III-1.c. By applying formula, ^6Li and ^7Li were estimated along the polymer electrolyte (Figure A-III-2).

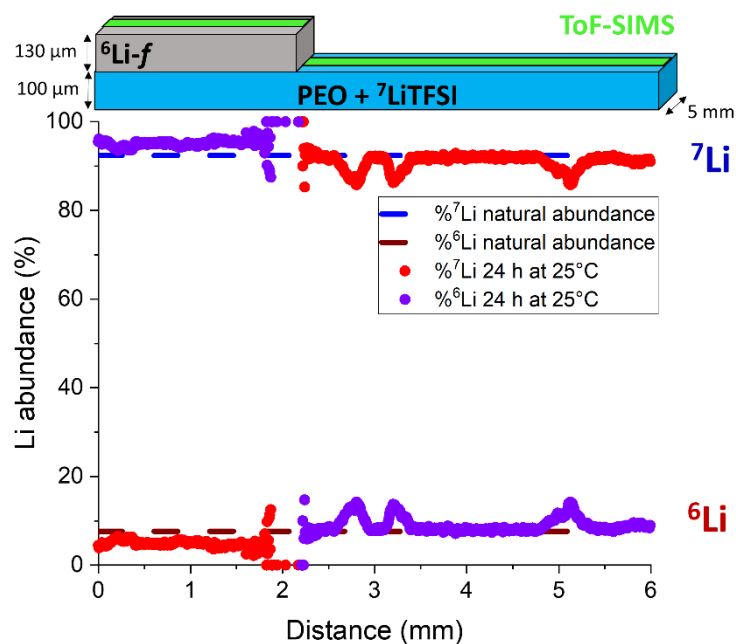


Figure A-III-2. Lithium self-diffusion at 25 °C in PEO/LiTFSI electrolytes analysed by ToF-SIMS after 24 h.

The green surfaces, first on top of the ${}^6\text{Li}$ -foil, and then on top of the polymer electrolyte were analysed by ToF-SIMS. According to ToF-SIMS results presented on Figure A-III-2, no self-diffusion occurs at room temperature between a lithium foil enriched in ${}^6\text{Li}$ and a polymer electrolyte at lithium natural isotopic abundance.

It is possible to wonder if an enrichment in ${}^6\text{Li}$ did not occur in the hidden area by the ${}^6\text{Li}$ -foil, and if longer contact time could lead to finally detect lithium self-diffusion. Thus, other experiments were carried out with a longer contact time of 88 h. Raw data are presented on Figure A-III-3. ToF-SIMS 2DLA scan was performed on the surface of the device from the ${}^6\text{Li}$ -foil to the polymer electrolyte, after 88 h of contact time at 25° C (Figure A-III-3).

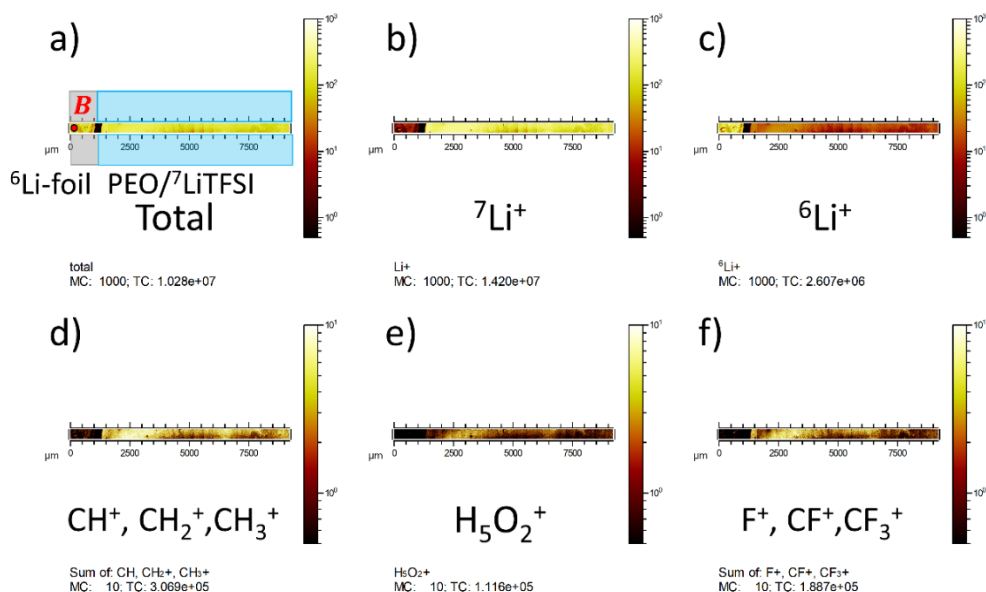


Figure A-III-3. ToF-SIMS 2DLA scan on the surface of the device from the ${}^6\text{Li}$ -foil to the polymer electrolyte, after 88 h of contact time at 25 °C: a) Intensity of all the detected molecular fragments, b) Intensity of ${}^7\text{Li}^+$, and c) Intensity of ${}^6\text{Li}^+$ d) Sum of the CH^+ , CH_2^+ and CH_3^+ intensities e) Sum of the F^+ , CF^+ and CF_3^+ intensities, and f) Intensity of H_5O_2^+ .

There is still a not analysed area from 1000 to 1400 μm (Figure A-III-3.a). The ${}^6\text{Li}$ -foil can clearly be detected on Figure A-III-3.c. By applying formula, ${}^6\text{Li}$ and ${}^7\text{Li}$ were estimated along the polymer electrolyte (Figure A-III-4).

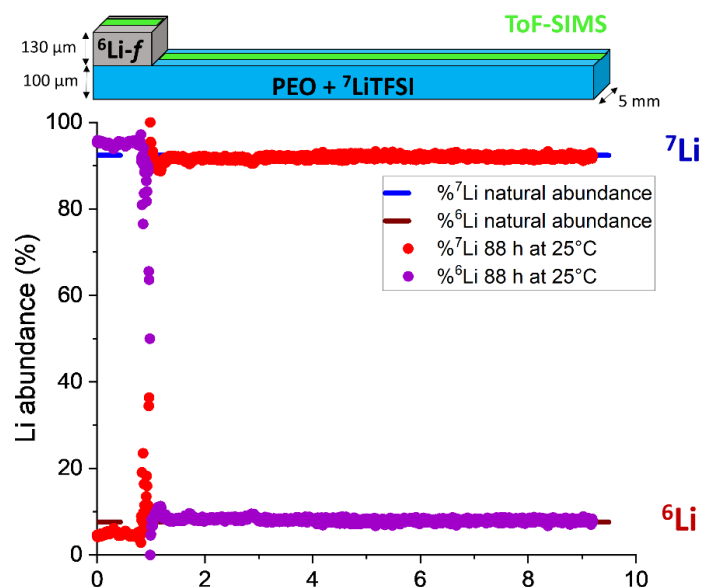


Figure A-III-4. Lithium self-diffusion at 25 °C in PEO/LiTFSI electrolytes analysed by ToF-SIMS after 24 h.

Even after 88 h of contact time, no lithium self-diffusion was detected (Figure A-III-4). However, the presence of the thick ${}^6\text{Li}$ -foil is still creating shading effects. Thus, the part of the polymer electrolyte close to the ${}^6\text{Li}$ -foil was not accessible. Having access to the enrichment in ${}^6\text{Li}$ values is crucial. That is why the ${}^6\text{Li}$ -foil will be removed in the future ToF-SIMS analyses.

A-III-2. Parametric studies to set appropriate numerical value of $D_{6Li^+}^p$, $D_{6Li^+}^f$, and ν

The *in-plane* device was let 72 h at 60° C. Numerical simulations (solid curves) performed with various set of parameters were compared with experimental data (red dotted curves). On each figure, the effect of one parameter was tested, while the others were set between each numerical simulation. On Figure A-III-5 and Figure A-III-6, the ${}^6\text{Li}^+$ self-diffusion coefficient into the polymer electrolyte ($D_{6Li^+}^p$) was tested.

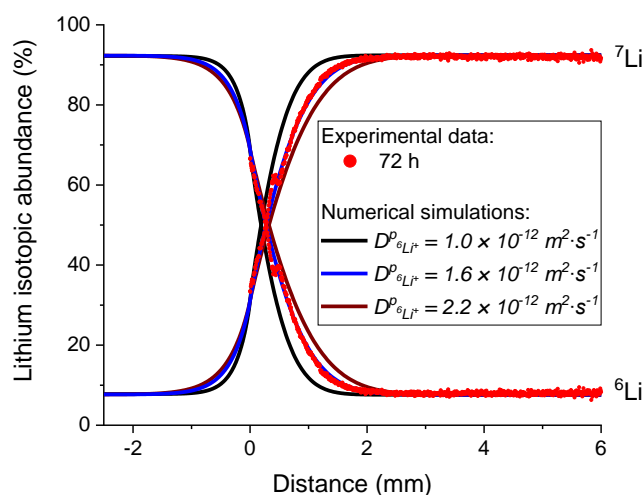


Figure A-III-5. Effect of $D_{6Li^+}^p$ variations. Comparison between on three numerical simulations (solid lines) and experimental data obtained after 72 h of contact time.

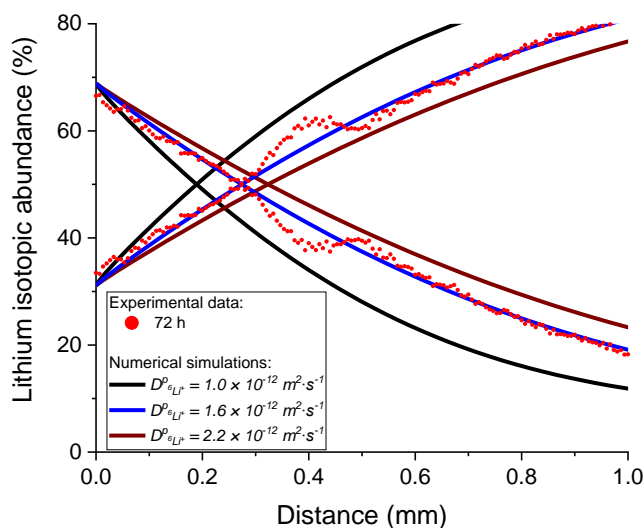


Figure A-III-6. Effect of $D_{6Li^+}^p$ variations. Zoom of Figure A-III-5.

On Figure A-III-5 and Figure A-III-6, the ${}^6\text{Li}^+$ self-diffusion coefficient into the polymer electrolyte ($D_{6Li^+}^p$) was set at either $1.0 \times 10^{-12} \text{ m}^2 \cdot \text{s}^{-1}$ (black curve) or $1.6 \times 10^{-12} \text{ m}^2 \cdot \text{s}^{-1}$ (blue curve) or $2.2 \times 10^{-12} \text{ m}^2 \cdot \text{s}^{-1}$ (brown curve). The other parameters $D_{6Li^+}^f$ and ν are set at $10^{-14} \text{ m}^2 \cdot \text{s}^{-1}$, and $2 \times 10^{-9} \text{ s}^{-1}$. According to the parameters of interested set on Figure III-9, the experimental curves (red dotted curves) match with numerical simulations while $D_{6Li^+}^p$ is equal to $1.6 \times 10^{-12} \text{ m}^2 \cdot \text{s}^{-1}$.

On Figure A-III-7 and Figure A-III-8, the ${}^6\text{Li}^+$ self-diffusion coefficient into the polymer electrolyte ($D_{6\text{Li}^+}^p$) was tested.

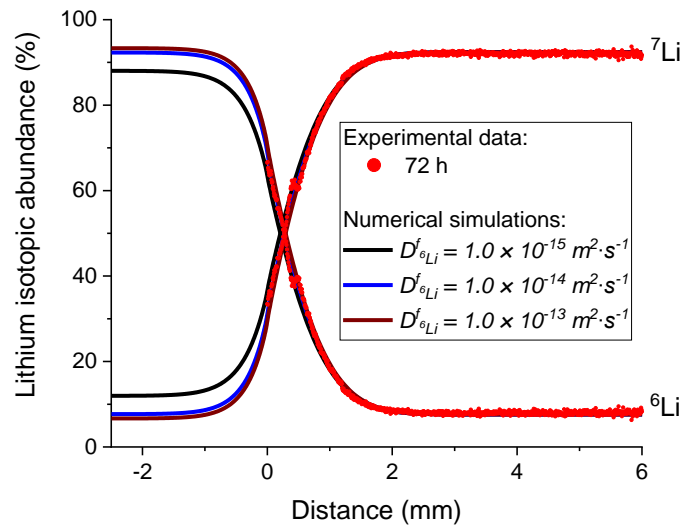


Figure A-III-7. Effect of $D_{6\text{Li}}^f$ variations. Comparison between on three numerical simulations (solid lines) and experimental data obtained after 72 h of contact time.

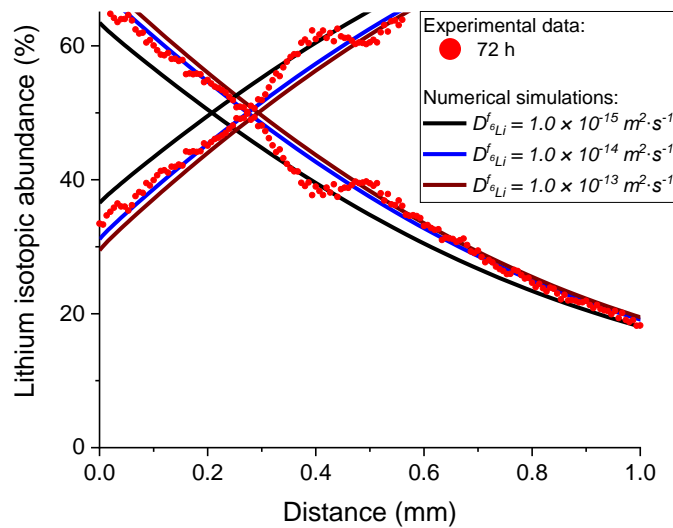


Figure A-III-8. Effect of $D_{6\text{Li}}^f$ variations. Zoom of Figure A-III-7.

On Figure A-III-7 and Figure A-III-8, the ${}^6\text{Li}^+$ self-diffusion coefficient into the polymer electrolyte ($D_{6\text{Li}}^f$) was set at either $1.0 \times 10^{-15} \text{ m}^2 \cdot \text{s}^{-1}$ (black curve) or $1.0 \times 10^{-14} \text{ m}^2 \cdot \text{s}^{-1}$ (blue curve) or $1.0 \times 10^{-13} \text{ m}^2 \cdot \text{s}^{-1}$ (brown curve). The other parameters $D_{6\text{Li}^+}^p$ and ν are set at $1.6 \times 10^{-12} \text{ m}^2 \cdot \text{s}^{-1}$ and $2 \times 10^{-9} \text{ s}^{-1}$. According to the parameters of interested set on Figure III-9, the experimental curves (red dotted curves) match with numerical simulations while $D_{6\text{Li}}^f$ is equal to $1.0 \times 10^{-14} \text{ m}^2 \cdot \text{s}^{-1}$.

On Figure A-III-9 and Figure A-III-10, the ${}^6\text{Li}^+$ self-diffusion coefficient into the polymer electrolyte (ν) was tested.

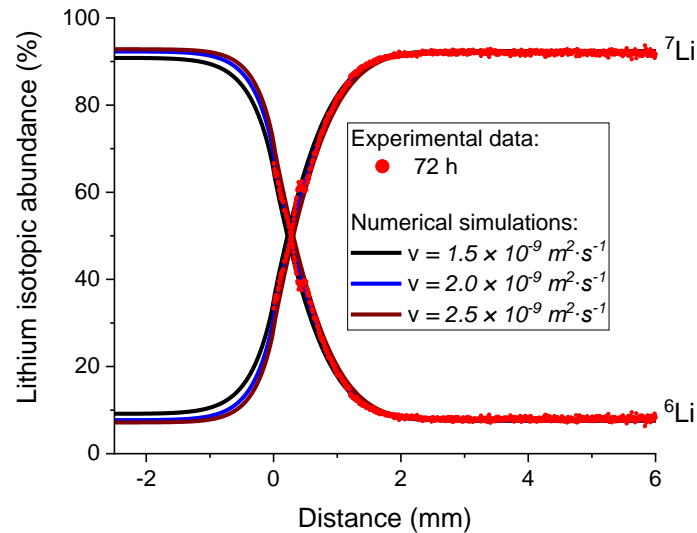


Figure A-III-9. Effect of ν variations. Comparison between on three numerical simulations (solid lines) and experimental data obtained after 72 h of contact time.

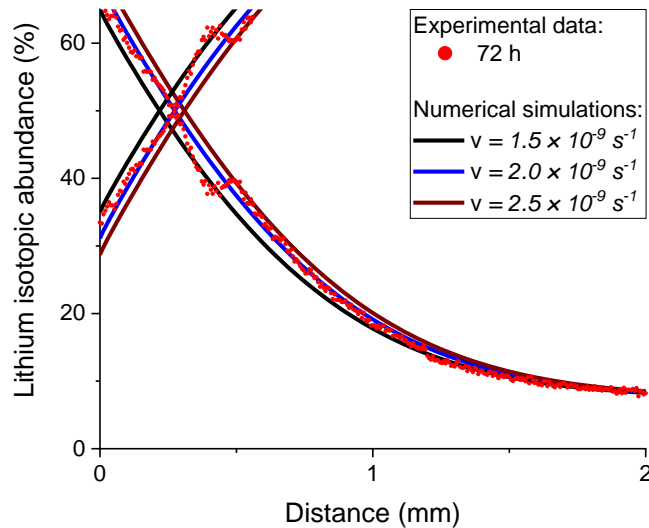


Figure A-III-10. Effect of ν variations. Zoom of Figure A-III-9.

On Figure A-III-9 and Figure A-III-10, the ${}^6\text{Li}^+$ self-diffusion coefficient into the polymer electrolyte (ν) was set at either $1.5 \times 10^{-9} \text{ s}^{-1}$ (black curve), $2 \times 10^{-9} \text{ s}^{-1}$ (blue curve) or $2.5 \times 10^{-9} \text{ s}^{-1}$ (brown curve). The other parameters $D_{6\text{Li}^+}^p$ and $D_{6\text{Li}^+}^f$ are set at $1.6 \times 10^{-12} \text{ m}^2 \cdot \text{s}^{-1}$ and $1.0 \times 10^{-14} \text{ m}^2 \cdot \text{s}^{-1}$. According to the parameters of interested set on Figure III-9, the experimental curves (red dotted curves) match with numerical simulations while ν is equal to $2 \times 10^{-9} \text{ s}^{-1}$.

The same comparisons between experimental data and simulated results were performed with experimental results obtained after 24 h, 120 h and 255 h of contact time. They led to the same conclusions that the highest consistency set of parameters was obtained by setting $D_{6\text{Li}^+}^f$, $D_{6\text{Li}^+}^p$ and ν at $10^{-14} \text{ m}^2 \cdot \text{s}^{-1}$, $1.6 \times 10^{-12} \text{ m}^2 \cdot \text{s}^{-1}$ and $2 \times 10^{-9} \text{ s}^{-1}$, respectively.

A-III-3. Conversion of ppm in Hz

The chemical shift δ_x of the contribution x is expressed in *ppm* on the high-resolution ssNMR spectrum. It is possible to convert it in *Hz* by using the following Equation A-III-1,

$$\delta_x = \frac{|(\nu_x - \nu_0)|}{\nu_0} \cdot 10^6 \quad \text{A-III-1}$$

with ν_0 the frequency of the contribution x in *Hz*, and ν_0 the reference Larmor frequency in *Hz*. Equation A-III-2 expresses the relation between frequency difference and chemical shift difference,

$$\Delta\nu = |(\nu_{sb} - \nu_0) - (\nu_{ip} - \nu_0)| = \left(\frac{|\nu_{sb} - \nu_0|}{\nu_0} \cdot 10^6 - \frac{|\nu_{ip} - \nu_0|}{\nu_0} \cdot 10^6 \right) \cdot \nu_0 \cdot 10^{-6} = |\delta_{sb} - \delta_{ip}| \cdot \nu_0 \cdot 10^{-6} \quad \text{A-III-2}$$

with ν_{sb} and ν_{ip} the frequencies of the spinning sideband and of the isotropic peak, respectively, in *Hz*, and δ_{sb} and δ_{ip} the chemical shifts of the spinning sideband and of the isotropic peak, respectively, in *ppm*. To sum up, the frequency separation $\Delta\nu$ between an isotropic peak and a spinning sideband is expressed by the following Equation A-III-3,

$$\Delta\nu = |\delta_{sb} - \delta_{ip}| \cdot \nu_0 \quad \text{A-III-3}$$

with $\Delta\nu$ in *Hz*, $|\delta_{sb} - \delta_{ip}|$ in *ppm* and ν_0 in *MHz*. In the case of probing ${}^7\text{Li}$ in a magnetic field of 11,74 T, $\nu_0 = 194.317 \text{ MHz}$. On both spectra Figure III-14, only one isotropic contribution was detected, which corresponds to the chemical environment of the lithium contained into the polymer electrolyte. On the left, the ${}^6\text{Li}$ spectrum is plotted. The chemical shift of the isotropic peak is -0.8932 ppm . On the right, the ${}^7\text{Li}$ spectrum is plotted. The chemical shift of the isotropic peak is -0.7894 ppm . In addition, spinning sidebands appear on the spectrum. The distance from the isotropic peak to the first spinning sidebands, Δ_{ip-sb} , were calculated in *ppm* (Equation A-III-4 and Equation A-III-5).

$$\Delta_{ip-sb \text{ right}} = |-0.7894 + 52.2615| = 51.5 \text{ ppm} \quad \text{A-III-4}$$

$$\Delta_{ip-sb \text{ left}} = |50.5265 + 0.7894| = 51.3 \text{ ppm} \quad \text{A-III-5}$$

As explained above, these distances in *ppm* can be converted in *Hz*. According to Equation A-III-3, $\Delta_{ip-sb \text{ right}}$ and $\Delta_{ip-sb \text{ left}}$, are equal to 10,002 *Hz* and 9,972 *Hz*, respectively. It matches with the set rotation speed of 10,000 *Hz*. Thus, the peaks indicated by asterisks are spinning sidebands.

A-IV-1. Polymer electrolyte and Li electrodes preparation

a. Preparation of the polymer electrolyte

The polymer electrolyte preparation was already described in chapter II. The dried polymer electrolyte film was 100 μm thick. Rectangles of $5 \times 13 \text{ mm}^2$ were cut in a dry room. The thickness was measured using a Digital Micrometer[®] 49-56 from Messmer Büchel[™]. The relative uncertainty provided by the supplier is in a [1;3] μm range.

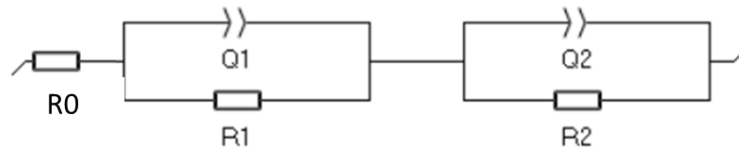
b. Preparation of Li electrodes

Lithium chunks enriched at 95.4% in ^6Li (Sigma-Aldrich, chunks, in mineral oil, 95.4% of ^6Li) were washed with cyclohexane (Sigma-Aldrich, anhydrous, 99.5%). Then, they were laminated to obtain a ^6Li -foil with a thickness of 130 μm .

Lithium foils are connected to nickel (Ni) tabs to be integrated into the electrical circuit. A copper grid was pressed on the lithium foils, and welded to Ni-tabs in order to connect them (Figure III-1 and Figure IV-2). The use of a grid ensures a homogeneous electric contact between the Li-foil and the Ni-tabs. The Ni-tabs allow the electrical connection after sealing out of the future packaging.

A-IV-2. Determination of the electrical equivalent circuit of each device.

a. Sandwich configuration (equivalent to standard coin cell assembly)



b. In-plane configuration

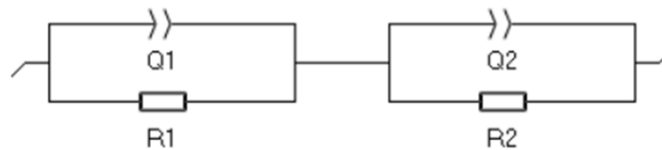


Figure A-IV-1. Electrical equivalent circuits used to fit the impedance spectra of a) the Li/PEO+LiTFSI/Li sandwich configuration equivalent to standard coin cell assembly and b) the in-plane configuration.

The electrical equivalent circuit presented on Figure A-IV-1.a was used to fit impedance spectra of the sandwich configuration. It is a mix of the ones proposed by Bouchet et al. [114], by Xie et al. [162] and by Han et al. [163]

The electrical equivalent circuit presented on Figure A-IV-1.b was used to fit impedance spectra of the *in-plane* configuration. It was proposed by Jeanne-Brou *et al.* in order to characterise the same design. [135] Notice that the bulk resistance of the electrolyte is here determined at the end of the semi-circle.

A-IV-3. Présentation du modèle utilisé

La variation en concentration en ion lithium est simulée de façon habituelle par une relation de Nernst-Planck :

$$\frac{\partial c_{Li}}{\partial t} = \underline{\nabla} \cdot \left(D \underline{\nabla} c_{Li} + F \frac{D c_{Li}}{RT} \underline{\nabla} V \right) \quad (1)$$

Le premier terme concerne la force motrice liée à la présence d'un gradient en concentration dans l'électrolyte, et le second terme résulte de la force motrice induite par un gradient de potentiel électrique.

En réalité, cette forme est une approximation d'une loi plus générale de mélange, basée sur le gradient des potentiels électrochimiques des composants de l'électrolyte.

Afin de comprendre la dynamique des électrolytes solides à base de polymère conducteur ionique, un modèle basé sur la théorie des polymères en solution [1] est proposé dans ces travaux.

Chaque flux va être écrit comme le produit d'un terme de mobilité et d'une force motrice électrochimique

$$\underline{J}_i = -\Lambda_i \underline{\nabla}(\mu_i + qZ_i V) \quad (2)$$

avec

$$\Lambda_i = \frac{\phi_i D_i}{k_B T} \quad (3)$$

Les concentrations, ou plutôt fractions volumiques, de la totalité des espèces chimiques de l'électrolyte sont résolues en respectant des règles de couplage entre les flux pour conserver les deux relations locales suivantes :

$$\sum_{i=1}^n \phi_i = 1 \quad (4)$$

$$\sum_{i=1}^n \underline{J}_i = 0 \quad (5)$$

Ainsi, pour n espèce chimique mélangées, la relation de conservation (3) permet de ne résoudre que $n - 1$ équations de continuité s'écrivant de la forme suivante :

$$\frac{\partial \phi_i}{\partial t} = -\underline{\nabla} \cdot \underline{J}_i + S_i \quad (6)$$

Avec les flux de mélange définis par la relation suivante :

$$\underline{J}_i = - \sum_j \Lambda_{ij}^{th} \underline{\nabla} \left(\frac{\partial \Delta \bar{G}}{\partial \phi_j} \right) - q \frac{\Lambda_i^V}{\Omega_i} \underline{\nabla} V \quad (7)$$

et S_i le terme source pouvant décrire un transfert aux interfaces du domaine ou des réactions chimiques liées au composé i .

Les flux de mobilités mutuelles thermodynamiques et de mobilités électriques s'écrivent souvent de la forme suivante :

$$\Lambda_{ij}^{th} = \sum_k \Lambda_k \Omega_k (\delta_{ik} - \phi_i) (\delta_{kj} - \phi_j) \quad (8)$$

$$\Lambda_i^V = \Omega_i \sum_k \left(\frac{Z_k}{\Omega_k} - \frac{\rho}{q} \right) \Lambda_k \Omega_k (\delta_{ik} - \phi_i) \quad (9)$$

Le potentiel chimique de mélange $\mu_j = \frac{\partial \Delta \bar{G}}{\partial \phi_j}$ s'écrit comme la dérivée de la densité d'énergie libre de Gibbs :

$$\Delta \bar{G} = k_B T \sum_{i=1}^n \left(\frac{\phi_i}{\Omega_i} \ln \phi_i + \frac{1}{2} \sum_{\substack{j \neq i \\ j=1}}^n \chi_{ij} \phi_i \phi_j \right) \quad (10)$$

Afin de simuler complètement le système, une équation permettant de résoudre le potentiel électrique dans l'électrolyte est nécessaire. Pour cela, l'équation locale de conservation de la charge est ajoutée au groupe d'équations de continuité :

$$\frac{\partial \rho}{\partial t} + \underline{\nabla} \cdot \left(\sum_i \underline{J}_i^{elec} \right) = 0 \quad (11)$$

Avec \underline{J}_i^{elec} la densité de courant associée au flux \underline{J}_i :

$$\underline{J}_i^{elec} = \frac{Z_i q}{\Omega_i} \underline{J}_i \quad (12)$$

Enfin, une propriété importante des électrolytes permet d'imposer l'électro-neutralité dans la majeure partie de l'électrolyte. En effet, seule une très fine couche d'interface avec les matériaux actifs perd cette électroneutralité (quelques nanomètres). Cette propriété peut être simplifiée par l'ajout d'une capacité à l'interface, en évitant cette résolution fine et exigeante en termes de maillage. Finalement, l'électroneutralité imposée permet d'ajouter deux simplifications :

$$\rho = q \sum_{i=1}^n \frac{Z_i \phi_i}{\Omega_i} = 0 \quad (13)$$

$$\frac{\partial \rho}{\partial t} = 0 \quad (14)$$

Afin de résumer le modèle ainsi défini, le modèle mathématique est appliqué à un électrolyte ternaire constitué d'ions lithium Li^+ , de contre-ions $TFSi^-$ et de polymère POE, avec les paramètres de charge effectives, respectivement, $Z_{Li^+} = 1$, $Z_{TFSi^-} = -1$ et $Z_{POE} = 0$:

$$\begin{aligned} \frac{\partial \phi_{Li^+}}{\partial t} &= -\nabla \cdot \underline{J}_{Li^+} + S_{Li^+} && \text{équation (6)} \\ \phi_{TFSi^-} &= \frac{\Omega_{TFSi^-}}{\Omega_{Li^+}} \phi_{Li^+} && \text{déduit de l'équation (13)} \\ \phi_{POE} &= 1 - \phi_{Li^+} \left(1 + \frac{\Omega_{TFSi^-}}{\Omega_{Li^+}} \right) && \text{déduit des équations (4) et (13)} \\ \underline{J}_{Li^+} &= -\sum_j \Lambda_{Li^+j}^{th} \nabla \left(\frac{\partial \Delta \bar{G}}{\partial \phi_j} \right) - q \frac{\Lambda_{Li^+}^V}{\Omega_{Li^+}} \nabla V && \text{équation (7)} \\ \underline{J}_{TFSi^-} &= -\sum_j \Lambda_{TFSi^-j}^{th} \nabla \left(\frac{\partial \Delta \bar{G}}{\partial \phi_j} \right) - q \frac{\Lambda_{TFSi^-}^V}{\Omega_{TFSi^-}} \nabla V && \text{équation (7)} \\ \nabla \cdot \left[q \sum_j \left(\frac{\Lambda_{Li^+j}^{th}}{\Omega_{Li^+}} - \frac{\Lambda_{TFSi^-j}^{th}}{\Omega_{TFSi^-}} \right) \nabla \left(\frac{\partial \Delta \bar{G}}{\partial \phi_j} \right) + \sigma \nabla V \right] &= 0 && \text{déduit des équations (7), (11),} \\ &&& \text{(12) et (14)} \\ \sigma &= q^2 \left(\frac{\Lambda_{Li^+}^V}{\Omega_{Li^+}^2} - \frac{\Lambda_{TFSi^-}^V}{\Omega_{TFSi^-}^2} \right) \end{aligned}$$

Dans le cas où la population de lithium est séparée en deux groupes isotopiques, dont les volumes et les charges effectifs sont égaux ($\Omega_{6Li^+} = \Omega_{7Li^+} = \Omega_{Li^+}$, $Z_{6Li^+} = Z_{7Li^+} = Z_{Li^+}$), le système à résoudre devient :

$$\begin{aligned} \frac{\partial \phi_{6Li^+}}{\partial t} &= -\nabla \cdot \underline{J}_{6Li^+} + S_{6Li^+} && \text{équation (6)} \\ \frac{\partial \phi_{7Li^+}}{\partial t} &= -\nabla \cdot \underline{J}_{7Li^+} + S_{7Li^+} && \text{équation (6)} \\ \phi_{TFSi^-} &= \frac{\Omega_{TFSi^-}}{\Omega_{Li^+}} (\phi_{6Li^+} + \phi_{7Li^+}) && \text{déduit de l'équation (13)} \\ \phi_{POE} &= 1 - (\phi_{6Li^+} + \phi_{7Li^+}) \left(1 + \frac{\Omega_{TFSi^-}}{\Omega_{Li^+}} \right) && \text{déduit des équations (4) et (13)} \\ \underline{J}_{6Li^+} &= -\sum_j \Lambda_{6Li^+j}^{th} \nabla \left(\frac{\partial \Delta \bar{G}}{\partial \phi_j} \right) - q \frac{\Lambda_{6Li^+}^V}{\Omega_{Li^+}} \nabla V && \text{équation (7)} \\ \underline{J}_{7Li^+} &= -\sum_j \Lambda_{7Li^+j}^{th} \nabla \left(\frac{\partial \Delta \bar{G}}{\partial \phi_j} \right) - q \frac{\Lambda_{7Li^+}^V}{\Omega_{Li^+}} \nabla V && \text{équation (7)} \\ \underline{J}_{TFSi^-} &= -\sum_j \Lambda_{TFSi^-j}^{th} \nabla \left(\frac{\partial \Delta \bar{G}}{\partial \phi_j} \right) - q \frac{\Lambda_{TFSi^-}^V}{\Omega_{TFSi^-}} \nabla V && \text{équation (7)} \\ \nabla \cdot \left[q \sum_j \left(\frac{\Lambda_{6Li^+j}^{th}}{\Omega_{Li^+}} + \frac{\Lambda_{7Li^+j}^{th}}{\Omega_{Li^+}} - \frac{\Lambda_{TFSi^-j}^{th}}{\Omega_{TFSi^-}} \right) \nabla \left(\frac{\partial \Delta \bar{G}}{\partial \phi_j} \right) + \sigma \nabla V \right] &= 0 && \text{déduit des équations (7), (11),} \\ &&& \text{(12) et (14)} \\ \sigma &= q^2 \left(\frac{\Lambda_{6Li^+}^V}{\Omega_{Li^+}^2} + \frac{\Lambda_{7Li^+}^V}{\Omega_{Li^+}^2} - \frac{\Lambda_{TFSi^-}^V}{\Omega_{TFSi^-}^2} \right) \end{aligned}$$

[1] Rubinstein & Colby « Polymer Physics » 2003

A-IV-4. Simplification du modèle de mélange

Dans cette partie, la simplification du modèle de mélange existante lorsque les concentrations en lithium sont considérées comme diluées permet de retrouver l'équation classique de diffusion de Nernst-Planck.

L'énergie libre de mélange de Gibbs peut être simplifiée par son terme d'énergie entropique, sans considérer la contribution des autres éléments :

$$\Delta\bar{G} \approx k_B T \frac{\phi_{\text{Li}^+} \ln \phi_{\text{Li}^+}}{\Omega_{\text{Li}^+}} + C$$

Et sa dérivée :

$$\frac{\partial \Delta\bar{G}}{\partial \phi_{\text{Li}^+}} \approx \frac{k_B T}{\Omega_{\text{Li}^+}} \ln \phi_{\text{Li}^+}$$

Dans cette approximation, les termes croisés peuvent être négligés dans l'équation du flux volumique :

$$\begin{aligned} \underline{J}_{\text{Li}^+} &\approx -\Lambda_{\text{Li}^+ j}^{th} \nabla \left(\frac{\partial \Delta\bar{G}}{\partial \phi_i} \right) - q \frac{\Lambda_{\text{Li}^+}^V}{\Omega_{\text{Li}^+}} \nabla V \\ \underline{J}_{\text{Li}^+} &\approx -\Lambda_{\text{Li}^+ \text{Li}^+}^{th} \frac{k_B T}{\Omega_i} \nabla (\ln \phi_i) - q \frac{\Lambda_{\text{Li}^+}^V}{\Omega_{\text{Li}^+}} \nabla V \end{aligned}$$

Les termes de mobilité mutuelle sont également simplifiés ce qui finalement donne les mobilités de l'autodiffusion :

$$\Lambda_{\text{Li}^+ \text{Li}^+}^{th} \approx \Lambda_{\text{Li}^+}^V \approx \Lambda_{\text{Li}^+} \Omega_{\text{Li}^+} = \frac{\Omega_{\text{Li}^+} \phi_{\text{Li}^+} D_{\text{Li}^+}}{k_B T}$$

En utilisant la relation mathématique suivante

$$\frac{\partial \ln \phi}{\partial x} = \frac{\partial \ln \phi}{\partial \phi} \frac{\partial \phi}{\partial x} = \frac{1}{\phi} \frac{\partial \phi}{\partial x}$$

Le flux peut s'écrire finalement de la manière suivante :

$$\underline{J}_{\text{Li}^+} \approx -\Lambda_{\text{Li}^+ \text{Li}^+}^{th} \frac{k_B T}{\Omega_{\text{Li}^+} \phi_{\text{Li}^+}} \nabla (\phi_{\text{Li}^+}) - q \frac{\Lambda_{\text{Li}^+}^V}{\Omega_{\text{Li}^+}} \nabla V$$

Ce qui permet de définir la relation connue

$$\underline{J}_{\text{Li}^+} \approx -D_{\text{Li}^+} \nabla (\phi_{\text{Li}^+}) - \frac{q \phi_{\text{Li}^+} D_{\text{Li}^+}}{k_B T} \nabla V$$

A-IV-5. Conductivité céramique dans le modèle sandwich

La théorie de mélange est appliquée dans le milieu céramique. La contre charge négative est portée par le réseau de matériaux, et est ramenée à une contre charge effective statique. Dans ces conditions, l'électroneutralité du matériau est maintenue en considérant une concentration en lithium stationnaire et homogène à tout moment de la simulation. Cependant des échanges ${}^6\text{Li}$ et ${}^7\text{Li}$ sont possibles.

La relation établie précédemment pour définir la conductivité est toujours valide et permet d'estimer un coefficient de diffusion pour les ions lithium :

$$\sigma = q^2 \left(\frac{\Lambda_{{}^6\text{Li}^+}^V}{\Omega_{{}^6\text{Li}^+}^2} + \frac{\Lambda_{{}^7\text{Li}^+}^V}{\Omega_{{}^7\text{Li}^+}^2} \right)$$

$$\sigma = \left(\frac{q}{\Omega_{\text{Li}}} \right)^2 \left(\Lambda_{{}^6\text{Li}^+}^V + \Lambda_{{}^7\text{Li}^+}^V \right)$$

avec la définition des coefficients de mobilité électrique $\Lambda_{{}^6\text{Li}^+}^V$ et $\Lambda_{{}^7\text{Li}^+}^V$ définis par l'équation 9, on peut écrire :

$$\Lambda_{{}^6\text{Li}^+}^V = \Omega_{{}^6\text{Li}^+} \left[\left(\frac{Z_{{}^6\text{Li}^+}}{\Omega_{{}^6\text{Li}^+}} \right) \Lambda_{{}^6\text{Li}^+} \Omega_{{}^6\text{Li}^+} (1 - \phi_{{}^6\text{Li}^+}) - \phi_{{}^6\text{Li}^+} \left(\frac{Z_{{}^7\text{Li}^+}}{\Omega_{{}^7\text{Li}^+}} \right) \Lambda_{{}^7\text{Li}^+} \Omega_{{}^7\text{Li}^+} \right]$$

$$\Lambda_{{}^7\text{Li}^+}^V = -\Omega_{{}^7\text{Li}^+} \left[\phi_{{}^7\text{Li}^+} \left(\frac{Z_{{}^6\text{Li}^+}}{\Omega_{{}^6\text{Li}^+}} \right) \Lambda_{{}^6\text{Li}^+} \Omega_{{}^6\text{Li}^+} - \left(\frac{Z_{{}^7\text{Li}^+}}{\Omega_{{}^7\text{Li}^+}} \right) \Lambda_{{}^7\text{Li}^+} \Omega_{{}^7\text{Li}^+} (1 - \phi_{{}^7\text{Li}^+}) \right]$$

Les coefficients d'auto-diffusion définis à l'équation 3 sont :

$$\Lambda_{{}^6\text{Li}^+} = \frac{\phi_{{}^6\text{Li}^+} D_{{}^6\text{Li}^+}}{k_B T}$$

$$\Lambda_{{}^7\text{Li}^+} = \frac{\phi_{{}^7\text{Li}^+} D_{{}^7\text{Li}^+}}{k_B T}$$

Ainsi,

$$\Lambda_{{}^6\text{Li}^+}^V = \Omega_{{}^6\text{Li}^+} \left[\Lambda_{{}^6\text{Li}^+} (1 - \phi_{{}^6\text{Li}^+}) - \phi_{{}^6\text{Li}^+} \Lambda_{{}^7\text{Li}^+} \right]$$

$$\Lambda_{{}^7\text{Li}^+}^V = -\Omega_{{}^7\text{Li}^+} \left[\phi_{{}^7\text{Li}^+} \Lambda_{{}^6\text{Li}^+} - \Lambda_{{}^7\text{Li}^+} (1 - \phi_{{}^7\text{Li}^+}) \right]$$

$$\Lambda_{{}^6\text{Li}^+}^V + \Lambda_{{}^7\text{Li}^+}^V = \frac{D_{{}^6\text{Li}^+} \Omega_{{}^6\text{Li}^+}}{k_B T} \left[\phi_{{}^6\text{Li}^+} (1 - \phi_{{}^6\text{Li}^+} - \phi_{{}^7\text{Li}^+}) + \phi_{{}^7\text{Li}^+} (1 - \phi_{{}^7\text{Li}^+} - \phi_{{}^6\text{Li}^+}) \right]$$

$$\Lambda_{{}^6\text{Li}^+}^V + \Lambda_{{}^7\text{Li}^+}^V = \frac{D_{{}^6\text{Li}^+} \Omega_{{}^6\text{Li}^+}}{k_B T} (\phi_{{}^6\text{Li}^+} + \phi_{{}^7\text{Li}^+}) (1 - \phi_{{}^7\text{Li}^+} - \phi_{{}^6\text{Li}^+})$$

Finalement, la conductivité s'écrit par la relation suivante :

$$\sigma = \left(\frac{q}{\Omega_{Li}} \right)^2 \frac{D_{\text{Li}^+} \Omega_{\text{Li}^+}}{k_B T} (\phi_{\text{Li}^+} + \phi_{\text{Li}^+}) (1 - \phi_{\text{Li}^+} - \phi_{\text{Li}^+})$$

Cela permet de définir le coefficient de diffusion au sein de la céramique par la relation suivante :

$$D_{\text{Li}^+} = \left(\frac{\Omega_{Li}}{q} \right)^2 \frac{\sigma k_B T}{\Omega_{\text{Li}^+} (\phi_{\text{Li}^+} + \phi_{\text{Li}^+}) (1 - \phi_{\text{Li}^+} - \phi_{\text{Li}^+})}$$

La somme des fractions volumiques des ions lithium peut être ramenée à la concentration en ions mobile au sein de la céramique par la relation suivante :

$$\phi_{\text{Li}^+} + \phi_{\text{Li}^+} = \Omega_{Li} C_{Li}^{cer} N_A$$

En remplaçant cette relation dans la formule précédente, et en modifiant $qN_A = F$, on peut écrire la diffusion en fonction de la conductivité mesurée et la concentration d'ions mobiles :

$$D_{\text{Li}^+} = \left(\frac{1}{F} \right)^2 \frac{\sigma RT}{C_{Li}^{cer} (1 - \Omega_{\text{Li}^+} C_{Li}^{cer} N_A)}$$

A-V-1. Determination of the electrical equivalent circuit of each device.

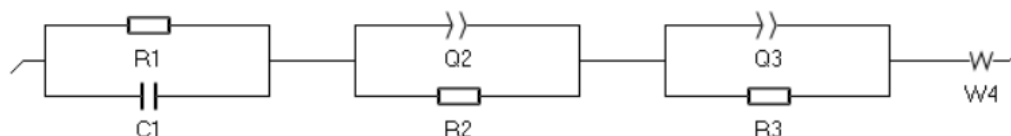


Figure A-V-1. Electrical equivalent circuits used to fit the impedance spectra of the dispersion device is based on the ones proposed in various studies. [21] [44] [164]

A-V-2. Segmentation results on each composite electrolyte.

Results from the segmentation protocol presented on Figure A-V-2, Figure A-V-3 and Figure A-V-4 are gather on Figure V-24. Average ${}^6\text{Li}$ abundance of the considered domain is indicated below each image. ${}^6\text{Li}$ abundance is mapped (a) and segmentation results of the ceramic particles (b), the polymer electrolyte matrix (c), and the interface between both materials located at the edge of the ceramic particles (d) are obtained.

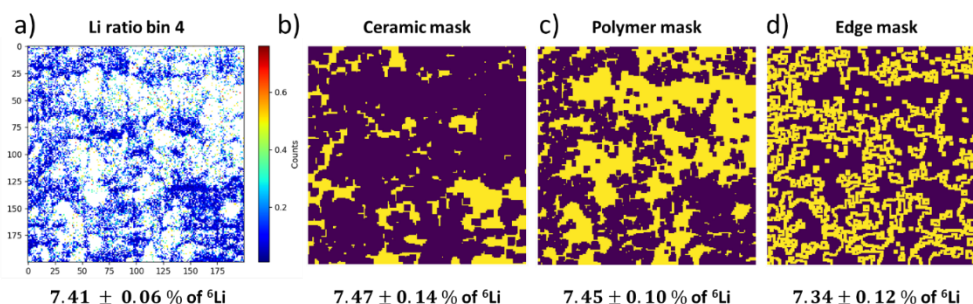


Figure A-V-2. ${}^6\text{Li}$ abundance mapping obtained by *o*-ToF-SIMS characterisations of C1.

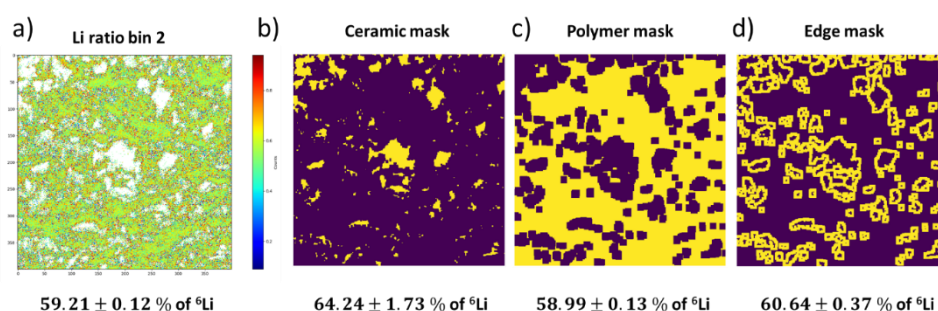


Figure A-V-3. ${}^6\text{Li}$ abundance mapping obtained by *o*-ToF-SIMS characterisations of C2.

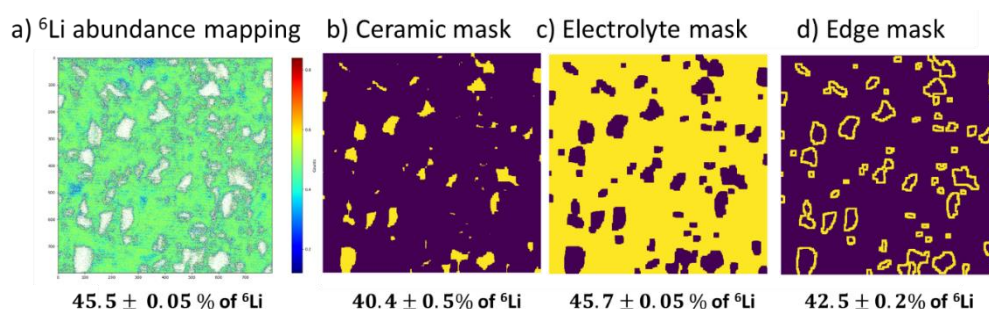


Figure A-V-4. ${}^6\text{Li}$ abundance mapping obtained by *o*-ToF-SIMS characterisations of C3.

Introduction

Le principal objectif de l'Accord de Paris adopté en 2015 réside dans la limitation du réchauffement climatique en dessous de 2 °C. Pour atteindre cet objectif, il est nécessaire de réduire de manière drastique les émissions de gaz à effet de serre. L'Accord de Paris a affirmé que les pays développés doivent fournir un soutien financier aux pays en développement pour faire face aux défis climatiques. Le développement des véhicules électriques est présenté comme l'une des voies potentielles pour réduire les émissions de gaz à effet de serre et est inclus dans de nombreux plans de transition énergétique établis par les pays développés. C'est cet essor des véhicules électriques qui conduit à celui des batteries lithium, point d'ancrage de ce travail de recherche.

Le développement des batteries tout-solide s'accélère avec de forts enjeux liés à l'amélioration de la sécurité et à l'augmentation des densités d'énergie stockées. Les industriels souhaitent commercialiser des batteries toujours plus denses en énergie, non inflammables et éviter les fuites d'électrolytes liquides en cas d'accident. L'utilisation d'électrolytes solides est l'une des solutions envisagées. Pour développer un électrolyte solide performant, différents critères sont considérés : sa conductivité ionique, le nombre de transport de l'ion lithium et sa stabilité électrochimique, thermique et mécanique. L'un des avantages potentiels des batteries tout-solide est de pouvoir utiliser du lithium métal à l'électrode négative. Cela permet d'augmenter les densités d'énergie car le lithium est un métal plus léger et plus réducteur que les matériaux d'électrode négative de la technologie Li-ion tels que le graphite ou le silicium. Son potentiel standard est de $-3,05 \text{ V/ESH}$ et sa capacité spécifique est de $3,8 \text{ Ah} \cdot \text{g}^{-1}$. Cependant, plusieurs verrous technologiques majeurs ont été identifiés parmi lesquels la formation de dendrites qui conduit à des courts-circuits, ou la génération de fortes résistances aux interfaces qui limite les échanges.

Dans ce travail de thèse divisé en cinq chapitres, nous étudions la mobilité du lithium dans un électrolyte solide polymère-céramique également nommé électrolyte composite ou hybride. Le marquage isotopique du lithium de certains composants d'une batterie, combiné à la spectrométrie de masse des ions secondaires par temps de vol (ToF-SIMS) et à la spectroscopie de résonance magnétique nucléaire à haute résolution en phase solide (ssNMR), ainsi qu'aux simulations numériques, sont les pierres angulaires de ce travail de recherche. Diverses études ont montré l'intérêt des méthodologies basées sur les spectroscopies ToF-SIMS et ssNMR afin de déterminer l'abondance isotopique du lithium dans des matériaux de batterie. En effet, notre groupe a déjà démontré la puissance de cette approche pour étudier les anodes de graphite et de silicium avec des électrolytes liquides, en particulier certaines recherches liées à la formation de l'interface électrolyte solide (SEI).

Chapitre I :

Ce premier chapitre explique l'intérêt des batteries à l'état solide. Une attention particulière est accordée aux électrolytes solides. Les travaux basés sur le marquage isotopique du lithium de matériaux de batterie sont discutés en détail. Les techniques de caractérisation avancées mises en œuvre pour suivre l'évolution spatiale et temporelle des isotopes du lithium sont également présentées et comparées.

De nos jours, la majorité des batteries Li-ion disponibles sur le marché contiennent un électrolyte liquide. Ces derniers évoluent continuellement pour devenir plus efficaces et fiables en termes de performances électrochimiques et de sécurité. Une technologie de batterie fondée sur un électrolyte solide pourrait pallier les limites des batteries Li-ion. Cependant, les électrolytes solides doivent encore être améliorés pour atteindre les propriétés et performances ciblées. Parmi tous les électrolytes solides, une dispersion de céramiques conductrices ioniques dans une matrice d'électrolyte polymère offre des perspectives significatives en vue d'une commercialisation des batteries « tout-solide » grâce à son potentiel pour améliorer la sécurité des batteries et augmenter leur densité énergétique.

Table. Avantages et inconvénients d'un électrolyte polymère et céramique.

Electrolyte polymère (POE + LiTFSI)	Electrolyte céramique (LLZTO)
Avantages	
<ul style="list-style-type: none"> - Inflammables comparés aux électrolytes liquides et non-volatiles - Conductivité électronique négligeable 	
<ul style="list-style-type: none"> - Faible résistance aux interfaces avec les matériaux d'électrode - Flexible, facile à mettre en œuvre - Préparation à des températures comprises entre 25 et 60 °C 	<ul style="list-style-type: none"> - Forte résistance aux interfaces avec les matériaux d'électrode - Difficile à mettre en œuvre - Frittage à haute température - Fragile
<ul style="list-style-type: none"> - Faible conductivité ionique ($< 10^{-4} S \cdot cm^{-1}$) - Formation de dendrites de lithium possible - Faible stabilité thermique et chimique 	<ul style="list-style-type: none"> - Conductivité ionique élevée ($10^{-3} - 10^{-2} S \cdot cm^{-1}$) - Permet l'utilisation de lithium métal - Bonne stabilité thermique, chimique et mécanique
Inconvénients	
<ul style="list-style-type: none"> - Conductivité ionique toujours faible par rapport aux électrolytes liquides 	

Les batteries « tout-solide » sont une alternative attrayante aux batteries Li-ion traditionnelles, grâce à leur densité énergétique plus élevée et sécurité renforcée. L'un des principaux objectifs est de développer des batteries « tout-solide » contenant du lithium métal à l'anode. Les électrolytes solides composites sont particulièrement prometteurs pour le développement des batteries « tout-solide » car ils combinent les avantages à la fois des électrolytes solides céramiques et des électrolytes solides polymères. Cependant, en raison de résistances élevées aux interfaces entre les deux milieux organiques/inorganiques, ils sont connus pour avoir une faible conductivité ionique comparés aux électrolytes liquides traditionnels. Par conséquent, il est essentiel de mieux comprendre les paramètres qui contrôlent la dynamique du lithium au sein de ces matériaux composites. Une meilleure compréhension des mécanismes régissant le transport des ions lithium au sein de ces matériaux et à travers les interfaces existantes est nécessaire. Le comportement du lithium

dans le volume et aux interfaces reste peu clair et nécessite une compréhension plus approfondie.

Une méthode pour étudier les mécanismes de transport du lithium dans ces matériaux solides contenant déjà du lithium consiste à réaliser des expériences de traçage isotopique. Ces expériences reposent sur l'utilisation de matériaux enrichis en ${}^6\text{Li}$. Certaines techniques de caractérisation avancées permettant de détecter simultanément ou indépendamment les isotopes de lithium ${}^7\text{Li}$ et ${}^6\text{Li}$ ont été brièvement détaillées. Le choix de la technique utilisée dépendra de la nature du matériau, ainsi que des informations requises. Un résumé des divers avantages et inconvénients liés à chaque technique est fourni. Leurs applications ont été illustrées au travers d'articles pertinents impliquant l'utilisation du marquage isotopique du lithium. À noter que celui-ci est utilisé pour l'étude des matériaux de batterie seulement depuis 2011. Tous ces travaux de recherche visent à une meilleure compréhension de la dynamique du lithium dans les matériaux de batterie. Par exemple, l'estimation du coefficient d'autodiffusion du lithium, le choix des meilleures couches minces perméables, les mécanismes de formation de l'interface électrolyte solide (SEI) et l'estimation de son épaisseur ont pu être étudiés avec succès. De plus, les compositions d'électrodes ou d'électrolytes solides composites pourraient être optimisées afin d'améliorer les performances électrochimiques des dispositifs. Enfin, la formation de dendrites, a été étudiée pour mieux comprendre ce processus indésirable.

Par définition, des isotopes sont liés au même noyau. Ils ont le même nombre de protons (Z) mais un nombre différent de neutrons (N), ce qui entraîne une différence de masse. Dans le cas du lithium, il existe deux isotopes stables, ${}^6\text{Li}$ et ${}^7\text{Li}$. Leur masse (Z+N) diffère de la masse d'un neutron. Notons que les isotopes d'un noyau présentent des propriétés chimiques similaires car ils ont le même nombre de protons. L'abondance d'un élément fait référence à sa proportion sur Terre (à l'état naturel) ou dans un matériau. Ici, l'abondance isotopique est définie comme la quantité relative d'un isotope par rapport à la quantité totale de tous les isotopes du même atome.

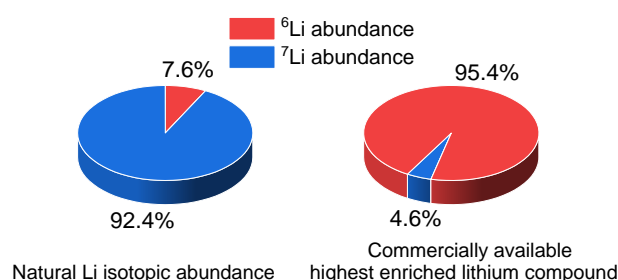


Figure. Abondance isotopique naturelle du lithium dans les composés conventionnels par rapport aux composés de lithium les plus enrichis disponibles commercialement.

D'une part, lorsque notre travail fait référence à un composé avec une abondance isotopique naturelle du lithium, les pourcentages de $\% {}^6\text{Li}$ et de $\% {}^7\text{Li}$ valent 7,6% pour $\% {}^6\text{Li}$ et 92,4% pour de $\% {}^7\text{Li}$. D'autre part, des composés disponibles commercialement contenant 95,4% de ${}^6\text{Li}$ et 4,6% de ${}^7\text{Li}$ ont été utilisés pour préparer des matériaux enrichis en isotopes de lithium à divers niveaux.

Chapitre II :

Le deuxième chapitre, dont les résultats ont été publiés, est fondamental dans le sens où les chapitres suivants reposent sur le développement des méthodologies mises en œuvre. Ce chapitre est fortement inspiré de notre publication : “Lithium Self-Diffusion in a Polymer Electrolyte for Solid-State Batteries: ToF-SIMS/ssNMR Correlative Characterization and Modeling Based on Lithium Isotopic Labeling” publiée dans ACS Applied Material & Interfaces en 2023.

Il présente les matériaux étudiés et les techniques utilisées. Le traçage isotopique du lithium est un outil puissant pour mieux comprendre sa dynamique dans les matériaux d'électrode pour batterie ou les électrolytes liquides ou solides. Plus précisément, il permet d'étudier le comportement du lithium aux différentes interfaces présentes dans un système électrochimique. Tout d'abord, le polymère, le sel de lithium et la céramique conductrice ionique étudiés dans ce travail sont présentés. Des tests électrochimiques sont également décrits. Ensuite, les paramètres les plus pertinents des techniques ToF-SIMS et ssNMR sont déterminés pour une caractérisation efficace des isotopes du lithium. Ces méthodologies fournissent des estimations précises de l'abondance isotopique du lithium dans les matériaux lithiés. Elles sont validées en les appliquant à des électrolytes polymères présentant différentes abondances de ^6Li pour en démontrer la robustesse.

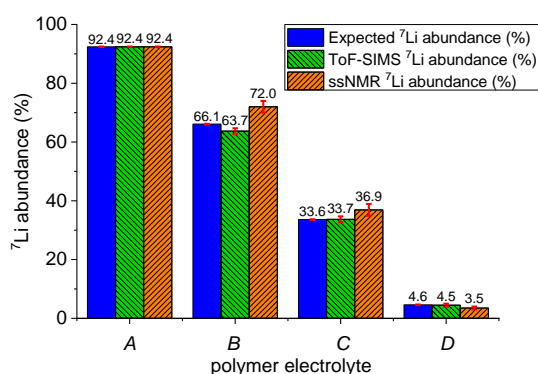


Figure. Comparaison des abondances attendues de ^7Li (barres bleues) avec celles estimées par ToF-SIMS (barres vertes) ou par ssNMR (barres orange).

Il a été démontré que les caractérisations par ToF-SIMS et par ssNMR peuvent offrir des estimations précises de l'abondance isotopique du lithium avec une incertitude de 1% et 2%, respectivement. Pour atteindre cette haute précision, les méthodologies prennent en compte les conditions d'acquisition ainsi que les étapes de traitement des données. Les deux techniques avancées sont complémentaires. D'une part, la technique ToF-SIMS fournit des informations chimiques locales notamment la composition de la surface. Des fragments moléculaires sont détectés et leurs abondances sont moyennées sur une zone micrométrique. L'estimation de l'abondance isotopique du lithium est basée sur les intensités des fragments moléculaires $^6\text{Li}^+$ et $^7\text{Li}^+$. D'autre part, les caractérisations de ssNMR du ^6Li et du ^7Li donnent accès à des informations globales sur les environnements chimiques du lithium. L'abondance isotopique du lithium peut également être estimée en sondant les spectres de ssNMR du ^6Li et du ^7Li . De plus, la quantification des isotopes du lithium est possible, ce qui n'est pas le cas avec les caractérisations par ToF-SIMS. Il convient de noter que ces méthodologies peuvent être appliquées à d'autres matériaux lithiés.

Chapitre III :

Le troisième chapitre vise à étudier la dynamique du lithium dans un électrolyte polymère (POE+LiTFSI) à 60°C. Dans cette configuration nommée *in-plane*, la détermination du coefficient d'auto-diffusion du lithium devrait être facilitée. Cela est réalisé en combinant les résultats expérimentaux de ToF-SIMS avec des simulations numériques.

Les méthodologies développées au chapitre II sont utilisées pour décrire les échanges isotopiques de lithium entre un feuillard de lithium enrichie à 95,4% en ^6Li et l'électrolyte polymère. L'utilisation de ^6Li -métal permet de suivre le lithium dans un matériau contenant déjà du lithium à une abondance naturelle. De plus, une approche par modélisation fondée également sur le marquage isotopique du lithium offre une compréhension plus approfondie du comportement du lithium dans chaque matériau et aux interfaces en fournissant des dynamiques de transfert à l'interface et de l'autodiffusion du lithium dans les deux matériaux.

À partir de la comparaison entre les résultats expérimentaux et les simulations numériques, le modèle présentant la plus grande cohérence a été obtenu en réglant les coefficients de diffusion $D_{6\text{Li}}^f$, $D_{6\text{Li}^+}^p$ et la fréquence de transfert ν à $10^{-14} \text{ m}^2 \cdot \text{s}^{-1}$, $1.6 \times 10^{-12} \text{ m}^2 \cdot \text{s}^{-1}$ et $2 \times 10^{-9} \text{ s}^{-1}$, respectivement. Les résultats suivants ont été obtenus avec cet ensemble spécifique de paramètres.

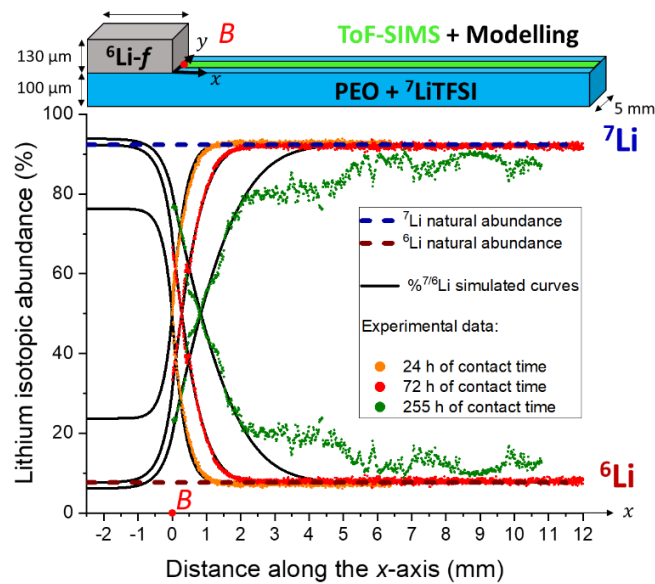


Figure. Comparaison des profils d'abondance isotopique du lithium à 60 °C dans un électrolyte polymère déterminés par ToF-SIMS (lignes pointillées colorées) et simulés (lignes noires continues) à trois temps de contact différents de 24h, 72h et 255h. Chaque analyse a été réalisée sur des échantillons différents.

Les échanges spontanés de lithium entre les deux matériaux ont été simulés à 60 °C après 24h, 72h et 255h de temps de contact. Les règles régissant la dépendance de la dynamique des échanges de lithium en fonction de la température ont pu être représentées à l'aide d'un modèle prenant en compte le traçage isotopique du lithium.

Chapitre IV :

Dans le quatrième chapitre, deux configurations plus complexes sont étudiées. La configuration *in-plane* correspond à celle présentée dans le chapitre III mais une tension constante est appliquée en plus de la température. Une configuration *sandwich* est également réalisée afin d'introduire une pastille céramique conductrice d'ions lithium entre deux couches d'électrolyte polymère. La dynamique du lithium est étudiée après l'application d'une densité de courant constante dans ce cas. Pour ces deux configurations, une électrode positive en lithium enrichi à 95,4% en ${}^6\text{Li}$ et une électrode négative en lithium à l'abondance isotopique naturelle (7,6% de ${}^6\text{Li}$) sont utilisées pour favoriser la migration de ${}^6\text{Li}$ dans le système en appliquant une contrainte électrique adaptée. Des caractérisations par spectroscopie d'impédance sont également mises en œuvre pour accéder à la conductivité des dispositifs. Des modèles numériques décrivant la dynamique du lithium sous contrainte électrique sont utilisés pour mieux comprendre le comportement du lithium au sein des différents dispositifs étudiés. Un modèle conventionnel basé sur la théorie de mélange et un modèle plus avancé permettant de mettre en œuvre le traçage isotopique du lithium sont mis en œuvre. Les résultats simulés de la dynamique isotopique du lithium sont enfin comparés aux résultats expérimentaux.

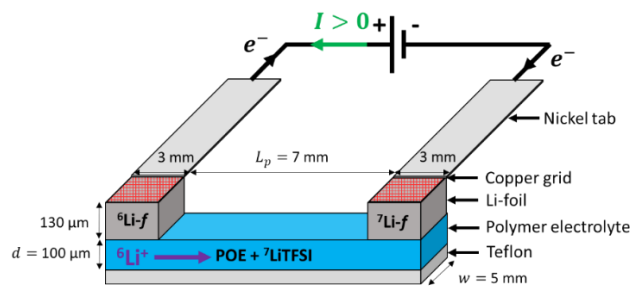


Figure. Configuration *in-plane* composée d'un feuillard de ${}^6\text{Li}$ et de ${}^7\text{Li}$ collés à la surface de chaque extrémité de l'électrolyte polymère. Un circuit électrique externe les relie.

Les résultats des analyses par ToF-SIMS en ssNMR sont présentés ci-dessous.

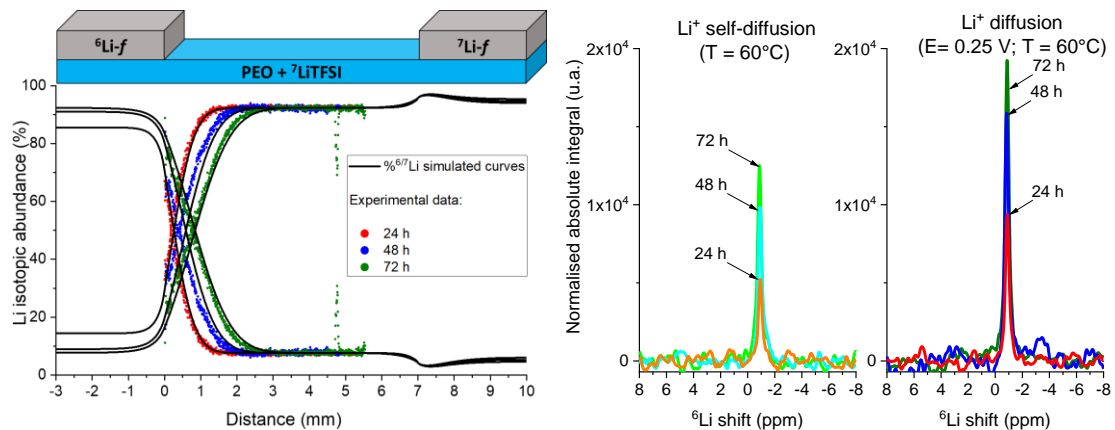


Figure. A) Profils des abondances isotopiques déterminées par ToF-SIMS (en pointillé) et par simulation (courbes noires) après l'application d'une tension constante. B) Spectres du ${}^6\text{Li}$ obtenus par ssNMR : Comparaison entre des échantillons de référence (juste étuvés à 60°C) avec des échantillons sous tension à 60°C pendant 24h, 48h ou 72h.

Les profils de migration des ions ${}^6\text{Li}^+$ ont été obtenus en combinant les cartographies ToF-SIMS des ions ${}^6\text{Li}^+$ et ${}^7\text{Li}^+$ après l'application d'une tension constante de $0,25\text{ V}$ à $60\text{ }^\circ\text{C}$ pendant 24 h , 48 h et 72 h . Plus le temps d'application de la tension est grand, plus le front de diffusion se décale vers la droite. Les mêmes échantillons ainsi que les échantillons de référence ont été caractérisés par ssNMR pour déterminer l'abondance isotopique globale en lithium.

En complément de ces caractérisations, un modèle développé au CEA en parallèle de ma thèse permet de modéliser la diffusion du lithium dans de telles conditions et notamment de déterminer le courant d'échange aux interfaces (i_{BV}). Pour étudier la dynamique des isotopes du lithium dans les systèmes étudiés, les géométries sont implémentées dans COMSOL Multiphysics et un modèle de mélange isotopique fondé sur l'équation thermodynamique du mélange prend en compte le traçage isotopique du lithium.

La configuration *sandwich* contient notamment une pastille céramique conductrice ionique, $\text{Li}_{6.4}\text{La}_3\text{Zr}_{1.4}\text{Ta}_{0.6}\text{O}_{12}$, entre deux couches d'électrolyte polymère. Elle est présentée dans la figure ci-dessous.

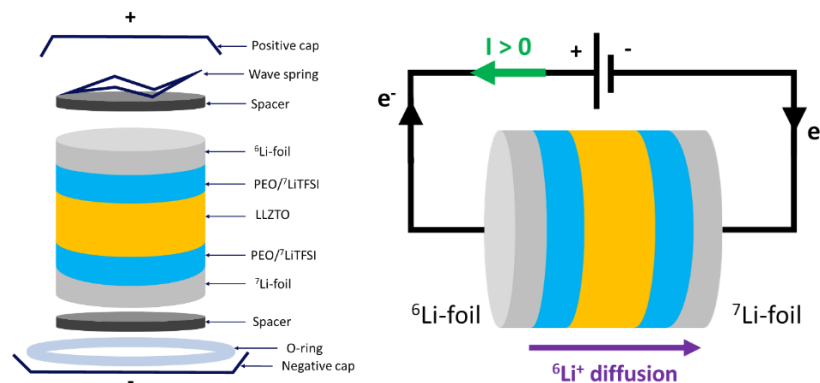
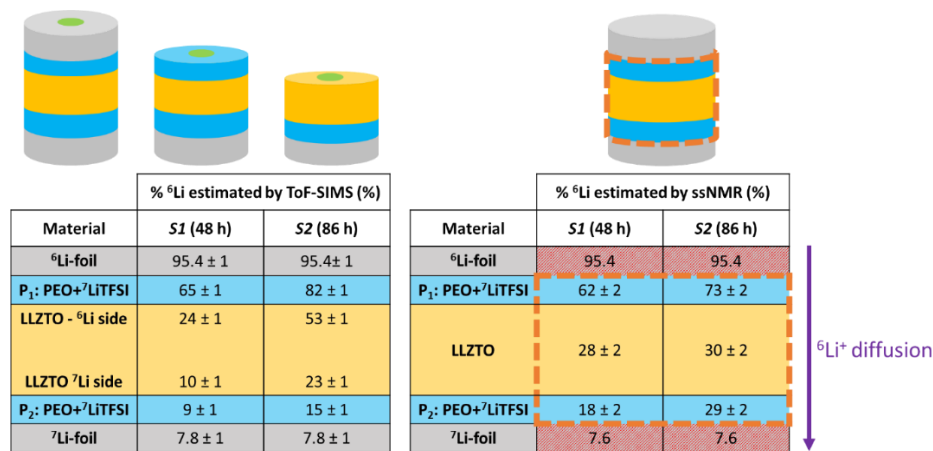


Figure. Schéma du dispositif sandwich composé d'une pastille céramique placée entre deux couches d'électrolyte polymère assemblées dans une pile bouton.

L'objectif d'un tel dispositif est de faciliter les caractérisations du comportement du lithium aux différentes interfaces. Le tableau ci-dessous confronte les estimations d'abondance en ${}^6\text{Li}$ des couches composant S1 et S2 par ToF-SIMS et par ssNMR.

Tableau. Récapitulatif des estimations des abondances en ${}^6\text{Li}$ par ToF SIMS et par ssNMR après avoir appliqué une densité de courant constante de $50 \mu\text{A} \cdot \text{cm}^{-2}$ pendant 48h sur S1 et pendant 86h sur S2.



Le principal résultat est que dans les deux cas (S1 et S2), l'abondance en ${}^6\text{Li}$ de P2 est supérieure à l'abondance isotopique naturelle du lithium en ${}^6\text{Li}$. Cela constitue une preuve que le lithium migre à travers toutes les couches dans un tel dispositif lors de l'application d'une densité de courant constante de $50 \mu\text{A} \cdot \text{cm}^{-2}$.

Les abondances en ${}^6\text{Li}$ issues des simulations sont déterminées à partir de la fraction volumique simulée de chaque isotope du lithium.

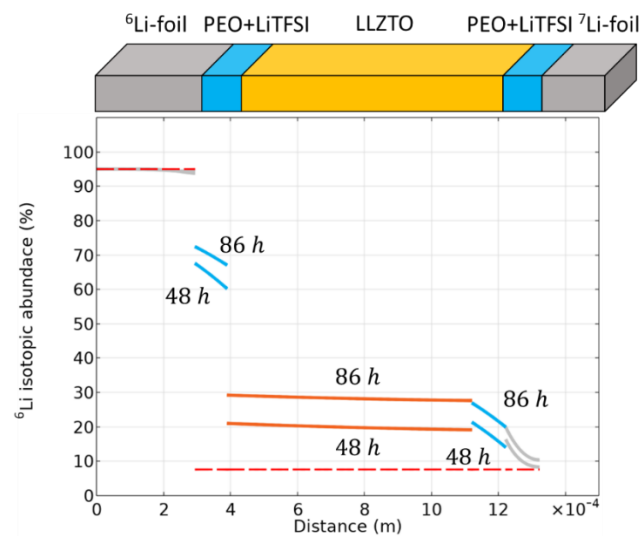


Figure. Variations de l'abondance de ${}^6\text{Li}$ dans chaque composant simulée après l'application d'une densité de courant constante de $50 \mu\text{A} \cdot \text{cm}^{-2}$ sur un dispositif en sandwich pendant 48h ou 86h à 60°C .

En résumé, la migration de Li^+ dans un dispositif sous tension à 60°C a été caractérisée en ayant recours aux échanges isotopiques de lithium. Les résultats expérimentaux ont permis de développer un modèle de mélange isotopique pour simuler la dynamique du lithium, en particulier aux interfaces Li-métal/polymère et polymère/céramique. Sur la base de ces résultats, la dynamique du lithium peut être étudiée dans un électrolyte composite plus complexe.

Chapitre V :

Pour finir, dans ce dernier chapitre, une matrice d'électrolyte polymère contenant une dispersion de particules de céramique est étudiée. Une telle configuration, logiquement nommée *dispersion*, présente des perspectives prometteuses dans le domaine des applications de batteries tout-solide. Elle est schématisée dans la figure ci-dessous.

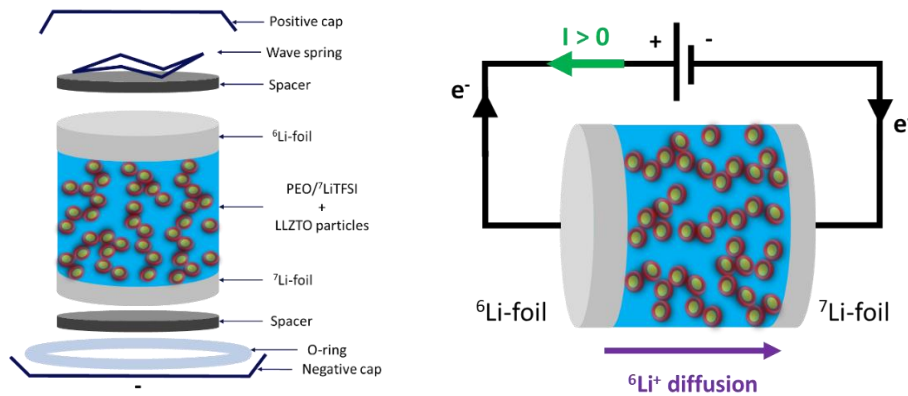


Figure. Schéma de la dispersion composée d'un électrolyte polymère (PEO/LiTFSI) contenant 20% en volume de particules céramiques submicroniques (LLZTO).

Après l'application d'une densité de courant constante, l'abondance en ${}^6\text{Li}$ est déterminée par ssNMR. Parallèlement, une collaboration avec la société Orsay Physics permet d'explorer la pertinence des caractérisations par ToF-SIMS orthogonal (o-ToF-SIMS) pour obtenir une résolution latérale améliorée par rapport aux analyses ToF-SIMS conventionnelles. Les abondances estimées de ${}^6\text{Li}$ sont résumées ci-dessous.

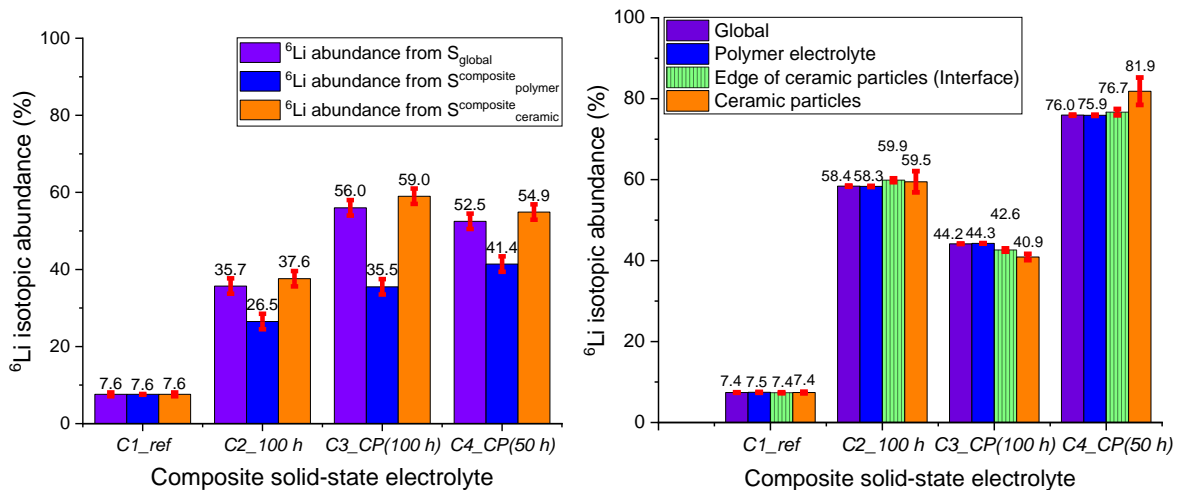


Figure. Abondance en ${}^6\text{Li}$ déterminée dans chaque échantillon et dans chaque domaine par ssNMR (gauche) et par o-ToF-SIMS (droite). C1 est utilisé comme échantillon de référence à l'abondance isotopique naturelle.

Les résultats obtenus par ssNMR et o-ToF-SIMS sont en bon accord. Globalement, les particules céramiques sont plus enrichies en ${}^6\text{Li}$ que l'électrolyte polymère. Ainsi, les ions ${}^6\text{Li}^+$ semblent diffuser préférentiellement au travers des particules de céramique.

À partir des cartographies de l'abondance en ${}^6\text{Li}$ obtenues par o-ToF-SIMS, un programme de segmentation sur Python permet de distinguer trois domaines : les particules céramiques, la matrice d'électrolyte polymère et le bord des particules de céramique.

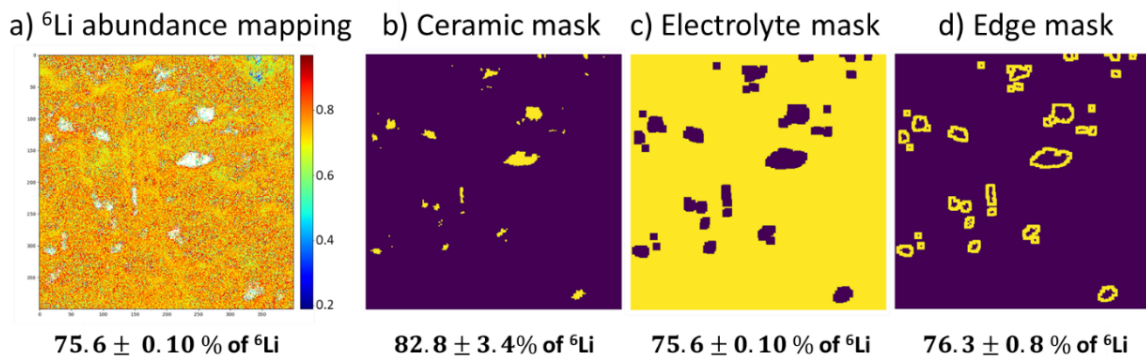


Figure. a) Cartographie de l'abondance de ${}^6\text{Li}$ obtenue par les caractérisations o-ToF-SIMS de C4. Résultats de segmentation : b) les particules de céramique, c) la matrice d'électrolyte polymère et d) le bord des particules de céramique. Les domaines sélectionnés sont remplis en jaune. L'abondance moyenne de ${}^6\text{Li}$ du domaine considéré est indiquée sous chaque image.

En résumé, il a été confirmé par la ssNMR et par l'o-ToF-SIMS que les ions ${}^6\text{Li}^+$ diffusent de manière préférentielle à travers les particules de céramique. La technique o-ToF-SIMS est puissante pour imager les particules de céramique. L'étude de la percolation des céramiques serait la prochaine étape pour mieux comprendre la dynamique du lithium. Une approche par modélisation appliquée à cette géométrie spécifique pourrait apporter des informations complémentaires.

Conclusion

Grâce à ce travail de recherche, des méthodologies basées sur les spectroscopies ToF-SIMS et ssNMR ont été mises en place pour déterminer avec précision l'abondance isotopique du lithium dans des électrolytes solides. Des échanges des isotopes du lithium ont été détectés à 60°C , sans l'application d'une force électrochimique. Ces échanges spontanés ont été suivis expérimentalement au cours du temps et modélisés. Diverses géométries (*in-plane*, *sandwich* et *dispersion*) de complexité croissante ont été caractérisées pour comprendre étape par étape les mécanismes de diffusion du lithium, notamment aux différentes interfaces. Les résultats finaux montrent qu'un enrichissement plus élevé en ${}^6\text{Li}$ est détecté dans les particules de céramique par rapport à l'électrolyte polymère. Cependant aucune amélioration des performances électrochimiques n'a été obtenue avec l'ajout de particules de céramique, d'après les mesures de spectroscopie d'impédance. Parallèlement, des modèles prenant en compte le marquage isotopique du lithium et la thermodynamique des polymères en solution ont été développés. La comparaison des résultats expérimentaux aux simulations numériques a permis d'optimiser les modèles. Il est important de noter que ces méthodologies établies peuvent être étendues à d'autres géométries ou d'autres matériaux lithiés. Ce travail confirme que pour concevoir des électrolytes solides performants, les matériaux composites doivent être caractérisés plus en profondeur et l'ingénierie de surface doit être améliorée.

